MESOSCOPIC MODELING OF CAPILLARITY-WETTABILITY INTERACTION

A thesis submitted in partial fulfillment of the requirements for the degree of

DOCTOR OF PHILOSOPHY

By

PITAMBAR RANDIVE

DEPARTMENT OF MECHANICAL ENGINEERING

INDIAN INSTITUTE OF TECHNOLOGY GUWAHATI

GUWAHATI 781039, INDIA

SEPTEMBER 2014

MESOSCOPIC MODELING OF CAPILLARITY-WETTABILITY INTERACTION

A thesis submitted in partial fulfillment of the requirements for the degree of

DOCTOR OF PHILOSOPHY

By

PITAMBAR RANDIVE

(Roll No. 10610305)

DEPARTMENT OF MECHANICAL ENGINEERING

INDIAN INSTITUTE OF TECHNOLOGY GUWAHATI

GUWAHATI 781039, INDIA

SEPTEMBER 2014

CERTIFICATE

It is certified that the work contained in the thesis entitled **"Mesoscopic Modeling of capillarity-wettability interaction"** by **Pitambar Randive**, has been carried out under my supervision and that this work has not been submitted elsewhere for a degree.

(Amaresh Dalal)
Assistant Professor
Department of Mechanical Engineering
Indian Institute of Technology Guwahati

September, 2014

ABSTRACT

Multiphase flows play an important role, not only in many natural processes, but also in several industrial applications, such as petroleum processing, fuel cells, power plants and boiling water reactors. Researchers have invested significant effort over the last few decades in the development of multidimensional, mathematical models in order to provide detailed insight into complex interacting multiphase flow situations. Multiphase flows, in particular two-phase flows have been simulated using three methods: the volume of fluid, the level set method, and the front tracking method. These methods consider both phases with one set of equations and use a separate equation to simulate the behavior of the interface. However, the short interactions between two fluids are difficult to model with these techniques; for example, on a micro-scale level with the Knudsen number order of unity, the above mentioned continuum mechanics approaches are not suitable. On the other hand, the microscale estimations for such systems based on the molecular dynamics approach are computationally expensive. The lattice Boltzmann method (LBM), which focuses on the mesoscale, may be the best choice in such complex flow problems, being able to capture both macro and micro-flows. Besides being a particle method, the LBM can easily include interfacial phenomena. Color-fluid model, interparticle potential model, free energy model and mean field theory model are four main lattice Boltzmann based approaches for investigating two-phase flows. This method also has the added advantages of being easily coded and parallelized.

The present thesis employs Shan and Chen LBM model to simulate the motion of a droplet and a blob in a microchannel as they are encountered in a wide range of physical phenomena. Understanding of how two fluids interact with each other and their surroundings is important in order to control the droplet and blob behavior. This is particularly important in applications such as fuel cell, enhanced recovery of oil. For example, in fuel cell, it is necessary to gain insight into the motion of a droplet in cathode channel etc.. Similarly, it is reported that about 377 million barrels of oil are left trapped in reservoirs after primary and secondary recovery processes. Huge research efforts are being directed to enhance the recovery of this oil. Although, it is difficult to recover all the trapped oil, the enhance oil recovery process can be made more efficient by the use of excitation by elastic waves. In this context, the effect of acoustic excitation on oil extraction can be explained with insight as it has been done by mobilization experiments. Hence, investigation on mobilization of trapped blob and its dependence on various physico-chemical factors which include wettability, capillarity induced resonance and geometry needs to be accomplished in greater rigor.

Keeping these motivations in mind, this doctoral thesis focuses on mesoscopic modelling of multiphase dynamics. The overall objective of this work is to develop a comprehensive, predictive framework encompassing pore-scale modeling and theoretical analysis which will garner fundamental understanding of the underlying transport mechanisms involved in liquid displacement. The primary focus is to gain a detailed understanding of the underlying multiphase dynamics of liquid displacement due to gravitation and acoustic excitation. The detailed research objectives are given below.

Firstly, numerical investigation has been carried out to study the effect of surface wettabilities on droplet dynamics. It may be noted that most of the work in this context explores droplet dynamics on hydrophobic and hydrophilic surfaces. Hence,

the present study deals with the droplet motion on superhydrophobic and mixed-wetted surface in particular. Shan and Chen model of lattice Boltzmann method has been employed to study the droplet motion. The code is validated with the static droplet test and bubble test. The motion of droplet is governed by the competition of capillary force, viscous force and gravity. When the surface wettability is considered, it also has an influence on the interface profiles. Effect of capillary number and droplet size on the droplet displacement behavior has been discussed. Next, the dependency of the non dimensional wetted length and wetted area on capillary number in superhydrophobic region is studied. It was observed that as capillary number increases, the deformation of droplet becomes more due to increase in viscous stresses along the interface resulting in an increase in both wetted length and wetted area. However, the increase in the value of wetted length is greater in magnitude than wetted area. For the non-wetting droplet, both wetted length and area decrease with time. It was observed that the larger droplet takes little more time to detach partially or completely as compared to the smaller one. This is attributed to the fact that the increase in the area of the droplet increases the capillary number along with velocity. The effect of the walls also becomes increasingly more important due to the fact that more fluid is pushed through an increasingly smaller gap. Together, these result in more viscous force and deformation. This may lead to detachment of all or part of the droplet from the wall or a pinch off from the rest of it at smaller body force strength.

The surfaces in most of the practical situations do not possess the uniform wettability. It may be noted that suitable alteration to surface chemistry or structure can improve surface wetting properties. In this context, it would be interesting to observe the droplet spreading behavior on a surface with mixed wettability. The droplet detaches from the hydrophobic surface whereas it elongates and spreads on the hydrophilic surface after some time. As far as the surface with mixed wettability is concerned, the hydrophilic and hydrophobic nature of the surface keep affecting

the changes in wetted length and area of the droplet with time. This leads to the elongation of the droplet while in motion especially when the droplet lies partially in both the regions. In general, it is found that the droplet motion is slower in the case of mixed-wetted surface. In order to understand the spreading and elongation of the droplet, the time evolution of wetted length and wetted area are plotted for a surface with mixed wettability. The changes in the wetted length follow the changes in wetted area but with some delay in time. This happens primarily due to the tendency of the droplet to spread as soon as it comes out of hydrophobic region and wetted length again starts increasing following the trend of wetted area. It can be observed that fluctuations or the magnitude of the change in the wetted area and the length are more for a surface with more width of mixed-wetted pattern as compared to one with smaller width. This can be justified on the basis of the fact that for larger width of the mixed-wetted pattern, the droplet stays in any region (hydrophobic or hydrophilic) for a longer duration during its motion. This allows it either to shrink or spread depending on the wettability of the surface. However, for smaller widths, though fluctuation of wetted length and wetted area are observed more frequently, effect of wettability alteration is not felt so intensely resulting in fluctuations of a smaller magnitude.

Since the viscosity ratio also affects the droplet displacement, a separate investigation has been carried out on droplet dynamics for a range of viscosity ratios between the displaced and displacing fluid in different wettability scenarios. It was observed that the nature of deformation of droplet looks similar on hydrophobic surfaces irrespective of viscosity ratio as seen from the bending of interfaces. However, the wetted area reduces with increase in viscosity ratio which indicates a strong cohesive force which results in lesser contact area with the wall. In case of the hydrophilic surface, the capillary force and external forces, such as gravity deform the shape of the droplet which lies on a wall. Also, the tendency of liquid to wet the hydrophilic surface leads to more deformation and bending of meniscus as compared

to the hydrophobic surface. The spreading of the droplet looks similar irrespective of viscosity ratio. It was found that the wetted length and area grow monotonically for the wetting droplet for lower values of viscosity ratio. However, for higher values of viscosity ratio, the wetted length and area decrease till the droplet gets detached. This is due to the fact that the area of the droplet adhering to wall for higher viscosity ratios gets reduced because of the effect of strong cohesive force. On the contrary, for lower viscosity ratios, the hydrophilicity dominates and hence the droplet continues to spread and adhere to the wall increasing both wetted area and length. This shows that for hydrophilic surfaces, the wettability is influential only at low viscosity ratios. It can be adjudged that displacement of droplet is faster on hydrophobic surfaces with high viscosity ratio regime. This is justifiable since high viscosity and hydrophobicity both result in less contact area which assists in moving the droplet faster along wall. Thus, it can be concluded that high viscosity ratio and hydrophobicity together form key element for droplet displacement.

The confinement of a droplet also has an impact on its motion. Hence, the effect of confinement on droplet dynamics has been studied. The simulation has demonstrated that confinement ratio influences the dynamic behavior of droplet. It is observed that confinement effect combined with wall wettability plays a significant role on droplet dynamics. Temporal evolution of wetted length and wetted area shows that change in droplet morphology is greater at low confinement ratios. However, the change in the droplet shape depends on wettability also. Droplet shape is highly affected by wettability and degree of confinement, especially at low capillary number. More pronounced change in the morphology of the droplet is observed on a hydrophobic surface as compared to a hydrophilic surface for low confinement ratios.

Earlier efforts in enhanced oil recovery proved that capillarity induced resonance can be useful in mobilization of trapped blobs. Since the surface wettability tends to change in the pores, it is imperative to investigate how the mechanism of capillarity

induced resonance affects the mobilization of blob in different wettability scenarios. The detailed analysis on mobilization of blob in case of sinusoidal channel and tube with variyng radius is presented. The overall influence of capillarity-wettability interaction on blob dynamics has been discussed. The effect of the width of the channel, amplitude of the force, wettability, viscosity and frequency on blob dynamics have been investigated. Since the blob response is influenced by the structural resistance owing to the difference in geometries of the domain, the effect of curvature on pore geometry has also been studied. The domains of different shapes with uniform and varying cross sections studied were namely, rectangular, tubular, convergent-divergent, sinusoidal and tube with varying radius.

In general, the results of numerical experiments confirm the hypothesis that trapped blobs can be mobilized by using capillarity induced resonance. It is found that the mean displacement of the blob and the frequency response changes with the thickness of the blob and width of channel. The channel with more width shows more mean displacement for the same volume of the blob. Surfaces with mixed wettability show lesser displacement of the blob as compared to surfaces with uniform wettability. The displacement of the blob has been observed to be less in the case of sliding contact line case as compared to pinned contact line. It has been observed that the mobilization of the blob is governed by the nature of geometry i.e., curvature of surface. The blob trapped in the domain with varying cross sections shows less mobilization as compared to the one with uniform cross section for the same input conditions. The study on combined effect of wettability and geometry reveals that mobilization is more for hydrophobic surfaces on geometries with uniform cross section. However, effect of geometry and wettability are not so significant at a high capillary number. In a nutshell, the optimal use of resonance frequency can be very decisive for obtaining maximum displacement. This could be of great practical importance while dealing with mobilization of trapped blobs.

The investigation is further extended to understand the behavior of two-phase flow through porous media. The advancement of the front of the fluid moving through porous microstructure has been analyzed. It may be noted that the fluid advancement through porous media mainly depends on the relative magnitude of capillary force, pressure gradient and acoustic force. Although the role of capillary force is of special importance in a porous medium and governs the displacement; the study reveals that the displacement of the fluid through porous media also depends on parameters like wettability of the surface and frequency along with the porosity. It is observed that vibration in the form of acoustic excitation can be significant in the mobilization of fluid through the porous media. The mean displacement of the fluid is more in the case of wetting invading phase. Flow through the porous media over a range of porosity have been discussed. The study further emphasizes the importance of an optimal excitation of the fluid flow based on the frequency of excitation, amplitude of force applied and surface wettability for the mobilization of fluid flow which may be useful in porous networks. The thesis is concluded with a summary of the main findings and recommendations for future work.

Dedicated to my wife Kavita

Acknowledgements

I gratefully acknowledge my advisor, Dr. Amaresh Dalal, for his guidance, persistence and inspiration throughout the course of my Ph.D. Our communication includes a thousand questions and answers, and he was always keen to help me understand a few more things about CFD and LBM. His patience to explain some issues was unbelievable, taking into account the fact that he sometimes explained the same thing five times in row. His willingness to help whenever I had problems is fascinating. He made me believe that I can accomplish this research work which otherwise would not have been possible. I am especially thankful for his advice and support in making this dissertation possible from creating this research topic to finishing this final document.

I am grateful to Dr. Partha P. Mukherjee from Texas A & M, USA, whose genius inspired me to begin the research on droplet displacement behavior and mentored during my dissertation work. My thanks go to Professor Anoop K. Dass, Professor Pinakeshwar Mahanta and Professor Anugrah Singh for their service on my doctoral thesis committee and for their suggestions and insightful comments on my work.

I would also like to extend my sincerest appreciation and thanks to Dr. S. D. Kore, Dr. Arnab K. De, Dr. Ganesh Natarjan and Dr. C. M. Somayaji from IIT Guwahati for motivating me during this study. I want to also thank to Dr. Nilaj, Dr. Madhukar Deshmukh, Dr. S. B. Thombre, Dr. M. R. Patkar, Shri. K. J. Jadhav, Dr. Debayan Dhar, Dr. Bokare, Dr. Yogesh Deshpande, Brijesh kumbhani and sandy for their constant encouragement throughout my Ph.D. research.

I wish to acknowledge a great many friends and colleagues who made my study enjoyable: Mukul, Subrat, Vinod, Manik, Saurabh, PreetiRekha, Simon, Jitendra patel, Nitin Chavan, Hemanshul and Quesar. These people have taught me many good values and habits for which I will be always indebted to them.

This work couldnt have been accomplished without the help of many people. My thanks go to all the people, whom I dont mention here due to space requirements

(it can be ten pages of names). There are many of them who are actively involved in my life and stay behind it. I would never be able to fully express my gratitude to my wife and my elder brother Sharad, who were helpful, supportive and allowed me to spend some extra time on my studies. In fact, I remember Sharadbhau who put me in the school and make sure that I attend it religiously. Finally, I would like to dedicate this thesis to my wife and my family members whose endless encouragement and love made it possible to finish this research work.

Contents

List of Figures

List of Tables

Nomenclature

a_0	Initial droplet height
A	Wetted area
$\frac{A}{A_0}$	Dimensionless wetted area
b	Wetted length
$\frac{b}{b_0}$	Dimensionless wetted length
f_i	Probability density function
f_i^{eq}	Equilibrium density function
g_{1w}	Interactive force strength between non-wetting phase and wall
g_{2w}	Interactive force strength between wetting phase and wall
g_k	Interactive strength between the component k and wall
$G_{k\bar{k}}$	Interactive potential
n_w	Number density of the wall
Q	Collision integral
$\mathbf{u}$	Macroscopic velocity of particle

Greek Symbols

ϕ	Porosity
θ	Contact angle
μ	Dynamic viscosity
ν_k	Kinematic viscosity of k^{th} component
δt	Change in time
ρ_k	Density of k^{th} component
σ	Surface tension
τ	Relaxation parameter
Ψ_k	Effective mass density function
ω	Collision frequency
Ω	Collision operator

Abbreviations

Ca	Capillary number
EOR	Enhanced oil recovery
HI	Hydrophilic
HO	Hydrophobic
LB	Lattice Boltzmann
LBM	Lattice Boltzmann model
MEA	Membrane electrode assembly
MPL	Microporous layer
N-S	Navier-Stokes
NWP	Non-wetting phase
PEMFC	Proton exchange membrane fuel cell
PTFE	Polytetrafluoroethylenee
S-C	Shan and Chen model
WP	Wetting phase

Chapter 1

Introduction

1.1 Background and Motivation

Multiphase flows are common in several engineering applications. The relevant examples are petroleum processing, fuel cells, power plants and boiling water reactors. The significant amount of research effort has been focused to understand the physical mechanisms underlying multiphase flows owing to its complexity. This has led to the development of multidimensional, mathematical models to gain insight into the complex interacting flow situations. The modeling of such flows have been done with three methods: the volume of fluid, the level set method, and the front tracking methods. These methods consider both phases with one set of equations and use a separate equation to simulate the behavior of the interface. However, the short interactions between the two fluids are difficult to model with these techniques; for example, in a micro-scale regime with the Knudsen number around unity, the continuum mechanics framework is not suitable. On the contrary, the microscale estimations for these systems dependent on the molecular dynamics approach are computationally expensive.

The lattice Boltzmann method (LBM), which focuses on the mesoscale, may be the prime choice in such complicated flow problem, being capable to reveal macro and micro-flows. Besides being a particle method, the LBM can easily include interfacial phenomena. Color-fluid model [2], interparticle potential model [3, 4], free energy model [5] and mean field theory model [6] are the four main lattice Boltz-

mann (LB) based approaches for exploring two-phase flows. This method also has the added advantages of being easily coded and parallelized. The present thesis employs LBM Shan and Chen model [3] to simulate the motion of a droplet and a blob in a microchannel as they are encountered in a wide range of physical phenomena. Understanding of how two fluids interact with each other and their surroundings is important in order to control the droplet and blob behavior. This is particularly important in applications such as fuel cell, enhanced recovery of oil. For example, in fuel cell, it is necessary to gain insight into the motion of a droplet in cathode channel etc.. Similarly, it is reported that about 377 million barrels of oil is left trapped in reservoirs after primary and secondary recovery processes [7]. Huge research efforts are being directed to enhance the recovery of this oil. Although, it is difficult to recover all the trapped oil, the enhance oil recovery process can be made more efficient by the use of excitation by elastic waves. In this context, the effect of acoustic excitation on oil extraction can be explained with insight as it has been done by mobilization experiments. Hence, investigation on mobilization of trapped blob and its dependence on various physico-chemical factors which include wettability, capillarity induced resonance and geometry needs to be accomplished in greater rigor.

With these motivations in the mind, this doctoral thesis focuses on mesoscopic modelling of two-phase dynamics. In this regard, comprehensive literature review has been presented in the following section followed by research objectives.

1.2 Review of Literature

The main aim of this research work is to study the effect of physico-chemical properties which includes wettability, geometry, capillarity induced resonance on transport phenomena in multiphase flows. In this regard, displacement behavior of droplet, blob in a channel and fluid flow through porous media has been undertaken for the present research work. A detailed review of the literature on the droplet and blob dynamics along with fluid flow through porous media is given below.

1.2.1 Literature review on droplet motion

Droplet dynamics in confined geometries is of paramount importance in the field of multiphase flows in porous media, network of channels, for understanding physiological flows from microfluidic technology to fuel cell design and spray painting. The droplet dynamics is influenced by heterogeneities on the surface. However, with the arrival of microfabrication techniques, manipulation of the chemical or topographical patterning of a substrate is attainable on micrometer length scales. This leads to the possibility of revealing the new physics for novel applications. Superhydrophobic substrates on the leaves of the lotus plant is one such example. These surfaces strongly repel the water droplets which show the contact angles up to 160^o [6, 8] as a result of the topological patterning. This can be compared to conventional ways of increasing the contact angle. It is possible to achieve an angle of more than 120^o with surface coatings and chemical modifications of the substrate.

Continued developments of multiphase flows require understanding of droplet traffic, drop break up, drop resistance etc. [9]. Kang et al. [10, 11] have studied the displacement of the two and 3-D immiscible droplet in a channel. They investigated the effect of the wettability and capillary number on droplet dynamics. It is well known that superhydrophobic surfaces lower drag owing to combined effect of hydrophobicity and roughness. Superhydrophobic surfaces reduces the viscous drag of thin micro channels when compared to simple smooth channels. It also prevent the clogging or adhesion of suspended analytes [12]. Further, a very large contact angle can be obtained in case of a hydrophobic texture with a modified surface profile [13]. Thus the enhanced mobility of liquids on superhydrophobic surfaces make them self cleaning. This leads to rolling of droplets instead of sliding under gravity and rebound instead of spreading upon impact [14].

1.2.1.1 Experimental investigations

Many researchers have conducted experimental investigations on superhydrophobic surfaces to investigate the drag reduction abilities. Wang and Hashimot [15], Choi and Yang [16] and Ou et al. [17] have fabricated the surfaces which lower pressure loss by 19%, 14 %, and 40 %, respectively. Tsai et al. [18] have experimentally investigated impact dynamics of droplets on superhydrophobic surfaces consisting of regular polymeric micropatterns and rough carbon nanofibers. They have observed

that the influence of atmospheric air pressure is negligible in the parameter regime of Weber number (We) between $We \geq 120$ to $We \leq 150$. Francois et al. [14] have established the experimentally relevant limit of thin channels and obtained rigorous bounds on the effective slip length for any two-component (e.g., low slip and high slip) texture with given area fractions. Among all anisotropic textures, parallel stripes attain the largest (or smallest) possible slip in a straight, thin channel for parallel (or perpendicular) orientation with respect to the mean flow. Tighter bounds for isotropic textures further constrain the effective slip. They argued that their results provide a framework for the rational design of superhydrophobic surfaces.

Reyssat et al. [19] have described a few characteristics of rebounds of droplet impact and present new experiments where impact is accompanied by remarkable patterns directly related to the existence of a texture on the solid surface. Kwak et al. [20] have used measurements of water droplet impact dynamics to characterize the influence of surface energy on the wetting transition. They also discussed the stability of the fabricated superhydrophobic surface and also provided the guidelines for the design of stable nano structured surfaces that are non wetting with respect to water. Feuillebois et al. [12] have presented theoretical results to optimize transverse hydrodynamic phenomenon in superhydrophobic channels. They worked on the micro and nanofluidic geometry of a parallel plate channel with an arbitrary two-component low-slip and high-slip coarse texture. They have optimized the parameters like area fractions, geometry, orientation of the surface texture and slip lengths to increase transverse flow based on rigorous bounds on permeability and over all possible patterns.

1.2.1.2 Numerical investigations

In recent past, several researchers have investigated droplet dynamics numerically. Mukherjee et al. [21, 22] have discussed the mesoscopic model to study the effect of the wettability and pore structure on liquid transport and interfacial dynamics in fuel cell. They studied capillary dominated transport in the catalyst layer and the effect of the mixed wettability on the flooding dynamics in the gas diffusion layer (GDL). Mukherjee et al. [23] and Wang et al. [24] has given an excellent critical review on progress and prospects of pore-scale modeling for two-phase transport in

the fuel cell. Adroher and Wang [25] investigated the air-water two-phase flow in a single flow channel of polymer electrolyte membrane (PEM) fuel cells. Cho et al. [26, 27] studied the droplet dynamics in a microchannel through theoretical, experimental and numerical analysis. They examined forces on water droplet, droplet deformation and detachment. Hao and Cheng [28] simulated liquid transport in gas diffusion layer of a fuel cell using LBM to study the influence of wettability on transport dynamics in GDL.

Salah et al. [29] simulated the two-phase flow in a of a polymer electrolyte membrane fuel cell using the lattice Boltzmann method to analyse the drainage performance of the fuel cell gas channel. Chang and Alexander [30] investigated the behavior of a microscale fluid droplet on a heterogeneous surface. They studied the effect of the width of hydrophobic strip, wettability, gravity and initial location of the droplet relative to the strips on spreading behavior of droplet. Zu and Yan [31] analysed the droplet dynamics on partial wetting surfaces using lattice Boltzmann method. They analysed the dynamic behavior of droplet on partial wetting surfaces to study the droplet breaking up, migration and spreading, etc. Huang et al. [32] studied the droplet behaviors on substrates with controlled wettability by using the lattice Boltzmann method. Sinha and Wang [33] studied liquid transport in a mixed-wet gas diffusion layer of a fuel cell. They commented that there is a need for controlled polytetraflouroethyene (PTFE) treatment and proposed wettability-tailored GDL.

Meanwhile, numerical studies on superhydrophobic surfaces includes the work by Lauga and Stone [34] who discussed the slip velocity in channels using computational fluid dynamics (CFD). Davies et al. [35] investigated the influence of roughness on pressure drop using commericial software Ansys Fluent. However, these investigators have not included the influence of surface wettability. Zhang and Kwok [36] employed the by the mean field free energy lattice Boltzmann method to study the dynamic behavior of liquid columns in microchannels. Osborn et al. [37] used the free energy approach to propose a LB multiphase and multicomponent model. He et al. [38] developed LB multiphase model with the kinetic equation for multiphase flow.

An insight into the droplet dynamics explaining the rheological behavior is essential to understand the nature of droplet dispersions which is of utmost interest for

several industrial applications, e.g., cosmetics and food emulsions. In this context, the droplet dynamics have been studied by several researchers [39, 40] both, experimentally and theoretically. A comprehensive review is given in several recent reviews [41]. Borhan and Mao [42] have investigated the deformation of axisymmetric droplets in straight capillaries for a range of droplet to fluid viscosity ratios, droplet sizes and capillary numbers (Ca). They have observed that the deformation of the droplet increases with viscosity ratio. However, for large Peclet number (Pe), the shape of the droplet becomes independent of the viscosity ratio. For the lower viscosity ratios, the internal flow is eliminated due to Marangoni stresses which immobilize the surface of the droplet. In case of higher viscosity ratios, the surface velocity and internal flow remain very small irrespective of the effects of surfactants. Manga [43] numerically studied the deformable drops for high viscosity ratios. He reported the tendency of the droplets to aggregate and form clusters. Dimitrakopoulos and Higdon [44] found the yield conditions for a two dimensional droplet sticking to a plane solid surface in a shear flow for a wide range of Bond number (Bo), Ca and viscosity ratios. The dynamic behavior of viscous and inviscid droplets is found to be qualitatively different. Schleizer and Bonnecaze [45] discussed the dynamics of two-dimensional liquid droplet between parallel plates in a pressure-driven flow. They reported that the deformation of the droplet increases with the viscosity ratio. Boonen et al. [46] have investigated the effect of varying the balance of shearing and elongational flow components and changing viscosity ratio on the deformation and orientation of the droplets.

Several researchers used lattice Boltzmann Shan and Chen (S-C) model [10, 11, 21] to study contact line problems due to its interaction potential based approach. Also, it is simple to implement boundary conditions in complicated porous structures. Moreover, it is easy to handle fluid phases with different densities, wettabilities and viscosities and is capable to incorporate different equations of state using this model. However, the primary focus in these studies has been to simulate the contact line motion and to study the corresponding displacement behavior. Mukherjee [21] investigated 3-D droplet motion using D3Q19 two-phase Shan and Chen LB model on a patterned channel wall with varying wettability. Immiscible displacement on solid wall is a moving contact-line problem and the two-phase. The mixed wettability refers to the varying wetting characteristics of the solid wall comprised of hydrophilic (HI) and hydrophobic (HO) regions. Fakhari and Rahiman [47]

have studied falling droplet using LBM for a range of Eotvos and Ohnesorge (Oh) numbers. Zhang and Kwok [48] discussed the wetting phenomenon and contact line dynamics of droplet confined between two superhydrophobic surfaces using mean field free energy lattice Boltzmann model. They reported two regimes for the flow velocity as a function of surface roughness which is a function of flow resistance and driving force.

Gunstensen et al. [2] have proposed a LB model based on a two component lattice gas model. Hazlett and Vaidya [49] have carried out simulation of a propagating captive droplet in a virtual capillary tube of defined equilibrium contact angle using Gunstensen LBM model to examine different Hysteresis effects and demonstrated that the LBM model can be calibrated to yield local contact angle assignments. Aminfar and Mohammad [50] used free energy based lattice Boltzmann (LB) model for modelling and simulation of microsized droplet. They studied transport and spreading behavior of a microsized fluid droplet on a flat substrate owing to electrowetting. They further developed new relations for surface tensions on the basis of free energy functional minimization. Cui et al. [51] used SC LBM model to simulate channel flow with different surfaces. Mukherjee and Abraham [52] used the two-phase axisymmetric lattice Boltzmann model to study the drop impingement on dry walls for range of Weber number, Ohnesorge number and drop wall equilibrium contact angle. They have investigated the effect of contact angle during drop spread and recoil on impact outcomes. Kawasaki et al. [53] used Gunstensen LBM model for 2D simulations of contact-line motions to reproduce the hysteresis phenomena without the implementing the slip model, similar to the one in the continuum mechanics based simulations.

In summary of the above review regarding the studies on droplet motion, it can be inferred that the effect of wettability on the dynamics of immiscible displacement of droplet has been studied extensively [10, 11, 22, 45, 54, 55]. Most of these studies have focused on droplet dynamics on hydrophobic and hydrophilic surface only. The droplet motion on superhydrophobic surface is also explored by few investigators [36, 56, 57]. However, the effect of important parameters like contact angle, capillary number and droplet size on droplet dynamics over the superhydrophobic and mixed-wet surface remain largely overlooked. Also, the viscosity ratio is the key factors which govern the dynamics of the displacement of the fluid. The interfacial

instability is observed when fluid filling the voids of a porous medium is displaced by a less viscous one [58, 59]. In the present work, a mesoscopic model, based on the two-phase lattice Boltzmann formulation is presented to elucidate the role of surface wettability and viscosity ratio on the droplet dynamics in microfluidic confinements.

1.2.2 Literature review on displacement of fluid using acoustic effect

Enhanced oil recovery (EOR) uses the methods like steam, water, and gas flooding; hydraulic and explosive fracturing; injection of surfactants etc.. However, these methods has many limitations with some undesirable side effects. For instance, some methods are costly, need shutting in production, or may create harmful ecological consequences. These impediments have forced engineers and geophysicists to find for new methods of stimulation. In particular, the use of elastic wave stimulation has been proposed, not as a replacement for conventional EOR techniques, but as an alternative or complimentary tool which, in certain situations, may make conventional methods more efficient. Numerous observations during the last 50 years show that seismic wave excitation may enhance oil production due to appreciable increase in the mobility of fluids. Many case studies and laboratory experiments/tests [60, 61, 62] have confirmed the effect of elastic waves on the permeability of saturated rock. In the next section, review of the methods and results of enhanced oil recovery achieved by the use of elastic waves is discussed.

1.2.2.1 Experimental investigations

Mobilization of blobs entrapped by capillary forces has been actively studied by petroleum engineers due to its relevance to oil recovery. Gardescu [63] performed experiments to ascertain the pressure required to mobilize an isolated bubble of gas entrapped in a pore constriction. He used Laplace‘s law of capillary pressure for an explicit determination of the pressure needed to overcome the capillary entrapment. Taber [64] conducted several experiments to correlate the volume of mobilized oil phase with a parameter ratio $\frac{\Delta p}{L\sigma}$, where σ is the interfacial tension and ΔP is the pressure drop across the length of the porous core sample (L). Several field observations and laboratory experiments [65] has illustrated that capillary induced resonance can significantly enhance the recovery of non wetting fluids from porous

media.

Continuous research/industrial efforts were made around 1980s to understand earthquake effects owing to the use of vibrators above a targeted zone. However, these attempts did not succeed due to lack of commercial viability. Roberts et al. [66] experimented on cylindrical sand packs saturated with water and offered laboratory evidence of seismic stimulation. Further, Li et al. [67] conducted experiments on flooding of water across a glass plate applied with and without vibrations in the direction of flood. Thereafter, Occidental of Elk Hills (Oxy) has employed in-situ seismic stimulation to enhance the recovery of oil in declining reservoirs [68]. Oxys seismic-stimulation project at the declining Elk Hills Field near Bakersfield, California (USA) have reported an improved oil recovery and increased flow. Since the 1970s, this turned out to be the first departure from variants on traditional stimulation methods like polymer, thermal, microbial and chemical to be introduced commercially.

Hilpert [69] modelled the dynamics of the trapping forces and blob mobilization to understand the behavior of the three-phase contact lines. These contact lines might slide if sound waves are applied or remain pinned to the heterogeneities of the solid surface. Hilpert et al. [70] proposed the hypothesis that oil blobs trapped in porous media also exhibits meniscus resonances like the liquid column trapped in a capillary tube. They further argued that the pinned contact lines is observed not only for oscillatory flows but also for oscillatory vibrations of the solid surface. It is seen that pinned contact lines occur in natural porous media due to their surface roughness and chemical heterogeneities and hence it is more likely to result in nonexistence of sliding contact lines. They suggested that sliding contact lines can be seen only in case if the solid phase is covered completely by a film of liquid primarily due to no contact between the contact lines and the defects of the solid surface. For such systems the three-phase contact line is not seen. Hilpert [1] suggested that blobs (binary large object) shows resonance due to inter facial tension in porous media and these blobs can be excited by capillary induced resonant frequency. Lattice gas automata incorporates with sound wave propagation in the small perturbation. Numerical and theoretical method for sound wave technique was simulated by Margolus et al. [71]. Chen et al. [72] proposed a model to simulate linear sound wave without considering the sound wave as a small perturbation limit.

It may be noted that all the work done by Hilpert et al. [1, 70] is for two dimensional domain. In this work the author intend to explore it further for 3-D domain. The objective of the present work is to apply another LB multiphase multicomponent Shan and Chen model to understand the capillarity-induced resonance of blobs in porous media to obtain new perspectives on solutions reported in the literature. In this study, authors intend to investigate the dynamic behavior of a 3-D immiscible blob in a channel using Lattice Boltzmann S-C model.

1.2.2.2 Numerical investigations

Many investigators work in the area of sound propagation in porous media saturated with multiple immiscible fluids and tried to explore contact line dynamics explicitly [73, 74, 75, 76, 77] but could not provide expressions for the resonances. Hilpert et al. [70] have presented quantitative assessment of whether resonances occur for the frequencies used in a given multiphase porous media system. The use of elastic waves to the subsurface [78, 79] enhances the efficiency of water flooding of oil reservoirs. Beresnev and Johnson [80] reviewed use of elastic waves. It is well known that the recovery of non wetting phase blobs is difficult just by imposing a flow on the surrounding wetting phase. This is particularly due to the large wetting phase velocities required and also is restricted to longer blobs along which the pressure gradient in the wetting phase can impose a greater force [81, 82, 83]. This is the major barrier in the process of oil extraction from its natural reservoir or non aqueous phase liquid (NAPL) contamination from water-wet aquifers. Vapor extraction, in situ biodegradation, surfactant flushing, cosolvent flushing, steam injection etc. are the methods used for mobilization of trapped non wetting phase blobs.

Notable works in this area include Dimon et al. [84] and Charliax and Gayvallet [85] who have studied the resonance of a meniscus in a capillary tube resulting from an imposed oscillatory flow. They concluded that the response of the meniscus depends on the chemical and geometrical properties of the solid, the flow amplitudes, and the frequency. Iassonov and Beresnev [86] theoretically explored the effect of low frequency sonic vibrations on the flow of non aqueous phase liquids through a porous medium. They mainly focussed on the yield stress rheology of the pore filling fluid and capillary trapping and found that both produce the similar behavior at the

macroscopic level which are important to understand the mobilization of fluids in the reservoir with acoustic stimulation technologies. They further established the fact that vibrations can considerably reduce the value of minimum pressure gradient needed to mobilize entrapped fluid and increase the average flow rate. They claimed that the vibrations are most effective in the zones of relatively low pressure gradients. They further reiterated that application of sound can increase the efficiency of oil recovery methods [65].

Palan et al. [87] have used vibro-acoustics method to remove the water for the better fuel cell performance. The motion of water droplets was achieved by applying acoustics excitation. They compared different approaches to obtain the minimum energy required for the formation of droplet for the input excitation frequency and amplitude. Buick et al. [88] generated the sound wave by implementing the sinusoidal source. The wave generated by sinusoidal source is compared with inviscid shock wave concept with the solution of Bergers equation. Flow through porous media assuming the single pore as periodically constricted tube [89, 90, 91] and the total pore space represented by a network of tubes [92], is studied extensively. In most of the studies, the randomly varying geometry is modelled as a tube with sinusoidally varying cross-section for studying the single-phase flow [93]. It is well known that the recovery of non wetting phase blobs in porous media by imposing a flow on the surrounding wetting phase is cumbersome. This is solely due to the large wetting phase velocities required and also is limited to longer blobs along which the pressure gradient in the wetting phase can impose a greater force [81, 82, 83]. This is the major hindrance in the process of oil extraction from its natural reservoir or non aqueous phase liquid contamination from water-wet aquifers.

1.2.3 Literature review on simulation of two-phase transport in porous media with acoustic excitation

Understanding the multiphase flow and the transport problems in a multifluid porous medium is useful in many applications, e.g. fuel cell, oil extraction etc. In such cases, the functional relationship between capillary pressure, saturation and interfacial area are the key determinants for modeling the interfacial mass transfer, including the problems such as non aqueous phase liquid dissolution. The information about the fluid phase distribution is a must along with the fluid saturation to characterize the

NAPL dissolution adequately [94, 95]. This is so because the distribution of fluids at the pore scale controls both the interfacial area between the fluid phases and the relative permeability of the medium to each fluid. Reeves and Celia [96] developed the network model for establishing these relationships. Zhao et al. [97] investigated the collision between a liquid droplet and a porous surface. They employed a novel multiphase LBM using new interaction potential functions. The simulation is also carried out for the droplet collision with a porous surface. The unique feature of this simulation is that both the droplet scale flow and pore scale flow are directly simulated at the same time. Hilpert and Ben-David [98] proposed a model for infiltration of droplets into porous media that considers not only dynamic contact angle of the droplet but also hysteresis of the equilibrium contact angle.

Earlier investigation in this context is done by Saffman and Taylor [99] in which the displacement of one fluid by another one in a Hele-Shaw cell is discussed. Larson et al. [100] explained the correlation between the residual saturation of non wetting phase in porous media after displacement by a wetting phase and the capillary number. Dullien [101] has described the experiments and modeling on drainage type displacement in porous media. Jamaloei et al. [102] characterized pore-scale flow of low-interfacial tension flow through mixed-wet porous media with various pore geometries. Flow through porous media considering the single pore as periodically constricted tube [89, 90, 91] and the complete pore space represented by a network of tubes [92] is studied widely.

The displacement of immiscible fluids had been studied by many researchers [10, 11, 103, 104]. Dawson et al. [105] have studied the trapping and release of bubbles from a linear pore. They observed that the release of bubble is possible only if the work of the pressure forces over the length of the trap is greater than the surface energy needed for the trapped bubble to come back in the constricted square tube. Mondal et al. [106] have simulated motion of water droplet in fuel cell flow channels with hydrophilic surfaces to analyse the effect of surface wettability properties.

Recently Kang et al. [107] have presented thorough review on recent developments in lattice Boltzmann method for reacting flows in porous media. Kang et al. [108] reported application of lattice Boltzmann method for mesoscopic modelling of physico-chemical transport phenomena in porous media. They simulated

the two-phase behavior and flooding phenomena in fuel cells and electro osmosis in homogeneously charged porous media and stated that lattice Boltzmann method can be used for capturing physics at the fundamental scale for multiple, coupled physico-chemical processes in these systems. In this context, it is proposed to study dynamics of multiphase flow in 3D porous structures under acoustic excitation.

To this extent, although substantial research, both theoretical and experimental, has been conducted as far as the the dynamics of the droplet as well as blob and fluid flow through porous microstructure is concerned; there is serious paucity of fundamental understanding about the overall capillarity-wettability interaction influencing the transport of two-phase flow. This in turn leads to the outstanding questions pertaining to the dynamics of fluid flow which can be resolved using LBM modeling of these fluid flow. LBM modeling is promising in unveiling the intricate capillarity-wettability transport interactions because of its mesoscopic nature. This will allow excellent versatility to explore transport phenomena due to the detailed information available at the microscopic level.

1.3 Research Objectives

The primary focus of the present work is to gain a detailed understanding of the underlying multiphase dynamics of liquid displacement due to gravitation and acoustic excitation. The work is focused on exploring the role of surface wettability on droplet dynamics. An attempt is made to understand the effect of physico-chemical parameters like droplet size and capillary number on droplet displacement behavior. It is well known that surfaces in most of the practical situations do not possess the uniform wettability. Hence, the study is also conducted on mixed-wet surfaces. Since the viscosity ratio also affects the droplet displacement, a separate investigation is carried out on droplet dynamics for a range of viscosity ratio between the displaced and displacing fluid in different wettability scenarios. Furthermore, the effect of confinement on the droplet dynamics has also been studied.

As earlier discussed, the enhance oil recovery process can be made more efficient by using the acoustic excitation which could induce oscillations of the trapped oil blobs, thus increasing the mobility of the trapped blobs [1, 69, 70]. Earlier efforts

in this area proved that capillarity induced resonance can be useful in mobilization of trapped blobs. Since the wettability scenarios tend to change in the pores, it is imperative to investigate as to how the mechanism of capillarity induced resonance behaves in different wettability scenarios. In present work, mobilization of trapped blobs due to capillarity induced resonance in varied wettability scenario has been explored. The overall influence of capillarity-wettability interaction on blob dynamics is discussed. The effect of the width of the channel, amplitude of the force, wettability, viscosity and frequency on blob dynamics are investigated. Since the blob response is influenced with the structural resistance owing to the difference in geometries of the domain, the effect of curvature of pore geometry is also studied. The domains of different shapes with uniform and varying cross section studied were namely, rectangular, tubular, convergent-divergent and sinusoidal.

The investigation is further extended to understand the behavior of the two-phase flow through porous media. An advance front of the fluid moving through the porous microstructure is analyzed. It may be noted that the fluid advancement through porous media mainly depends on the relative magnitude of capillary forces, pressure gradient and acoustic force. Although the role of capillary forces is of special importance in a porous medium and governs the displacement; the present study attempts to explore the effect of capillarity induced resonance on displacement of the fluid through porous media for different wettability and porosity configurations. The study further emphasizes the importance of an optimal excitation of the fluid flow based on the frequency of excitation, amplitude of force applied and surface wettability for the mobilization of fluid flow which may be useful in porous networks.

1.4 Thesis Overview

The work is presented in self contained chapters. The overall structure of this report is as follows:
A thorough literature review on droplet motion, blob dynamics and fluid flow through porous media including both experimental and numerical investigation is given in chapter 1. The LBM formulation with S-C model is discussed in chapter 2 in detail along with a analytical model implemented for studying the capillarity induced resonance. Also, the validation of the code and methodology is described

in this chapter. The static droplet test and bubble test are carried out to calibrate the model. The validation results show good agreement with that of the reported literature.

Chapter 3 discusses the importance of fundamental understanding of droplet dynamics and the concomitant implications of wall wettability. The mesoscopic illustration, based on the two-phase lattice Boltzmann model, of droplet dynamics in a microchannel is presented in order to unveil the role of superhydrophobicity and mixed wettability. The impact of critical physico-chemical determinants, including capillary number and droplet size is explored in the context of droplet-wettability interactions. Temporal evolution of wetted length and wetted area for a combination of wettability scenarios is furnished in detail in order to elucidate the droplet displacement dynamics. In chapter 4, the influence of wall wettability and viscosity on droplet dynamics are discussed to understand the viscosity-wettability interaction. Temporal evolution of wetted length and wetted area for a combination of viscosity ratios and wettability scenarios is furnished in detail in order to elucidate the droplet displacement dynamics. It is observed that capillary number and viscosity ratio play an important role with disparate droplet behavioral patterns stemming from uniform and mixed-wet wall scenarios. Chapter 5 describes the effect of confinement on the droplet displacement behavior.

Chapters 6 and 7 discuss the analysis of mobilization of trapped non wetting phase blob owing to capillarity induced resonance in a sinusoidal channel and tube with varying constriction respectively. The study deals with the displacement of a three dimensional immiscible blob subject to oscillatory acoustic excitation using the lattice Boltzmann method. Both pinned and unpinned (sliding) configurations are studied. The effect of the width of the channel, amplitude of the force, wettability, viscosity and frequency on blob dynamics are investigated. Comparative analysis of effect of geometry on the mobilization of trapped blob is also presented.

Chapter 8 explains the dependence of mobilization of blob on geometrical configuration in conjunction with capillarity induced resonance. In this context, lattice Boltzmann Shan and Chen model is employed to investigate the mobilization of a three-dimensional immiscible blob subject to acoustic excitation trapped in the channels of different geometrical configurations. The influence of physicochemical

parameters which include geometry, wettability and frequency on blob dynamics is discussed. The role of geometry on mobilization of the trapped blob is studied to understand the structure-wettability relationship.

Chapter 9 describes the influence of the microstructure and wetting characteristics on the underlying two-phase behavior subjected to acoustic excitation. The dynamic behavior of the fluid flow has been explored based on displacement of the fluid for different set of conditions namely, wettability, porosity and forcing strength i.e., the acoustic excitation applied. In this regard, numerical experiments have been devised in order to evaluate the time evolution of saturation and displacement of the fluid flow as a direct manifestation of the underlying pore morphology. Finally, the main findings and suggestions for future work are summarized in Chapter 10.

Chapter 2

LBM Formulation and Its Validation

2.1 Introduction to Lattice Boltzmann Method

Macroscopic physical property of matter depends on the physics of its microscopic constituents. It is very useful to understand and simulate the underlying microscopic physics for determining macroscopic physical properties, as we can see from the advances in material science and biology those have resulted from quantum and molecular simulations. In the past few decades, the relation between the Boltzmann equation and Navier-Stokes equation for the study of multiphase dynamics has been topic of extensive research [109, 110]. LBM originated from lattice gas Automata uses different kind of non conventional techniques for application in computational fluid dynamics. Since lattice gas automatic (LGA) suffered from some drawbacks such as lack of Galilean invariance, statistical noise and unphysical solution, LBM was developed to overcome these difficulties of LGA.

LBM can be perceived as a simplified fictitious molecular dynamics model in which time, space and particle velocities are discrete inspired from kinetic theory of gases. It describes the state of fluid at the computational node using set of real numbers which are defined as 'population'. The populations are analogous to microscopic density function of Boltzmann equation. These populations are convected in discrete time steps from one lattice to the other. The populations are relaxed towards

local equilibrium value between every convection. The mass and momentum is conserved in relaxation step. This is done in much similar way as in respect of particle collision in kinetic theory. In LBM, collision operator is linearized by Bhatnagar-

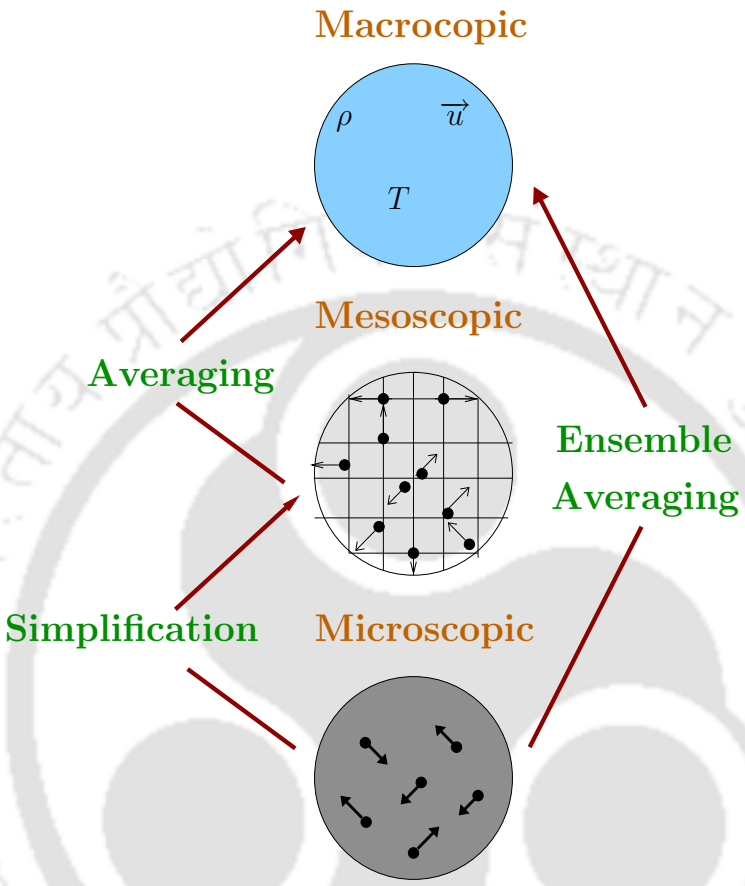

Figure 2.1: Concept of scale bridging in the lattice Boltzmann model

Gross-Krook (BGK) collision model [111]. In this approach it is believed that the macroscopic dynamics of a fluid is basically the result of collective behavior of several microscopic particles which does not specifically depends on the details of the microscopic phenomena shown by the individual molecules. LBM describes the macroscopic behavior of fluids, although describing the fluid in a microscopic way through its use of stable and efficient numerical calculations (see Fig. 2.1). The kinetic nature of the LBM presents three important aspects. The first one is linear convection operator in phase space (or velocity space). Hence, the computational efforts are greatly decreased as compared to conventional methods. Secondly, using an equation of state the pressure calculation can be done. In conventional methods

solving the Poisson equation for the pressure is subjected to numerical difficulties which need special treatment. Finally, the LBM uses a minimal set of velocities in phase space. In the phase space of the traditional Boltzmann equation with the Maxwell equilibrium distribution complete functional space is considered and the averaging process involves information from the whole velocity phase space. However, one or two speeds along with a few directions are used in LBM . This makes the transformation relating the microscopic distribution function and macroscopic quantities extremely simple (see Fig. 2.1). As a result it can be seen that an increasing number of researchers simply use LBM as an optional method compared to conventional numerical methods.

2.1.1 Evolution of LBM: From lattice gas cellular automata to lattice Boltzmann models

Historically the evolution of LGA up to the development of LBM can be described briefly in following stages.

1. Hardy et al. [112] in 1973 proposed the LGA using square lattice with discrete particles residing on a corner. In 1986, Frisch et al. [113] removed the problem of non isotropy by introducing the use of hexagonal lattice to establish the isotropy.

2. In 1987 Frisch et al. [114] used lattice Boltzmann equations at the cradle of lattice-gas cellular automata to calculate the viscosity of LGCA.

3. Lattice Boltzmann models as an independent numerical method for hydrodynamic simulations were introduced by McNamara and Zanetti [115] in 1988. The main motivation for the transition from LGCA to LBM was the attempt to get rid of noise. The Boolean fields were replaced by continuous distributions over the face centered hyper cubic (FCHC) and Frisch, Hasslacher and Pomeau (FHP) lattices. Fermi-Dirac distributions were used as equilibrium functions.

4. In 1989, linearization of collision operator by Higuera et al. [116] made LBM simple.

5. In 1991, introduction of a single relaxation parameter by Chen et al. [117] made LBM simpler which is widely accepted as LBGK (Lattice Bhatnagar Gross-Krook) method. Boltzmann distribution instead of Fermi-Dirac distributions was employed.

The LBM utilizes the probability distribution function to determine a particle at a certain time and at a certain location. Therefore, the method does not track a separate molecule, as in molecular dynamic simulations. However, a whole ensemble of molecules (particle) gives the probability distribution function. The macroscopic variables such as, density, velocity or shear stress are calculated by taking the integration of the probability distribution function in velocity space. The LBM can be

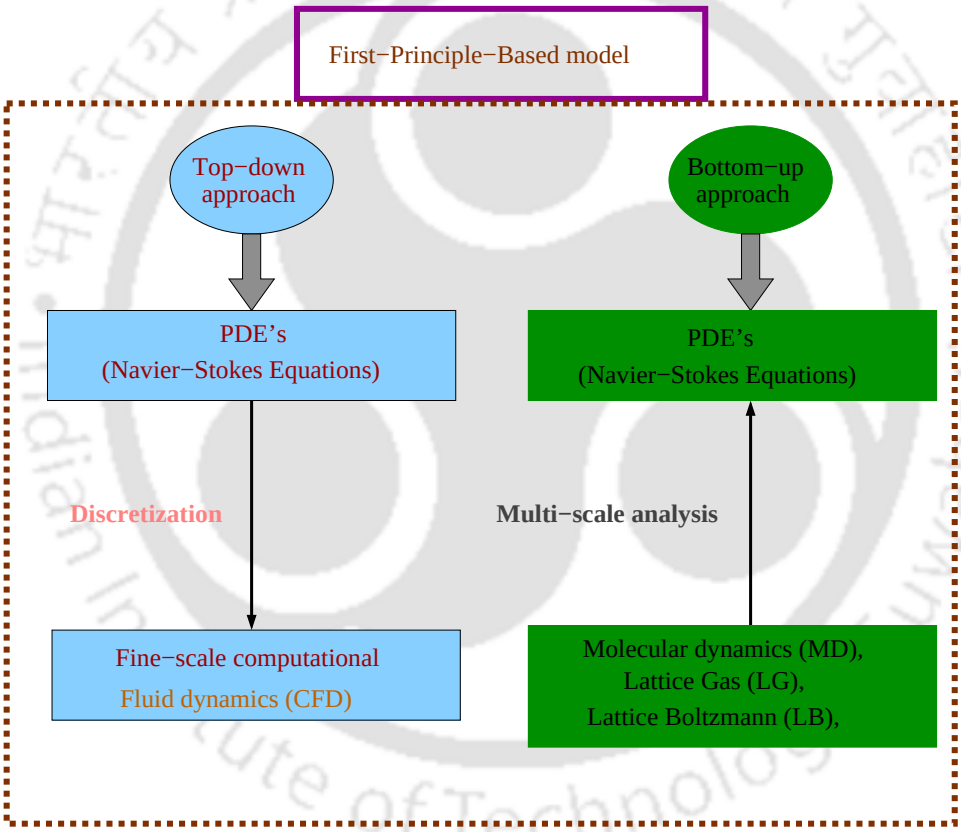

Figure 2.2: Top-down and Bottom-up approach in numerical simulations

considered as a particle method in comparison with the traditional method, though being able to recover continuity macroscopic variables. The method is the bridge between continuity approaches as in all conventional CFD methods, and computationally demanding molecular dynamic (MD) simulations. In MD Simulation,

the microscopic scale of simulations is visible only for very small systems owing to computer resources requirements. It is impractical to apply MD for macroscale problems. On the other hand, it is very inconvenient to use conventional CFD for complicated flow problems owing to the difficulties of tracing moving boundaries, modeling interaction between phases, handling surface tension at the macroscale level, etc. In fact, the method does not compete with the two well established methods (CFD and MD) but bridges the gap between them and thus becomes an ideal scale bridging numerical scheme, depicted schematically in Fig. 2.2.

The LBM covers the region between the macro (the so called mesoscopic world) and micro worlds, utilizes the benefits of both earlier mentioned methods. This offers the combination of the best of both methods: the large scale resolution of continuum methods with the geometrical flexibility of particle methods. Also, the kinetic nature of the LBM makes it easy to incorporate many physical phenomena into the LBM because they can be always explained on the molecular level. LBM can be applied easily to solve complex phenomena such as moving boundaries (multiphase, solidification, and melting problems).

The first-principle-based approaches solves the governing partial differential equations (PDE), namely the Navier-Stokes (N-S) equations to solve the underlying transport processes. The PDEs can be computed by using either the coarse-grain approach i.e., the bottom-up approach or by fine scale conventional CFD methods, the so called top-down approach (see Fig. 2.2). The MD, LG and LB methods comes under the bottom-up approach category. With a given set of suitable boundary conditions, the governing differential equations can be properly discretized on a computational grid using standard CFD techniques, namely finite volume, finite difference, or finite element methods. LBM is based on fundamental equation given by Ludwig Boltzmann whose great achievement was in the development of statistical mechanics, which describes how the properties of atoms and molecules (microscopic properties) determine the phenomenological (macroscopic) properties of matter such as thermal conductivity, viscosity and diffusion coefficient. The distribution function i.e the probability of finding the particle at certain location in finite range in certain time replaces the tagging of each particles as in molecular dynamic simulations. The idea of distribution function results in a huge saving of computer resources.

2.1.2 LBM vs N-S equation solver

As a numerical tool, the lattice Boltzmann method is different from incompressible Navier-Stokes equation based methods as follows [118].

1. N-S equations are second order PDEs whereas LBM consists of a set of first-order PDEs (kinetic equations).

2. Navier-Stokes equations contain nonlinear convection terms whereas the convection terms in LBM are linear.

3. Lattice Boltzmann equation is basically the discretized kinetic equation and Navier-Stokes equation however, can take integral or differential forms.

4. LBM depends on lattice structure; Navier-Stokes equations are in vector form which does not depend on the coordinate and grids.

5. The Navier-Stokes solver normally uses iterative procedure to obtain a converged solution; the LBM is explicit in form and do not require iterative procedures.

6. In LBM, the boundary conditions are expressed in the form of particle distribution functions.

Also it is known that there is no continuum assumption involved in the LBM. Since LBM is based on Boltzmann equation which is valid for the whole range of Knudsen number, it is very convenient to use in microflow simulation.

2.1.3 Lattice model structure

Lattice Boltzmann method and its predecessor lattice gas method takes into account the behavior of a collection of particles, consisting of large number of molecules, moving on a regular lattice, thereby decreasing the degrees of freedom of the system instead of tracking all the individual molecules. These particles residing on the nodes of lattice structure interact according to a velocity distribution function. These particles stream along given directions (lattice links) and collide at the lattice sites.

Lattice Boltzmann models can be worked with a number of different lattices, both triangular and cubic, and with or without rest particles in the discrete distribution function. The usual way of categorizing the various methods by lattice is the DnQm scheme. Here 'Dn' indicates for 'n' dimensions while 'Qm' stands for 'm' speeds. For example, D3Q19 model as shown in Fig. 2.3 is a three-dimensional lattice Boltzmann model on a cubic grid, with rest particles present. Lattice model incorporates a rest

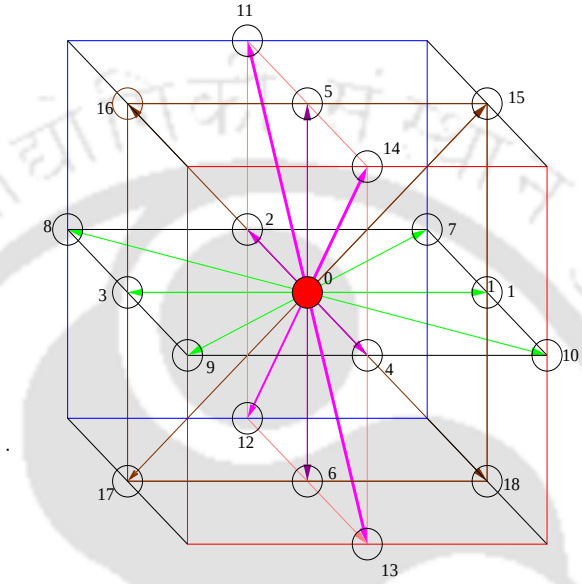

Figure 2.3: D3Q19 lattice structure schematic

particle in discrete velocity set because the LBM models with rest particle have more computational stability and reliability. Each node with crystal shape can stream particles to each of the six neighboring nodes which share a surface. The eight neighboring nodes shares a corner and itself. Mostly the simulations using lattice Boltzmann method, δ_x is taken as a basic unit for lattice spacing. If the length of the domain is L and has N lattice units along its entire length, the space unit is defined as $\delta_x = L/N$. Speeds in lattice Boltzmann simulations are describes in terms of the lattice speed. The discrete time unit can therefore be given as $\delta_t = \frac{\delta_x}{c}$, where the denominator c is the lattice speed.

2.1.4 Boltzmann transport equation

Boltzmann equation gives the probability of the particles positions in the phase space. A statistical description of a system can be given by distribution function

$f(r, c, t)$ where $f(r, c, t)$ is number of particles at a time t located between r and $r + dr$ which have velocities between c and $c + dc$. An external force F acting on a gas molecule of unit mass changes the velocity of the molecule from c to $c+ F\ dt$ and its position from r to $r + cdt$. The number of molecules, $f(r, c, t)$, before the application of external force is equal to the molecules after disturbances, $f(r + cdt, c + Fdt, t + dt)$, if no collisions take place between the molecules. Hence,

$$f\left(r + cdt, c + Fdt, t + dt\right) drdc - f\left(r, c, t\right) drdc = 0. \tag{2.1}$$

If collision takes place between the molecules, the number of molecules will be different at a location in the interval $drdc$. The collision operator (Ω) gives the rate of change between final and initial status of the distribution function. Hence, the equation for evolution of the number of the molecules can be given as,

$$f\left(r + cdt, c + Fdt, t + dt\right) drdc - f\left(r, c, t\right) drdc = \Omega(f) drdcdt. \tag{2.2}$$

Dividing the above equation by $dtdrdc$ and as the limit $dt \longrightarrow 0$ gives,

$$\frac{df}{dt} = \Omega(f) \tag{2.3}$$

The above equation gives the total rate of change of the distribution function is equal to the rate of collision. Since f is a function of r, c and t, the total rate of change can be expressed as,

$$df = \frac{\partial f}{\partial r} dr + \frac{\partial f}{\partial c} dc + \frac{\partial f}{\partial t} dt \tag{2.4}$$

For the system without external force the Boltzmann equation can be stated as,

$$\frac{\partial f}{\partial t} + \mathbf{c} \cdot \nabla f = \Omega\left(f_1, f_2\right) \tag{2.5}$$

where collision operator Ω is given by

$$\Omega\left(f_1, f_2\right) = \int \int \sigma\left(\alpha\right) \ |u - v| \ \left[f_1\left(u'\right) f_2\left(v'\right) - f_1\left(u\right) f_2\left(v\right)\right] dvd\alpha \tag{2.6}$$

Here $\sigma\left(\alpha\right)$ is differential collision cross section for the two-particle collision which transforms the velocities from u, v (incoming) into u', v' (outgoing). The position in physical space is denoted by $\mathbf{x}$ and the velocity in the momentum (or velocity) space is denoted by u, v. α is the solid angle in which the particles are scattered.

2.1.5 BGKW approximation

Boltzmann equation is difficult to solve since the collision term in the equation is complex. Bhatnagar et al. [111] introduced a simplistic model for collision operator. They approximated the collision operator with simple linear operator without introducing considerable error to the outcome of the solution in 1954. Welander [119] independently, introduced similar operator at the same time. The BGK collision model substitutes a huge amount of the two-body collision details with some qualitative and average properties of the original Boltzmann collision operator. This collision integral is based on several assumptions [120]. The particles are considered to interact by way of two-particle collisions only. This presumes that the interactions involving more then two particles can be assumed to be insignificant since large amount of details of two-body interactions is not likely to affect significantly the values of experimentally measured quantities. For all two-particle collisions, it is assumed that they appear locally in a sense that they take place at a single point $\mathbf{x}$ (i.e. not in between). A similar condition holds true for time t, it is considered that the time duration of a collision is negligible. Particles involved in a collision are supposed to be uncorrelated and the collision itself is modeled assuming that the collisions are elastic. Thus, the kinetic energy and especially momentum are conserved. The velocities before collision are denoted by u and v, and the velocities after collision by u' and v'. Since the collision is elastic the following two equations have to be fulfilled (note that particles have same mass).

$$u + v = v' + w' \tag{2.7}$$

$$u^2 + v^2 = |u'|^2 + |v'|^2 \tag{2.8}$$

Complicated collision integral is replaced by a single time relaxation term. This term is chosen in such a manner that it imitates specific properties of the original collision integral.

$$\Omega = \omega(f^{eq} - f) = \frac{1}{\tau}(f^{eq} - f) \tag{2.9}$$

where $\omega{=}\frac{1}{\tau}$, ω is called as collision frequency and τ is called as relaxation time factor. Inserting BGKW approximation the Boltzmann equation can be written as,

$$\frac{\partial f}{\partial t} + \mathbf{c} \cdot \nabla f = \frac{1}{\tau}\left(f^{eq} - f\right) \tag{2.10}$$

The discretized equation can be written as given below

$$\frac{\partial f_i}{\partial t} + \mathbf{c}_i \cdot \nabla f_i = \frac{1}{\tau}\left(f_i^{eq} - f_i\right) \tag{2.11}$$

The explicit lattice Boltzmann equation should be solved in two steps: a streaming step and a collision step. The update order may be changed without changing the simulation itself, i.e., first the streaming and then the collision (stream-collide) or first the collision and then the streaming (collide-stream). Each step can be viewed as solving a part-equation. LB method makes use of first order discretizations of the dimensionless discrete velocity Boltzmann equation in both time and space. The dimensionless time step and lattice spacing are set equal. With these effects included, the LB method is a second order method in both space and time for the simulation of the N-S equations.

2.1.6 Equilibrium distribution function

The most important element in applying the lattice Boltzmann method is equilibrium distribution function f^{eq}. Equations for solving the energy, momentum, diffusion and advection are same and only difference is in equilibrium distribution function. Maxwell has given an equation for particles moving with macroscopic velocity $\mathbf{u}$ is called as Maxwell distribution function written as,

$$f = \frac{\rho}{\frac{2\pi}{3}} e^{-\frac{3}{2}(\mathbf{c}-\mathbf{u})^2} \tag{2.12}$$

Above equation can also be written as

$$f = \frac{\rho}{\frac{2\pi}{3}} e^{-\frac{3}{2}(\mathbf{c}^2)} e^{3(\mathbf{c}\cdot\mathbf{u}-\mathbf{u}^2)/2} \tag{2.13}$$

where c = lattice speed and $\mathbf{u}$ = macroscopic velocity of particle. Hence, Maxwell equation can be expanded around stationary state as,

$$f = \frac{\rho}{\frac{2\pi}{3}} e^{-\frac{3}{2}(\mathbf{c}^2)} \left[1 + 3\left(\mathbf{c}\cdot\mathbf{u}\right) - \frac{3}{2}\mathbf{u}^2 + ...\right] \tag{2.14}$$

The general form of equilibrium distribution function can also be written as,

$$f_i^{eq} = \Phi\omega_i \left[A + B\mathbf{c}_i \cdot \mathbf{u} + C\left(\mathbf{c}_i \cdot \mathbf{u}\right)^2 + D\mathbf{u}^2\right] \tag{2.15}$$

In above equation A, B, C, D are the constants which can be calculated by conservation of mass, conservation of momentum and conservation of energy. Φ is scalar

parameter such as density (ρ), temperature (thermal energy density), or species concentration. Summation of all of these parameter is equal to one.

$$\Phi = \sum_{i=0}^{i=n} f_i^{eq} \tag{2.16}$$

$$f_i^k\left(\mathbf{x} + \mathbf{c}_i\delta_t, t + \delta_t\right) - f_i^k\left(\mathbf{x}, t\right) = -\frac{f_i^k\left(\mathbf{x}, t\right) - f_i^{k(eq)}\left(\mathbf{x}, t\right)}{\tau_k} \tag{2.17}$$

For $D3Q19$ model $f_i^{k(eq)}$ has the following form.

$$f_i^{k(eq)} = d_k n_k - \frac{1}{2} n_k \mathbf{u}_k^{eq} \cdot \mathbf{u}_k^{eq} \quad \text{for} \quad i = 0 \tag{2.18}$$

$$f_i^{k(eq)} = \frac{1 - d_k}{12} n_k + \frac{1}{6} n_k \left(\mathbf{c}_i \cdot \mathbf{u}_k^{eq}\right) + \frac{1}{4n_k}\left(\mathbf{c}_i \cdot \mathbf{u}_k^{eq}\right)^2 - \frac{1}{12} n_k \mathbf{u}_k^{eq} \cdot \mathbf{u}_k^{eq} \tag{2.19}$$

for i=1,2,3,...6

$$f_i^{k(eq)} = \frac{1 - d_k}{24} n_k + \frac{1}{12} n_k \left(\mathbf{c}_i \cdot \mathbf{u}_k^{eq}\right) + \frac{1}{8} n_k \left(\mathbf{c}_i \cdot \mathbf{u}_k^{eq}\right)^2 - \frac{1}{24} n_k \mathbf{u}_k^{eq} \cdot \mathbf{u}_k^{eq} \tag{2.20}$$

for i=7,8,.....18

$$\mathbf{c}_i = \begin{cases} (0,0,0) & i = 0 \\ (\pm 1, 0, 0), (0, \pm 1, 0), (0, 0, \pm 1) & i = 1 - 6 \\ (\pm 1, \pm 1, 0), (\pm 1, 0, \pm 1), (0, \pm 1, \pm 1) & i = 7 - 18 \end{cases}$$

$$\left(c_s^k\right)^2 = \frac{(1 - d_k)}{2} \tag{2.21}$$

Where d_k is a free parameter, which relates to speed of sound c_s^k of pure k^{th} component. It should be noted that the macroscopic quantities like density and mean velocity are calculated by taking the moments of the distribution function as given below.

$$n_k = \sum_i f_i^k \tag{2.22}$$

where n_k is the number density of k^{th} component. The macroscopic density and momentum density of each component are calculated as below.

$$\rho_k = m_k n_k = m_k \sum_i f_i^k \tag{2.23}$$

$$\rho_k \mathbf{u}_k = m_k \sum_i \mathbf{c}_i f_i^k \tag{2.24}$$

The kinematic viscosity in lattice unit is

$$\nu_k = \frac{(2\tau_k - 1)\,(c_s^k)^2}{6} \tag{2.25}$$

where c_s is the speed of sound of a region of pure k^{th} component, m_k is mass of k^{th} component and τ_k is relaxation parameter. The total density and momentum density of multicomponent flow are given by

$$\rho = \sum_k m_k \sum_i f_i^k \tag{2.26}$$

$$\rho \mathbf{u} = \sum m_k \rho_k \mathbf{u}_k \tag{2.27}$$

When the local equilibrium distribution is properly chosen through the Chapman-Enskog expansion, one can recover governing continuity and Navier-Stokes equations from Eq. 2.17 [121].

2.1.7 Streaming step

During this step, the particles of a lattice moves to the neighboring sites along the $D3Q19$ discrete velocity directions as shown in Fig. 2.4. It can be observed that,

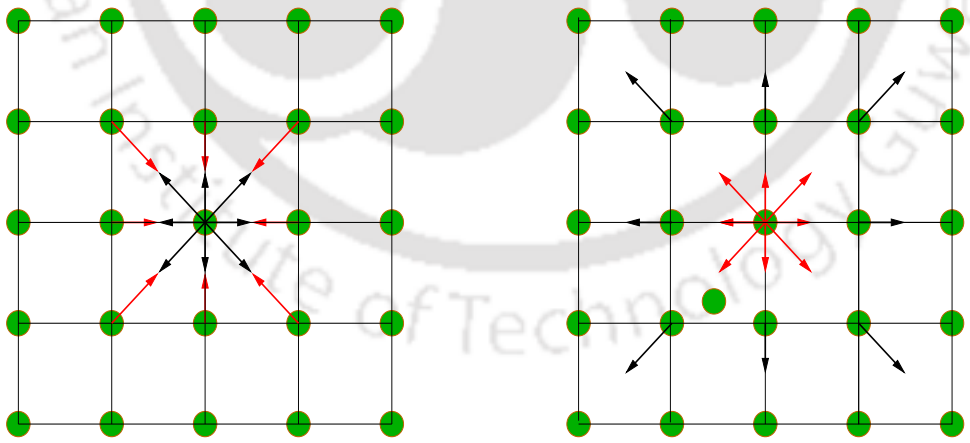

Before streaming After streaming

Figure 2.4: Pre-streaming and post-streaming conditions in LBM

the particles of the middle cell moved to the neighboring cells whereas the particles of the neighboring cells moved to the middle cell. The velocity direction is conserved by the streaming, i.e., particles that move along the north direction from the source cell have reached at the north direction in the destination cell and so on. The corresponding equation part is

$$f(\mathbf{x}, t + \delta t) = f(\mathbf{x}) \tag{2.28}$$

2.1.8 Collision step

After arriving at the new cell, the fluid particles are subjected to collisions that modify the distribution function, relaxing it toward the equilibrium state. It is assumed that the collision take place between two particles approaching each other (exclusion principle) at node node only (not in between the nodes) (see Fig. 2.5). A particles change their velocity i.e., momentum during collision before they finally reach equilibrium (see Fig. 2.6).

$$f(\mathbf{x}, t + \delta t) = f(\mathbf{x}) - \frac{1}{\tau}\left(f_i - f_i^{eq}\right). \tag{2.29}$$

2.1.9 Boundary conditions in LBM

2.1.9.1 Bounce back (no slip) boundary condition

Since solid boundary cells cannot have fluid neighbor cells on one side, the streamed particles are reversed (no-slip boundary condition). In this boundary condition, as a particle distribution streams to a wall node, it scatters back to the fluid node in the direction of its incoming link. In halfway bounce back, the wall is considered to located at halfway between a fluid node and a bounce-back node. In one time step a fluid particle goes to the boundary site, reverses its velocity and comes back.

2.1.9.2 Free-slip condition

Since boundary cells can not have fluid neighbor cells on one side, the streamed particles are reflected in their component normal to the wall (free slip boundary condition) as shown in Fig. 2.8. In this case, the tangential motion of the fluid

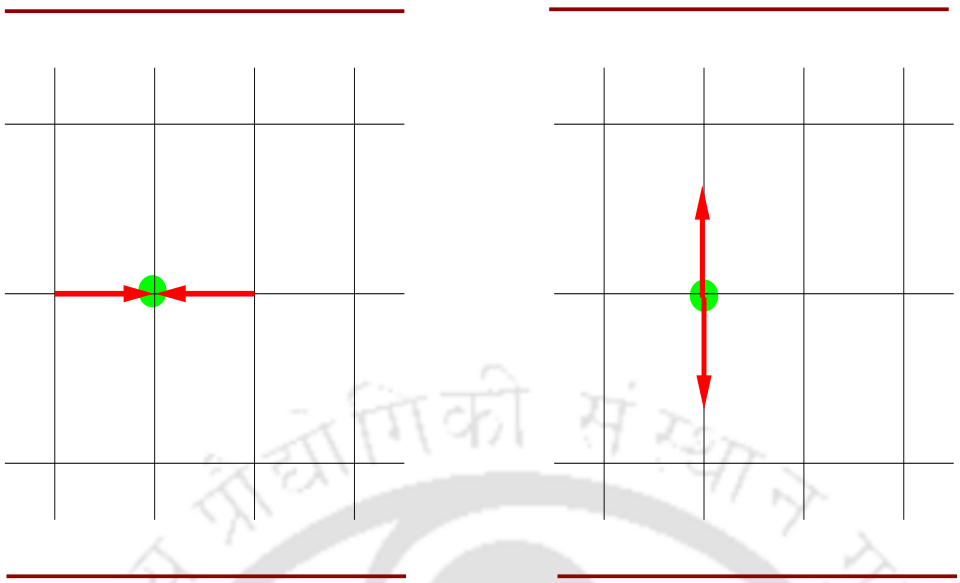

Figure 2.5: Two particles collision in LBM

on the wall is free and no momentum exchange with the wall takes place along the tangential component.

2.1.9.3 Periodic boundary condition

In periodic boundary condition, the system becomes closed by the edges being treated as if they are attached to opposite edges. By using periodic boundary condition, boundary effects of the simulation domain can be ignored. The cubical (rectangular in 2D) simulation box is replicated throughout space to form an infinite domain. When a particle moves in the simulation box, its periodic image in every one of the other boxes moves in exactly the same way. Thus, as a particle leaves the simulation box, one of its images will enter through the opposite face. Figure 2.9 shows the mechanism of applying a periodic boundary condition in the horizontal direction in a 2D simulation domain. Special attention should be given to the corner sites. For example, for the site at the right-bottom corner of a D2Q9 domain, f_1 will go to the left-bottom corner site, f_4 to the right-top corner and f_8 to the left top corner. Such boundary treatment will become more complicated for 3D and/or geometrically more complex systems. The example given below shows

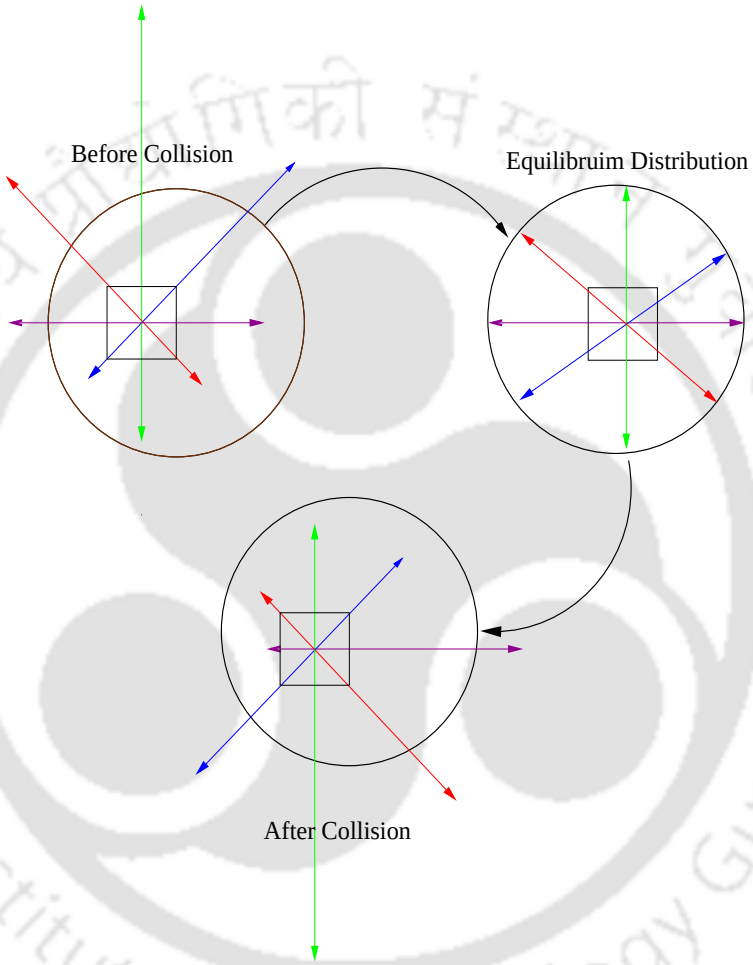

Figure 2.6: Collision process in LBM

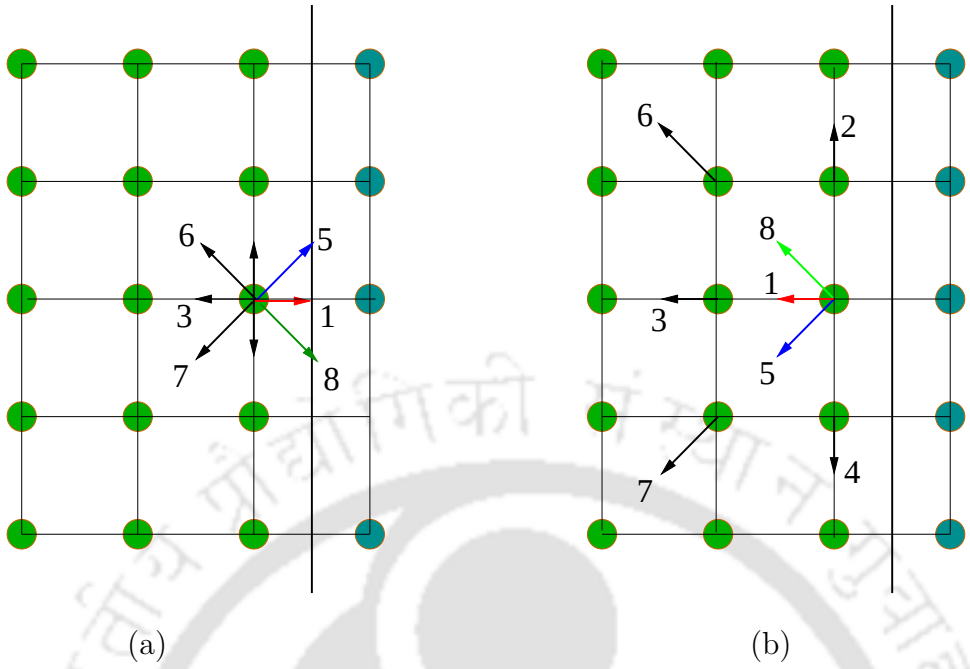

(a) (b)

Figure 2.7: Bounce back and post-streaming conditions in LBM

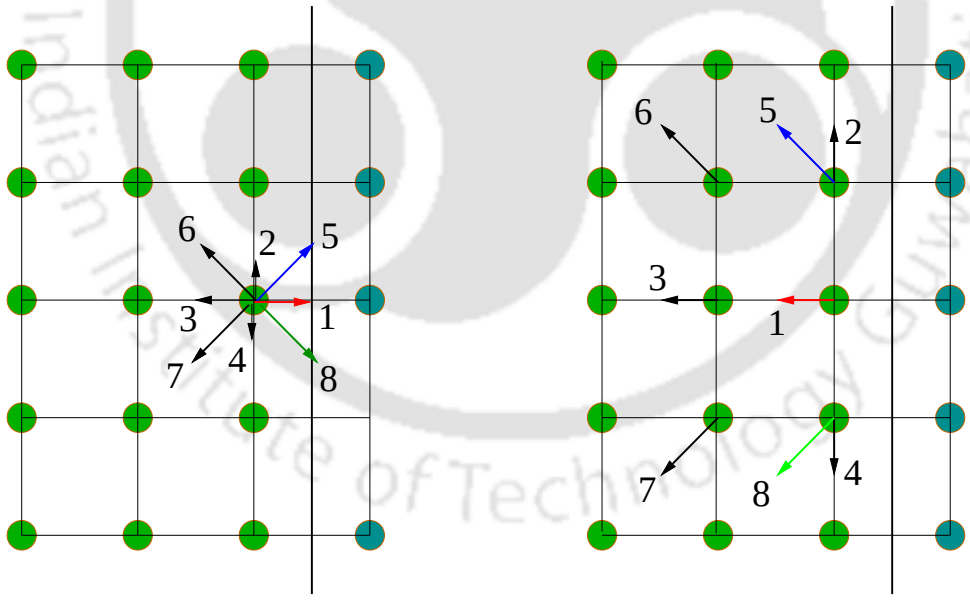

(a) (b)

Figure 2.8: Free slip condition in LBM schematic

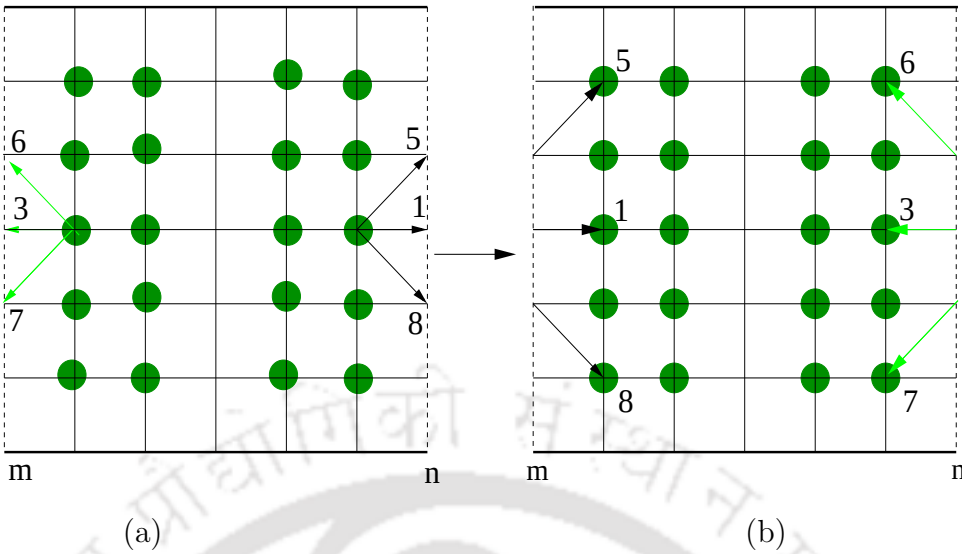

Figure 2.9: Periodic boundary condition in LBM

(see Fig. 2.10) typical application of periodic boundary condition in 2D. The figure shows that in the domain near line m

$f_{4a}=f_{4b}$, $f_{7a}=f_{7b}$, $f_{8a}=f_{8b}$

whereas for the distribution near line n

$f_{2b}=f_{2a}$, $f_{5b}=f_{5a}$, $f_{6b}=f_{6a}$

2.1.9.4 Mirror/symmetry boundary condition

In some situations, the advantage of symmetry can be taken to significantly reduce the computation requirement. In LBM, one can just imagine that the fluid properties (actually, the distribution function f's) on one side of symmetric plane are mirror reflection of those on the other side (see Fig. 2.11). The distribution functions from the image sites are set to be equal to their images on boundary sites

$f_3 = f_1$, $f_4 = f_2$, and $f_6 = f_5$.

2.1.10 Lattice Boltzmann algorithm

In LBM, domain (space) is divided into a regular lattice (for instance, a D3Q19 cubic lattice). The real numbers at each site indicates the particle distribution function at that location. It is equal to the probable number of identical particles in

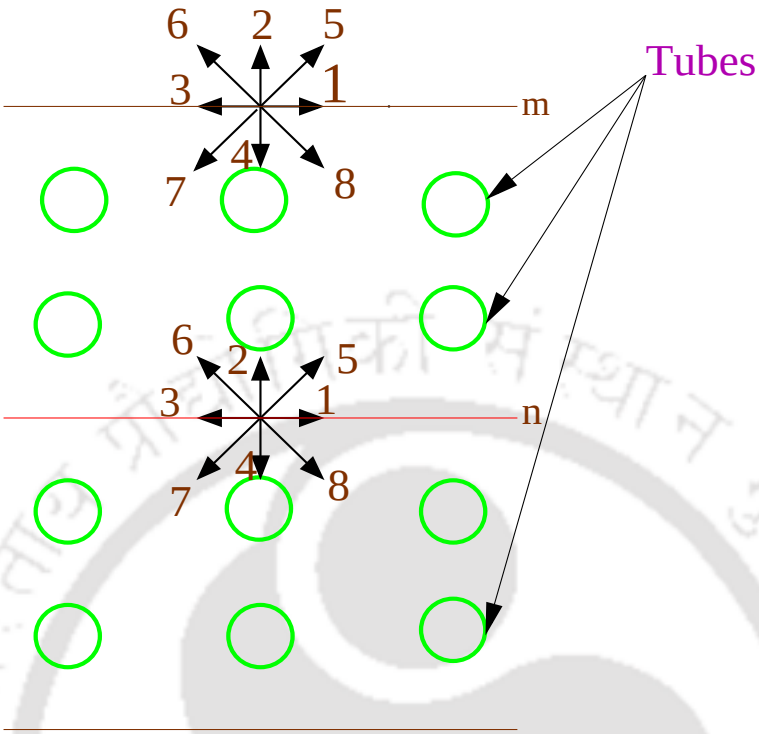

Figure 2.10: Periodic boundary condition in LBM

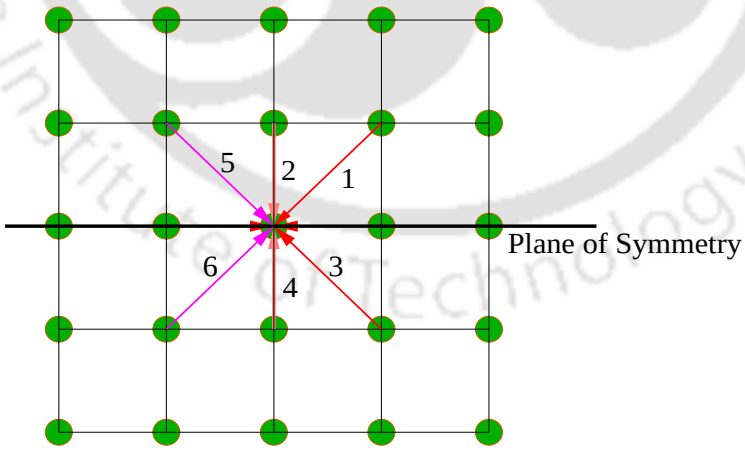

Figure 2.11: Mirror boundary condition in LBM

each of the available particle states i. In this method, each particle state i is given by a particle velocity, which is limited to a discrete set of velocities. During each time step, particles move, or hop, to the nearby lattice site along their directions of motion.

Particles 'collide' with other particles those arrive at the same site. The result of the collision is found out by solving the kinetic (Boltzmann) equation for the new particle distribution function at that site and the particle distribution function (f_i) is modified and updated. First operation in each time step Δt of the calculation is to stream the particles to the next lattice along their directions of motion. In general, the units are taken such that the distance to nearest neighbors δx and Δt are unity. This gives $c = 1$ and the lattice vector $\mathbf{c}_i$ numerically becomes equal to the velocity of the particles moving in direction i. If the mass of each particle is set equal to unity, the momentum in direction i at site $\mathbf{x}$ and time t is just $f_i(\mathbf{x}, t)\mathbf{c}_i$. The second

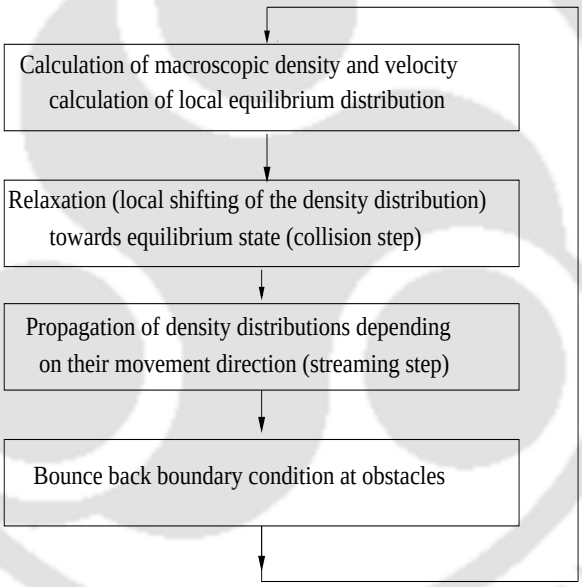

Figure 2.12: Algorithm in LBM

operation is basically the simulation of particle collision, which leads to scattering of the particles at each lattice site in various directions. The collision rules are chosen to keep the sum of the f_i's remain unchanged (i.e., no particles are lost). The total energy and momentum at each lattice site are conserved. Generally "bounce back" boundary condition is imposed to ensure that the particles have zero average velocity at the walls (both perpendicular and parallel to the walls). Any flux of particle that collides with a boundary/wall simply reverses its velocity making the average

velocity at the boundary zero. The result of collisions is simply approximated by assuming the redistribution of the momenta of the interacting particles at some constant rate toward an equilibrium distribution. This simplification is known as the single time relaxation approximation. The momentum distribution at each lattice site is pushed toward the equilibrium distribution at each time step in single time relaxation approximation. The equilibrium distribution of a state with zero net momentum equals the amounts of momentum in each direction in the absence of external forces. A fluid simulation with the lattice Boltzmann method is therefore a repetition of the streaming and collision steps until equilibrium is reached or until a given end-time. The entire solution procedure is schematically shown in Fig. 2.12.

2.1.11 Multiphase model

The mixing or the separation of the phases is basically the result of interactions at the microscopic level between the fluid molecules. This underlines the existence of a long range interparticle force between the fluid molecules which can be defined in terms of interaction potential. Shan and Chen (S-C) model proposed by Shan et al. [3] introduces a non-local interaction between particles at neighboring lattice sites. An arbitrary number of components depending on the amount of computer memory available, with different molecular masses can be simulated in this model. Interaction potentials for each of the components control the form of the equation of state of the fluid. The interaction between the particles of different components are incorporated in the kinetics through a set of potentials. It may be noted that the collision operator does not conserve total particle momentum at each site owing to the inclusion of interparticle interactions,. However, the total momentum of the whole system remains conserved. The interaction results in an extra momentum transfer flux among the lattice sites. The separation of fluid or fluid mixture into different phases depends upon the interaction potentials.

The multicomponent multiphase LBE model by Shan et al. [3] also considers the BGK collision term. Main distinction lies in determination of equilibrium velocity to include the interaction between different fluid component. The separation of fluid phases or components in the S-C model is automatic. This is significant improvement in numerical efficiency as compared to original LBM multiphase models. This model improves the isotropy of the surface tension and is preferred because of its convenience in handling fluid/solid interaction. The interaction force between

the particles of k^{th} component at location $\mathbf{x}$ and $k'^{\,th}$ component at location $\mathbf{x}'$ is assumed to be proportional to the product of their effective mass $\psi\ (\rho_k)$.

$$\mathbf{F}_{1k}(\mathbf{x}) = -\psi_k\left(\mathbf{x}\right)\sum_{\mathbf{x}'}\sum_{k=1}^{s} G_{k\bar{k}}\left(\mathbf{x},\mathbf{x}'\right)\psi_{\bar{k}}\left(\mathbf{x}'\right)\left(\mathbf{x}'-\mathbf{x}\right) \tag{2.30}$$

where $G_{k\bar{k}}\left(\mathbf{x},\mathbf{x}'\right)$ is called as the Green's function such that

$$G_{k\bar{k}}\left(\mathbf{x},\mathbf{x}'\right) = G_{k\bar{k}}\left(\mathbf{x}',\mathbf{x}\right) \tag{2.31}$$

In a multi-phase system, the coexistence of both phases is possible only at critical temperature whereas for the multicomponent case, the components are immiscible i.e., do not mix up in the absence of diffusion in the system, i.e., for null or negative diffusion coefficient. In the interaction force these aspects are modelled with the help of the Green function. The Green function is defined as follows in $D3Q19$.

$$G_{k\bar{k}}\left(\mathbf{x},\mathbf{x}'\right) = g_{k\bar{k}} \quad \text{for} \quad |\mathbf{x}-\bar{\mathbf{x}}| = 1 \tag{2.32}$$

$$G_{k\bar{k}}\left(\mathbf{x},\mathbf{x}'\right) = \frac{g_{k\bar{k}}}{2} \quad \text{for} \quad |\mathbf{x}-\bar{\mathbf{x}}| = \sqrt{2} \tag{2.33}$$

$$G_{k\bar{k}}\left(\mathbf{x},\mathbf{x}'\right) = 0 \quad \text{otherwise} \tag{2.34}$$

$G_{k\bar{k}}\left(\mathbf{x},\mathbf{x}'\right) > 0$ leads to repulsion and $G_{k\bar{k}}\left(\mathbf{x},\mathbf{x}'\right) < 0$ leads to attraction between the particles. While a large value of $G_{k\bar{k}}\left(\mathbf{x},\mathbf{x}'\right)$ makes the interface sharper, it can lead to numerical instabilities since it increases the interaction force and thus the spurious velocities. Interaction potential $V(\mathbf{x},\mathbf{x}')$ can be expressed in terms of Greens' Function as

$$V\left(\mathbf{x},\mathbf{x}'\right) = G_{k\bar{k}}\left(\mathbf{x},\mathbf{x}'\right)\psi_{\bar{k}}\left(\mathbf{x}'\right)\left(\mathbf{x}'-\mathbf{x}\right) \tag{2.35}$$

2.1.12 Effective masses

Other vital parameter of the S-C model is the effective mass of the phase or component. It is basically a function of the density and so far no direct derivation from physical laws has been found like fluid-fluid interaction parameter G_c has been related to the temperature or the diffusion coefficient. There is currently no deterministic way to map the fluid properties to a given effective mass. Although each fluid should theoretically have a different effective mass, Shan et al. [3] proposed

$$\psi\left(\rho\right) = \rho_0\left[1 - e^{-\frac{\rho}{\rho_0}}\right] \tag{2.36}$$

which simplifies by assuming $\rho_0 = 1$ to $\psi_k = f(\rho_k(x))$ which is a function of x through its dependency on n_k. For S-C model, a two components system can basically be modeled in following ways.

1. The molecules of the same substance attract each other then g_{kk} not equal to 0. If molecules have no interaction with the molecules of the other substances then $g_{kk'} = 0$. As stated above an attraction is modeled by a negative value of $G_c = g_{kk'}$

2. The molecules of the same substance have no interaction with each other, then $g_{kk} = 0$ and repel the molecules of the other substances when $g_{kk'} \neq 0$. So a repulsion is modelled by a positive value of $G_c = g_{kk'}$.

3. The molecules of the same substance interact with each other then $g_{kk} \neq 0$ and as well as with the ones of other substances $g_{kk'} \neq 0$.

2.1.13 Inclusion of interaction into the lattice Boltzmann method

With the interaction force known, it needs to be incorporated in the normal lattice Boltzmann scheme. This is included by using an altered velocity in the equilibrium distribution function. The new momentum taking the interaction force into account is given by the parameter $\mathbf{u}_k^{eq}$ which is determined by the following relation.

$$\rho_k \mathbf{u}_k^{eq} = \rho_k \mathbf{u}' + \tau_k \mathbf{F}_k \tag{2.37}$$

where $\mathbf{u}'$ is a an extra component on the top due to inter particle interaction which is added for each component. Total force acting on the k^{th} component is give by the following equation.

$$\mathbf{u}' = \left(\sum_{k=1}^{s} \frac{\rho_k \mathbf{u}_k}{\tau_k} \right) / \left(\sum_{k=1}^{s} \frac{\rho_k}{\tau_k} \right) \tag{2.38}$$

The Interactive force between the fluid and wall is given as

$$\mathbf{F}_{2k}(\mathbf{x}) = -n_k(\mathbf{x}) \sum_{\mathbf{x}'} g_{kw} n_w(\mathbf{x}')(\mathbf{x}' - \mathbf{x}) \tag{2.39}$$

where

n_w= number density of the wall, which is a constant at the wall and zero otherwise.

g_{kw}= interactive strength between the component k and the wall.
$\mathbf{F}_{2k}$ is the force that is perpendicular to the wall. Hence, it does not effect the no slip boundary condition. g_{kw} is negative for wetting fluid and positive for non wetting fluid. Body force is given by,

$$\mathbf{F}_{3k} = \rho_k \mathbf{g} = m_k n_k \mathbf{g} \quad \text{if the driving force is gravity}$$

$$\mathbf{F}_{3k} = \rho_k \mathbf{W}(t) \quad \text{if the driving force is acoustic excitation}$$

where

$$\mathbf{W}(t) = \mathbf{W}(0) + \delta\mathbf{W}(t)$$

where $\mathbf{W}(0)$ and $\delta\mathbf{W}(t)$ is a constant body force and perturbation respectively.
It may be noted that equation of state is used to calculate pressure as given below:

$$P = \sum_k \frac{(1 - d_k)\, m_k n_k}{2} + 3 \sum_{k,\bar{k}} g_{k,\bar{k}} \psi_k \psi_{\bar{k}} \tag{2.40}$$

Total force can be calculated as

$$\mathbf{F}_k = \mathbf{F}_{1k} + \mathbf{F}_{2k} + \mathbf{F}_{3k} \tag{2.41}$$

where,
$\mathbf{F}_{1k}$ = Fluid fluid interaction
$\mathbf{F}_{2k}$ = Fluid solid interaction
$\mathbf{F}_{3k}$ = External force

2.2 Static and Dynamic Contact Angle

Wettability studies usually comprise of the contact angle measurement as one of the primary data, which reflects the degree of wetting when a solid and liquid interact. The liquid moves to expose its fresh surface and to wet the fresh surface of the solid in turn. This implies that the phenomenon of wetting is not merely a static phenomenon.Although, the present work assumes the static contact angle throughout the study of capillarity-wettability interaction, the brief discussion on static and contact angle is given below for the sake of completeness.

2.2.1 Static Contact Angle

When an immiscible droplet comes into contact with a solid phase, there is a contact line between the wetting and non wetting fluids and the solid surface. The contact angle between the fluids and the surface can be calculated through Youngs equation provided the interfacial tension between the fluid components and between each component and the solid surface are known via Youngs law [122].

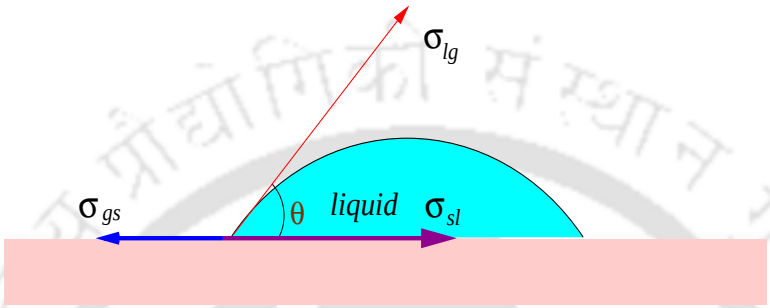

Figure 2.13: Contact angle of a droplet

$$\cos\theta = \frac{\sigma_{sg} - \sigma_{sl}}{\sigma_{lg}} \tag{2.42}$$

where

σ_{lg} - liquid-gas surface tension

σ_{sg} - solid-gas surface tension

σ_{sl} - solid-liquid surface tension

θ - contact angle

A surface is hydrophilic if the value of the contact angle is less than 90^o and is hydrophobic is greater than 90^o. Surfaces with the contact angle between 150^o and 180^o are called superhydrophobic.

2.2.2 Dynamic Contact Angle

If the three-phase contact line is in actual motion, the contact angle produced is called a dynamic contact angle. The contact angle depends on surface energy, roughness, the manner of surface preparation, surface cleanliness. Since solid surfaces are often rough or chemically heterogeneous, even equilibrium contact angles may not be single-valued, but will depend on whether the interface has been advanced or

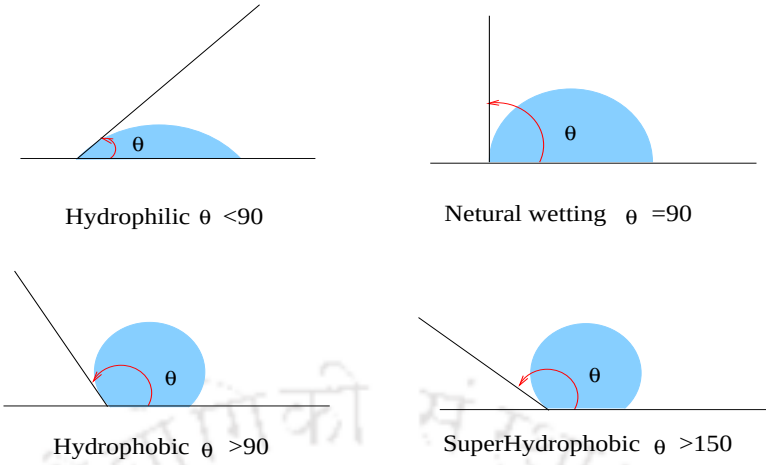

Figure 2.14: Contact angle for hydrophilic, hydrophobic and superhydrophobic

recessed, a phenomenon known as contact angle hysteresis. It is further classified as advancing contact angle and receding contact angle.

2.2.2.1 Advancing Contact Angle, θ_a

Consider the process of partially immersing a thin slab of the solid into liquid moving it vertically downward very slowly and stopping when contact line reaches point z_1 as shown in Fig. 2.15. The partially wetting liquid forms an equilibrium contact angle at point z_1 which is designated as θ_a. Because the contact angle was established after advancing the contact line over dry solid it is referred as the advancing contact angle.

2.2.2.2 Receding Contact Angle, θ_r

Consider the process of partially moving a thin slab of the solid out of liquid vertically upward very slowly and stopping when contact line reaches point z_2 (Fig. 2.15). The partially wetting liquid forms an equilibrium contact angle at point z_2 (Fig. 2.15) which is designated as receding contact angle θ_r. Because the contact angle was established after receding moves over the portions of surface initially covered with liquid .For a droplet moving along the solid surface, the contact angle at the front of the droplet (advancing contact angle) is greater than that at the back of the droplet (receding contact angle), due to the roughness and surface heterogeneity, resulting in the contact angle hysteresis. Hydrophobic surfaces can be constructed

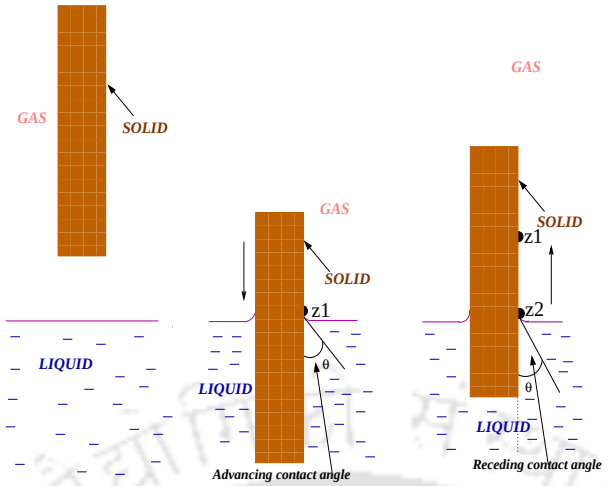

Figure 2.15: Advancing and receding contact angles

by using low surface energy materials, coatings such as polytetrafluoroethylene or wax. The hydrophobicity of a surface can also be increased by increasing the surface area by increasing surface roughness and/or creation of air pockets. Air may be trapped in the cavities of a rough surface, resulting in a composite solidairliquid interface, as opposed to the homogeneous solidliquid interface. Superhydrophobic surfaces have very low water contact angle hysteresis, and also the low difference between the advancing and receding contact angles. In addition to high contact angle, another wetting property of interest for liquid flow applications is a very low water roll-off angle, which denotes the angle to which a surface may be tilted for roll off of water drops (i.e., very low water contact angle hysteresis) [123, 124]. Superhydrophobic surfaces are extreme water-repellent properties. This property can be utilized to facilitate the droplet motion in fuel cell channels.

2.3 Validation of the Code

The present multiphase multicomponent lattice Boltzmann code is validated solving for static droplet test and the results are compared with Mukherjee et al. [21].

2.3.1 Static droplet test

A static droplet test is performed in the presence of solid wall in order to evaluate the fluid/solid interaction parameter for the $D3Q19$ two-phase S-C lattice Boltzmann model, which controls the wall wettability effect through the resulting contact angle at the solid/fluid interface. In the present contact angle simulation, a half liquid droplet of radius 10, in lattice units, is placed initially at the geometric center of the bottom solid wall of the computational domain with $50 \times 50 \times 50$ lattices. The periodic boundary conditions is applied in the x direction and no-slip boundary condition in the y and z directions. In this simulation, no body force is applied. The input parameters are fluid/solid interaction parameter, $g_{1w} = -g_{2w}$. The bounce-back scheme [125, 126, 127] is used at the walls to obtain no-slip boundary condition.

2.3.2 Determination of contact angle

When a static droplet is formed, the contact angle is evaluated from the final steady state values of the droplet radius R, droplet height a_0, and wetted length of the droplet b_0, as shown in Fig. 2.16 using the following relation [101].

$$\tan(\theta_2) = \frac{b_0}{2(R - a_0)} \tag{2.43}$$

The final radius R, is evaluated from a_0 and b_0, using the following expression

$$R = \frac{a_0}{2} + \frac{{b_0}^2}{8} \tag{2.44}$$

Hereafter, θ_2 is referred to as the contact angle, θ for simplicity.

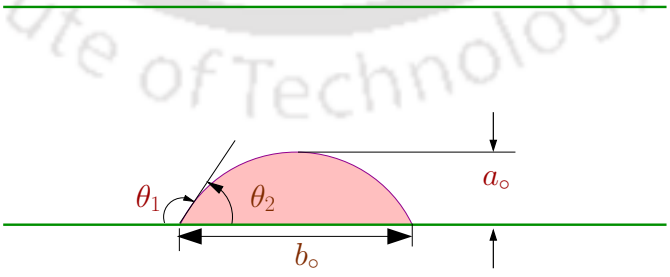

Figure 2.16: Static droplet after steady state

2.3.3 Comparison of results

The simulation parameters for carrying out the static droplet test are given below.
Relaxation time, $\tau_1 = 1$ $\tau_2 = 1.42$
Fluid-solid interaction parameter, $g_{1w} = -g_{2w}$
Fluid-fluid interaction parameter, $g_{11} = g_{22} = 0$, $g_{12} = g_{21} = G_c = 0.001$
Gravitational factor, $gvt = 0$
Initial density of fluid1, $\rho_1 = 150$
Initial density of fluid2, $\rho_2 = 0$
The values of fluid-solid interaction parameter g_{2w} are varied from -0.02 to 0.16 to obtain various values of contact angle θ as shown in Fig. 2.17. Simulations were carried out for 40000 time step to get the steady state results. The droplet gets detached at g_{2w} =0.16. The variation of contact angle for various values of g_{2w} is shown in Fig. 2.18. The result is comparable with good agreement with Mukherjee et al. [21]. A negative value of g_{2w} gives rise to a contact angle less than 90° indicating that the phase 2 tends to wet the surface leading to hydrophilic wettability. A contact angle greater than 90° is formed when g_{2w} is positive; indicating that the phase 2 is non-wetting and the wettability condition is termed as hydrophobic. For $g_{2w} = 0$, neither of the phases exhibits preferential wetting to the surface, which is defined as neutrally wet situation.

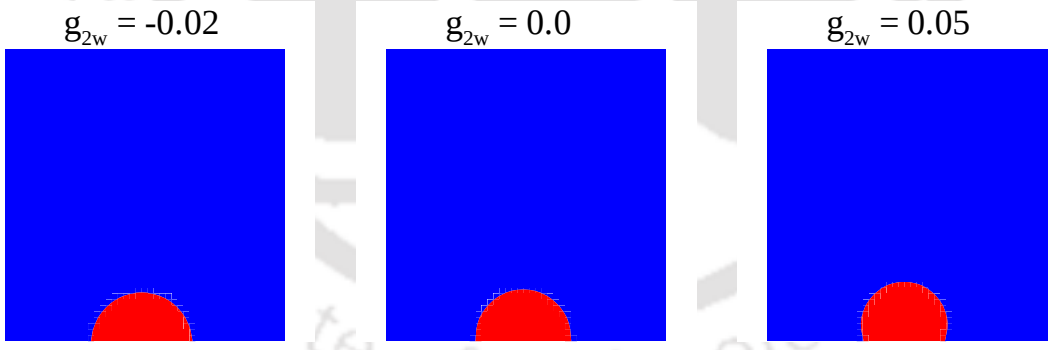

Figure 2.17: Three static contact angles obtained by adjusting fluid-solid interaction parameter (a) $g_{2w} = 0.02$, $\theta = 78°$,(b) $g_{2w} = 0$, $\theta = 90°$, (c) $g_{2w} = 0.05$, $\theta = 118°$

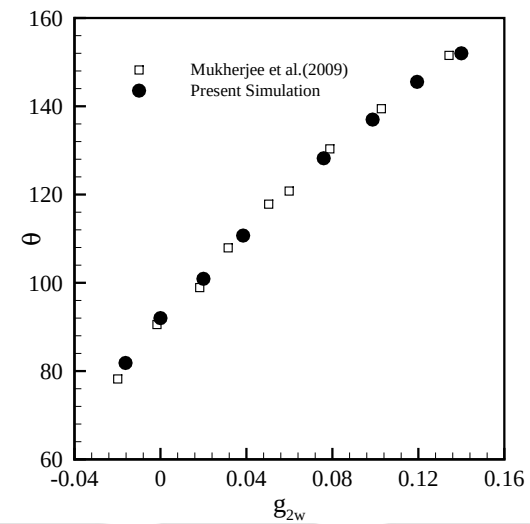

Figure 2.18: Variation of contact angle with g_{2w}

Chapter 3

Probing the Influence of Superhydrophobicity and Mixed Wettability on Droplet Displacement Behavior

3.1 Introduction

The displacement of immiscible fluids is a vital phenomenon for a wide range of engineering applications including microfluidic and nanofluidic, oil recovery. In the recent past the effect of wettability on the dynamics of immiscible displacement of droplet has been studied extensively [10, 11, 22, 45, 54, 55]. Most of these studies focussed on droplet dynamics on hydrophobic and hydrophilic surface only. The droplet motion on superhydrophobic surface is also explored by few investigators [36, 56, 57]. However, the effect of important parameters like contact angle, capillary number and droplet size on droplet dynamics over the superhydrophobic and mixed-wet surface remain largely overlooked. In the present work, a mesoscopic model, based on the two-phase lattice Boltzmann formulation is presented to elucidate the role of surface wettability on the droplet dynamics in microfluidic confinements.

The main aim of the current work is to capture the physics of droplet dynamics on the superhydrophobic surface with uniform and wettability graded solid wall. The

far reaching implication of this investigation is to understand the role of wettability in liquid water transport. The simulation of droplet motion on superhydrophobic surfaces can surely answer many queries and will give better insight. In view of this, the droplet motion using S-C model is explored for superhydrophobic range for uniform and mixed wettability. The displacement of a 3-D immiscible droplet subject to gravitational forces in a microchannel is studied.

3.2 Problem Definition

In the present work, displacement of droplet on superhydrophobic surface has been studied. Length, breadth and width of the computational domain (see Fig. 5.1) used are taken as 300, 81 and 41 (in lattice units). The droplet is initially placed at $z = 251$. The motion of the droplet is induced by a constant gravitational force along the z-direction. The dynamics of droplet was explored over superhydrophobic range for different contact angles ($\theta = 150°, 160°, 170°$) and also for Ca = 0.35, 0.66, 0.81 using Shan and Chen lattice Boltzmann Model. No slip boundary condition is applied at the walls in x- and y-direction whereas the periodic boundary conditions are applied in z-direction. Since the interface is diffused, it is taken at the location where both the fluid have equal density. Results are presented in the form of time evolution of wetted length (b) and wetted area (A) for different capillary numbers (Ca = $\frac{\rho_2 V g}{\sigma h}$), variable wettability surfaces and droplet sizes. It may be noted that capillary number basically indicates the ratio of viscous force and surface tension force. Other relevant non-dimensional numbers generally used for study of droplet motion is Bond number (Bo) which is nothing but the ratio of gravity force to surface tension force given by $Bo = \frac{g(\rho_2 - \rho_1)D^2}{\sigma}$.

3.3 Grid Independence Study

Grid refinement study was carried out to choose appropriate domain size for simulating the droplet motion. In this study, only two-fluid system with different densities and kinematic viscosities in lattice units is considered. The droplet displacement is simulated for grid size of 91×51×300, 81×41×300 and 71×31×300 for the same capillary number. Time evolution of wetted length b/b_0 and wetted area A/A_0 for grid 81×41×300 and 71×31×300 are qualitatively the same (around 3% deviation)

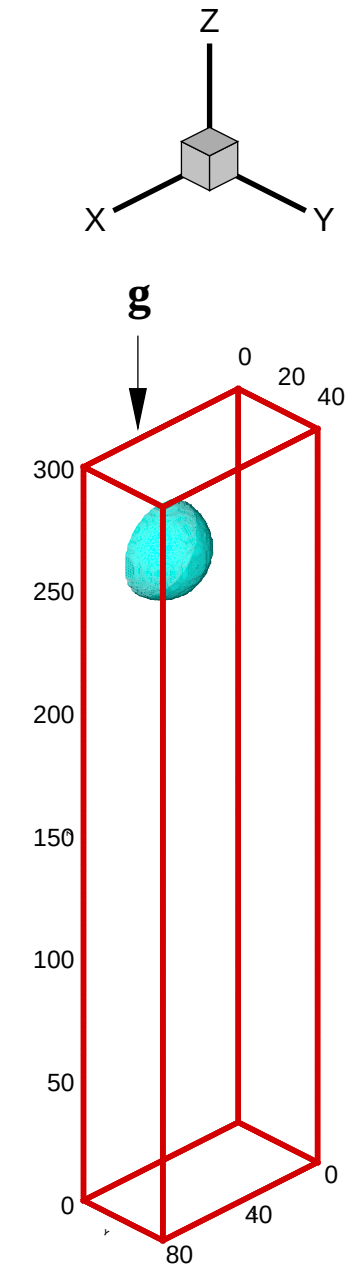

Figure 3.1: Computational domain

(see Fig. 3.2). Thus, the 81×41×300 was chosen in order to conduct the rest of the numerical simulations in this chapter.The simulations were performed on a Linux PC cluster with Intel Xeon 2.4 GHz processor. Simulations for droplet dynamics were conducted with 300×81×41 lattice nodes. A typical simulation using sixteen processors takes approximately 17 hours to run up to 40000 time steps.

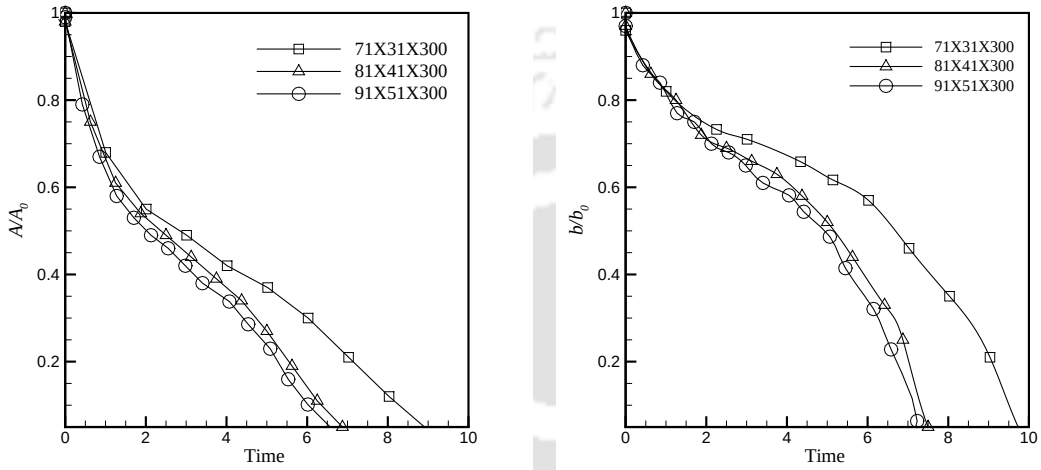

(a) (b)

Figure 3.2: Grid refinement study at Ca = 0.35 and $g_{2w} = 0.05$: (a) time evolution of wetted area, (b) time evolution of wetted length

3.4 Results and Discussion

3.4.1 Droplet dynamics on the surface with uniform wettability

The primary objective of this investigation was to systematically evaluate the two-phase constitutive closure relations via appropriate numerical experiments on droplet motion for the parameters like wettability (g_{2w}), wetted length, wetted area under the applied gravitational force. These relations could be incorporated into the macroscopic two-phase fuel cell models for reliable performance predictions.

Table 3.1: Parameter values used to study the droplet dynamics

Parameter		Value
Length of the microchannel (l)		300
Width(h)		40 in the x-direction
Breadth(w)		81 in the y-direction
Relaxation time of the wetting phase τ_1		1.0
Relaxation time of the non wetting phase τ_2		1.0
Fluid-fluid interaction parameter	$g_{11} = g_{22}$	0
	$g_{12} = g_{21}$	0.1
$\frac{V}{h^3}$		0.2

3.4.1.1 Droplet movement in a microchannel under gravity

A series of numerical simulations is carried out to understand the physics behind droplet motion in hydrophilic and hydrophobic range and then extended for super-hydrophobic range. In this study, only two-fluid system with different densities and

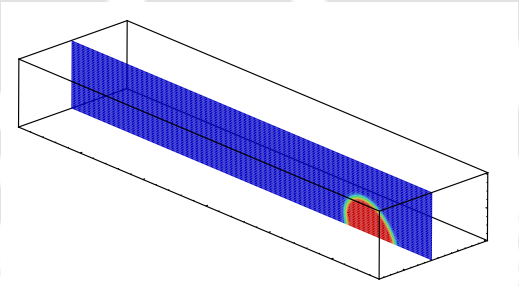

Figure 3.3: Droplet at mid-plane at $x = 40$ at time = 3.5 and Ca = 0.35

equal kinematic viscosities in lattice units is considered. The droplet configuration is shown in Figs. 3.3 and 3.4 after time 3.5 for Ca = 0.35 in different plane views. The fluid properties used in the simulations are listed in Table 3.1.

The droplet falling under gravity has been simulated for 40000 time steps (in

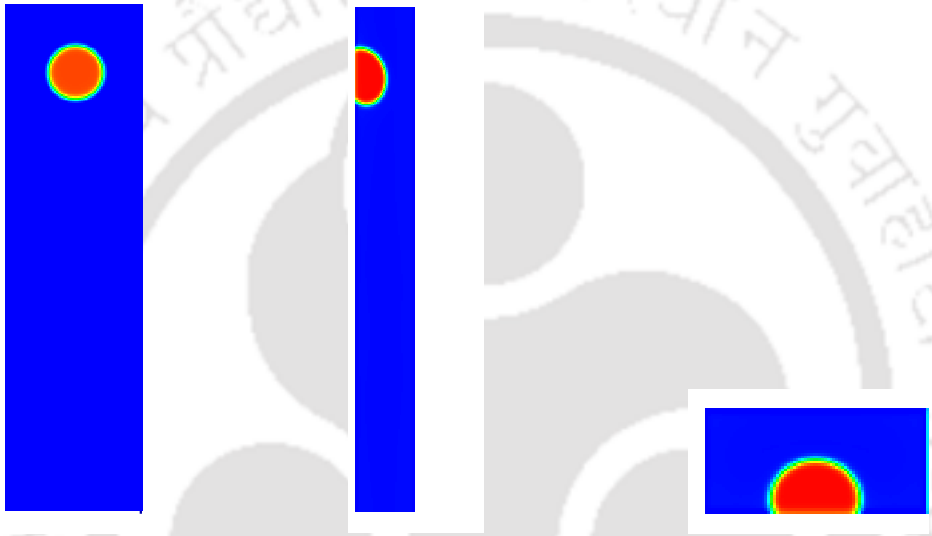

(a) (b) (c)

Figure 3.4: Droplet in different planes (a) $x-z$ plane, (b) $y-z$ plane, x mid plane, (c) $x-y$ plane at time = 3.5 and Ca = 0.35

lattice units) until steady state is achieved. The steady state here is taken as the state at which the droplet moves along the wall with a constant velocity and its shape does not vary with time [10]. It may be noted that each driving force term, responsible for initiating the droplet motion, can be perceived as representative of a particular capillary number. An immiscible droplet (fluid 2) with volume V is placed into a three-dimensional microchannel filled with (fluid 1). The interfacial strength between droplet (fluid 2) and wall g_{2w} is varied. The droplet motion under

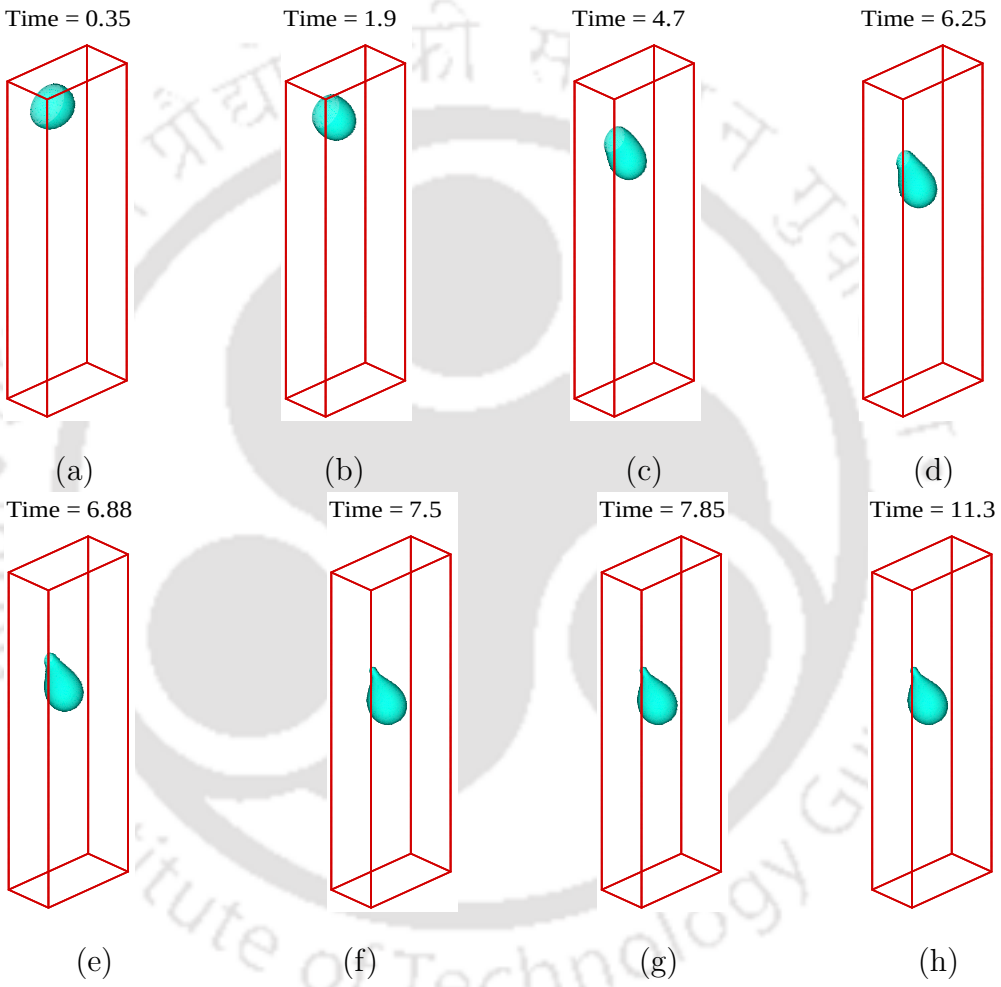

Figure 3.5: Dynamic behavior of the droplet falling under gravity at time (a) 0.35, (b) 1.9, (c) 4.7, (d) 6.25, (e) 6.88, (f) 7.5, (g) 7.85, (h) 11.30

wettability parameter $g_{2w} = 0.05$ and Ca $= 0.35$ is shown in Fig. 3.5. It is observed that there is a displacement of droplet in negative z-direction under the influence

of gravity with time which is quiet evident from the change in the location and geometry of droplet (see Fig. 3.6).Also, the motion of the droplet in terms of location versus time shows the change in shape on a graph to indicate how it changes with location or time. Contact line dynamics of droplet motion is best described by the

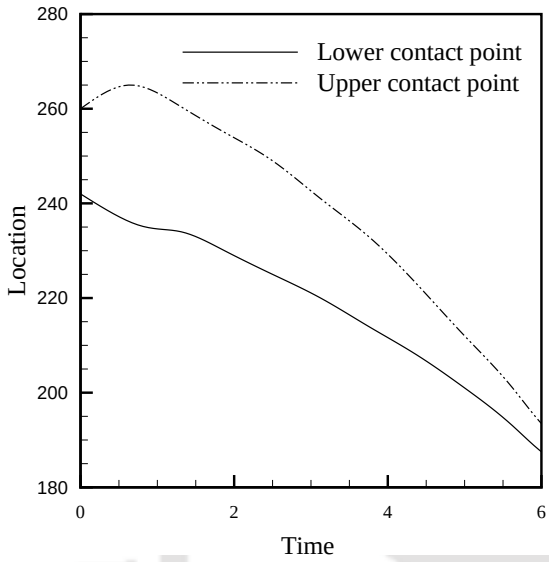

Figure 3.6: Motion of the droplet with location on hydrophobic surface for Ca = 0.35

movement of lower and upper contact points (Z_l and Z_u) with the surface (see Fig. 3.6) which corresponds to the contact point of the droplet with the surface.

It must be noted that the term time refers to non dimensional time. At time 0.35 the droplet is almost in spherical shape and sticking on the wall surface. There is gradual reduction in the contact surface area between droplet and wall with time. At time 7.5, the contact surface area between droplet and wall is very less. The droplet gets detached from the surface after time 7.85. There after it moves periodically in z-direction. It can be seen that the larger fraction of droplet is entrained in the bulk since contact angle θ is large i.e., 118° [45]. The process of detachment depends on velocity inside the upper and lower portion of the droplet. For the case of $\theta = 118°$, there is uniform velocity inside the droplet. This velocity being larger than that of fluid 1 near the wall results into large shear forces between the droplet and the wall making the entire droplet to detach from the wall.

3.4.1.2 Effect of wall wettability

The wettability suggests the existence of three interfaces between two fluids and a solid surface. The whole system tries to minimize its energy by adopting the optimal configuration. The transient motion and deformation of the interface of a droplet attached to a solid surface depends on wettability of the surface. For highly hydrophobic range i.e., for g_{2w} = 0.08, 0.10, 0.15 which corresponds to static contact angle of θ = 132°, 139° and 150° respectively, the droplet contact with the wall decreases resulting in lesser wetted length as shown in Fig. 3.7. At g_{2w} = 0.15, droplet gets detached before time 3.125. This underscores the basic fact that the motion of droplet will be with higher velocity on superhydrophobic surface. The high contact angle obtained with higher g_{2w} values gives smaller contact length and contact area. The droplet motion is faster and detaches prematurely at around time 3.5. The change in wetted length ratio b/b_0 and wetted area ratio A/A_0 with time is studied for hydrophilic (g_{2w} = -0.02), neutral (g_{2w} = 0.00) and hydrophobic surfaces (g_{2w} = 0.05). Figures 3.8 (a) and (b) show the time evolution of the dimensionless wetted length ratio b/b_0 and wetted area ratio A/A_0 between the wall and the sliding droplet at three contact angles. Figures show a good agreement with the results of Kang et al. [11]. At Ca = 0.81 for θ = 78° the wetted length grows monotonically for the wetting droplet, while the wetted area increases initially and then decreases. However, for θ = 90°, the wetted length is seen to increase continuously whereas the wetted area shows steady decrease till it becomes stable. In case of θ = 118°, both b/b_0 and A/A_0 show steady decrease with time. A larger portion pinches off first followed by the detachment of the remaining droplet from the wall. It can be observed that the droplet motion exhibits different time evolution characteristic of wetted length and area depending on the wettability of the surface.

3.4.2 Droplet dynamics on superhydrophobic surfaces

As already discussed earlier, superhydrophobic surfaces facilitates droplet motion due to higher contact angle. The effect of various parameters like capillary number and droplet size on superhydrophobic surfaces is explored in following sections. The displacement of droplet on superhydrophobic surface exhibits dynamic behavior similar to the one on hydrophobic surface. However, the wetted area and length are obviously less and reduce as the droplet moves further. Figures 3.9 (a)-(d) show

Figure 3.7: Effect of wall wettability g_{2w} at time = 3.5 (a) $\theta = 132^\circ$ ($g_{2w} = 0.08$), (b) $\theta = 139^\circ$ ($g_{2w} = 0.10$), (c) $\theta = 150^\circ$ ($g_{2w} = 0.15$)

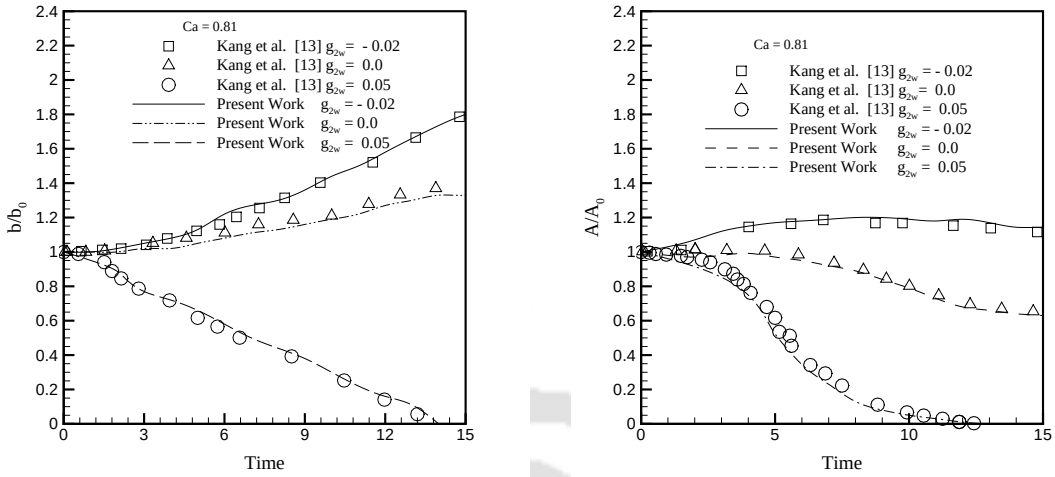

(a) (b)

Figure 3.8: Effect of wall wettability on hydrophilic, neutral and hydrophobic surface: (a) time evolution of the dimensionless wetted length b/b_0, (b) time evolution of the dimensionless wetted area A/A_0 at three contact angles $\theta = 78°$ (g_{2w} = -0.02), $\theta = 90°$ ($g_{2w} = 0.0$), $\theta = 118°$ ($g_{2w} = 0.05$) for Ca = 0.81.

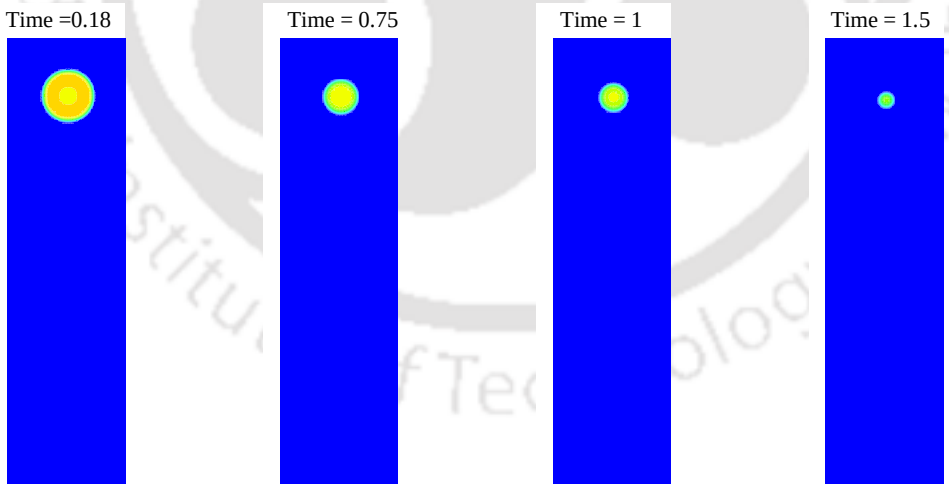

(a) (b) (c) (d)

Figure 3.9: The shape of the droplet ((x, z)-plane view at wall) at Ca = 0.35 on superhydrophobic surface $\theta = 150°$ at time (a) 0.18, (b) 0.75 (c) 1, (d) 1.5

the (x,z) plane view of the droplet at $\theta = 150°$ for Ca = 0.35. Both wetted length and wetted area decrease with time and so does the wetted width in the x-direction. The round shape of the interface remains almost unchanged when the wetted area diminishes.

3.4.2.1 Effect of contact angle

For the case of $\theta = 118°$ (non wetting case), both b/b_0 and A/A_0 dramatically decrease with time and reach zero at time 7.8, when the droplet totally detaches from the wall. The high contact angle obtained with higher g_{2w} values gives smaller contact length and contact area. The droplet motion is faster and detaches too early even around 1000 time step. In the superhydrophobic region i.e., for $g_{2w} = 0.14$, 0.15, 0.16 wetted length and area reduce with time (see Fig. 3.10) exhibiting similar variation as that of hydrophobic region. However, the droplet motion is faster in superhydrophobic region.

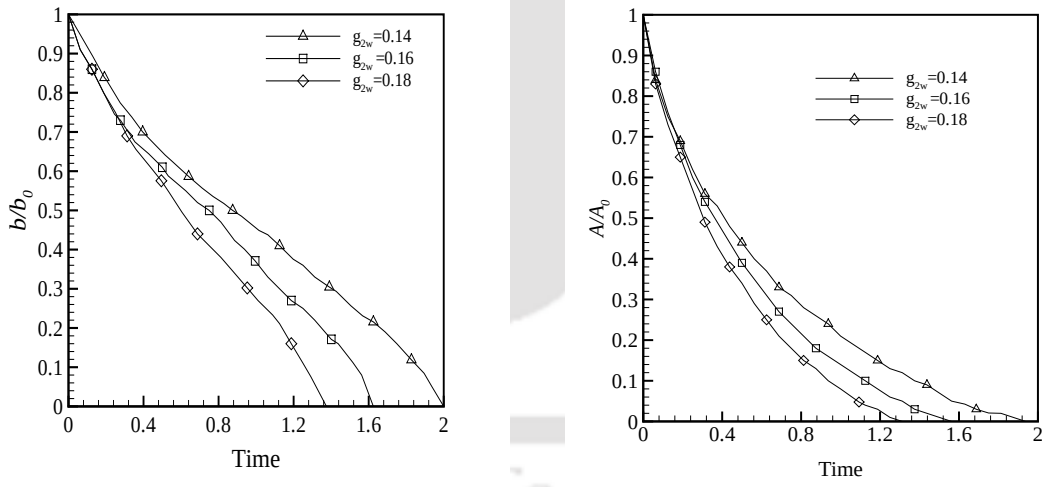

(a) (b)

Figure 3.10: Effect of contact angle on superhydrophobic surfaces at Ca = 0.35: (a) time evolution of dimensionless wetted length b/b_0, (b) time evolution of dimensionless wetted area A/A_0

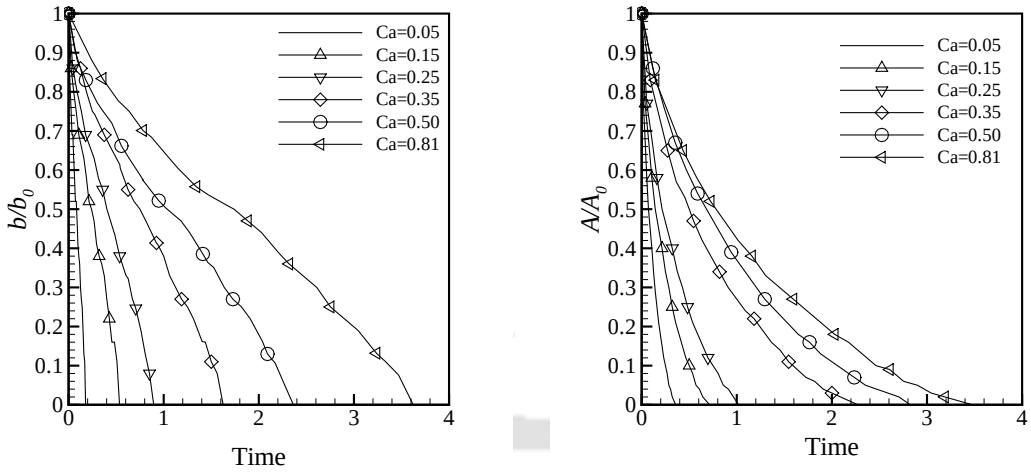

(a) (b)

Figure 3.11: Effect of capillary number for $g_{2w} = 0.16$: (a) time evolution of dimensionless wetted length b/b_0, (b) time evolution of dimensionless wetted area A/A_0

3.4.2.2 Effect of capillary number

Figure 3.11 shows the dependency of non dimensional wetted length b/b_0 and wetted area A/A_0 on capillary number in superhydrophobic region ($g_{2w} = 0.16$). Note that different capillary numbers were obtained by changing the gravitational factor, **g**. As Ca increases, the deformation of droplet becomes more due to the increase in viscous stresses along the interface resulting an increase in both b/b_0 and A/A_0. However, the increase in the value of b/b_0 is greater in magnitude than A/A_0. For the non wetting droplet, both b/b_0 and A/A_0 decrease with time. For low capillary numbers in the range of Ca = 10^{-3} to 10^{-4} the droplet detaches in a very short time i.e almost instantaneously. Figure 3.12 shows the effect of capillary number on time evolution of wetted length and area of the droplet on superhydrophobic surface. It can be observed that wetted area of droplet increases with the increase in capillary number. This reiterates the fact that viscous force increases with increasing capillary number resulting in greater contact area adhering to the wall.

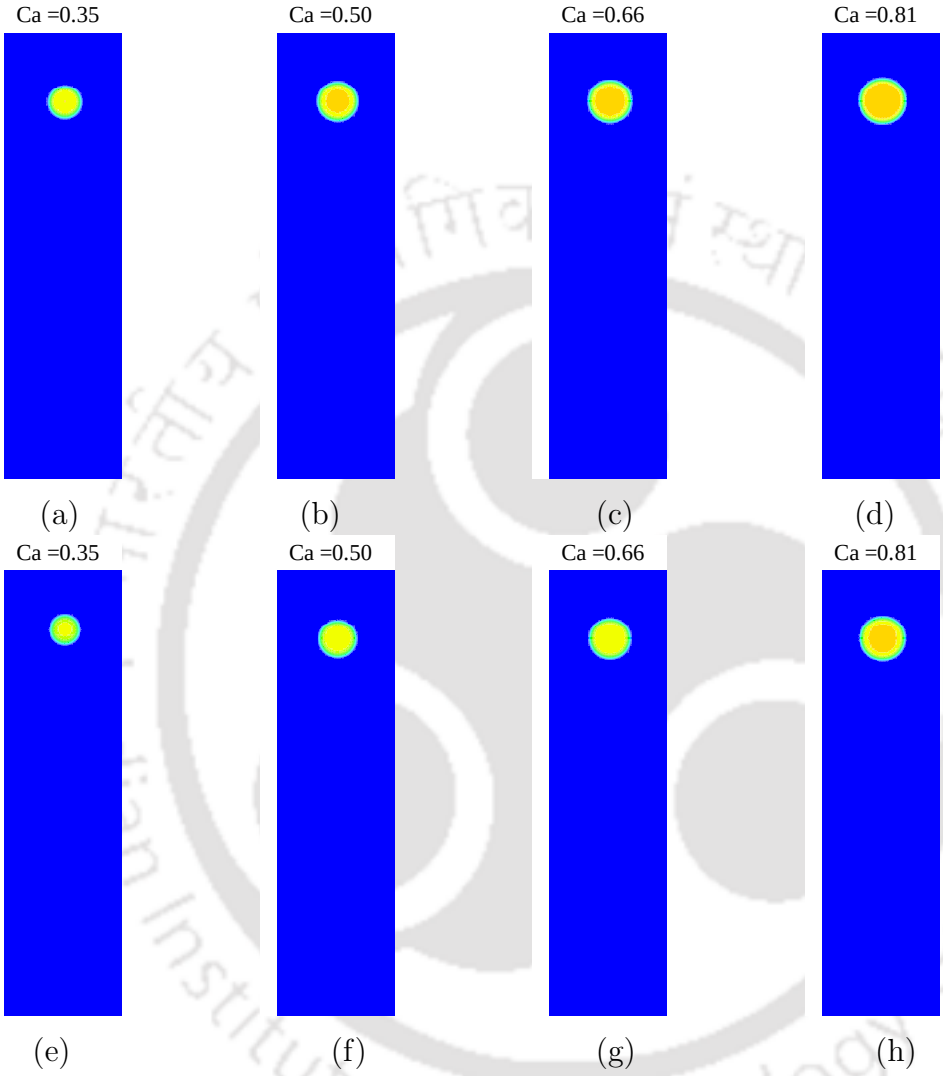

Figure 3.12: Effect of capillary number on superhydrophobic surface: the shape of the droplet in x-z plane view at wall at time = 0.75, (a)-(d) $\theta = 150°$, (e)-(h) $\theta = 160°$

3.4.2.3 Effect of droplet size

Deformation of interface depends on the size of the droplet. Hence, it is vital to study the effect of droplet size (area) on non dimensional wetted length b/b_0 and wetted area A/A_0 for superhydrophobic surfaces ($\theta \geq 150\,^{\circ}$). Figure 3.13 shows the effect of droplet size on the evolution of dimensionless wetted length and wetted area for g_{2w} = 0.16 and Ca = 0.35. As the area of the droplet increases, the capillary number increases along with velocity. Also, the effect of the wall becomes increasingly more important due to more fluid being pushed through an increasingly smaller gap [45]. These two factors together result in more viscous forces and deformation. This may lead to detachment of all or part of the droplet from the wall or pinch off from the rest of it at a smaller body force strength. Hence, the larger droplet takes little more time to detach partially or completely as compared to the smaller one. This is also evident from the time evolution of wetted length and area as shown in the Fig. 3.13.

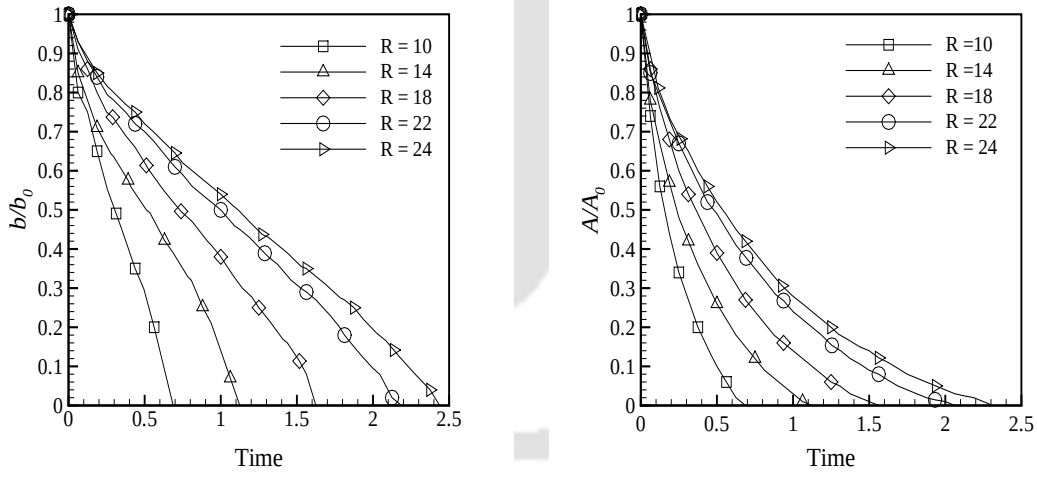

(a) (b)

Figure 3.13: Effect of droplet size on superhydrophobic surface at Ca = 0.35 and g_{2w} = 0.16: (a) time evolution of the dimensionless wetted length b/b_0 (b) time evolution of the dimensionless wetted area A/A_0

3.4.3 Effect of inclination on droplet displacement behavior

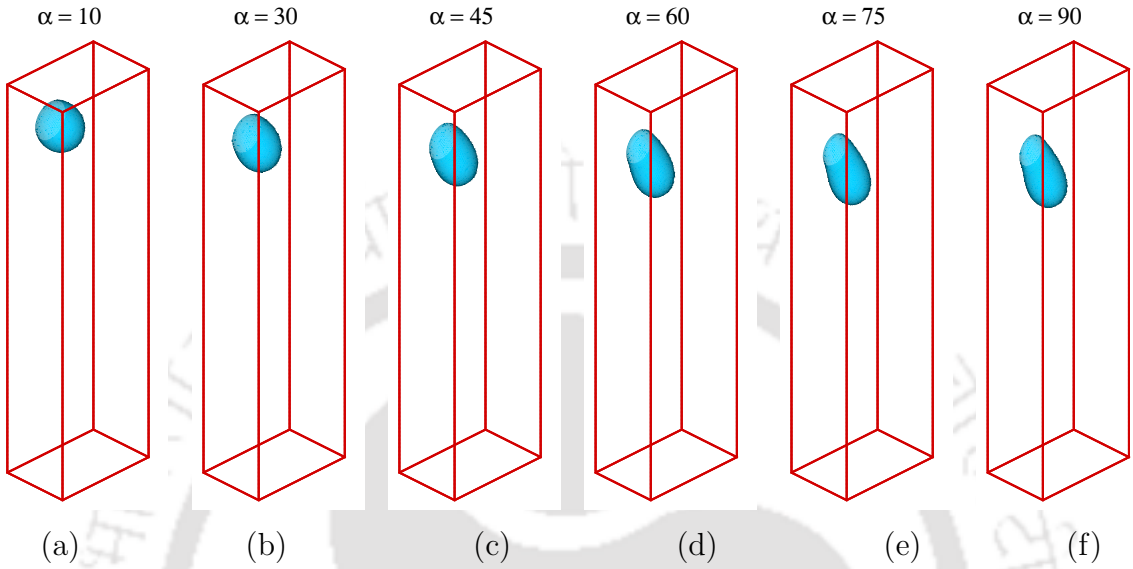

Figure 3.14: Shape of the droplet for different inclination at Ca = 0.35 for g_{2w} = 0.05 at time = 6.4

In order to investigate the effect of inclination angle in conjunction with wettability, simulations were performed on hydrophilic, hydrophobic and mixed-wetted surface. The fluid/solid interaction coefficient is taken as g_{2w}= -g_{1w} = 0.05 corresponding to a static contact angle of 118° whereas for the hydrophilic region g_{2w} = -g_{1w}= - 0.02 resulting in contact angle of 78° [10, 11]. Figure 3.14 shows the shape of the droplet at time = 6.4 on hydrophobic surface at different angles of inclination. At higher inclination angles, this finally yields in complete detachment of the droplet from the wall. However, at low angle of inclination, for example for $\alpha = 10°$ and 30°, the droplet adheres to the substrate and deformation of interface is also less. Time evolution of wetted length and area (see Fig. 3.15) also reiterates the same fact. The wetted length and wetted area decrease as the time progresses and reach zero when it detaches. It may be noted that the detachment time decreases with increasing angle of inclination.

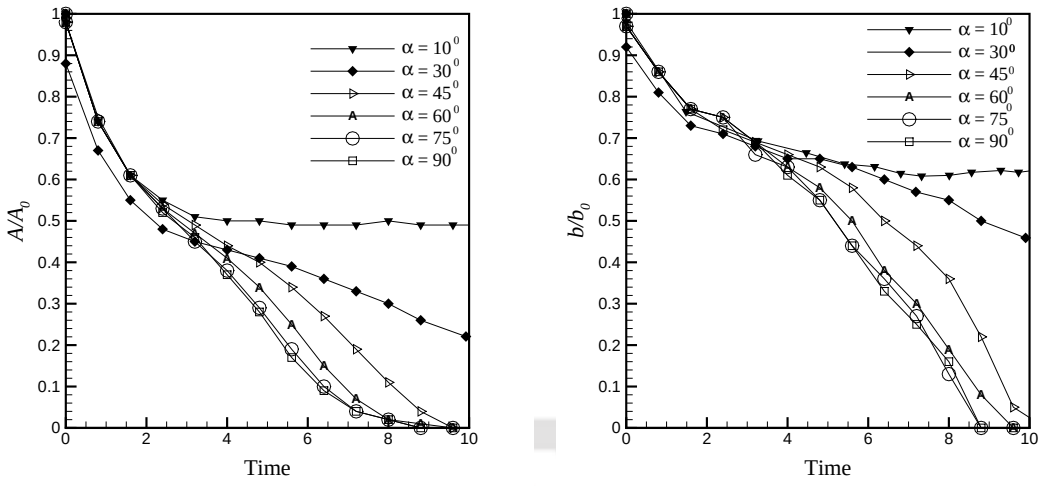

(a) (b)

Figure 3.15: Effect of inclination at Ca = 0.35 and $g_{2w} = 0.05$: (a) time evolution of wetted area, (b) time evolution of wetted length

3.4.4 Droplet dynamics on the mixed-wet surfaces

It is well known that surfaces in most of the practical situations do not possess uniform wettability. It may be noted that suitable alteration on surface chemistry or structure can improve surface wetting properties. Chemical modifications of surfaces alone can typically increase the water contact angles from 120° up to the extreme values of contact angles of 180° [128]. Micro-roughness can make the surfaces either more hydrophilic or more hydrophobic depending on the original chemical properties of surfaces. In this context, it would be interesting to understand the droplet spreading behavior on the surface with mixed wettability. LBM is employed here to study numerically the effects of mixed wettability on the displacement of the droplet. Figure 3.16 shows the schematic of domain with mixed wettability. As specified earlier the surface comprised of the hydrophilic and hydrophobic regions alternately. The displacement behavior of the droplet for Ca = 0.35 on the surface with wettability g_{2w} = -0.02 (i.e., hydrophilic), 0.05 (i.e., hydrophobic) and ±0.05 (mixed wettability) is compared as shown in Fig. 3.17. For $\theta = 78°$ (i.e., wetting case), both wetted length (b/b_0) and wetted area (A/A_0) increase with time at first, then decrease slowly and reach a steady-state value. However, in case of the surface with mixed wettability, the elongation of the droplet during the motion can be

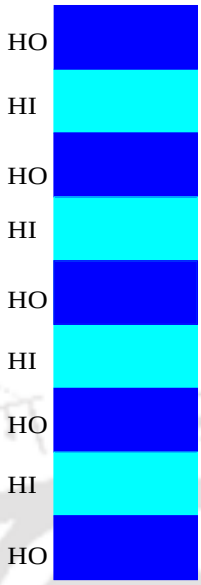

Figure 3.16: Schematic of the domain for the mixed wettability configuration

observed. This leads to increase in wetted length and reduction in wetted area at the time 7.5 when it is in between hydrophilic and hydrophobic regions as shown in Fig. 3.17. It may be noted that this behavior is repeated whenever the droplet is in the same situation thereafter. In order to understand the process of spreading and elongation of the droplet the time evolution of wetted length and wetted area are plotted for the Ca = 0.35 for surface with mixed wettability $g_{2w} = 0.05$ as shown in Fig. 3.18. The changes in the wetted length follows the changes in wetted area but with some delay in time. This happens primarily due to tendency of the droplet to spread as soon as it comes out of hydrophobic region and wetted length again starts increasing following the trend of wetted area. The comparison of time evolution of the wetted length and area is very clearly demonstrated in Fig. 3.18. This underscores the fact that droplet detaches on the hydrophobic surface whereas elongates and spreads in hydrophilic surface. As far as the surface with mixed wettability is concerned, the hydrophilic and hydrophobic nature of the surface keeps affecting the changes in wetted length and area of the droplet with time.

3.4.4.1 Deformation of the droplet

It can be inferred from Fig. 3.19 that the droplet spreads in hydrophilic region as expected in the early stages of flow evolution due to adhesive force of the surface.

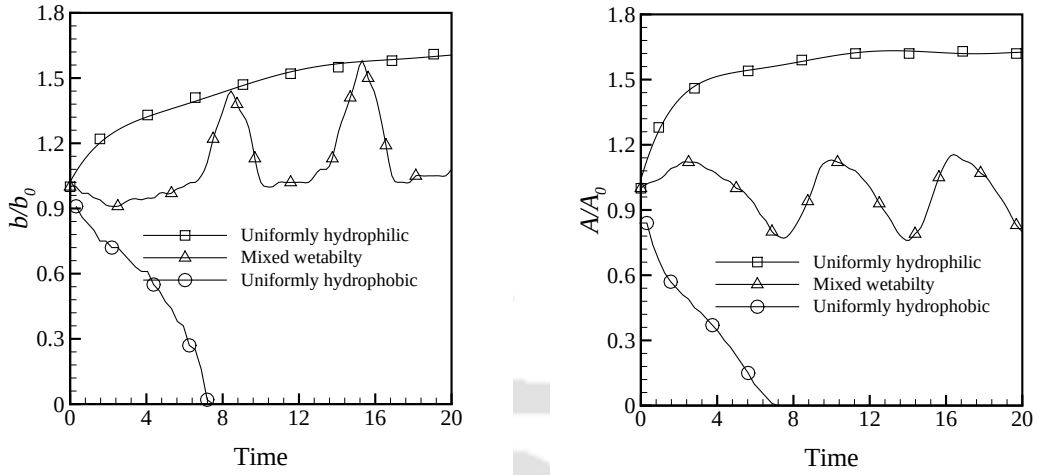

(a) (b)

Figure 3.17: Effect of uniform and mixed wettability: (a) time evolution of the dimensionless wetted length b/b_0, (b) time evolution of the dimensionless wetted area A/A_0

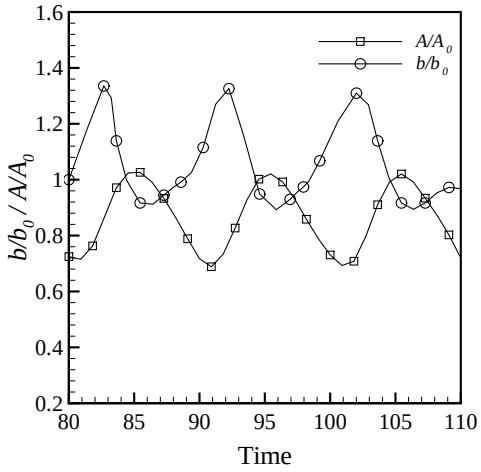

Figure 3.18: Comparison of time evolution of the wetted length and area for the surface with mixed wettability $g_{2w} = \pm 0.05$ at Ca = 0.35

However, it rapidly contracts inward along the hydrophobic surface thereby reducing its contact area in hydrophobic region. As time progresses, the droplet continues to spread on the hydrophilic area leading to the deformation of the initial shape. The

(a) (b)

Figure 3.19: The shape of the droplet at Ca = 0.35 and time = 0.75 for surface with mixed wettability (a) $g_{2w} = \pm\ 0.02$, (b) $g_{2w} = \pm = 0.05$

increase in contact area for mixed wettability increases with $\pm g_{2w}$. The spreading of droplet is more prominent for the surface with $g_{2w} = \pm 0.05$ as compared to with $g_{2w} = \pm 0.02$ for the same time. It is interesting to note that mixed wettability of the surface results in elongation of the droplet i.e., wetted length increases as seen in Figs. 3.20 (c) and (f) when the droplet is partially in both hydrophilic and hydrophobic region. The stretching of droplet can be seen at time 7.5 and time 14. Since the surface here is alternately wettable i.e., hydrophobic region followed by hydrophilic region the deformation of the droplet is also seen to be following pattern for Ca = 0.35.

3.4.4.2 Effect of strength of mixed wettability

Figure 3.21 shows the time evolution of wetted length and area for wettability alteration of different strengths i.e., $g_{2w} = \pm 0.02, \pm 0.05, \pm 0.16$. It can be observed that

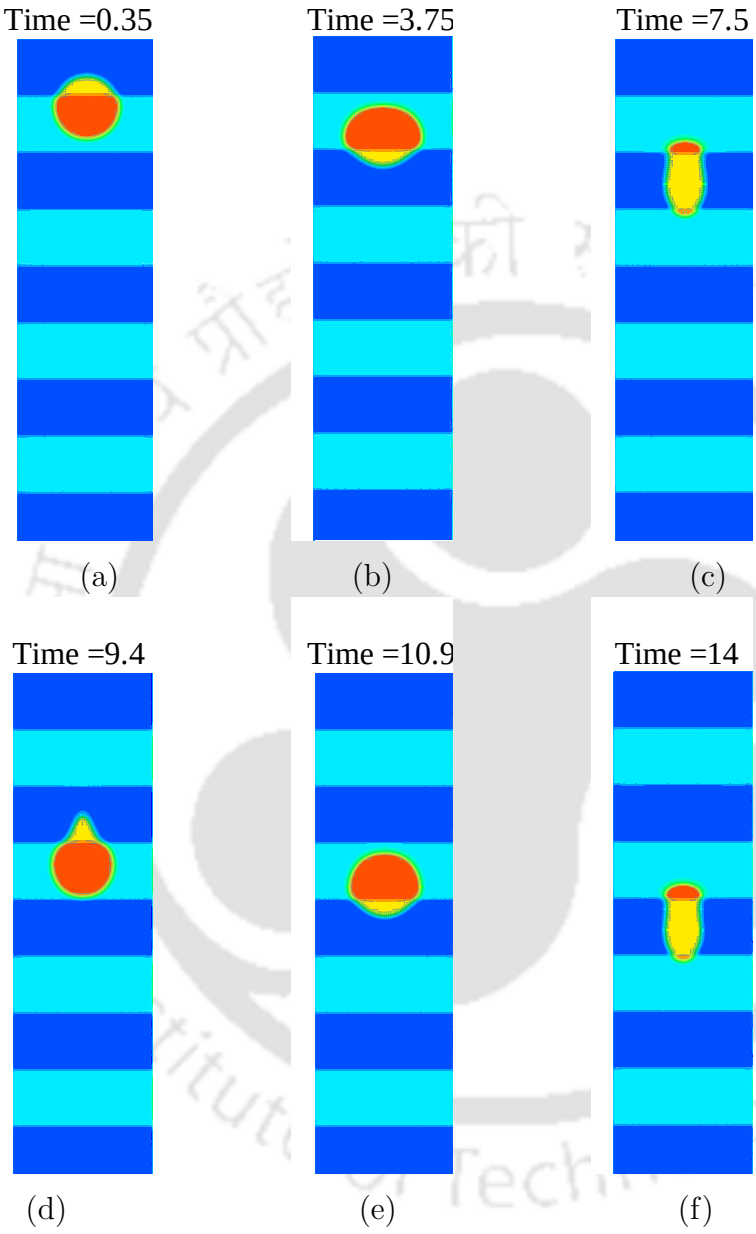

Figure 3.20: Dynamic behavior of the droplet at Ca = 0.35 for the surface with mixed wettability $g_{2w} = \pm 0.05$

for the surface with $g_{2w} = \pm 0.02$ the magnitude of the change in wetted length and area is more as compare to other surfaces. For the surface with $g_{2w} = \pm 0.16$ the magnitude of change of A/A_0 and b/b_0 is very less although the variation in wettability is high for the same capillary number. This can be explained with the fact that when the droplet is in the region where $g_{2w} = 0.16$, it will act like superhydrophobic surface causing very fast motion of droplet. On the contrary when the droplet is in the region with g_{2w} = -0.16 which represents highly hydrophilic wettability it will have the tendency to spread. This will reduce the speed of travel of droplet from this region making it to stay in the region for longer time.

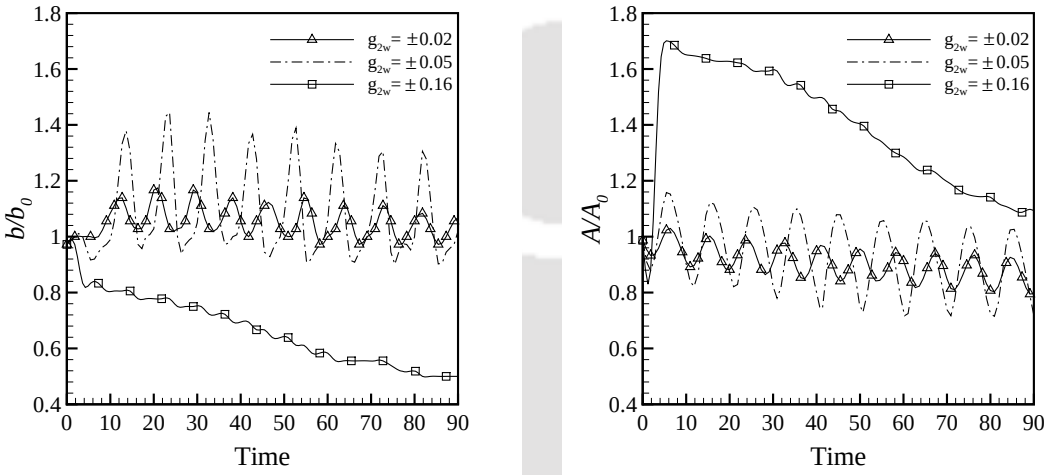

(a) (b)

Figure 3.21: Effect of strength of mixed wettability at Ca = 0.35: (a) time evolution of the wetted length, (b) time evolution of the wetted area

3.4.4.3 Effect of width of mixed-wet pattern

Figure 3.22 shows the time evolution of wetted length and area for different widths of the mixed-wet pattern with wettability ±0.02 for Ca = 0.35. It can be observed that fluctuation or the magnitude of the change in the wetted area and the length is more for the surface with more width of mixed-wet pattern as compared to the surfaces with smaller width. This can be justified since for higher width of mixed-wet pattern, the droplet stays in a particular region (hydrophobic or hydrophilic)

for a longer duration during its motion. This allows it either to shrink or spread depending on the wettability of the surface. However, for smaller width although fluctuation of wetted length and wetted area are observed more frequently, effect of wettability alteration will not be felt so intensely resulting into fluctuations of smaller magnitude. Also, the smaller width of mixed wet pattern will reduce the speed of travel of droplet since droplet has to respond to the change in wettability more often.

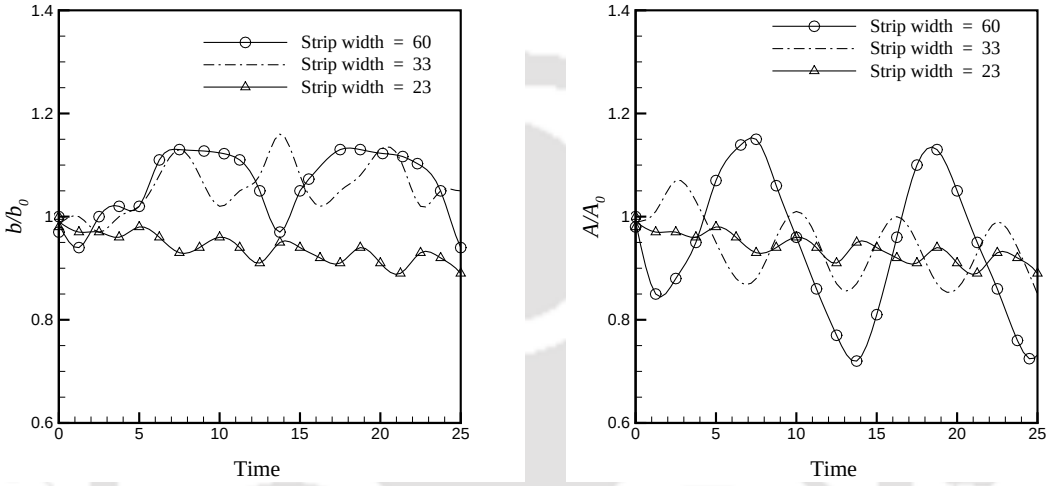

(a) (b)

Figure 3.22: Effect of the width of mixed-wet pattern at Ca = 0.35: (a) time evolution of the wetted length, (b) time evolution of the wetted area

3.4.4.4 Effect of capillary number on the surface with mixed wettability

Effect of capillary number on time evolution of wetted length and wetted area is analysed for the surface with wettability $g_{2w} = \pm 0.02, \pm 0.05$ and ± 0.14. Figures 3.23 and 3.24 show the (x,z)- and (y,z)-plane views of the steady-state shape of the droplet at Ca = 0.35, 0.50, 0.66, 0.81. From Fig. 3.23 it can be seen that the interface between the non wetting droplet and the wall deviates from its original round shape. This deviation becomes larger at higher capillary numbers. It can be inferred from Fig. 3.25 that with the increase in capillary number the motion of droplet becomes faster resulting in lesser wetted length and wetted area gradually.

For low capillary number i.e., Ca = 0.35 the changes in wetted length and area are periodic in nature. This is because as soon as the droplet enters hydrophilic region its wetted length and area increase. On the contrary, it will reduce its wetted length and area in hydrophobic region. At sufficiently higher Ca = 0.81, the droplet detaches completely after some time. It can be concluded that effect of mixed wettability will not be prominent for higher capillary numbers. From the above preliminary study, it is clear that mixed wettability has a significant role to play in droplet motion and subsequent transport. This study establishes the fact that the current two-phase S-C LB model correctly captures the droplet physics.

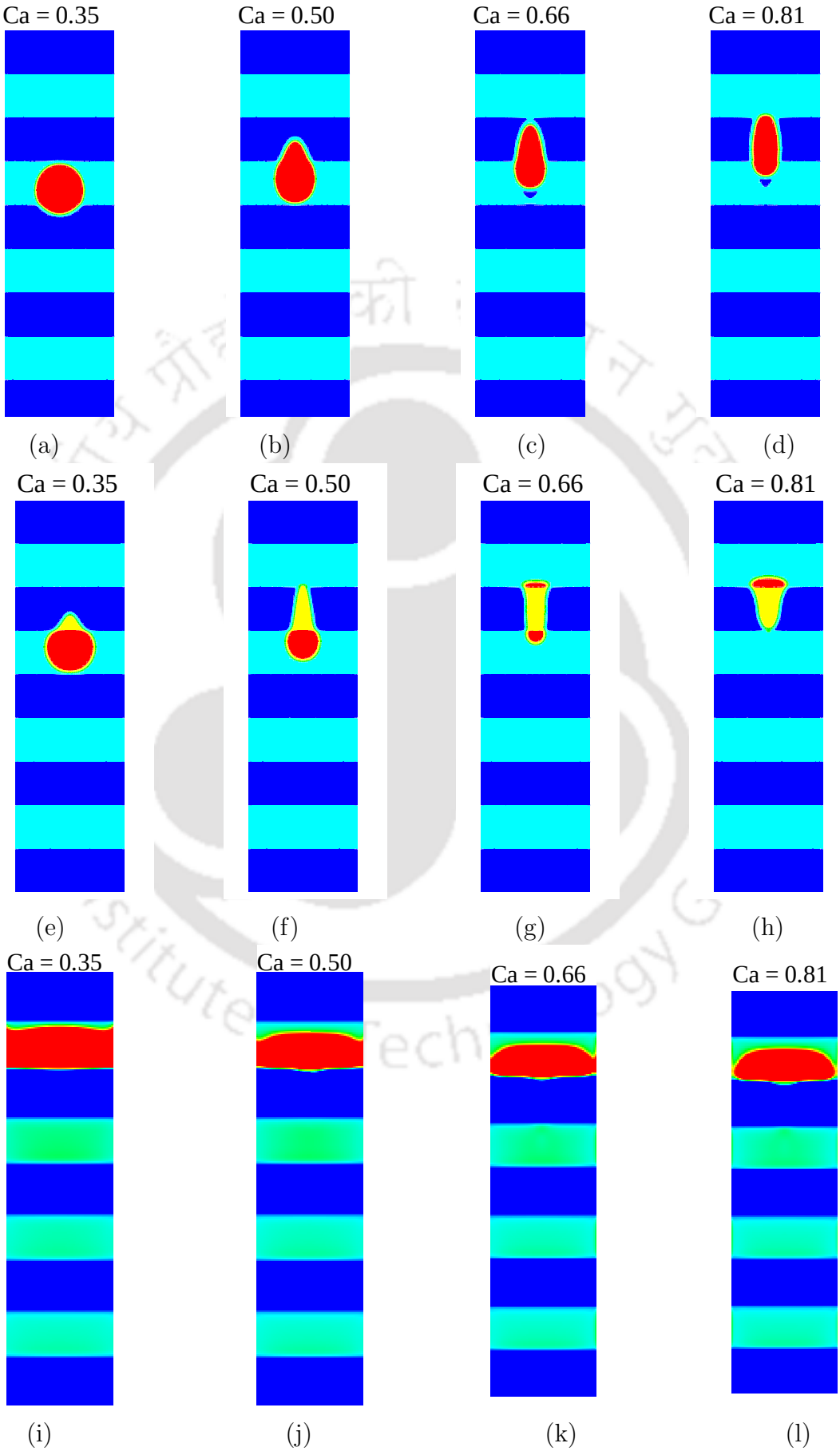

Figure 3.23: The shape of the droplet x-z plane view at wall at different capillary numbers time = 0.75, (a)-(d) $g_{2w} = \pm 0.02$, (e)-(h) $g_{2w} = \pm 0.05$, (i)-(l) $g_{2w} = \pm 0.14$

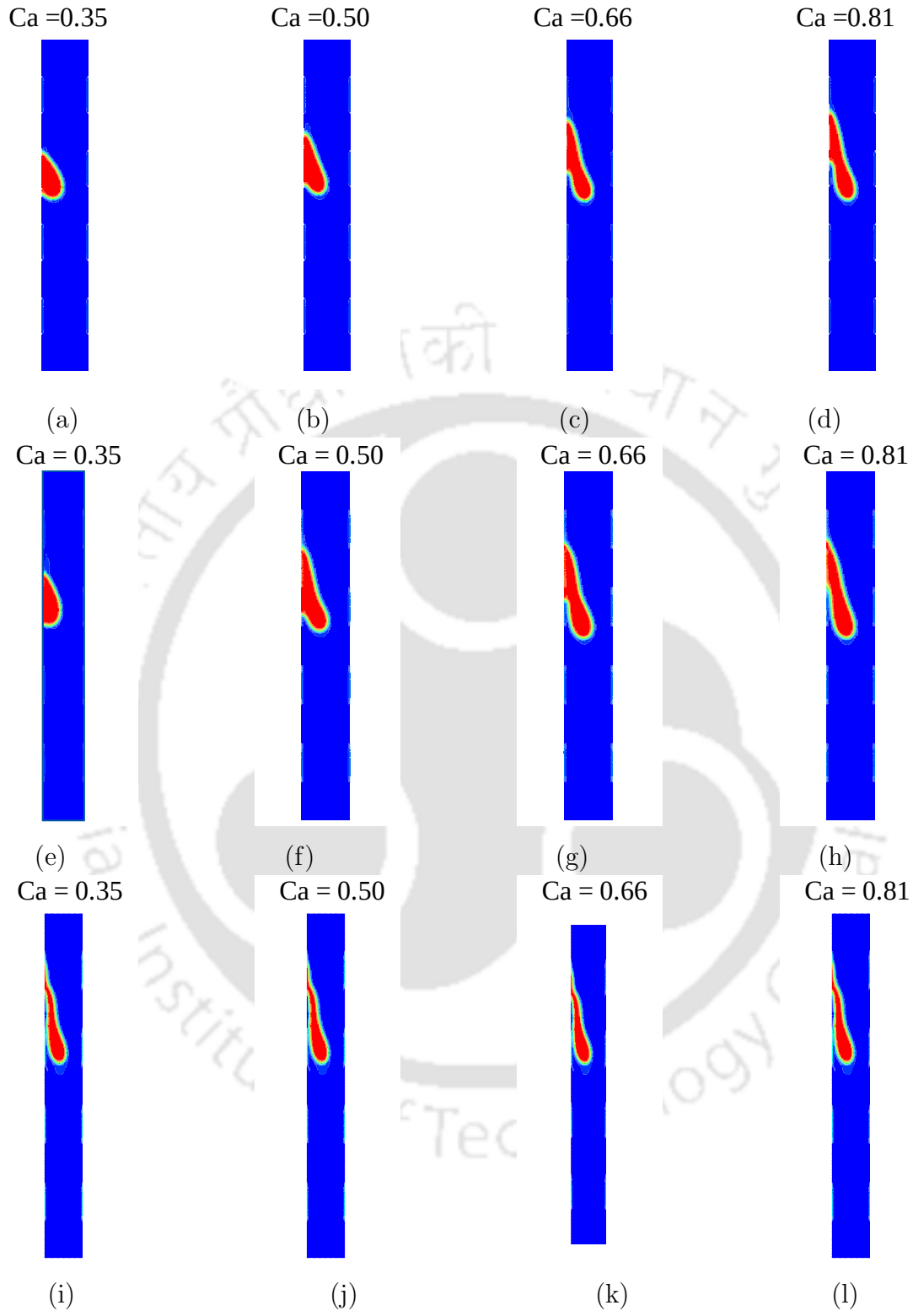

Figure 3.24: The shape of the droplet y-z plane view at wall at different capillary numbers time= 0.75, (a)-(d) $g_{2w} = \pm 0.02$, (e)-(h) $g_{2w} = \pm 0.05$, (i)-(l) $g_{2w} = \pm 0.14$

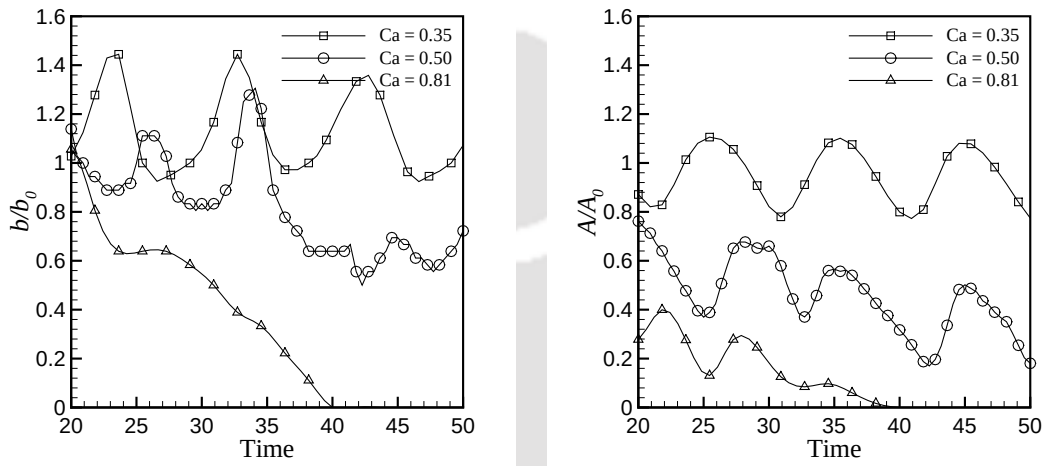

(a) (b)

Figure 3.25: Effect of capillary number for the surface with mixed wettability $g_{2w} = \pm 0.05$, (a) time evolution of the wetted length, (b) time evolution of the wetted area

3.5 Closure

Simulation of the displacement of a three-dimensional immiscible droplet on various wettabilities in a microchannel was carried out by the lattice Boltzmann method using gravitational force as the driving force. The two phase LB model calibration was done by bubble test and static droplet test. The wetted length and wetted area evolution for $\theta = 78°$, $90°$, $118°$ over hydrophilic to hydrophobic range was analysed and found that it shows similar trend as that of Kang et al. [11]. The study of displacement of droplet was then carried out for superhydrophobic surfaces. The physics of the droplet motion was explored considering various parameters such as capillary number, droplet size and contact angle. It has been observed that higher capillary number for the non wetting droplet droplet detaches completely without breaking especially on superhydrophobic surfaces. It was observed that the deformation of the droplet increases with angle of inclination of substrate. For the mixed-wet surface, the wetted length and area keeps changing with time between maximum and minimum values.

Chapter 4

Influence of Viscosity and Wettability on Droplet Displacement Behavior

4.1 Introduction

The displacement of immiscible fluids is vital in the processes, such as enhanced oil recovery or the transport of non-aqueous phase liquids in the soil via water or surfactant flooding. The net efficacy of these processes depends on transportation of fluids through the network of pores and throats that make up the medium. There are many possible fluid-fluid displacement scenarios in such cases. However, viscosity ratio and wettability remain the key factors which govern the dynamics of the displacement of the fluid. Also, the interfacial instability is observed when fluid filling the voids of a porous medium is displaced by a less viscous one [58, 59]. Saffman and Taylor [99] have shown that the interface is unstable in the absence of surface tension. Homsy [129] had given a comprehensive review for instability of interface. Several researchers [10, 21, 130, 131, 132, 133] studied the effect of wall wettability on the immiscible displacement of droplet. Dimitrakopoulos and Higdon [134] studied the displacement of fluid droplets in viscous pressure-driven flows. However, the influence of viscosity-wettability interaction on displacement of the droplet remains largely overlooked. In this context, the underlying two-phase dynamics of droplet

motion on the surface with uniform and mixed wettabilities is discussed.

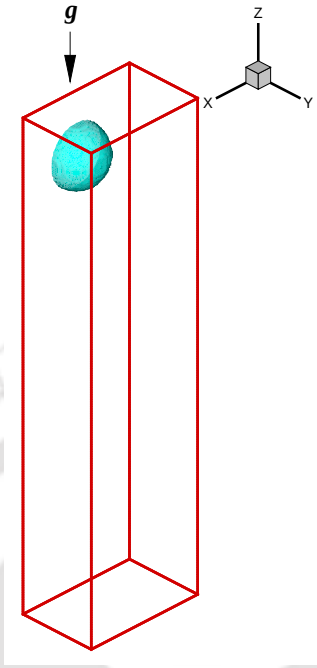

Figure 4.1: Computational domain

4.2 Problem Specification

In the present work, influence of viscosity and wettability on the displacement behavior of the droplet have been studied. Length, breadth and width of the used computational domain (see Fig. 5.1) are taken as 300, 81 and 41 (in lattice units). Simulation parameters are given in the Table 4.1. The droplet is initially placed at $z = 251$. The motion of the droplet is induced by a constant gravitational force along the z-direction. The dynamics of droplet is explored over a range of viscosity ratios for different contact angles ($\theta = 78°, 118°$) and also for Ca = 0.35, 0.66, 0.81 using S-C lattice Boltzmann Model. No slip boundary condition is applied at the walls in x- and y-direction whereas the periodic boundary conditions are applied in z-direction. Since the interface is diffused, it is taken at the location where both the fluids have equal number density. Results are presented in the form of time evolutions of wetted length (b) and wetted area (A) for different capillary numbers and wettability scenarios.

Table 4.1: Parameter values used in simulations for the study of viscosity-wettability interaction

Parameter		Value
length of the microchannel (l)		300
width(h)		40 in the x-direction
breadth(w)		81 in the y-direction
Relaxation time of the wetting phase τ_1		1.0
Relaxation time of the non wetting phase τ_2		1.0
Fluid-fluid interaction parameter	$g_{11} = g_{22}$	0
	$g_{12} = g_{21}$	0.1
$\frac{V}{h^3}$		0.2

4.3 Results and Discussion

Extensive research effort has been recently put on studying surface wettabilities [56, 135, 136, 137] because of its usefulness in industrial or engineering processes; for example, the enhanced oil recovery application process where wettability of reservoir rocks plays crucial role affecting the properties of fluid-rock interactions, such as residual oil saturation, relative permeability and capillary pressure. Also, viscosity becomes more important when the viscosity of residual oil is higher than that of the injected gas resulting in an unstable displacement. This in turn leads to undesirable phenomenon like viscous fingering causing poor recovery efficiency. Owing to the variation of rock composition, wettability alternation also affects the flow. Hence it is imperative to understand the combined effect of viscosity and wettability on the dynamics of multiphase flows. The following sections attempt to unveil the effect of these parameters on the displacement behavior of the droplet in various wettability scenarios.

4.3.1 Droplet dynamics on the surface with uniform wettability

The primary aim of this investigation is to systematically evaluate the two-phase constitutive closure relations via appropriate numerical experiments on droplet motion for the parameters like wettability (g_{2w}), viscosity ratio, capillary number on temporal evolution of wetted area and length under the applied gravitational force.

4.3.2 Effect of viscosity ratio on moving droplet

Simulation of droplet motion was performed to understand the effect of viscosity ratio keeping all other parameters constant. The taken viscosity ratios were $\frac{\mu_2}{\mu_1} = 1, 3, 5$. The viscosity ratios were obtained on similar lines as that of [138]. Relaxation parameter (τ) is chosen to get the desired kinematic viscosity and ultimately the viscosity ratio. The droplet motion shows reduction in wetted length and area as explained earlier (see Fig. 4.2). The high viscosity ratio indicates the strong cohesive force which results in lesser contact area with wall. Hence, it can be seen that the wetted area reduces with higher viscosity ratio. It must be noted that capillary number is not too high in this case. This has resulted in similar nature of deformation of droplet irrespective of viscosity as seen from the bending of interfaces.

4.3.3 Effect of viscosity ratio on hydrophilic surfaces

It is well known that wettability suggests the ability of one fluid to spread on a solid surface and to form a wetting film [139]. The nature of wettability affects displacement of fluid to a large extent, for example in the oil extraction from the rocks. Also, the pattern of wettability is governed by the nature of surface, fluid in contact etc. [140]. Hydrophilic surface allows a droplet of water to spread out. The affinity between water and a surface influences not only the behavior of a static drop of water, but also greatly affects the motion of a moving droplet. In order to study the effect of viscosity ratio, simulations were performed on hydrophilic surface with g_{2w} = - 0.02 at Ca = 0.35. Time evolution of wetted length and area on hydrophilic surface for various viscosity ratios is shown in Fig. 4.3.

With regard to a droplet which lies on a wall, the capillary forces and external

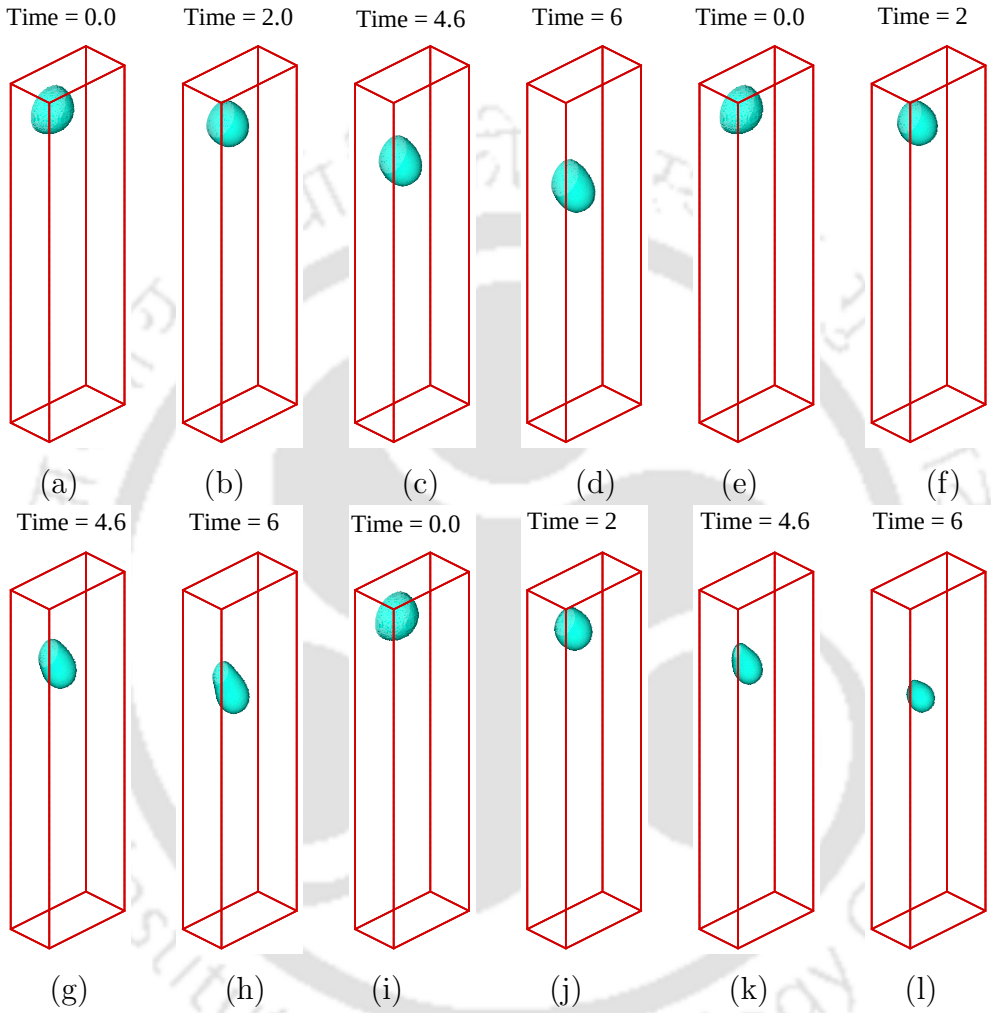

Figure 4.2: Dynamic behavior of the droplet with different viscosity ratio under gravity at Ca = 0.35 and $g_{2w} = 0.05$: (a)-(d) $\frac{\mu_2}{\mu_1} = 1$, (e)-(h) $\frac{\mu_2}{\mu_1} = 3$, (i)-(l) $\frac{\mu_2}{\mu_1} = 5$

forces like gravity deforms its shape (see Figs. 4.4 and 4.5). Also, the tendency of liquid to wet on hydrophilic surface leads to more deformation and bending of meniscus as compared to hydrophobic surface. The spreading of the droplet looks similar irrespective of the viscosity ratio as seen from the Fig. 4.5. The fluid/solid interaction can also be seen to affect from the evolution of the wetted area and wetted length (see Fig. 4.3) as droplet moves. It was found that the wetted length and area grow monotonically for the wetting droplet for lower viscosity ratios like 1, 2. However, for higher viscosity ratios like $\frac{\mu_2}{\mu_1} = 4, 5$, the wetted length and area decrease (see Fig. 4.3) till the droplet gets detached. This is due to the fact that at high viscosity ratio the area of the droplet adhering to wall will get reduced because of strong cohesive nature. But for low viscosity ratio, the hydrophilicity dominates and hence the droplet continues to spread and adhere to the wall increasing wetted area and length. This shows that for hydrophilic surfaces, the wettability will be influential at low viscosity ratios only.

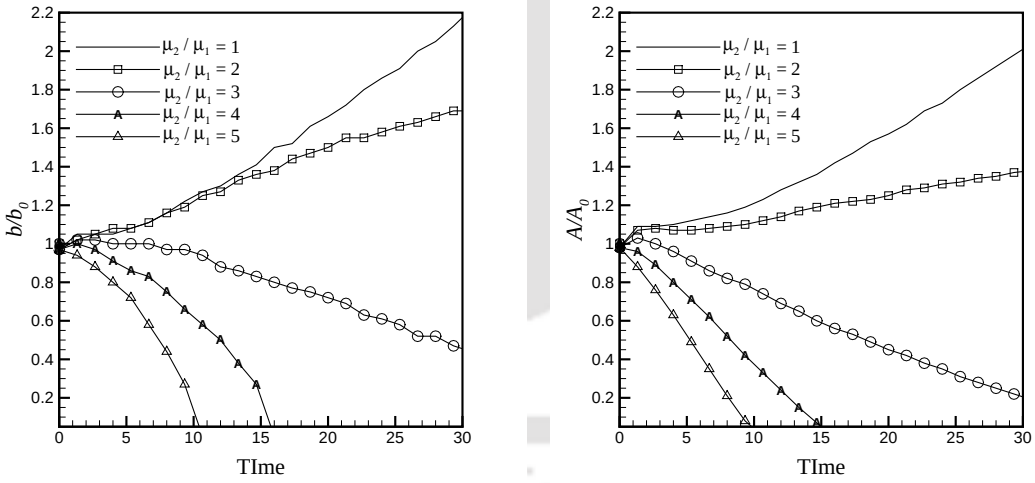

(a) (b)

Figure 4.3: Effect of viscosity ratio at Ca = 0.35 and g_{2w} = - 0.02 : (a) time evolution of wetted length, (b) time evolution of wetted area

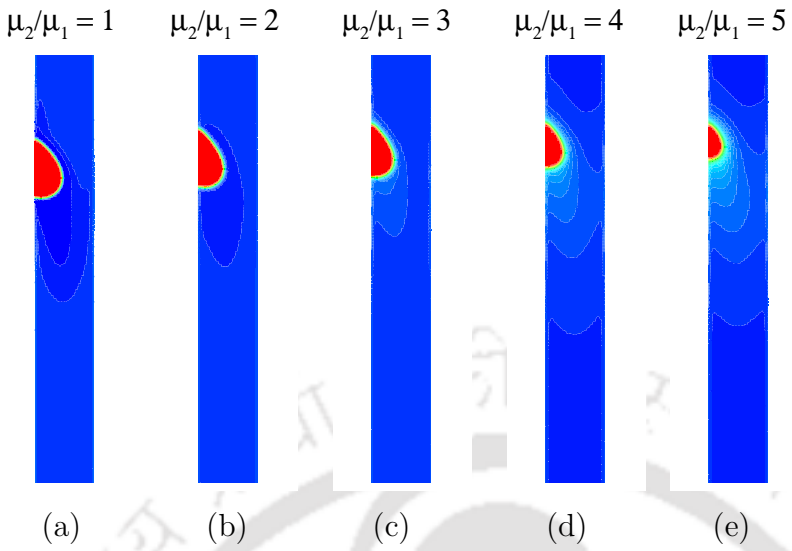

Figure 4.4: The shape of the droplet at different viscosity ratios at Ca = 0.35 and time = 5.3 for $g_{2w} = -0.02$ ((y,z)-plane view at $x = 40$): (a) $\frac{\mu_2}{\mu_1} = 1$, (b) $\frac{\mu_2}{\mu_1} = 2$, (c) $\frac{\mu_2}{\mu_1} = 3$, (d) $\frac{\mu_2}{\mu_1} = 4$, (e) $\frac{\mu_2}{\mu_1} = 5$

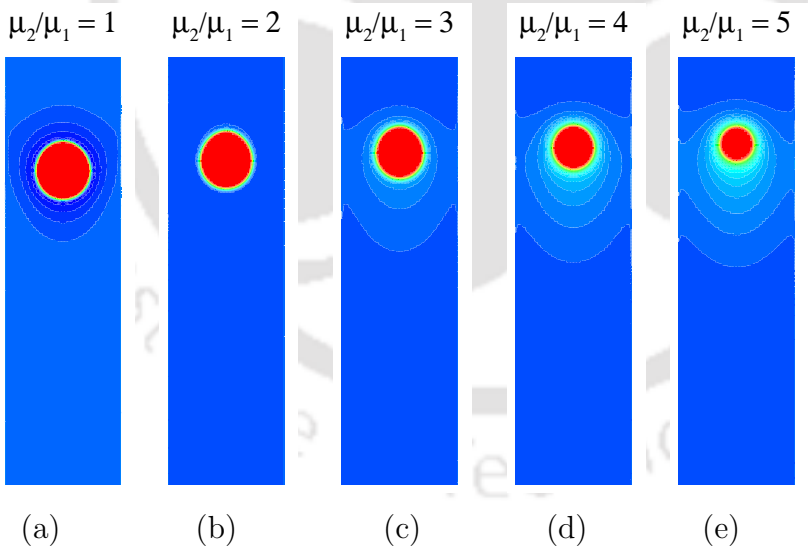

Figure 4.5: The shape of the droplet at different viscosity ratios for $g_{2w} = -0.02$ at Ca = 0.35 and time= 5.3 ($(x,\ z)$-plane view at wall): (a) $\frac{\mu_2}{\mu_1} = 1$, (b) $\frac{\mu_2}{\mu_1} = 2$, (c) $\frac{\mu_2}{\mu_1} = 3$, (d) $\frac{\mu_2}{\mu_1} = 4$, (e) $\frac{\mu_2}{\mu_1} = 5$

4.3.4 Effect of viscosity ratio on hydrophobic surfaces

The simulations were repeated for the hydrophobic surface with $g_{2w} = 0.05$ for Ca = 0.35 to understand the dynamic behavior of the droplet for a range of viscosity ratios (see Fig. 4.2). The wetted length and wetted area, both decrease with time as expected even for low viscosity ratios like $\frac{\mu_2}{\mu_1} = 1, 2$ as shown in Fig. 5.2. The hydrophobicity and cohesive forces along with the driving force help the droplet to move further. Hence, one can observe correspondingly quicker detachment of droplet as a whole compared to hydrophilic surface. This finally yields in complete detachment of the droplet from the wall as well (see Fig. 4.2). Thus, it can be concluded that hydrophobic surfaces do not show different character for low and high viscosity ratios. However, the deformation is more in the case of higher viscosity ratio which is consistent with hydrophilic surfaces. Also, the detachment of the droplet will be fast for higher viscosity ratios. The nature of deformation on hydrophobic surface looks similar in spite of different viscosity ratios as seen in Figs. 5.2, 4.7 and 4.8.

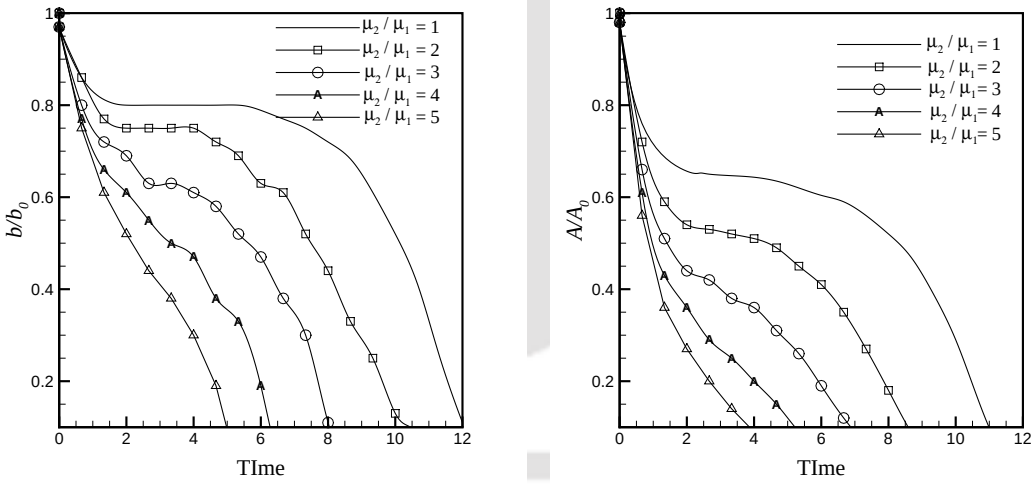

(a) (b)

Figure 4.6: Effect of viscosity ratio at Ca = 0.35 and $g_{2w} = 0.05$: (a) time evolution of wetted length, (b) time evolution of wetted area

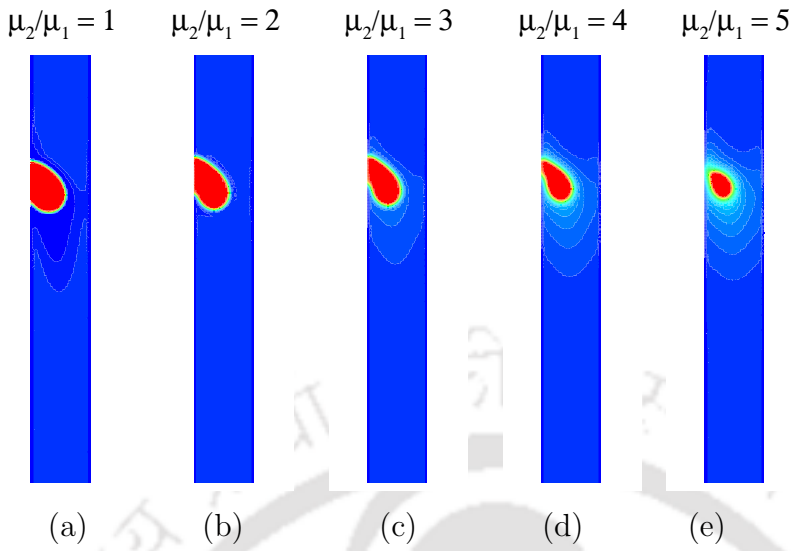

Figure 4.7: The shape of the droplet at different viscosity ratios for $g_{2w} = 0.05$ at Ca = 0.35 and time = 5.3 ((y, z)-plane view at $x = 40$): (a) $\frac{\mu_2}{\mu_1} = 1$, (b) $\frac{\mu_2}{\mu_1} = 2$, (c) $\frac{\mu_2}{\mu_1} = 3$, (d) $\frac{\mu_2}{\mu_1} = 4$, (e) $\frac{\mu_2}{\mu_1} = 5$

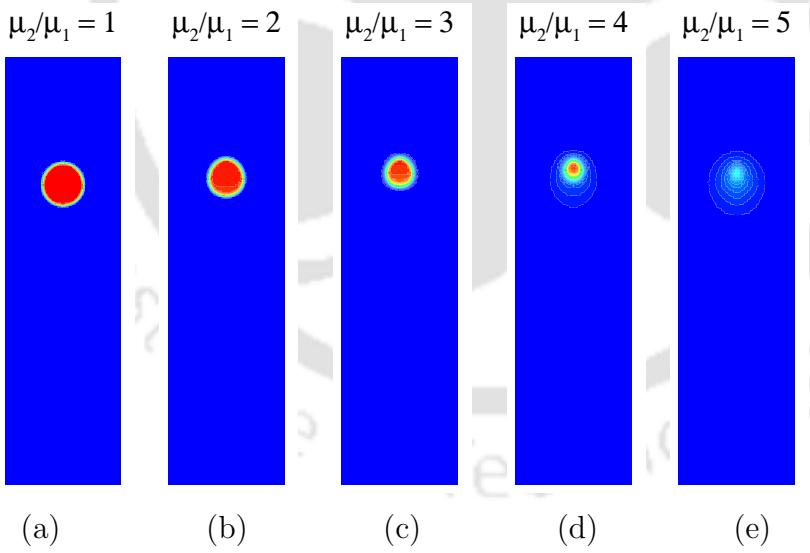

Figure 4.8: The shape of the droplet at different viscosity ratios for hydrophobic surface $g_{2w} = 0.05$ at Ca = 0.35 and time = 5.3 ((x, z)-plane view at wall): (a) $\frac{\mu_2}{\mu_1} = 1$, (b) $\frac{\mu_2}{\mu_1} = 2$, (c) $\frac{\mu_2}{\mu_1} = 3$, (d) $\frac{\mu_2}{\mu_1} = 4$, (e) $\frac{\mu_2}{\mu_1} = 5$

4.3.5 Effect of viscosity ratio on mixed-wet surfaces

It is well known that surfaces in many practical situations do not possess uniform wettability. Even it is possible to alter surface chemistry or structure to improve surface wetting properties. Chemical modifications of surfaces alone can typically enhance the water contact angles from 120° up to the extreme values of contact angles near 180° [128]. Adjustment of microroughness of the surface can make it either more hydrophilic or more hydrophobic depending on the original chemical properties of surfaces. In this context, it would be interesting to understand the effect of viscosity ratio on droplet behavior for mixed-wet surface. LBM is employed here to numerically study the effects of viscosity ratio on the displacement of the droplet on mixed-wet surface.

Simulations were carried out at Ca = 0.35 for the mixed-wet surface (see section 3.3.4) with $g_{2w} = \pm 0.02$. It can be inferred from Fig. 4.9 that the droplet spreads in hydrophilic region as expected in the early stages of flow evolution due to hydrophilicity of the surface. However, it rapidly contracts inward along the hydrophobic surface thereby decreasing its contact area in hydrophobic region. This can be observed from the variations of the wetted length and area as depicted in Fig. 4.10. The nature of deformation of the droplet is similar irrespective of the viscosity ratio (see Fig. 4.9). However, the wetted area and length decrease with increase in viscosity ratio which is consistent with earlier observation on hydrophobic surface. It may be noted that the stretching/elongation of the droplet which leads to increase in wetted length depends on capillary number. Since the capillary number in this case is not high, the viscosity and wettability play major role in time evolution of wetted length and area.

As time proceeds, the droplet continues to spread on the hydrophilic area leading to the deformation of the initial shape (see Fig. 4.11). The wetted area of the droplet is found to be reducing with time in case of higher viscosity ratio like $\frac{\mu_2}{\mu_1} = 5$. This is obvious as high viscosity ratio corresponds to strong cohesive forces which along with gravity force aid the droplet motion reducing its contact area as time proceeds till it gets detached. The orientation of the droplet along the direction of motions due to driving force bends the interface. However, the extent of bending has been observed to be more at higher viscosity ratios as shown in Fig. 4.12

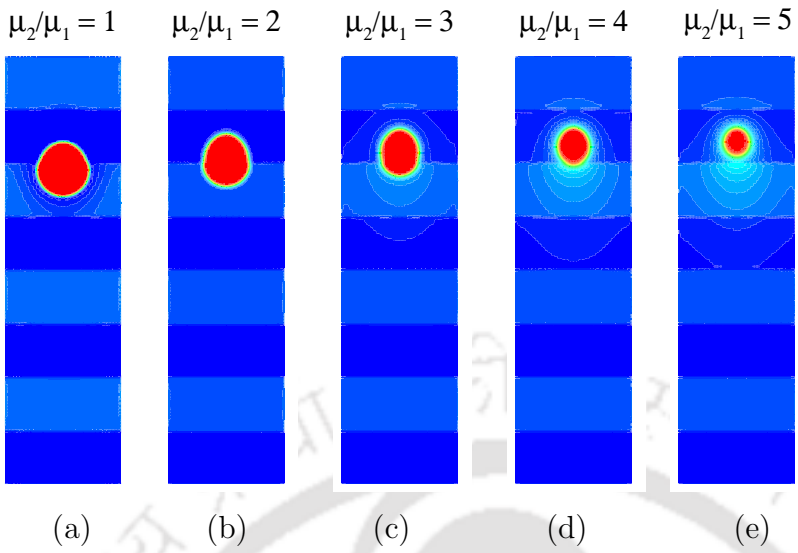

Figure 4.9: Shape of the droplet at different viscosity ratios for surface $g_{2w} = \pm 0.02$ at Ca = 0.35 and time = 5.3 ((x, z)-plane view at wall): (a) $\frac{\mu_2}{\mu_1} = 1$, (b) $\frac{\mu_2}{\mu_1} = 2$, (c) $\frac{\mu_2}{\mu_1} = 3$, (d) $\frac{\mu_2}{\mu_1} = 4$, (e) $\frac{\mu_2}{\mu_1} = 5$

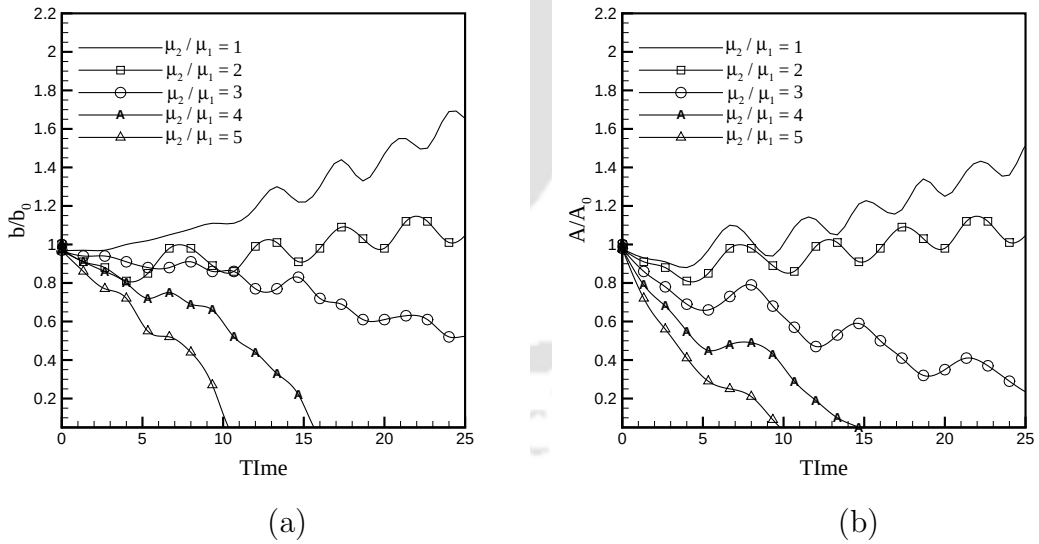

Figure 4.10: Effect of viscosity ratio at Ca = 0.35 and $g_{2w} = \pm 0.02$: (a) time evolution of wetted length, (b) time evolution of wetted area

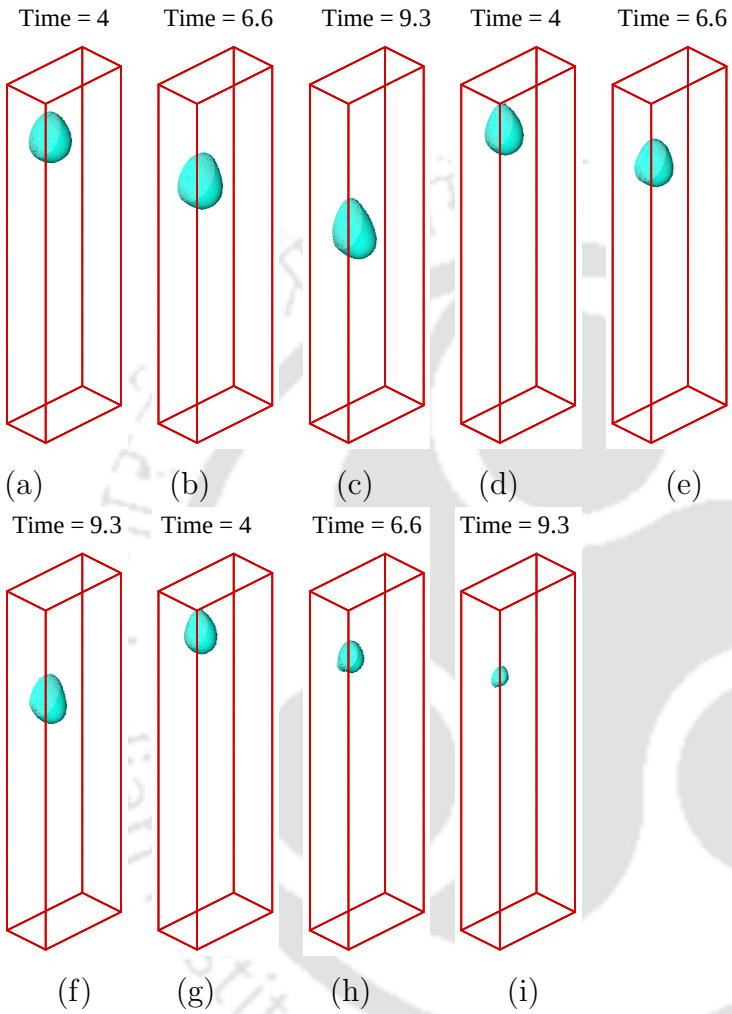

Figure 4.11: Dynamic behavior of the droplet at different viscosity ratios for the surface with wettability $g_{2w} = \pm 0.02$ and Ca = 0.35 (a)-(c) $\frac{\mu_2}{\mu_1} = 1$, (d)-(f) $\frac{\mu_2}{\mu_1} = 3$, (g)-(i) $\frac{\mu_2}{\mu_1} = 5$

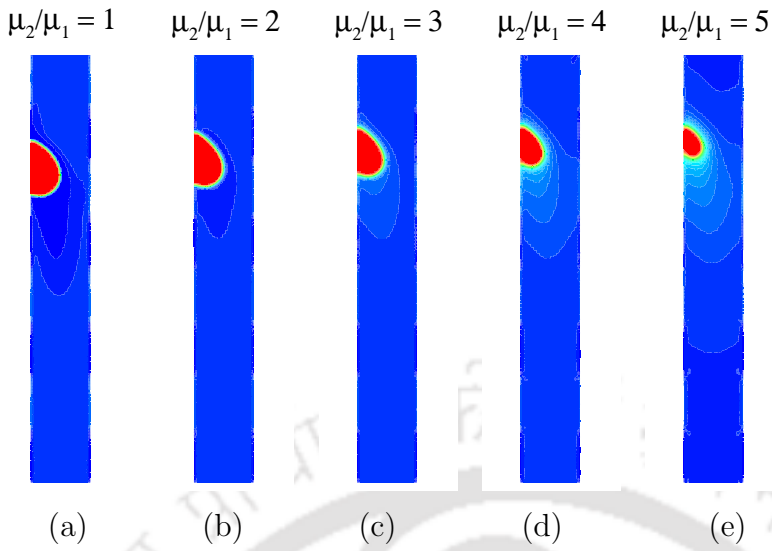

Figure 4.12: Shape of the droplet at different viscosity ratios for mixed-wet surface $g_{2w} = \pm 0.02$ at Ca = 0.35 and time = 5.3 ((y,z)-plane view at x = 40 wall): (a) $\frac{\mu_2}{\mu_1} = 1$, (b) $\frac{\mu_2}{\mu_1} = 2$, (c) $\frac{\mu_2}{\mu_1} = 3$, (d) $\frac{\mu_2}{\mu_1} = 4$, (e) $\frac{\mu_2}{\mu_1} = 5$

4.3.6 Effect of viscosity and capillary numbers on droplet dynamics

The displacement of the droplet is a complicated phenomenon in the presence of gravity. The motion of droplet is governed by the competition of capillary force, viscous force and gravity. When the surface wettability is considered, it also has an influence on the interface profiles. In order to investigate the effect of capillary number for different viscosity ratios on droplet displacement, simulations were performed for a range of Ca. The force required to set the droplet in motion must be greater than the viscous forces and surface tension forces taken together.

Figures 4.13 and 4.14 show the different patterns and flow regimes depending on the interplay between the various forces characterized by capillary numbers and viscosity ratios. It can be observed that at higher capillary number, the extent of deformation of droplet is more for all viscosity ratios as compared to low capillary number. Also, at low capillary number like Ca = 0.10, the viscosity ratio does not seem to be so effective as it is at high capillary number. This is justified since the wettability and surface tension are also responsible for deformation and displacement of the droplet. At Ca = 0.66, droplet breaking is seen at high viscosity ratio like

$\frac{\mu_2}{\mu_1} = 3, 5$ whereas for low viscosity ratio $\frac{\mu_2}{\mu_1} = 1$, the droplet is being stretched and is about to shed off the major portion of it. The wetted area reduces with the increase in Ca and viscosity ratio (see Fig. 4.14).

At low values of Ca = 0.10, the wetted length and area increase for lower viscosity ratios (e.g., $\frac{\mu_2}{\mu_1} = 1$) whereas for higher viscosity ratio $\frac{\mu_2}{\mu_1} = 3, 5$ reduce because of strong cohesive forces as explained earlier (see Figs. 4.15(a)-(b)). However, at higher values of Ca = 0.66 (see Figs. 4.15(c) -(d)), both wetted length and area reduce with time irrespective of viscosity ratio, because of the increase in viscous stresses along the interface.

For the mixed-wet surface, the displacement and deformation are different as compared to uniformly wet surface because of alteration in wettability from hydrophilic to hydrophobic. Figure 4.16 shows the effect of Ca for different viscosity ratio. It is clear that deformation is more at high values of Ca for all values of viscosity ratio but the nature of stretching scenario depends largely on location of the droplet. For example when droplet is completely in the hydrophilic region, it spreads more as compared to when it is in hydrophobic region. The elongation of droplet is more when it lies partially in hydrophobic and hydrophilic regions. Elongation of the droplet is maximum for high viscosity ratio at such position since high viscosity reduces the tendency to wet on the surface. When the droplet is in hydrophobic region, it contracts thereby reducing its wetted area but its wetted length increases to conserve the mass. It may be noted that even for high Ca = 0.66, there is no neck formation or shedding of some portion of droplet for mixed-wet surface. This shows that droplet motion is slower in any case for mixed-wet surface. Time evolution study also re-confirms this fact as shown in Fig. 4.17. Wetted length and area both decrease at high viscosity ratio like $\frac{\mu_2}{\mu_1} = 5$ whereas increase for low viscosity ratio like $\frac{\mu_2}{\mu_1} = 1$.

4.3.7 Viscosity-wettability interaction

A generic viscosity-wettability interaction can be best summarized by time evolution of wetted length and area as shown in Fig. 4.18. The wettability and viscosity dependence of the droplet displacement is manifested for a range of viscosity ratios. It can be safely adjudged that displacement of droplet is faster on hydrophobic and high viscosity ratio regime. This is justifiable since high viscosity and hydrophobicity both result in less contact area which assists in moving the droplet faster in the wall.

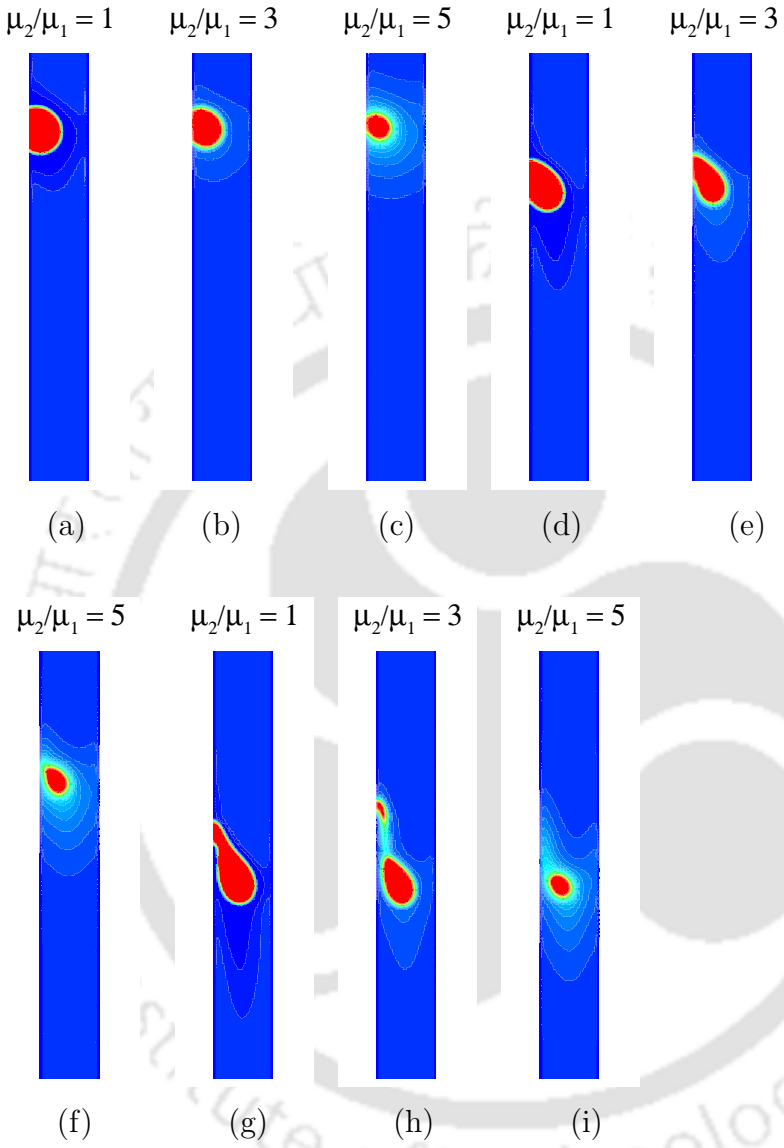

Figure 4.13: Effect of capillary number: The shape of the droplet at different viscosity ratios for hydrophobic surface $g_{2w} = 0.05$ at time = 5.3 ((y,z)-plane view at $x = 40$): (a)-(c) Ca = 0.10, (d)-(f) Ca = 0.35, (g)-(i) Ca = 0.66

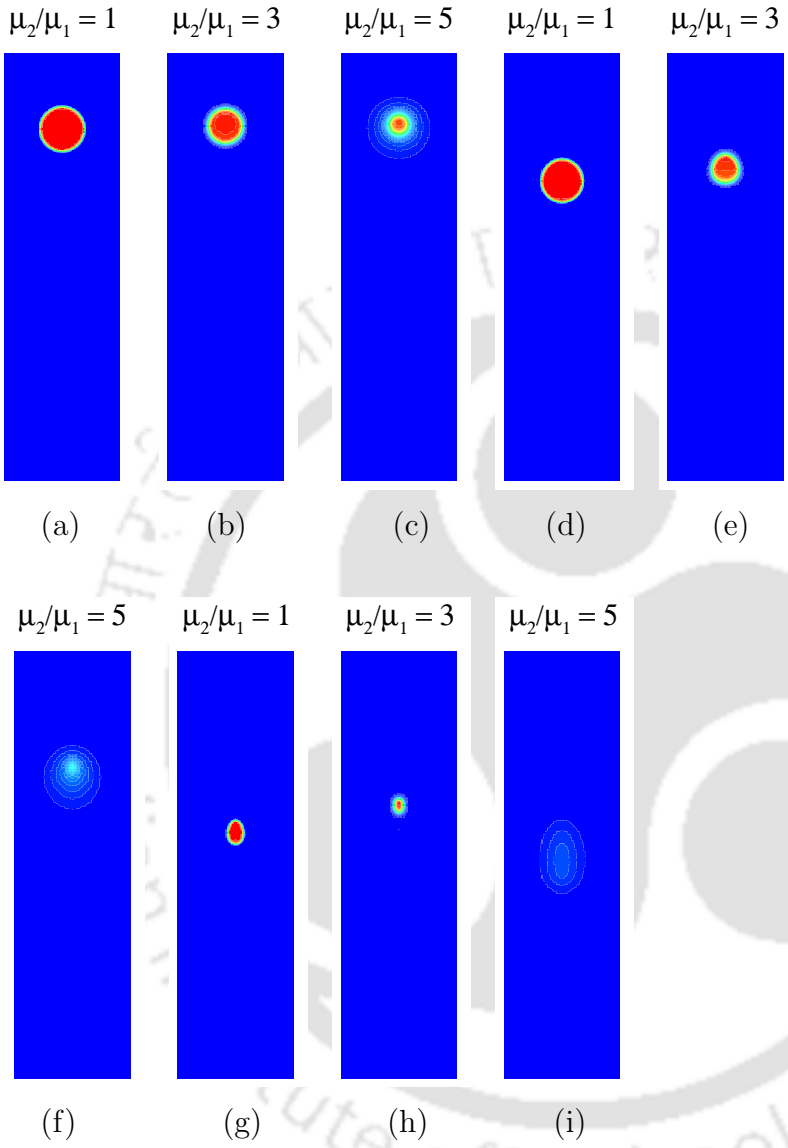

Figure 4.14: Effect of capillary number: The shape of the droplet at different viscosity ratios for hydrophobic surface $g_{2w} = 0.05$ at time = 5.3 ((x,z)-plane view at wall) for (a)-(c) Ca = 0.10, (d)-(f) Ca = 0.35, (g)-(i) Ca = 0.66

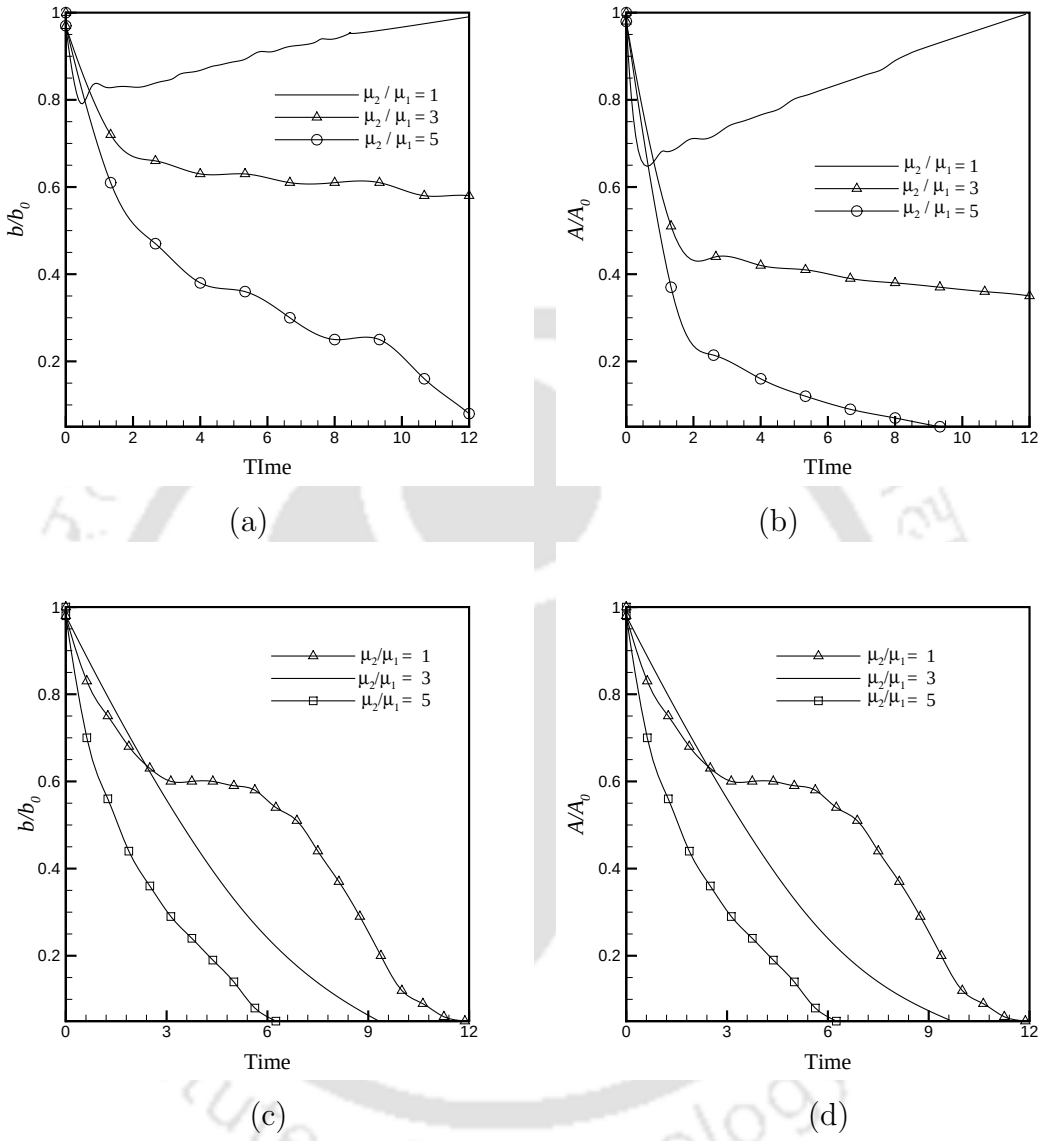

Figure 4.15: Effect of capillary number for different viscosity ratios on hydrophobic surface ($g_{2w} = 0.05$): (a) time evolution of wetted length for Ca = 0.10 , (b) time evolution of wetted area for Ca = 0.10, (c) time evolution of wetted length for Ca = 0.66 , (d) time evolution of wetted area for Ca = 0.66

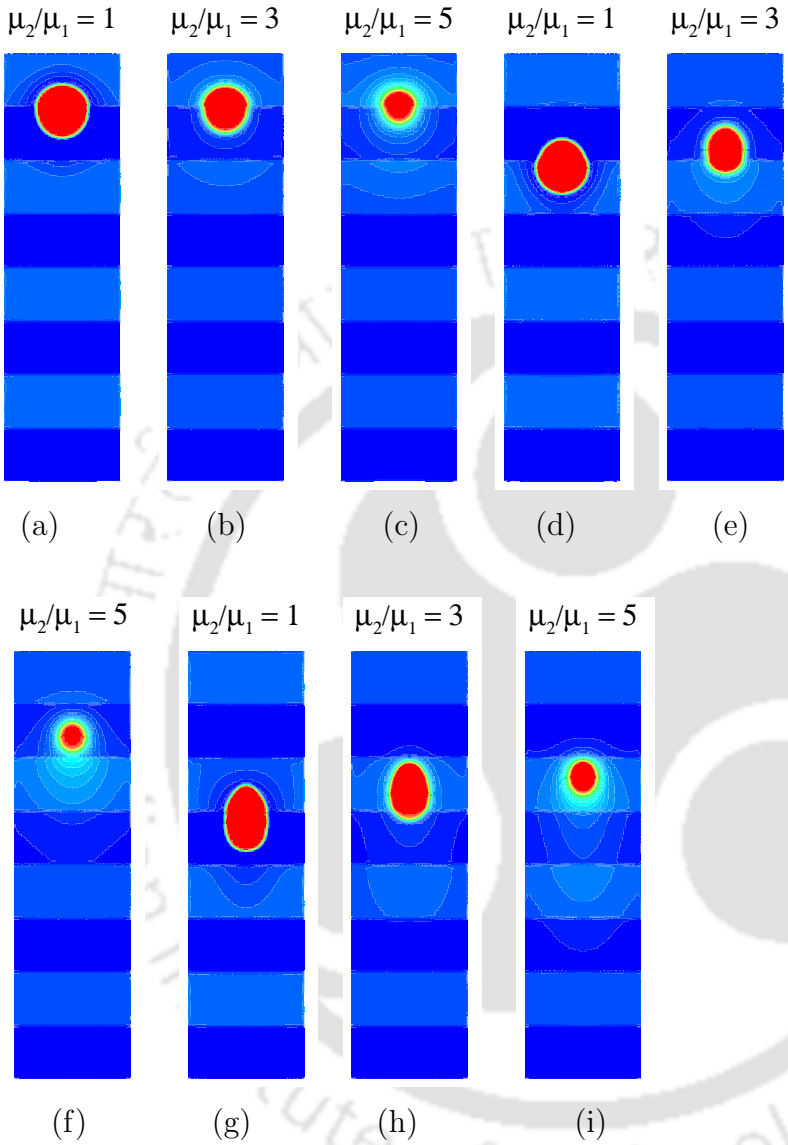

Figure 4.16: Effect of capillary number: shape of the droplet at different viscosity ratios for mixed wet surface $g_{2w} = \pm 0.02$ at time = 5 ((x,z)-plane view at wall) for (a)-(c) Ca = 0.10, (d)-(f) Ca = 0.35, (g)-(i) Ca = 0.66

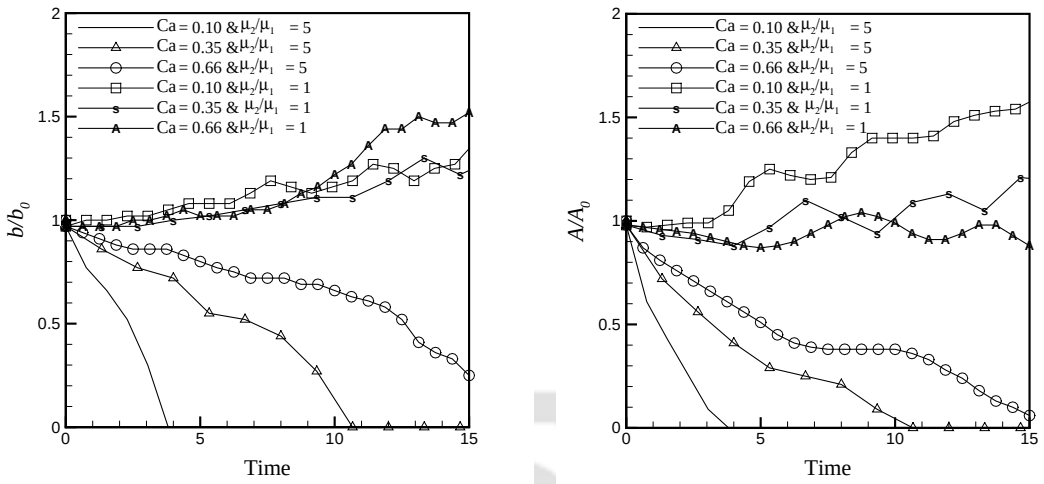

Figure 4.17: Effect of capillary number for the surface with $g_{2w} = \pm 0.02$: (a) time evolution of wetted length, (b) time evolution of wetted area

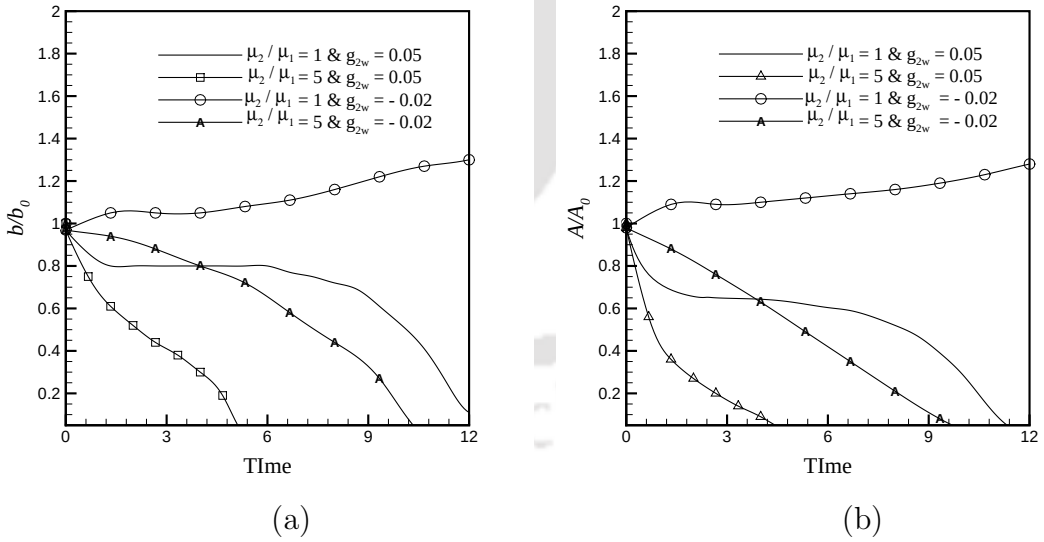

Figure 4.18: Comparison of effect of viscosity ratios for different wettability patterns for Ca = 0.35: (a) time evolution of wetted length, (b) time evolution of wetted area

Thus, it can be concluded that high viscosity ratio and hydrophobicity together form key ingredients for droplet displacement. It may be noted that the strength of wettability alteration can also affect the variations in wetted length and area and actually hinder the swift motion of the droplet. These results can be very useful in various applications, like enhance oil recovery and fuel cell wherein such wettability scenario is very common.

4.4 Closure

Simulations of the displacement of a three-dimensional immiscible droplet on various wettabilities and viscosity ratios in a channel were carried out to understand the physics of viscosity-wettability interaction. It was observed that temporal evolutions of wetted length and wetted area show that the displacement of droplet is faster on hydrophobic and high viscosity ratio regimes. It has been seen that the effect of viscosity ratio is not significant to influence the droplet motion at lower capillary number. However, at high capillary numbers, higher viscosity ratio aids droplet motion, reducing the wetted area.

Chapter 5

Combined influences of Confinement and Wettability on Droplet Displacement Behavior

Droplet dynamics in confined geometries has received a high degree of scientific attention in the last decades owing to its industrial applications, e.g., food emulsions, cosmetics and polymer blending. An insight into the droplet dynamics for different confinement configurations is vital since confinement affects the nature of deformation [141, 142] and the droplet surface interaction. For example, in case of the confined blends with a droplet-matrix structure, the size of the droplet phase may become comparable to the dimensions of the flow geometry. In this context, many investigators have attempted to explore the effect of confinement on the droplet dynamics [141, 143, 144]. In this context, the underlying two phase dynamics of droplet motion on the surface with different confinement configurations is discussed.

Earlier investigations start with the pioneering work of Taylor [145, 146] who analyzed the dynamics of droplets dispersed in an immiscible fluid. Kang et al. [10, 11] have simulated the displacement of the two and three dimensional immiscible droplet subject to gravitational forces in a duct with lattice Boltzmann method. They investigated the effects of the contact angle and capillary number on droplet dynamics. Mukherjee [21] investigated 3-D droplet motion using D3Q19 two-phase Shan and Chen lattice Boltzmann model on a patterned duct wall with varying wet-

tability. However, the effect of confinement in conjunction with wettability remain largely overlooked and needs to be studied in greater detail.

5.1 Problem Specification

In the present work, effect of confinement on the displacement behavior of the droplet has been studied. Length, breadth and width of the computational domain (see Fig.5.1) considered here are 300, 81 and 41 (in lattice units) respectively. The droplet is initially positioned at $z = 251$. The droplet motion is achieved due to gravitational force applied along the z-direction. S-C model is used with two immiscible fluids in which droplet (fluid 2) is placed in the domain filled with displacing fluid (fluid 1). No slip boundary condition is applied at the walls in x- and y-direction. The periodic boundary condition is applied in z-direction. Interface is taken at the location where both the fluid have equal number density since interface is diffused for S-C model. Results are discussed in the form of time evolution of wetted length (b) and wetted area (A) for the surface with different wettability in various confinement configurations. The simulation parameters used for all simulations are as given below

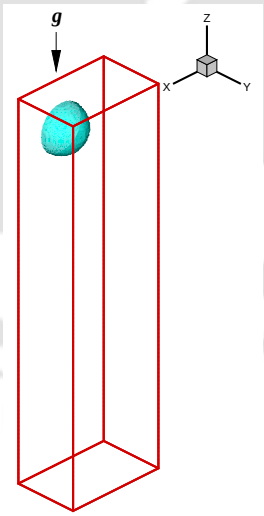

(a)

Figure 5.1: Computational domain

Table 5.1: Parameter values used to study the influence of confinement

Parameter	Value
Fluid-fluid interaction parameter :	
$g_{11} = g_{22}$	0
$g_{12} = g_{21}$	0.1

5.2 Results and Discussion

An insight into the droplet dynamics for different confinement configurations is vital since confinement affects the nature of deformation [141, 142] and the droplet surface interaction. For example, in case of the confined blends with a droplet-matrix structure, the size of the droplet phase may become comparable to the dimensions of the flow geometry. In this context, many investigators have attempted to explore the effect of confinement on the droplet dynamics [141, 143, 144]. Hence, it is imperative to understand the combined effect of confinement and wettability on the dynamics of multiphase flows. The following sections attempt to gain insight into the effect of these parameters on the displacement behavior of the droplet.

5.2.1 Droplet dynamics on the surface with uniform wettability

The primary goal of this investigation is to systematically evaluate the two-phase constitutive closure relations via appropriate numerical experiments on droplet motion for the parameters like wettability (g_{2w}), confinement on temporal evolution of wetted area and length under the applied gravitational force.

5.2.2 Effect of confinement on moving droplet

It is well known that confinement ratio of the droplet is a vital parameter in addition to the capillary number and the viscosity ratio as far as the droplet dynamics is concerned. Hence, the dynamic behavior of the confined droplet in duct is investigated as a function of wettability and confinement ratio. It may be noted that the

confinement ratio ($\frac{2R}{h}$) is defined as the ratio between the droplet diameter $2R$ and the wall separation h.

In this context, the simulation of droplet motion is performed for the hydrophobic surface with $g_{2w} = 0.05$ for Ca = 0.35 for $\frac{2R}{h} = 0.62$, 0.75, 0.86 and 0.94 (see Fig. 5.4). The fluid properties used in the simulations are listed in Table 5.1. The confinement ratio ($\frac{2R}{h}$) of the droplet in a duct is varied by changing the width (h) and the droplet radius (R). Figure 5.2 shows the time evolution of wetted area

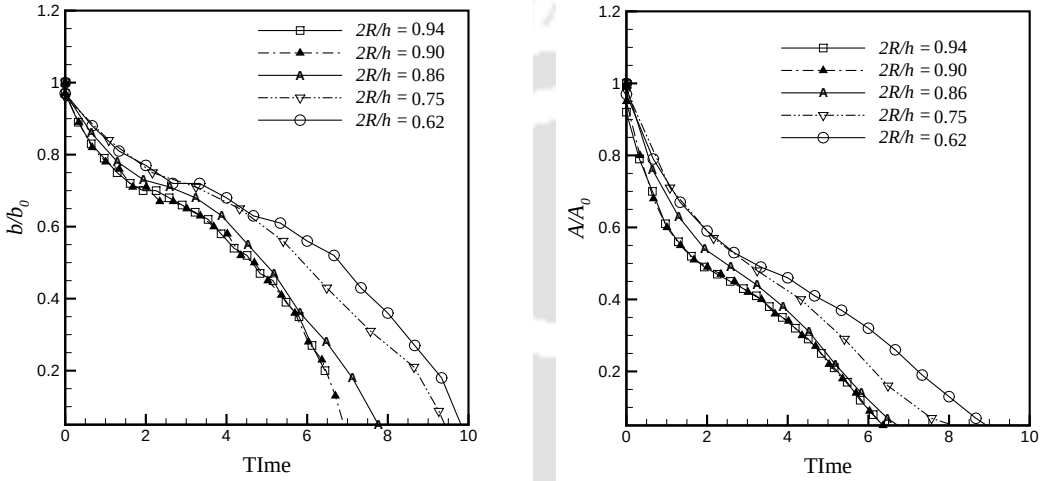

Figure 5.2: Effect of confinement at Ca = 0.35 and $g_{2w} = 0.05$: (a) time evolution of wetted length, (b) time evolution of wetted area

and length for hydrophobic surface. The reduction of wetted length and area with time is observed to be less in case of high confinement ratio i.e., $\frac{2R}{h} = 0.94$. As the droplet gets more confined, it aligns more in the direction of flow. Hence, the droplet experiences a weaker flow with additional stabilizing wall effects.

5.2.3 Effect of wettability on moving droplet with various confinement ratios

In order to investigate the effect of confinement ratio in conjunction with wettability, the simulations were performed on hydrophilic and hydrophobic surface. The fluid/solid interaction coefficient is set to g_{2w}= -g_{1w} = 0.05 corresponding to a static

contact angle of 118° whereas for the hydrophilic region g_{2w} = -g_{1w}= - 0.02 leading to a static contact angle of 78° [10, 11]. The hydrophobicity of the surface along with the driving force aids the droplet to move further. This finally yields in complete detachment of the droplet from the wall as well (see Fig. 5.3). It can be concluded that hydrophobic surfaces do not show different character for low and high confinement ratios. However, the deformation is more in case of low confinement ratios followed by the detachment of the droplet (see Figs. 5.3 (a)-(d)). On the contrary,

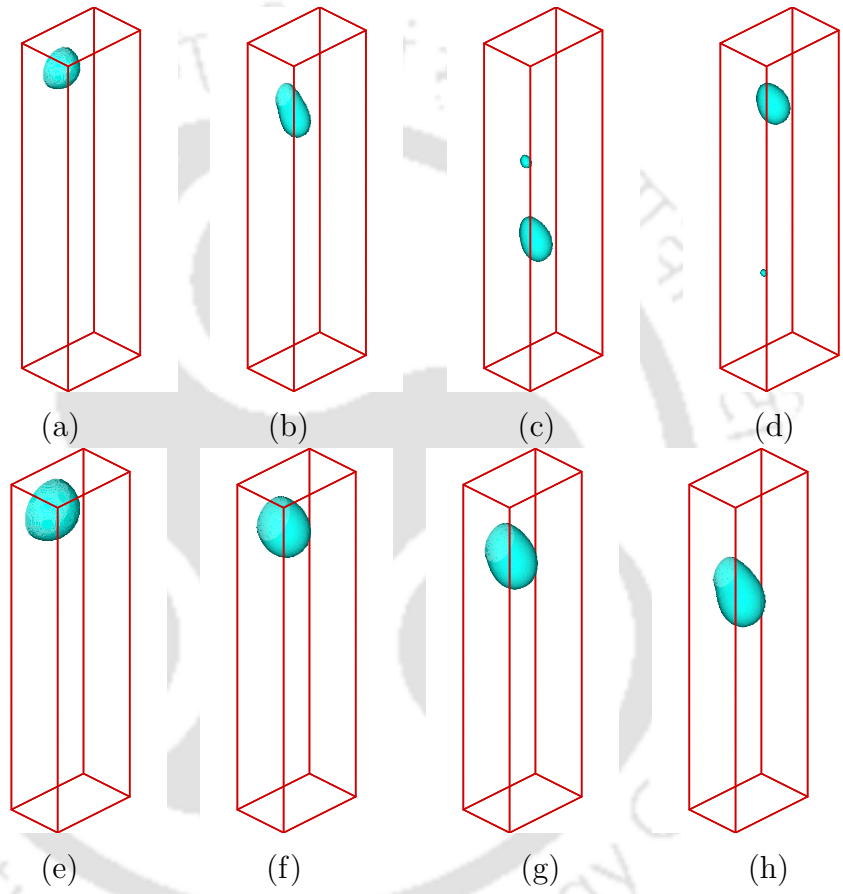

Figure 5.3: Shape of the droplet with different confinement ratio at Ca = 0.35 for g_{2w} = 0.05: (a)-(d) for $2R/h$ = 0.62 at time = 0, 3.12, 6.24 and 9.36, (e)-(h) for $2R/h$ = 0.94 at time = 0, 3.12, 6.24 and 9.36

the deformation of the droplet is different in nature in case of hydrophilic surface. This is particularly due to the wetting tendency of the droplet on hydrophilic surface. Although, the droplet elongates during deformation in the direction of motion along the wetting surface, it can be observed that the extent of elongation and

spreading of the droplet are found to be more (see Figs. 5.4 (a)-(d)) on the surface with low confinement. It may be noted that at higher confinement ratio, stabilizing effect of the wall and the wetting tendency of the surface causes deformation in the direction of motion only, thus flattening of the droplet along the surface (see Figs. 5.4 (e)-(h)). Figure 5.5 shows the time evolution of the dimensionless wet-

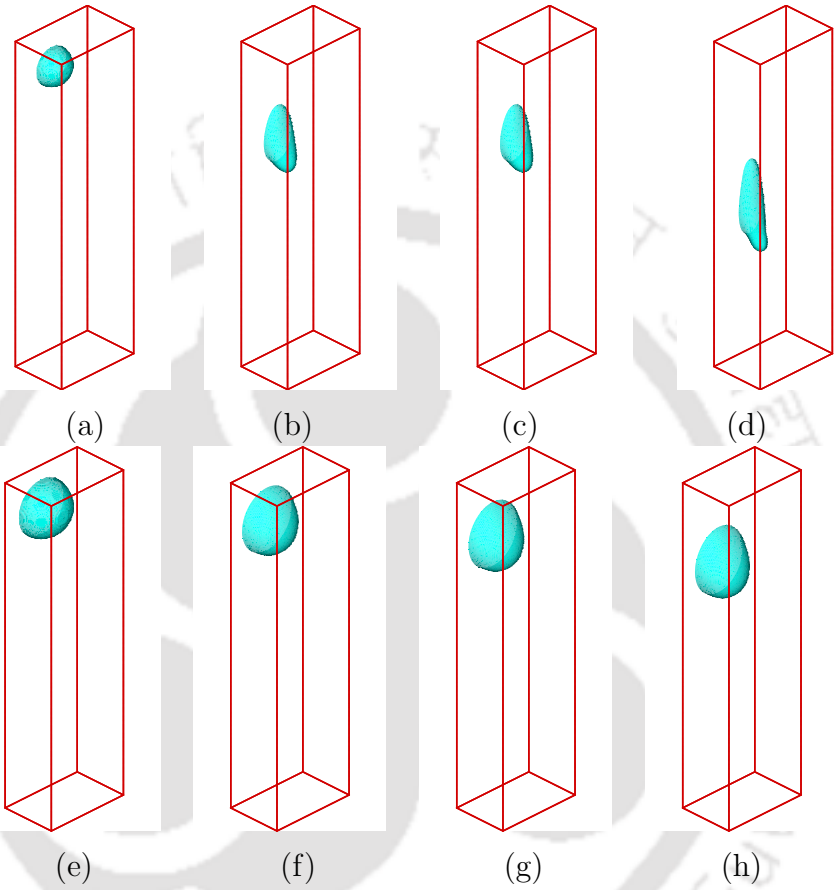

Figure 5.4: Dynamic behavior of droplet with different confinement ratios at Ca = 0.35 for g_{2w} = - 0.02: (a)-(d) for $2R/h = 0.62$ at time = 0, 3.12, 6.24 and 9.36, (e)-(h) for $2R/h = 0.94$ at time = 0, 3.12, 6.24 and 9.36

ted length b/b_0 and wetted area A/A_0 between the wall and the sliding droplet on hydrophobic and hydrophilic surface. For hyodophilic surface, both wetted length (b/b_0) and wetted area (A/A_0) increase with time at first, then decrease slowly. At low confinement ratio ($\frac{2R}{h} = 0.62$), it is observed that both wetted length and area increase monotonically due to the weaker wall effect which causes the droplet to flatten and spread along the surface. For the non wetting case, both b/b_0 and A/A_0

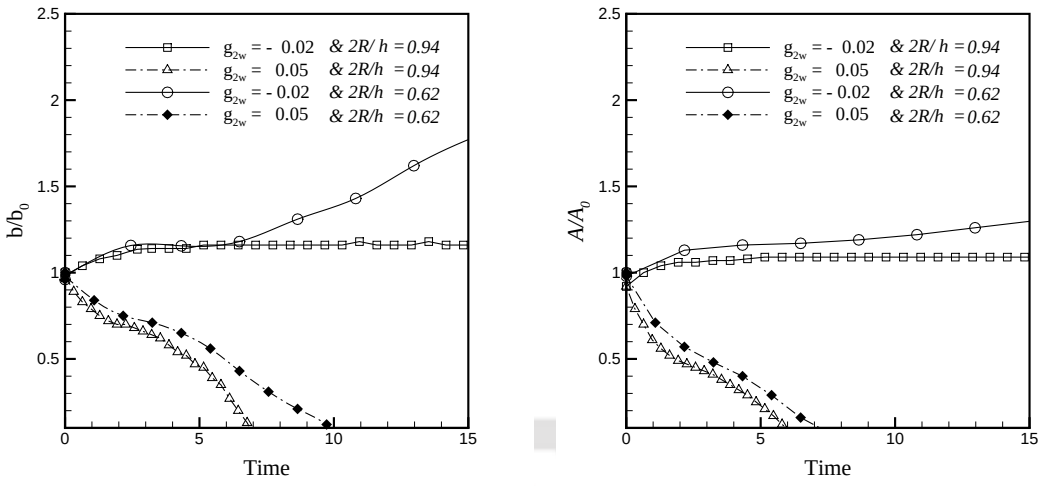

(a) (b)

Figure 5.5: Effect of wettability for various confinement ratios at Ca = 0.35 : (a) time evolution of wetted length, (b) time evolution of wetted area

dramatically decrease with time and reach zero when the droplet totally detaches from the wall. The time of detachment differs with the confinement ratios. It can be seen that the detachment of the droplet occurs earlier in case of low confinement ratios as compared to high confinement ratios. Figure 5.6 shows the effect on interface of the droplet due to different confinement ratios. It can be seen that the shape of the droplet is greatly stretched from its original static shape, especially for low confinement ratios matching with our earlier observations. The important point to note here is that the nature of the wettability of surface dictates the way in which droplet deforms. For instance, in case of hydrophilic surface the wetting tendency compels the droplet to adhere to the surface during deformation, whereas for hydrophobic surface, the droplet detaches as a result of deformation ultimately.

5.2.4 Effect of capillary number on moving droplet with various confinement ratios

It is well known that the displacement of the droplet not only depends on the relative magnitude of viscous forces and gravity, but also on their relative magnitude with respect to the heterogeneous capillary forces. A dimensionless number is defined to

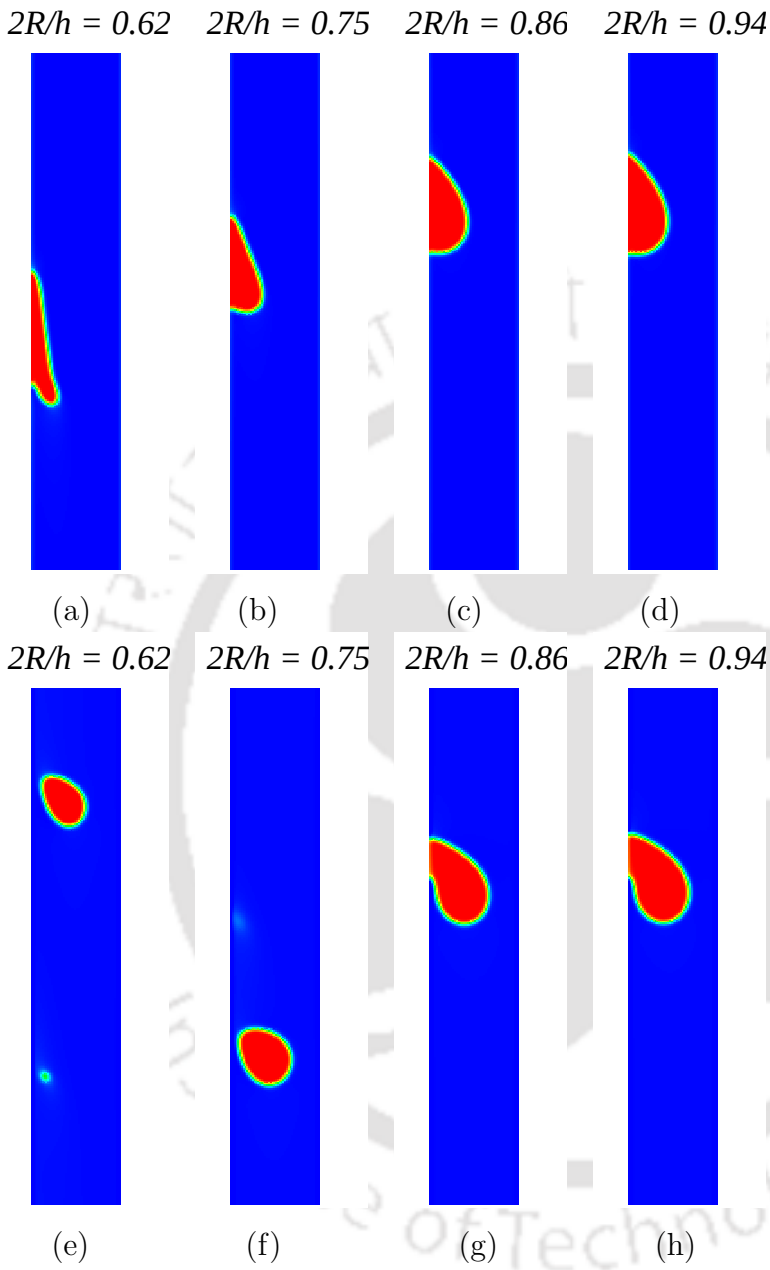

Figure 5.6: Effect of wettability for different confinement ratios at Ca = 0.35, y, z-plane view at x mid-plane, (a)-(d) contour plot for g_{2w} = - 0.02, (e)-(h) contour plot for g_{2w} = 0.05

quantify the relative magnitudes of these forces. The capillary number is the typical ratio of the viscous pressure drop at pore scale to the capillary pressure given by Ca $= \frac{\rho_2 V \mathbf{g}}{\sigma h}$ where V is the volume of the droplet. It must be noted that each driving force term, responsible for initiating the droplet motion, can be taken as a representative of a particular capillary number [11]. It may be noteworthy that different capillary numbers can be obtained by changing the gravitational factor, $\mathbf{g}$. In this study, numerical experiments are performed on different wettability patterning under the influence of different driving force terms i.e., Ca for a range of configuration ratios. Figure 5.7 depicts the dynamics of droplet on hydrophobic surface at different times for Ca = 0.1 and 0.35 for low and high confinement ratio i.e., $2R/h$ = 0.62, 0.94 respectively. It can be observed from time evolution of wetted length and area that

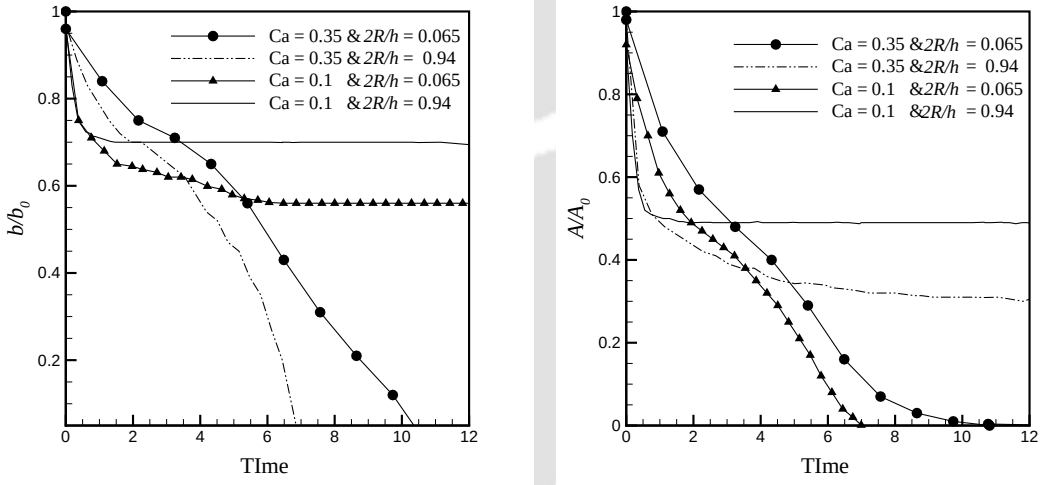

(a) (b)

Figure 5.7: Effect of capillary number for various confinement ratios for the hydrophobic surface (g_{2w} = 0.05): (a) time evolution of wetted length, (b) time evolution of wetted area

the contact length of the droplet decreases irrespective of confinement ratio. The droplet moves faster in the case of the high confinement ratio thereby detaching from the surface earlier as compared to the droplet with low confinement. This establishes the fact that confinement affect the droplet dynamics in addition to other factors like wettability. Most interesting observation is that for low Ca = 0.1, the rate of reduction of wetted length and area is slower initially up to certain

time. Thereafter wetted area and length of the droplet remain more or less constant because the droplet virtually gets stalled. The effect of confinement is not observed distinctly in this case as in high Ca case. However, the simulations on hydrophilic surfaces show the effect of wetting tendency of the surface besides the effect of confinement on droplet motion (see Fig. 5.8). For low Ca, it is seen that the

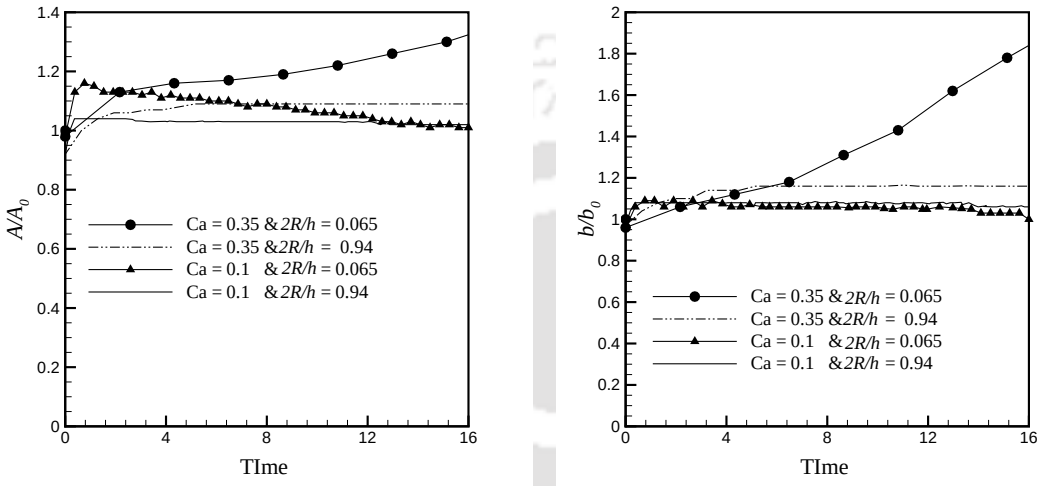

(a) (b)

Figure 5.8: Effect of capillary number for various confinement ratios for the hydrophilic surface (g_{2w} = - 0.02): (a) time evolution of wetted length, (b) time evolution of wetted area

wetting length and area of droplet reduces with time irrespective of confinement ratio. However, for Ca = 0.35, the wetted length and area are seen to increase with time for low confinement ratio i.e. $2R/h = 0.62$. This is attributed to the deformation and stretching of the meniscus due to the increase in viscous stresses along the interface. The high confinement ratio has the stabilizing effect on the droplet configuration thus maintaining the wetted length and area more or less constant. The contour plot in Fig. 5.9 shows more deformation of droplet along the direction of motion. It can be seen that the droplet starts beading up on the lower end for all confinement ratios and capillary numbers irrespective of the wettability of the surface. Although the deformation is low in the case of high confinement ratios ($2R/h = 0.94$), the shape of droplet and extent of interface bending is seen to differ depending on surface wettability. For example, at Ca =0.1, the droplet

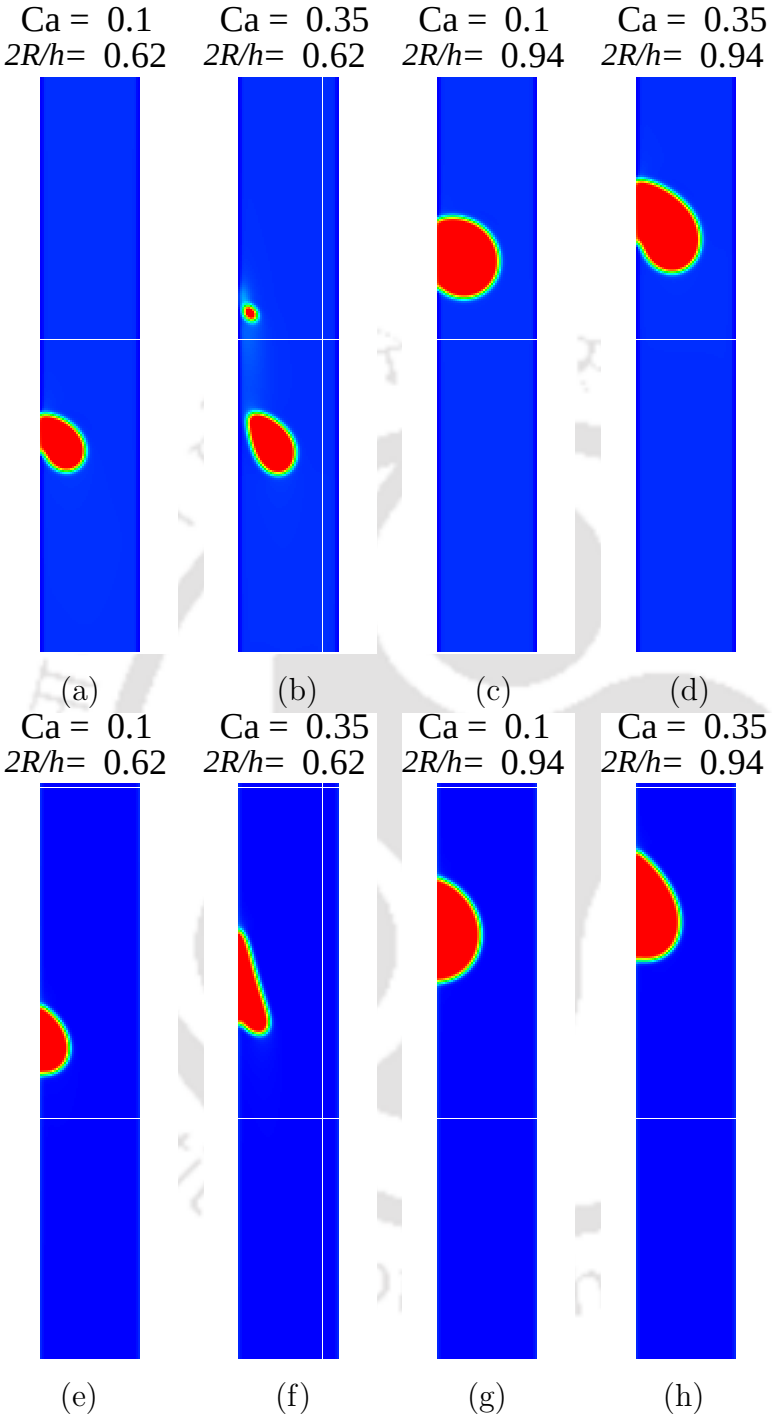

Figure 5.9: Effect of capillary number (contour plot at time = 6.25): (a)-(d) for the hydrophobic surface (g_{2w} = 0.05), (e)-(h) for the hydrophilic surface (g_{2w} = - 0.02)

is more or less of initial configuration on hydrophilic surface (see Fig. 5.9 (g)) whereas there is bending/deformation of interface on hydrophobic surface (Fig. 5.9 (c)). This observation can be seen more clearly in the case of high capillary number even in case low confinement ratios; although the interface literally flattens/orients along the hydrophilic surface (see Fig. 5.9 (f)) because of wetting tendency. This proves the fact that wettability and capillary number in conjunction with degree of confinement govern the dynamics of the droplet.

5.3 Closure

Simulations of the displacement of a three-dimensional immiscible droplet for different confinement ratios in a duct are carried out by the lattice Boltzmann method. The simulation has demonstrated that confinement ratio influences the dynamic behavior of droplet. Temporal evolution of wetted length and wetted area shows that change in droplet morphology is greater at low confinement ratios. Droplet shape is highly affected by wettability and degree of confinement, especially at low capillary number. Excessive change in the morphology of the droplet is observed on hydrophobic surface as compared to hydrophilic surface for low confinement ratios.

Chapter 6

Investigation of Mobilization of Trapped Blob in a Sinusoidal Duct under Capillarity Induced Resonance

6.1 Introduction

In the recent past, vibrational and acoustic stimulation of oil reservoirs has been investigated for possible application in enhanced oil recovery [66, 70, 80]. Hilpert et al. [70] estimated the frequencies of pulsing pressure in channel that increases the volume of the displaced non-wetting phase. Many studies have discussed how vibrations overcome capillary entrapment that keeps the fluids in place [86, 147] which emphasized the enhancement in two-phase flow by vibrations under field and laboratory conditions. Hilpert [1] discussed the use of capillarity induced resonance to mobilize blobs by exciting them at their resonant frequency. However, the influence of different wettability scenarios like uniform, mixed-wet in conjunction with capillarity induced resonance on mobilization of the trapped blob is hardly explored which is the main focus of the present study.

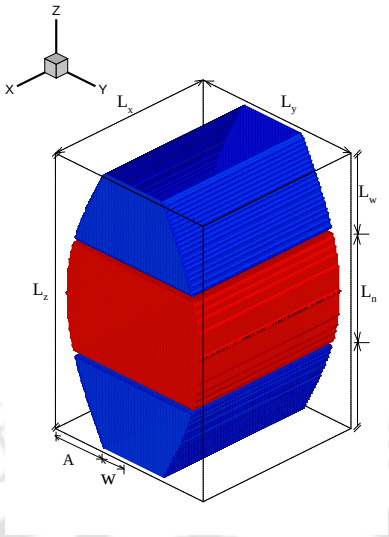

Figure 6.1: Simulation geometry showing non wetting phase blob in a sinusoidal channel with periodic boundary conditions

6.2 Problem Specification

The work in this chapter presents a lattice Boltzmann S-C method to simulate the acoustically induced oscillation of the interfaces of a trapped blob in a sinusoidal channel geometry. The main aim is to identify the operating parameters for the mobilization of the trapped blob, particularly as a function of surface wettability. Menisci are pinned at the solid surface as a result of geometric roughness, thus mobilization requires to overcome pinning. The acoustic excitation is modeled as a body force. Lattice Boltzmann S-C model is considered here for the system with two immiscible fluids in which blob (fluid 2) is placed in the domain filled with displacing fluid (fluid 1). Length, breadth and width of the computational domain (see Fig. 6.1 considered for the study are taken as 100, 48 and 48 (in lattice units). The blob is initially located at the center of the domain i.e., $z = 50$. The motion of the blob is induced by an acoustic force along the z-direction. The dynamics of the blob is studied for the parameters like thickness of the blob, frequency applied, nature of the wettability No slip boundary condition is applied at the walls in x- and y-direction whereas the periodic boundary conditions are applied in z-direction. Displacement of meniscus of the blob is found by locating the interface at the midsection along x axis where the number density of both the fluids is equal [11].

6.3 Theory: Linear Response of a Blob with Pinned Contact Lines in a Sinusoidal Channel

The fluid percolation through pore channel can be considered equivalent to finite yield stress in the fluid. In such case, it can be presumed that the flow takes place only after the application of a certain pressure gradient. This so called 'capillary trapping' is seen when meniscus is 'pinned' due to mechanical irregularities like roughness or chemical impurities on walls. Because of pinning of the interface, the curvature of the interfaces along the wall varies as the pressure increases. However, the three-phase contact line at the wall does not move. It adjusts the radius of curvature at surface [148]. It requires finite force to be applied to release the contact line [70, 86, 103, 149]. The system with pinned interface resonate much like a mass on a spring [84] and the damping is provided by the viscosities of the fluids. If the initially flat interface at equilibrium is distended, the surface tension acts like a spring to restore it to its flat configuration. If the fluids in the system are subjected to perturbations, the interface and the fluids should oscillate harmonically with frequency and resonance observed [84]. It is obvious that the displacement will be more at the resonating frequency.

In this work, it is assumed that the contact line between the fluid and the surface is pinned to surface. The surface roughness is modeled by adding solid-phase pixels on both sides of the channel for two selected sites where three-phase contact points could be pinned. The small roughness height is taken so that it does not have significant effect on the flow but will be able to 'trap' the three-phase contact line. The blob is subjected to transient body force in the z-direction. LB simulations are run to investigate whether the numerical model can simulate the resonance of trapped non wetting phase blobs. The transient force applied on the blob can be expressed as given below.

$$W(t) = W(0) + \delta W \sin(\omega t) \tag{6.1}$$

where
$W(0)$ is a constant body force
$\delta W \sin(\omega t)$ is the perturbation
The constant body force $W(0)$ can be taken equivalent to an imposed pressure gradient in the wetting phase [1] whereas the perturbation $\delta W \sin(\omega t)$ can be considered

Table 6.1: Parameter values used to study the effect of capillarity induced resonance

Parameter		Value
Density of fluid 1		0.035
Density of fluid 2		0.965
Length of the duct (l)		100
Breadth(h)		48 in the x-direction
Width(w)		48 in the y-direction
Fluid-fluid interaction parameter	$g_{11} = g_{22}$	0
	$g_{12} = g_{21}$	0.1
Relaxation time of the wetting phase		0.80
Relaxation time of the non wetting phase		0.80

as a vibration of the pore walls and/or an oscillatory pressure gradient. Hence, capillarity induced resonance can be exploited to mobilize trapped non wetting phase by acoustic and elastic waves. Since the no constant body force is applied, $W(0) = 0$ and $\theta_0^+ = \theta_0^-$; where $\theta_0^+ = \theta_0^-$ are the blob equilibrium contact angles at the top and bottom menisci, respectively. First the non wetting phase blob is initialized for a straight pore channel and equilibrium is reached through numerical simulation. The fluid properties used in the simulations are listed in Table 6.1.

A particle distribution function bounce-back scheme [125, 126, 127] is imposed at the walls to obtain no-slip boundary condition. It may be noted that for a node near a boundary, some of its neighboring nodes lie outside the flow domain. Hence, unique definition of the distribution functions at these no-slip nodes is not known. The bounce-back scheme is a simplest way to fix these distributions on the wall node [150]. The bounce-back scheme implies that when a particle distribution streams to a wall node, it scatters back to the node it has come from. Periodic boundary conditions applied along the channel axis at $z = 0$ and $z = l$. The channel radius is denoted by R whereas the non wetting phase blob length and length of the wetting phase blob are indicated by L_n and L_w respectively (see Fig. 6.1). It may be noted that the periodic boundary condition connects the non wetting phase blob over the

outlet and inlet of the channel. The simulations are carried out on similar lines of Hilpert [1]. Figure 6.1 shows the lengths L_n and L_w measured from the distances in the respective fluids between the three-phase contact points.

It may be noted that estimation of the viscous pressure drop for sinusoidal geometry is more complicated than for a straight pore channel. Hilpert [1] has used the model of Metzner [70, 151] to develop analytical model very similar to the one proposed for the straight pore channel. However, in model proposed by Hilpert [1], the radius of the pore channel varies according to Eq. (6.2).

$$R(z) = \text{width} + A * \sin\left(\frac{\pi}{lz} * z\right) \quad \text{for} \quad 0<z<lz \tag{6.2}$$

where
$A = (ly/2)$ - width
ly - length in y-direction
The calculation of characteristic frequency (see Eq. (6.6)) for the sinusoidal channel considers variable size of radius by defining mean radius $\bar{R}$ averaged over the regions occupied by the two fluids Eq. (6.3).

$$\bar{R}(z) = \frac{1}{L_n}\int R(z)\,dz \tag{6.3}$$

Resonating frequency ω_0 can then be calculated using equation given by Hilpert [1] as below.

$$\omega_0 = \sqrt{\frac{2\gamma\left(g\left(\theta_0^+\right) + g\left(\theta_0^-\right)\right)}{\left(L_n\rho_n + L_w\rho_w\right)\bar{R}^2}} \tag{6.4}$$

where

$$g(\theta_0) = \sin(\theta)\left(2 - \frac{\pi - 2\theta - \sin(2\theta)}{2}\frac{\sin(2\theta)}{\cos^4(\theta)}\right)^{-1} \tag{6.5}$$

ω_c is the characteristic frequency chosen to nondimensionalize δx and δW and is given by

$$\omega_c = \frac{\nu}{\bar{R}^2} \tag{6.6}$$

The non dimensional excitation frequencies are expressed as

$$X_n = \frac{\omega}{\omega_{cn}} \tag{6.7}$$

$$X_w = \frac{\omega}{\omega_{cw}} \tag{6.8}$$

It may be noted that subscript n and w indicate non wetting and wetting phase respectively

The frequency response can be given according to the equation [1] given below.

$$\chi = w_c^2 \frac{\delta x}{\delta W} \tag{6.9}$$

where

δx = Blob displacement

δW = Amplitude of the force applied

To quantify blob displacement the blob's center of mass is calculated [1] as follows :

$$z(t) = \frac{\int\int\int z\rho\,(x,y,z,t)\,dxdydz}{\int\int\int \rho\,(x,y,z,t)\,dxdydz} \tag{6.10}$$

6.4 Results and Discussion

The primary aim of this work is to systematically evaluate the two-phase constitutive closure relations via appropriate numerical experiments on mobilization of blobs due to capillary-induced resonance. The effect of various parameters like wettability (g_{2w}), blob thickness, width of blob and frequency on displacement of blob is explored. In this context, first, a series of numerical simulations are carried out to understand the physics behind blob motion for pinned contact surfaces.

6.4.1 Effect of frequency on the response of the blob

In order to understand the dynamics of the blob, numerical experiments are performed to estimate the mean displacement of the blob at various excitation frequencies. The change of displacement of blob with respect to time is plotted for a pinned contact line configuration. The simulation parameters used for this case are g_{2w}= 0.01, $\delta W = 0.0001$, $\omega = 0.002$. Figure 6.2 depicts the response of the blob excited by an oscillating body force $\delta W(t) = \delta W \sin(\omega t)$ in z-direction, where the ω is discrete excitation frequency ranging from 0 to 1.5 ω_0. The amplitude of force applied is $\delta W = 0.00005$. The kinematic viscosities of both fluids are equal, $\omega_{cn} = \omega_{cw}$. The lengths of the non wetting phase and wetting phase are 40 and 60 respectively. The χ values are determined from Eq. (6.9). The temporal response to a given excitation $\delta W\,(t)$ can be estimated from the frequency response $\chi\,(\omega)$. The overall agreement

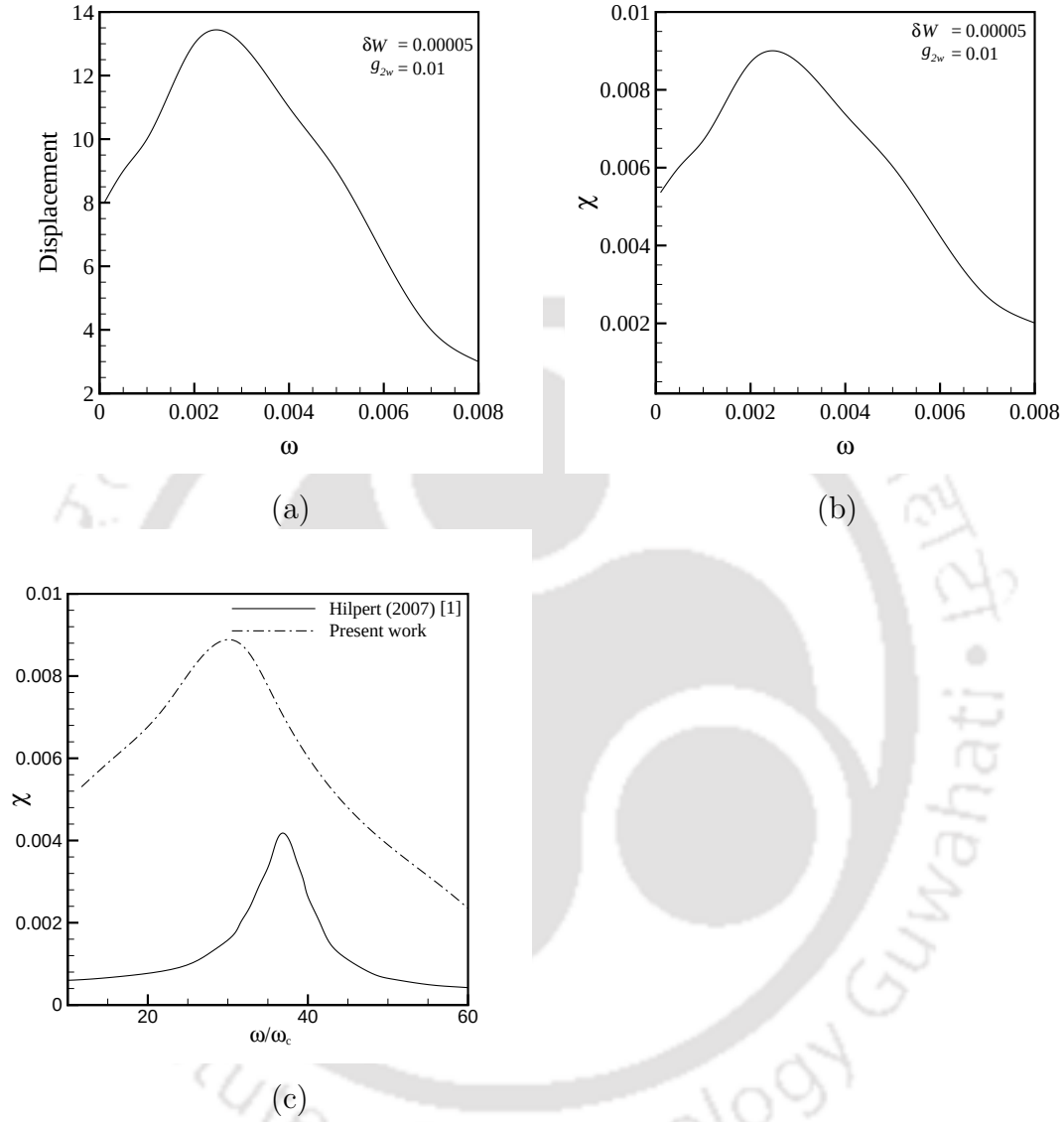

Figure 6.2: Effect of frequency on the blob with pinned contact lines in a sinusoidal channel (a) variation of displacement, (b) frequency response of the blob for acoustic excitation, (c) comparison of frequency response of the blob displacement in 3-D duct with that of Hilpert [1]

in the trend between the simulation results and that of Hilpert [1] is good (see Fig. 6.2 (c)), although the present study is done for three dimensional geometry whereas Hilpert [1] has performed LB simulation for two dimensional domain. The simulated resonant frequency is quite near to the predicted one by Eq. (6.4) given by Hilpert [1]. The deviation between the value of displacement δx and frequency response χ of our results and that of Hilpert [1] is likely due to the amplitude of force and the geometry they used (see Fig. 6.2 (c)). The characteristics frequency ω_c found from Eq. (6.6) is 0.000184. It can be seen that for resonant frequency $\omega = \omega_0 = 0.0026$, the mean displacement is maximum. The non dimensional resonant frequency X_0 is 14.24 for $g_{2w} = 0.01$. For the frequencies more than resonance frequency, the mean displacement of the blob decreases and becomes steady for very high frequencies.

6.4.2 Effect of capillary number on resonance behavior of two-phase flow

The equilibrium shape of meniscus of the liquid in contact with the solid surfaces is determined by the balance of capillary forces by acoustic excitation in the face of the wetting properties of the liquid/solid/gas system. This wettability-capillarity interaction governs the displacement behavior of two-phase flows. The extent to which the blob oscillates depends on the frequency and the amplitude of force δW, wettability of the surface, geometry and the capillary number. Also, at resonance the displacement is found to be maximum. Hence, it would be interesting to understand the resonance behavior of the trapped blob on differently wetted surface for various capillary numbers. It is well known that the capillary number is a measure of the relative importance of viscous and surface tension forces. For a given magnitude of acoustic excitation (δW), we defined the capillary number (Ca) $= \frac{\rho_2 V \delta W}{\sigma h}$, where ρ_2 indicates the density of non wetting phase and V is the volume of the trapped blob. The surface tension (σ) depends on viscosity and wettability and is actually indicative of the work of deformation required for the trapped blob to move through the narrow necks of pore channels. It may be noted that different capillary numbers are obtained by changing δW. Different flow regimes can be observed depending on the capillary number [152]. For very low Ca, the displacement is governed by the heterogeneity of the capillary pressures along the interface [152, 153] which results into capillary fingering regime. For high Ca values, the viscous forces overcome capillary

effects. This results into a viscous fingering regime with a rapid breakthrough of the non wetting fluid into the wetting fluid. Figure 7.10 (a) shows the displacement of the blob for various capillary numbers for the frequency close to the resonance frequency i.e., $\omega = 0.003$. The blob oscillates about its mean position in a periodic manner (see Figs. 7.10 (a) and 6.4 (c)-(d)) and displacement of the blob increases with capillary number. Contour plots as shown in Figs. 7.10 (c)-(e) also reiterates the same fact.

6.4.3 Effect of wettability on the response of the blob

In this section, the effect of wall wetting characteristics on the blob dynamics of pinned as well as sliding contact line is discussed. It is well known that wettability is the indication of the ability of one fluid to spread on a solid surface and form a wetting film [139]. The nature of wettability influences displacement of fluid to a large extent, for example in the oil extraction from the rocks. Also, the pattern of wettability varies depending on the nature of surface, fluid in contact [140]. For instance, the angles of contact for water-wet, neutrally-wet and oil-wet configuration are less than, close to and larger than $\pi/2$ respectively. Kovscek et al. [154] proposed a model which considers the variation in surface wettability of the rock by direct contact of oil. It is assumed that porous medium is filled with water i.e., water wet prior to invasion of oil. The formation of thin film of water once oil enters into the pore prevents direct contact of oil with the solid surface. However, this film can collapse at threshold capillary pressure resulting in direct contact of oil into solid surface thus changing wettability. Hence, the influence of wettability on response of the blob is studied here in detail. Figures 6.4 (a)-(b) show more displacement and χ for the hydrophilic surface with $g_{2w} = -0.01$ as compared to hydrophobic surface with $g_{2w} = 0.01$ for pinned configuration. This is primarily owing to the tendency of liquid to wet on hydrophilic surface leading to more deformation and bending of meniscus. Highly wetting surface $g_{2w} = -0.02$ (see Fig. 6.4 (c)) shows greater displacement and χ in comparison to weakly wetting surface $g_{2w} = -0.01$. The same holds true in case of strongly hydrophobic surfaces as shown in Fig. 6.4 (d). Thus we can conclude that the strength of wettability also determines the extent of displacement.

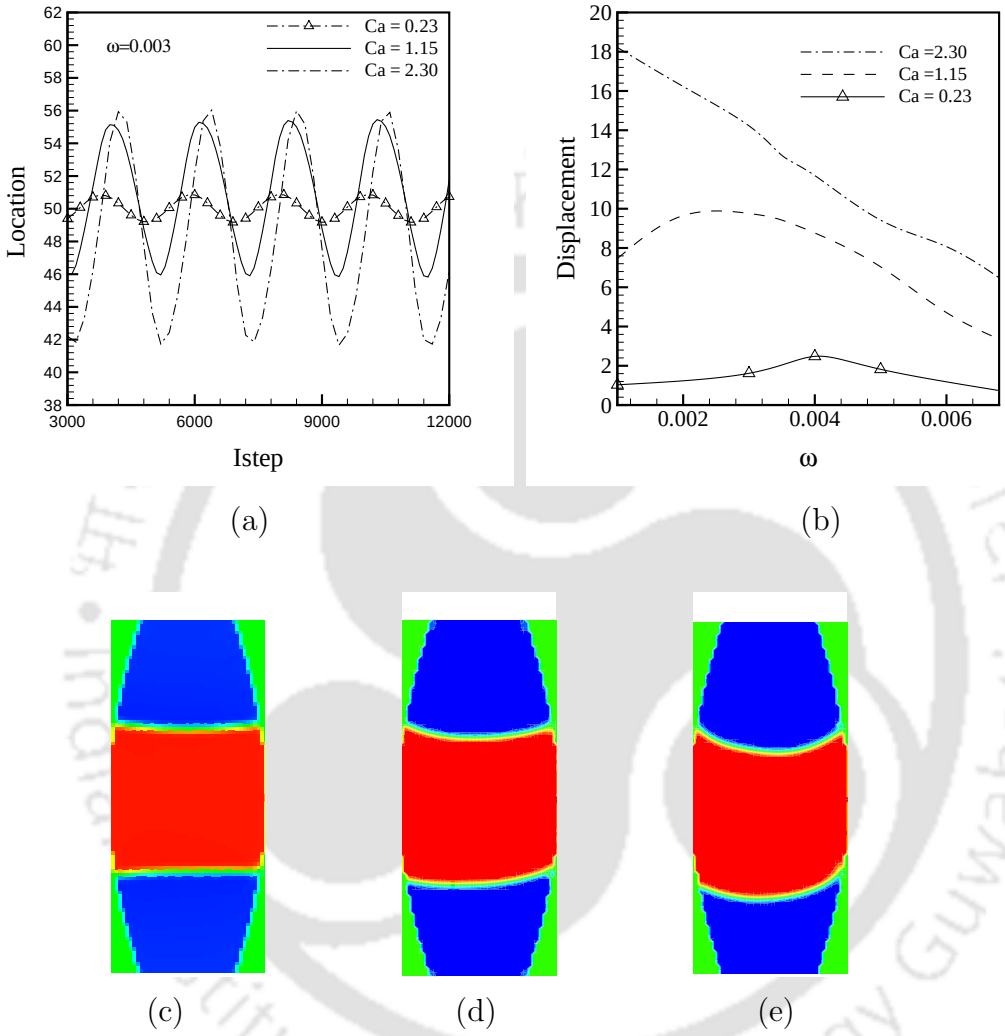

Figure 6.3: Effect of capillary number: (a) variation of displacement for $\omega = 0.003$, (b) frequency response of the blob, (c) snapshots of the blob at time step = 1800 for Ca = 0.23, (d) snapshots of the blob at time step = 1800 at Ca = 1.15, (e) snapshots of the blob at time step = 1800 at Ca = 2.30

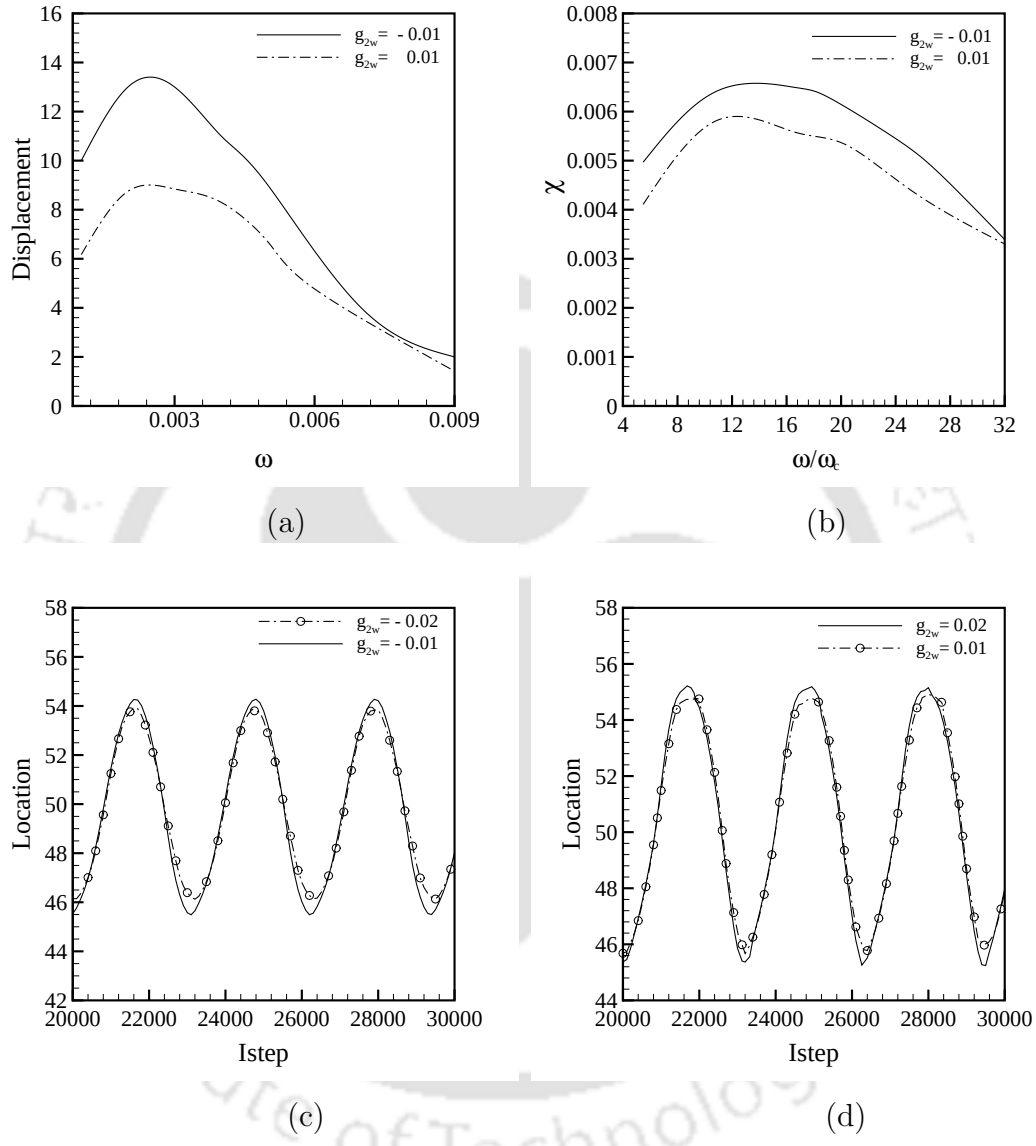

Figure 6.4: Effect of wettability: (a) displacement of the blob, (b) frequency response of the blob, (c) Dynamic behavior of the blob for hydrophilic surfaces, (d) Dynamic behavior of the blob for hydrophobic surfaces

6.4.4 Effect of mixed wettability on the response of the blob

This section explores the behavior of blob on the surface with mixed wettability which is a common characteristics in the case of rock oil reservoir. The blob is so placed that the meniscus has same wettability on either side (see section 3.3.4 for schematic). It has been found that the blob displaces to a lesser extent for the surface with mixed wettability as compared to the surface with uniform wettability (see Fig. 6.5 (a)). This happens due to varying contact angle in differently wetted region. Figure 6.5 (b) shows that the nature of the response of the blob is similar both for pinned and sliding contact line configuration in case of mixed wettability. However, displacement is centered around initial pinned location for pinned configuration as compared to sliding contact configuration where meniscus follows the moving contact line. This results in offsetting the displacement from initial position. Effect of frequency on the displacement and frequency response (χ) for mixed and uniform wettability is shown in Fig. 6.5 (c).

It can be observed that the peak displacement occurs at around $\omega = 0.0035$ for mixed wettability i.e., at relatively lesser frequency as compared to uniform wettability. The same behavior is seen for the frequency response χ as shown Fig. 6.5 (d). Hence, it can be concluded that resonance frequency changes with wettability and the change is less for the surface with mixed wettability as compared to the surface with uniform wettability.

6.4.4.1 Effect of capillary number for different wettability configuration

The wettability of two immiscible fluids for a given surface is a crucial factor which determines the shape of menisci and also the displacement. Hence, study is undertaken to understand the resonance behavior at differently wetted surface for Ca = 0.23, 2.30. The contour plots in Fig. 7.11 are plotted at resonance frequency $\omega = 0.003$ for a range of surface wettability. It has been seen that deformation/bending of the meniscus is more on hydrophilic surfaces i.e., $g_{2w} = -0.01, -0.02$ as compared to the hydrophobic surfaces (non wetting phase blob) i.e., $g_{2w} = 0.01, 0.02$. However, for surfaces with mixed wettabilities i.e., $g_{2w} = \pm 0.02, 0.05$, deformation is more as compared to the surface with uniform wettability. It may be noted that blob is so placed that meniscus lies in hydrophilic region where it tends to wet to a greater extent (see Fig. 4.15) and central portion of the blob is kept in hydrophobic region.

Also, it is interesting to note that the deformation is more for the surface with

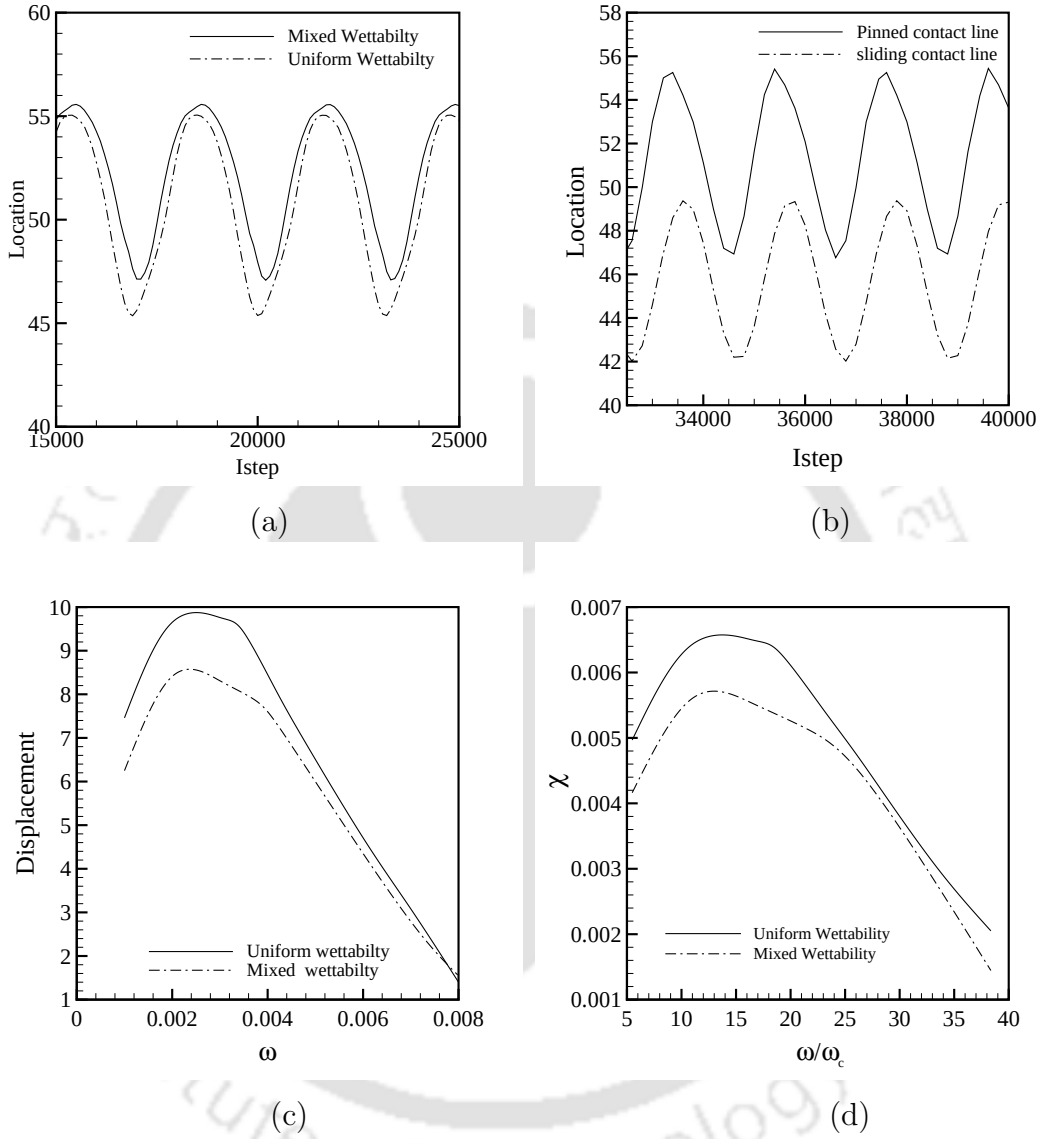

Figure 6.5: ((a)-(b) Comparison of dynamic behavior of the blob, (a) mixed and uniform wettability, (b) Comparison of dynamic behavior of the blob for pinned and sliding contact line configuration, (c)-(d) comparison of response of the blob for uniform and mixed-wet surface, (c) displacement, (d) frequency response.

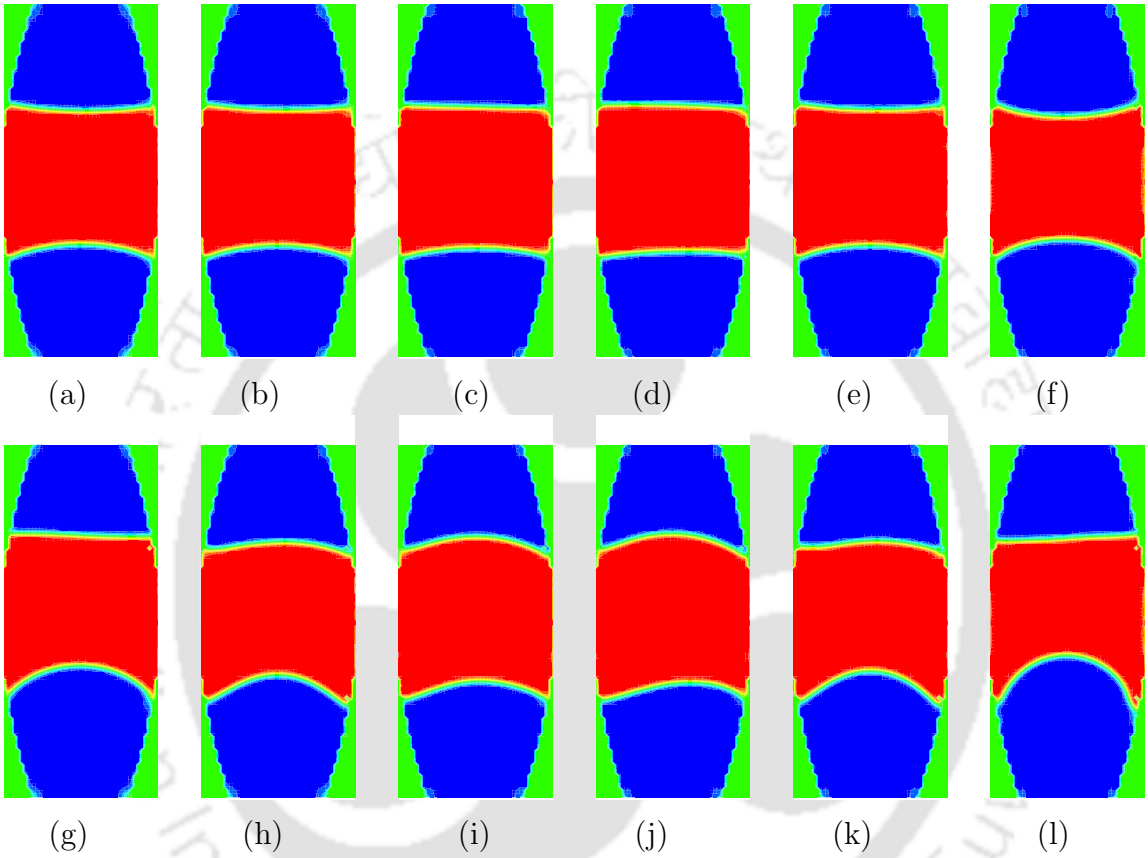

Figure 6.6: Behavior of the blob with pinned contact lines in a sinusoidal channel by acoustic excitation for different wettability configurations. Snapshots of the blob during excitation:(a)-(f) at Ca = 0.230 and (g)-(l) at Ca = 2.30, for g_{2w} = - 0.02, - 0.01, 0.01, = 0.02, ± 0.02, ± 0.05

$g_{2w} = \pm 0.05$ as compared to $g_{2w} = \pm 0.02$. This is quiet obvious since the alteration in wettability is higher in case of $g_{2w} = \pm 0.05$, so that when blob enters the hydrophilic strip/region with $g_{2w} = -0.05$ (see Figs. 7.11 (k)-(l)), the strong wetting tendency stretches the meniscus leading to more bending of the meniscus. The effect of capillary number can also be adjudged for the surface with different wettability configurations in terms of amount/magnitude deformation of the blob meniscus. The deformation of meniscus and the mean displacement are greater for higher capillary number.

6.4.5 Capillarity wettability interaction

A generic capillarity-wettability interaction can be best summarized by surface plots as shown in Fig. 7.12. The wettability dependence of the blob displacement is manifested for different capillary numbers for a range of frequencies. It can be safely argued that peak displacement occurs at the resonance frequency i.e., $\omega = 0.003$ (see Fig. 7.12 (a)). However, at higher capillary number for example, Ca = 2.30, the system shows overdamped behavior showing greater displacement throughout the range of frequency (see Fig. 7.12 (b)). The driving force dominates the effect of wettability of the surface. Hence, it can be stated that wettability tends to be more effective particularly at lower capillary numbers and use of resonance frequency can be of great help for greater displacement. This result could be very useful while dealing with mobilization of the trapped blobs.

6.4.6 Effect of width on the response of the blob

The thickness of the blob should be much shorter than the wave length of sound at an excitation frequency (ω) to satisfy the assumption of incompressibility [1]. Again the thickness of the blob L_n is taken such that $L_n \ll R$ so that the velocity field in the blob can be approximated by that in an infinitely long channel [86]. The width of the channel largely influences the viscous pressure drop. Viscous drop at the center will be lesser for higher width. In order to understand the influence of width on the displacement of the same volume of the blob, simulations are run for various values of width ($R = w/2$).

It can be seen from Figs. 6.8 (c)-(d) that for higher width, the displacement of the blob is more. However, the maximum χ value decreases as seen in Fig. 6.8 (b)

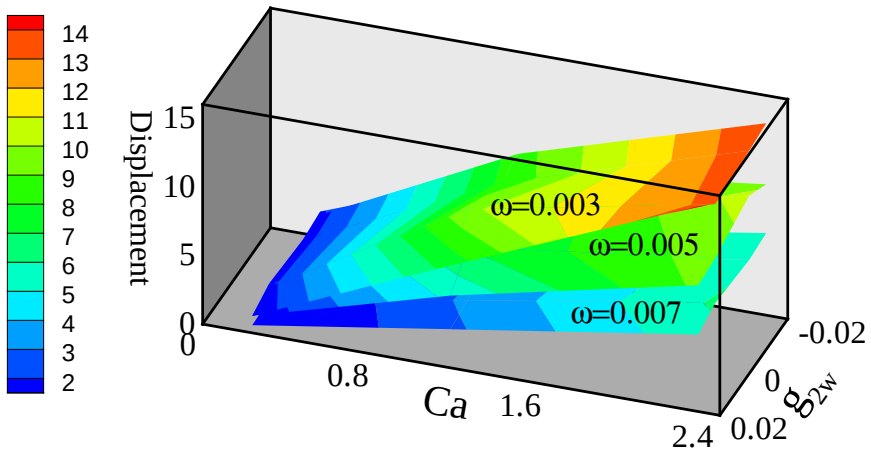

(a)

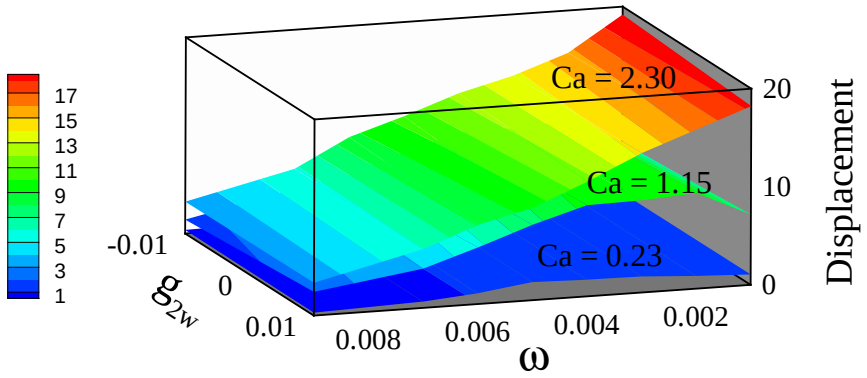

(b)

Figure 6.7: Capillarity wettability interaction for (a) $\omega = 0.003, 0.005, 0.007$, (b) Ca = 0.23, 1.15, 2.30

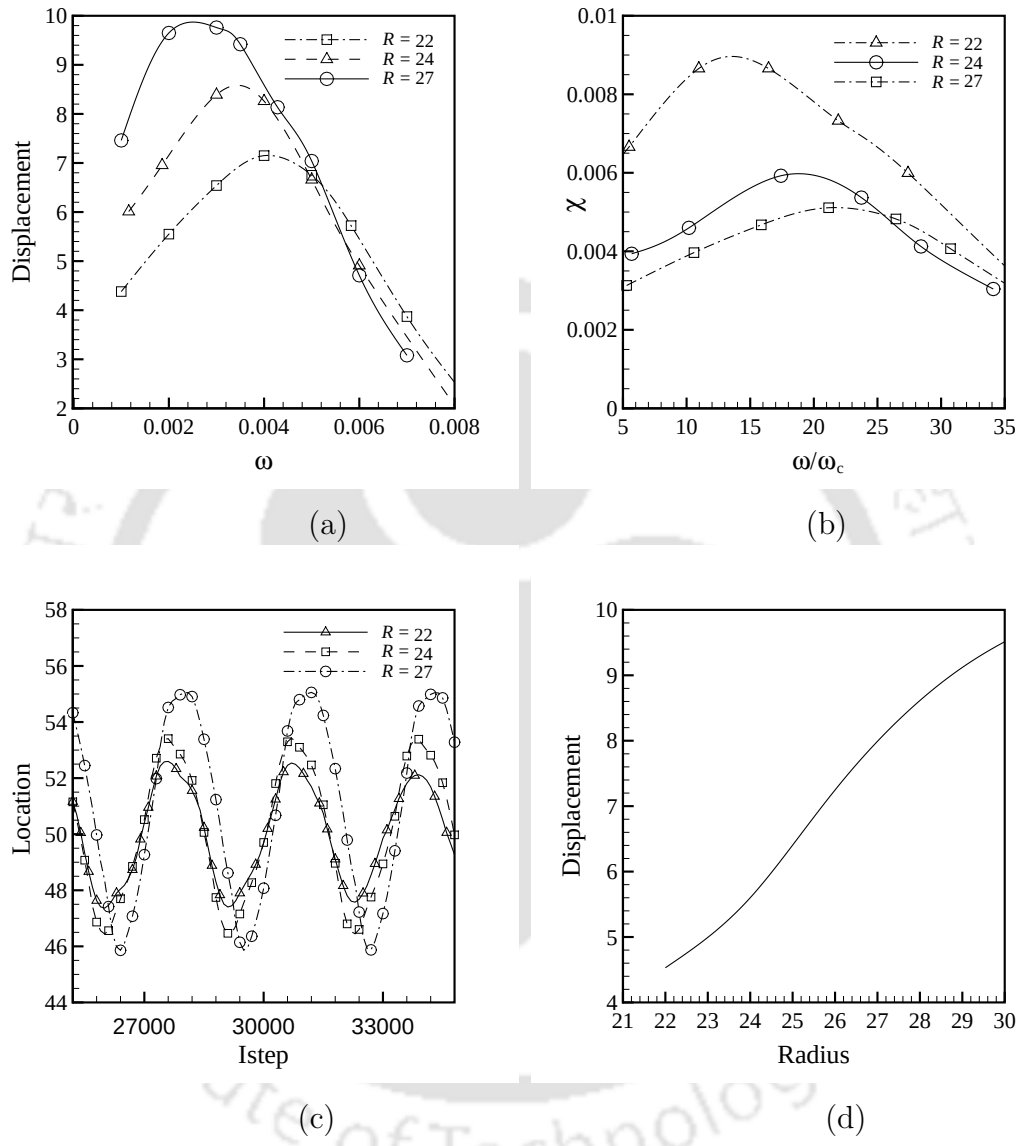

Figure 6.8: Effect of width on the response of the blob: (a) Displacement of the blob for a range of frequencies, (b) Frequency response of the blob, (c) Dynamic response of the blob for $\omega = 0.002$, (d) Variation of displacement for a range of width

since the value of χ is inversely proportional to the R^2(see Eq. (6.4)). So overall effect is that the displacement increases with the width but frequency response χ (see Fig. 6.8 (b)) decreases at the same time. Also, the shift in the value of frequency ratio $\frac{\omega}{\omega_c}$ at which the peak value of displacement or χ occurs can be observed. Also, for higher width the maximum value for displacement (see Fig. 6.8(a)) is observed at relatively lower frequency. It can be observed that for maximum value of frequency response, χ occurs at relatively higher frequency ratio (see Fig. 6.8 (b)). This could be very useful in estimating the displacement of the blob for network of pores where the width may vary from one location to the other.

6.4.7 Mobilization of trapped blobs

It is well known that irregular geometry provides more opportunities for the blob to be trapped than the simple-shaped channels. Also, the net displacement of the blob depends on how often the blob gets trapped because of the obstruction in the network of pores. Hence, it would be interesting to gain some more insight on the mobilization of the trapped blobs. In this context, investigation of the hypothesis that capillarity induced resonance can be exploited to mobilize blobs trapped in the sinusoidal pore channel is done. First, the numerical experiments are done to find out the frequency at which the blob shows maximum response. The blob as shown in Fig. 8.2 (a) is subjected to acoustic excitation $\delta W = \sin(\omega t)$ for a range of frequencies. The maximum displacement of the blob is found at around $\omega_{max} = 0.003$. Then, the blob is excited at selected frequencies ω_n ranging from 0 to 1.5 ω_{max} with a body force $W(t) = W(0) + \ deltaW \sin(\omega t)$. It may be noted that amplitude δW is varied such that mobilization has occurred for a small number of excitation frequencies ω presumably close to ω_{max}. It is found that the mobilization has occurred for $W(0)$ = 0.000046 and δW = 0.000006. Figure 8.2 shows the snapshots of the simulations for the blob at steady state for ω = 0.001 and 0.003. It can seen that for ω = 0.001, no mobilization has occurred. The head (top) meniscus, undergoes drainage and passes the pore throat. However, the blob gets trapped since the tailing (bottom) meniscus (undergoing imbibition) is stuck in a wide portion of the pore space(i.e., pore body). This demonstrates that the blob oscillates around the equilibrium state (see Fig. 6.10 (a) when it is excited at the frequency well below the resonant frequency ω_{max}. However, the blob moves a significant distance when excited at ω = 0.003 (close to ω_{max}) as shown in Fig. 6.10 (b). The blobs tailing meniscus

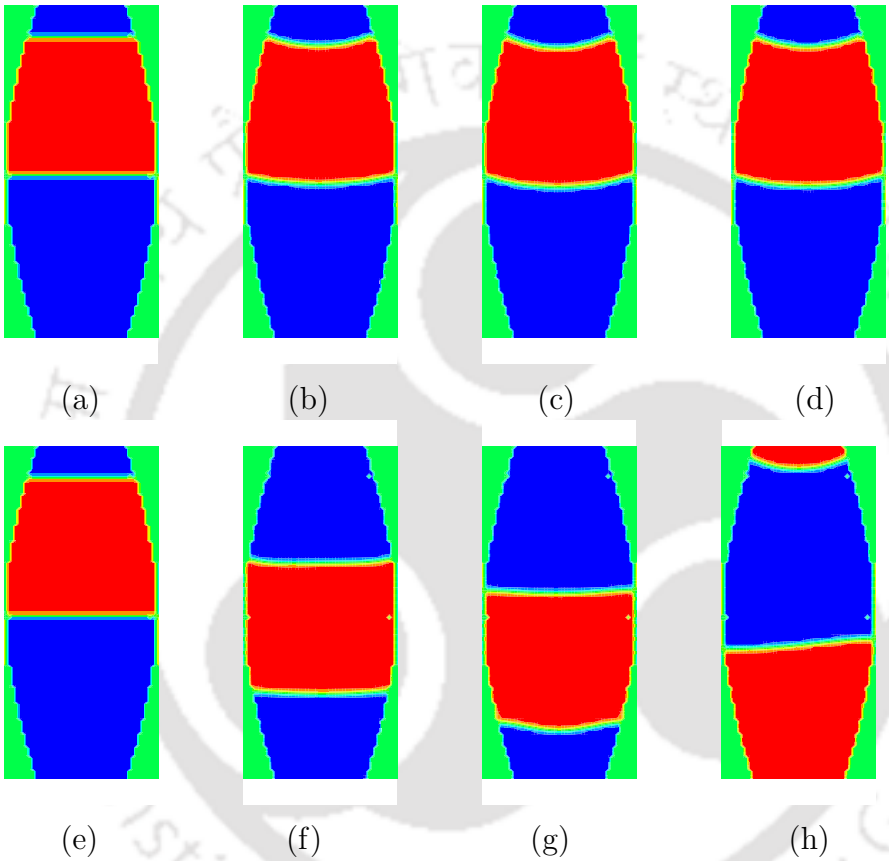

Figure 6.9: Snapshots of mobilized blob (a)-(d) at $\omega = 0.001$ and (e)-(h) at $\omega = 0.003$ for time step = 0, 12000, 13200, 16000 respectively

passes the pore body (see Fig. 8.2 (e)-(h)). To ascertain that whether mobilization occurred, the mean blob position is quantified by the time-average value of $z(t)$ during the last excitation cycle, z for all values of ω as shown in Fig. 6.10 (c).

The filled symbol shows mobilization. The frequency response χ of the blob is very high as expected for the value of ω near to ω_{max}. One can see that the blob moved a significant distance at a frequency close to ω_{max} and the trailing meniscus passes the pore body. It is observed that mobilization occurred for only a few excitation frequencies ($\omega = 0.0026$ and $\omega = 0.003$), both of which are close to ω_{max}. The blob is displaced by around 13 lattice units. Also, it can be seen that a net displacement i.e., mobilization of the blob has only occurred for a few frequencies, which are very close to ω_{max}. These results support the hypothesis that blob can be optimally mobilized by excitation at its resonant frequency. or

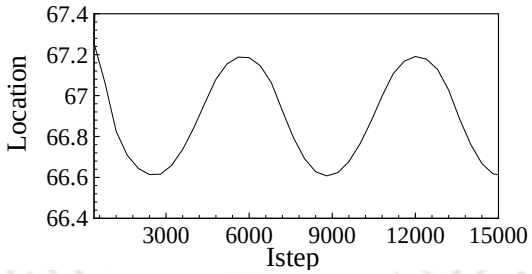

(a)

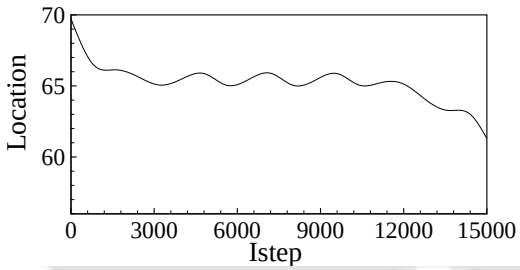

(b)

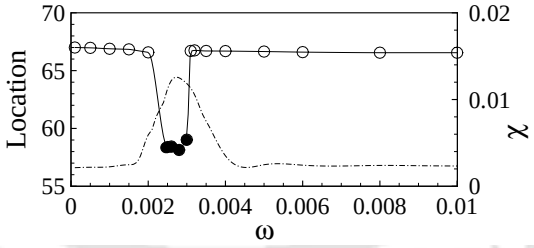

(c)

Figure 6.10: Mobilization of a blob in a sinusoidal pore channel: (a) excitation at ω = 0.001, (b) excitation of the blob at ω = 0.003, (c) mean blob position during the last excitation cycle at various values of ω

6.5 Closure

The response of the blob in the sinusoidal channel to an oscillatory force by the lattice Boltzmann method is simulated. The effect of the parameters like wettability of the surface, frequency, capillary number on menisci oscillation and consequently on the displacement of the blob is studied. Results of numerical experiments confirm the hypothesis that trapped blobs can be mobilized using capillarity induced resonance. The mobility of the blob reduces for the surfaces with mixed wettability as indicated by less displacement as compared to the surface with uniform wettability. It has been observed that the mobilization of the blob is governed by the nature of geometry i.e. curvature of surface. The blob trapped in domain with varying cross section shows less mobilization as compared to the one with uniform cross section for the same input conditions. The study on combined effect of wettability and geometry reveals that mobilization is more for hydrophobic surface on the geometries with uniform cross section. However, effect of geometry and wettability would not be so significant at high capillary number. It can be concluded that the excitation of a trapped blob near to its resonant frequency leads to a net displacement of the blob. In this context, an optimal excitation strategy might be significant in mobilization of residual non wetting phase in channels or real porous networks that these simple models represent.

Chapter 7

Mesoscopic Analysis of Blob Dynamics in a Tube with Varying Radius

7.1 Introduction

The displacement of the trapped blob is governed by the nature of geometry as discussed in earlier chapter since the shape of the geometry controls the nature of entrapment opportunities, magnitude of excitation and resonance frequency which in turn affect the mechanism of blob mobilization. The displacement is observed to be large for the polygonal and sinusoidal pore channels as compared to the channel with disc packing [1]. The understanding the fluid flow phenomena when it comes to the tortuous paths of rock pores, packed beds and lung bronchioli makes it even more complex as compared to that of a single straight tube. The process of mobilization of trapped blob is entirely different in case of varying cross-sectional geometry and an insight into the mechanism of mobilization may be useful in optimally utilizing the phenomenon of capillarity induced resonance. Hence, the effect of wettability coupled with capillarity induced resonance on mobilization of the trapped non wetting phase blob in a tube with varying constriction is studied.

7.2 Problem Specification

The objective of the present work is to simulate the displacement of the blob to bolster our understanding about the effect of physicochemical parameters like wettability, geometry and capillarity induced resonance on physical mechanism of mobilization. The dimensions of the computational domain (see Fig. 7.1) are as given in Table 7.1. The S-C model here considers the system with two immiscible fluids

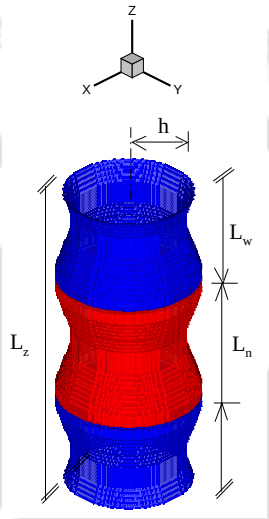

Figure 7.1: Computational domain showing non wetting phase blob in a tube with varying radius with periodic boundary conditions

in which blob (fluid 2) is placed in the domain filled with displacing fluid (fluid 1). The blob is initially placed in the center of the domain at $z = 50$. The motion of the blob is induced by a sinusoidal acoustic force along the negative z-direction. The dynamics of the blob was explored based on thickness of the blob, frequency applied, nature of the wettability using S-C lattice Boltzmann Model. No slip boundary condition is applied at the walls in x- and y-direction whereas the periodic boundary conditions are applied in z-direction. The transient force applied on the blob can be expressed as given below.

$$W(t) = W(0) + \delta W \sin(\omega t) \tag{7.1}$$

where $W(0)$ and $\delta W \sin(\omega t)$ are constant body force and perturbation respectively.

Table 7.1: Parameter values used to study the fluid flow through varying radius tube

Parameter		Value
Length of the tube (l)		100
Radius of the tube at inlet and outlet (h)		20
Maximum radius of the tube(h_{max})		24
Density of fluid1		0.035
Density of fluid2		0.965
Relaxation time of the wetting phase τ_1		0.80
Relaxation time of the non wetting phase τ_2		0.80
Fluid-fluid interaction parameter	$g_{11} = g_{22}$	0
	$g_{12} = g_{21}$	0.1

7.3 Results and Discussion

7.3.1 Dynamic response of the blob

In order to get insight on the dynamic behavior of the blob, the mean displacement of the blob for a range of excitation frequencies was analyzed. It is evident from the contour plot shown in Fig. 7.2 (a)-(c) that blob oscillates under the influence of acoustic excitation ($\delta W \sin(\omega t)$). It can be observed that the meniscus follows the flow by varying its radius of curvature [70]. The meniscus deformation largely depends on the volume ΔV of the trapped blob and motion of the contact line. It is noteworthy that the contact line may remain microscopically pinned for certain value of ΔV beyond which motion of contact line may occur. Charlaix and Gayvallet [85] have described the range of volume in this context. The variation of displacement of blob with respect to time is plotted for the surface with wettability $g_{2w} = 0.01$ for a pinned contact line at $\omega = 0.0035$ and amplitude of force $\delta W = 0.0001$. It can be seen from the Fig. 7.2 (d) that the meniscus of the blob oscillates about its mean position periodically. The period of oscillation depends on the frequency used. However, the amplitude of oscillations is governed by the parameters like

amplitude of force, wettability of the surface and geometry. Figure 7.3 shows the frequency response in which the blob was excited by an acoustic excitation $F_{3k} = \delta W \sin(\omega t)$, where the ω is discrete excitation frequencies ranging from 0 to 1.5 ω_0. The force amplitude is $\delta W = 0.00005$ and the characteristic frequencies of both the fluids are taken equal i.e., $\omega_{cn} = \omega_{cw}$. The lengths of the wetting phase slug and non wetting phase slug is 60 and 40 lattice units respectively. The χ values are estimated from Eq. (6.9). The frequency response $\chi(\omega)$ can be useful to calculate the temporal response to a given excitation $\delta W(t)$. Figure 7.3 shows the mean displacement about the equilibrium position for various frequencies (ω). First, the characteristic frequency ω_c found from Eq. (6.6) is 0.00025 which is used for all the simulations unless otherwise explicitly mentioned. It can be seen that at resonant frequency $\omega = \omega_0 = 0.0035$, the mean displacement is maximum. The non dimensional resonant frequency X_0 is 15 for $g_{2w} = 0.01$. For the frequencies more than resonance frequency, the mean displacement of the blob gradually reduces and becomes steady for very high frequencies.

7.3.2 Effect of force on the response of the blob

In order to study the influence of force on the response of the blob, the simulations were performed for two different amplitudes of the force $\delta W = 0.0001$ and 0.00005 for the same configuration. It can be observed that displacement of the blob was found to be greater for $\delta W = 0.0001$ as compared to $\delta W = 0.00005$ which is quiet obvious and physical also. The variation of χ is also plotted over frequency ratio $\frac{\omega}{\omega_c}$ which re-confirms the similar behavior. Figure 7.4 depicts that χ reduces with increasing frequency so also the displacement. It may be noted that although the nature of variation of χ is same however, the magnitude is more for $\delta W = 0.0001$.

7.3.3 Effect of damping on the response of the blob

The damping of the fluid has considerable effect on the dynamics of the blob. The magnitude of damping changes with viscosity of the fluid. Hence, the simulations were performed with various values of viscosity. Figure 7.5 shows the underdamped and overdamped system keeping all other parameters constant. It can be seen that the system exhibits the overdamped character for the applied frequency more than that of characteristic frequency w_c. It may be noted that the relaxation parameter

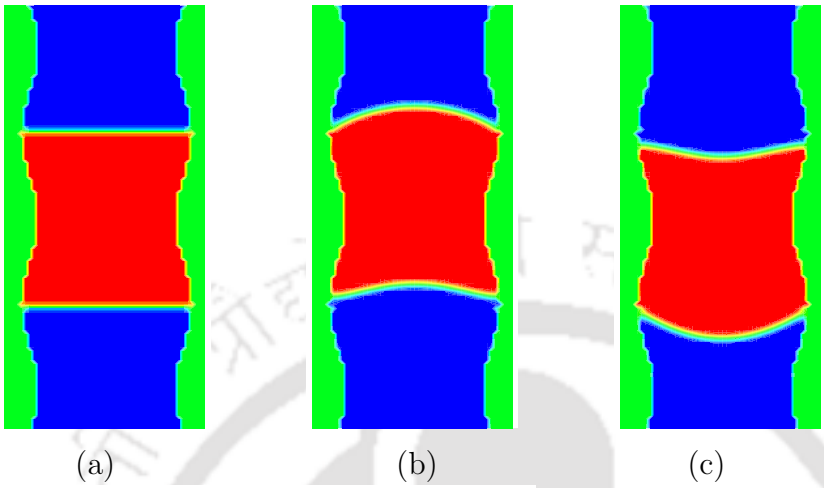

(a) (b) (c)

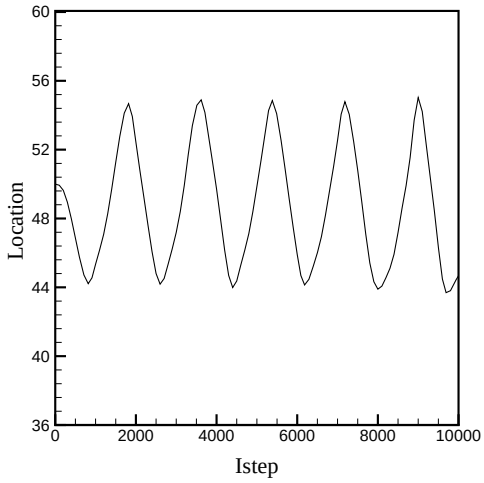

(d)

Figure 7.2: LB simulation of excitation of a blob with pinned contact lines by an oscillatory body force. Three snapshots of the blob during excitation at istep (a) 0, (b) 3600, (c) 4400 for $g_{2w} = 0.01$ at $\delta W = 0.0001$, (d) periodic oscillation of the meniscus for $\delta W = 0.0001$ at $\omega = 0.0035$.

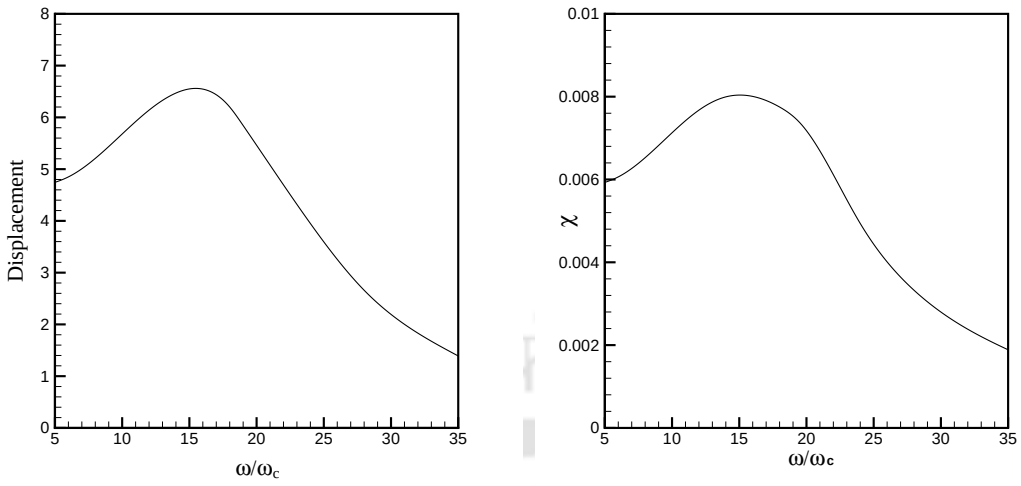

(a) (b)

Figure 7.3: Effect of Frequency (a) variation of displacement of the blob (b) frequency response with pinned configuration

τ determines viscosity which in turn decides the characteristic frequency. For ν = 0.1 and = 0.166, the characteristic frequencies are around 0.00025 and 0.0004 respectively. The non-dimensional resonant frequency X_0 is 8.75 for $\nu = 0.16$ whereas $X_0 = 14$ for $\nu = 0.1$. This indicates that for the frequencies corresponding to $X_0 > 8.75$, the system with $\nu = 0.16$ behaves like overdamped system whereas system with $\nu = 0.1$ shows underdamped character. Keeping all conditions being equal, it is expected that adding viscosity to the model increases the added resistive force. This in turn, increases the the threshold value of acceleration required to liberate a blob from its entrapped configuration. Thus, the fluid with more viscosity makes the system overderdamped.

7.3.4 Effect of radius on the response of the blob

In order to study the effect of radius on the displacement of the same volume of the blob, the simulations were done for various values of radius. For $\bar{R} = 24$ and 30, the characteristic frequency are around to be 0.00017 and 0.00011 respectively. It may be noted that the radius of the pore mainly affects the viscous pressure drop. The greater the radius the lesser will be viscous pressure drop at the center and hence,

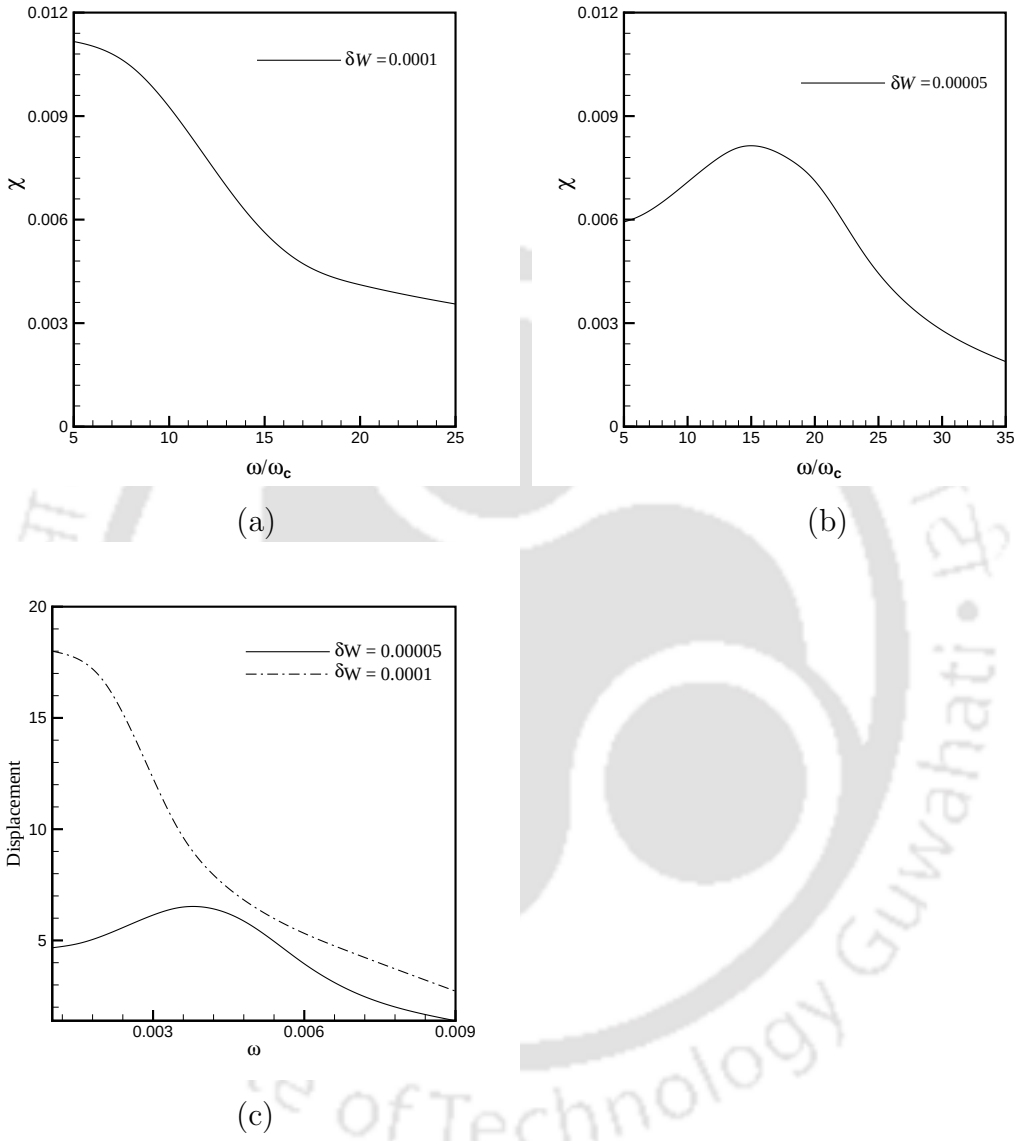

Figure 7.4: Effect of Force (a) frequency response for $\delta W = 0.0001$, (b) frequency response $\delta W = 0.00005$, (c) variation of displacement of the blob

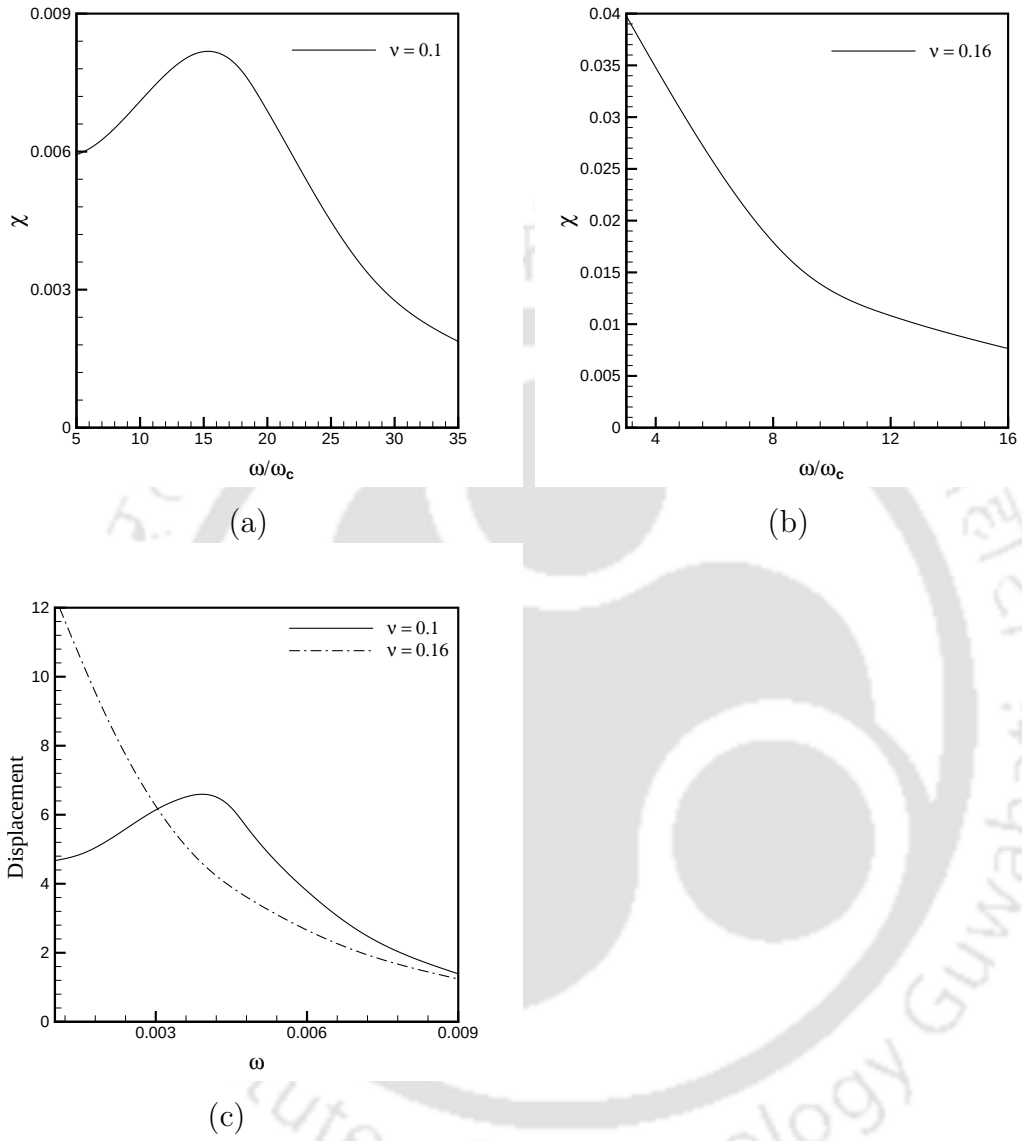

Figure 7.5: Effect of damping: Frequency response of an underdamped ($X_0 = 14$) and an overdamped($X_0 = 7.25$) blob with pinned contact lines (a) variation of displacement of the blob, (b) Variation of χ of the blob, (c) variation of $\frac{\chi}{\chi_{max}}$ with frequency

the greater displacement (see Fig. 7.6 (a)). It is observed from Fig. 7.6 (c) that the mean displacement of the blob increases with radius. The maximum χ value reduces as shown in Fig. 7.6 (b) since the value of χ is inversely proportional to the $\bar{R}^2$ (see Eq. (6.4)). Although the displacement increases with the radius (see Fig. 7.6 (b)) χ value reduces. There is a shift in the value of frequency ratio $\frac{\omega}{\omega_c}$ at which the maximum value of displacement or χ occurs. It is observed that at higher radius the peak value for displacement occurs at relatively lower frequency ratio whereas for χ it occurs at relatively higher frequency ratio. This could be useful in predicting the displacement of the blob for network of pores where the radius may vary from one location to the other.

7.3.5 Blob response for sliding and pinned contact line

As mentioned earlier pinned contact lines is observed in natural porous media due to their surface roughness and chemical heterogeneities. This may result into stationary contact line even when it is subjected to an oscillatory flow. The motion of the blob is governed mainly by amplitude and frequency of the flow field. It may be noted that the sliding contact lines do not occur normally except in hypothetical case where contact line do not touch the defects of the surface i.e., the surface is fully covered by a liquid film. Three phase contact line is not seen for such system. As already known the meniscus follows the induced flow without any change in shape for sliding motion of the contact line [84]. However, this type of motion requires a sufficiently wetting surface. It may be noted that total force required to mobilize the blob must overcome the viscous forces and surface tension forces. Figure 7.7 shows the response of the blobs for pinned and sliding contact lines. As seen from Fig. 7.7 (a) the mean displacement of the blob for the $\omega = 0.0035$ for pinned surface is more as compared to sliding contact line surface. It can be safely adjudged that the system with pinned contact line shows underdamped character whereas system with sliding blob shows overdamped character (see Figs. 7.7 (b) and (c)).

7.3.6 Effect of wettability on the response of the blob

In this section, attempt is made to gain fundamental understanding about the effect of wall wetting characteristics on the blob dynamics on pinned as well as sliding contact line. As already known wettability indicates the ability of one fluid to

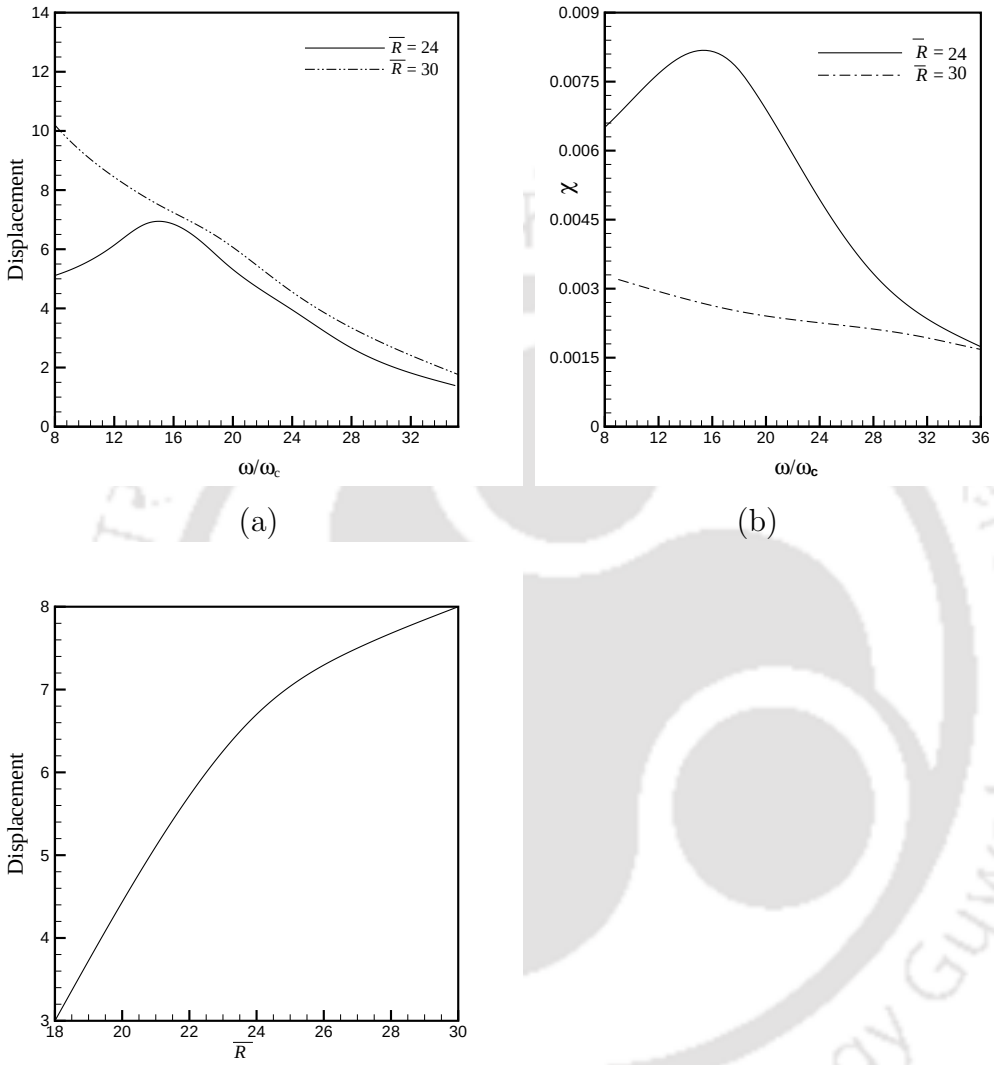

Figure 7.6: Effect of width (a) variation of displacement of the blob with frequency, (b) frequency response with pinned configuration, (c) variation of displacement of the blob with width

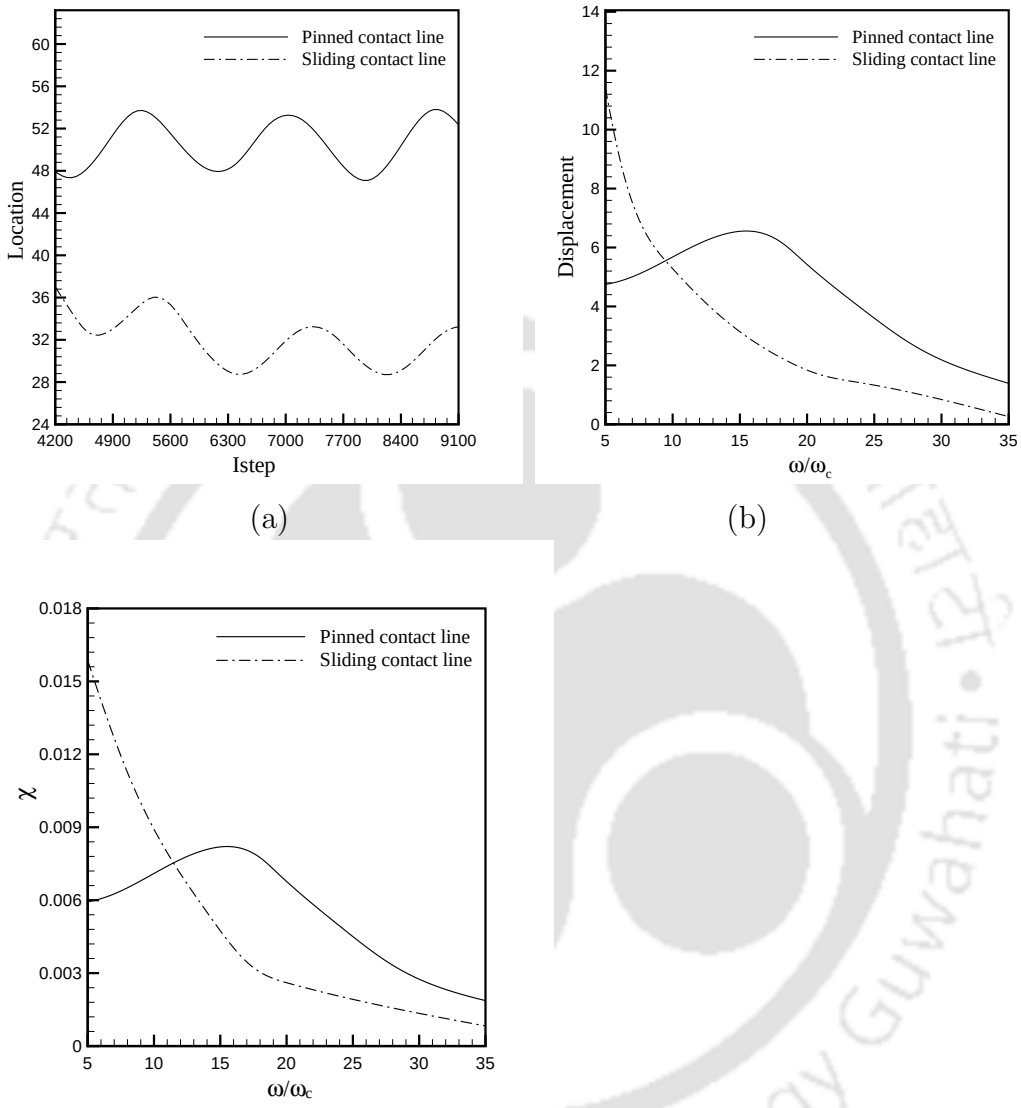

Figure 7.7: Comparison of the response of the blob for pinned and sliding contact line configuration: (a) displacement of the blob with time, (b) variation of displacement of the blob with frequency, (c) Frequency response for sliding and pinned configuration for $g_{2w} = 0.01$ and $\delta W = 0.00005$

spread on a solid and form a wetting film [139]. The nature of wettability affects the displacement of fluid to a great extent, e.g., in the extraction of oil from rocks. Moreover, the pattern of wettability changes depending on the nature of surfaces, fluids in contact [140]. For instance the contact angles for water-wet, neutrally-wet and oil-wet configuration are less than, close to and larger than $\pi/2$ respectively. Kovscek et al. [154] proposed a model which considers the change in wettability of the rock surface by the direct contact of oil. Porous medium is assumed to be filled with water and water wet prior to invasion of oil. As oil enters into it a thin film of water does not allow direct contact of oil with the solid surface. However, at threshold capillary pressure the film collapse which results in direct contact of oil into solid surface thus changing the wettability. Hence, the effect of wettability on response of the blob is studied in this section.

7.3.6.1 Effect of uniform wettability on the response of the blob

Figures 7.8(a)-(b) show greater mean displacement and χ for the hydrophilic surface with $g_{2w} = -0.01$ as compared to hydrophobic surface with $g_{2w} = 0.01$ for pinned configuration. Strongly wetting surface $g_{2w} = -0.04$ (see Fig. 7.8 (d)) shows less displacement and frequency response χ as compared to weakly wetting surface $g_{2w} = -0.01$. The same behavior is seen in case of strongly hydrophobic surfaces as shown in Fig. 7.8(c). This is due to the fact that flow in varying radius tube finds it difficult to mobilize because of sharp changes in wettability at the interface.

7.3.6.2 Effect of mixed wettability on the response of the blob

The blob response was explored for the surface with mixed wettability. The mixed wettability describes the varying wetting characteristics of the solid wall comprised of hydrophilic (HI) and hydrophobic (HO) regions. The blob was located in such a way that wettability on both side of meniscus is same for this study (see Fig. 7.9 (a)). It was seen that mean displacement of the blob was less for mixed-wet surface as compared to for the surface with uniform wettability (see Fig. 7.9 (b)). This is due to contact angle variation in differently wetted region. Figure 7.9 (c) shows that although the mean displacement for mixed wettability with pinned and sliding contact line is similar in nature, displacement for pinned configuration is centered around initial pinned location. However, the meniscus has followed the

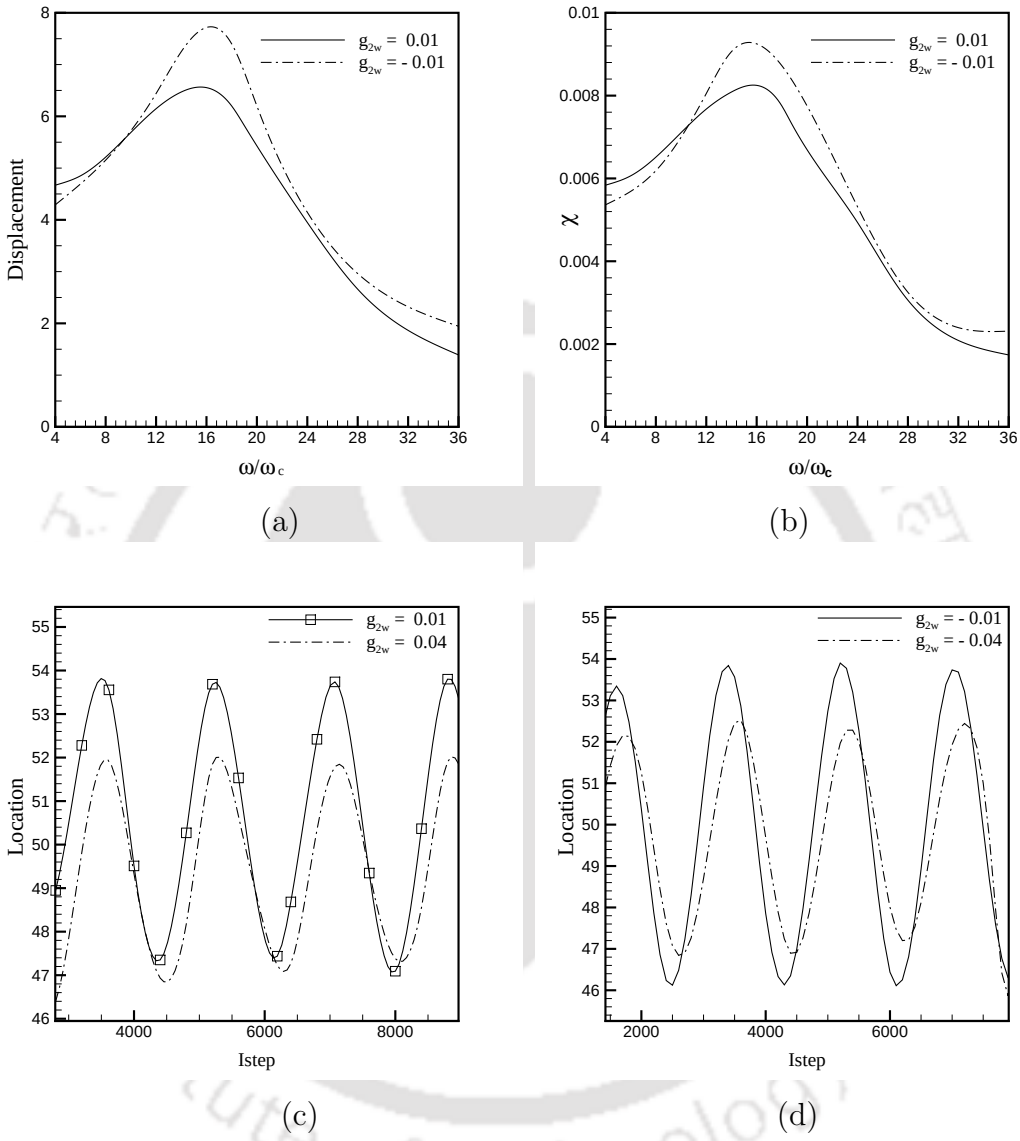

Figure 7.8: Effect of wettability on the response of the blob: (a) variation of displacement of the blob with frequency, (b) frequency response with pinned configuration, (c)-(d) effect of strength of wettability for: (c) hydrophobic surface, (d) hydrophilic surface

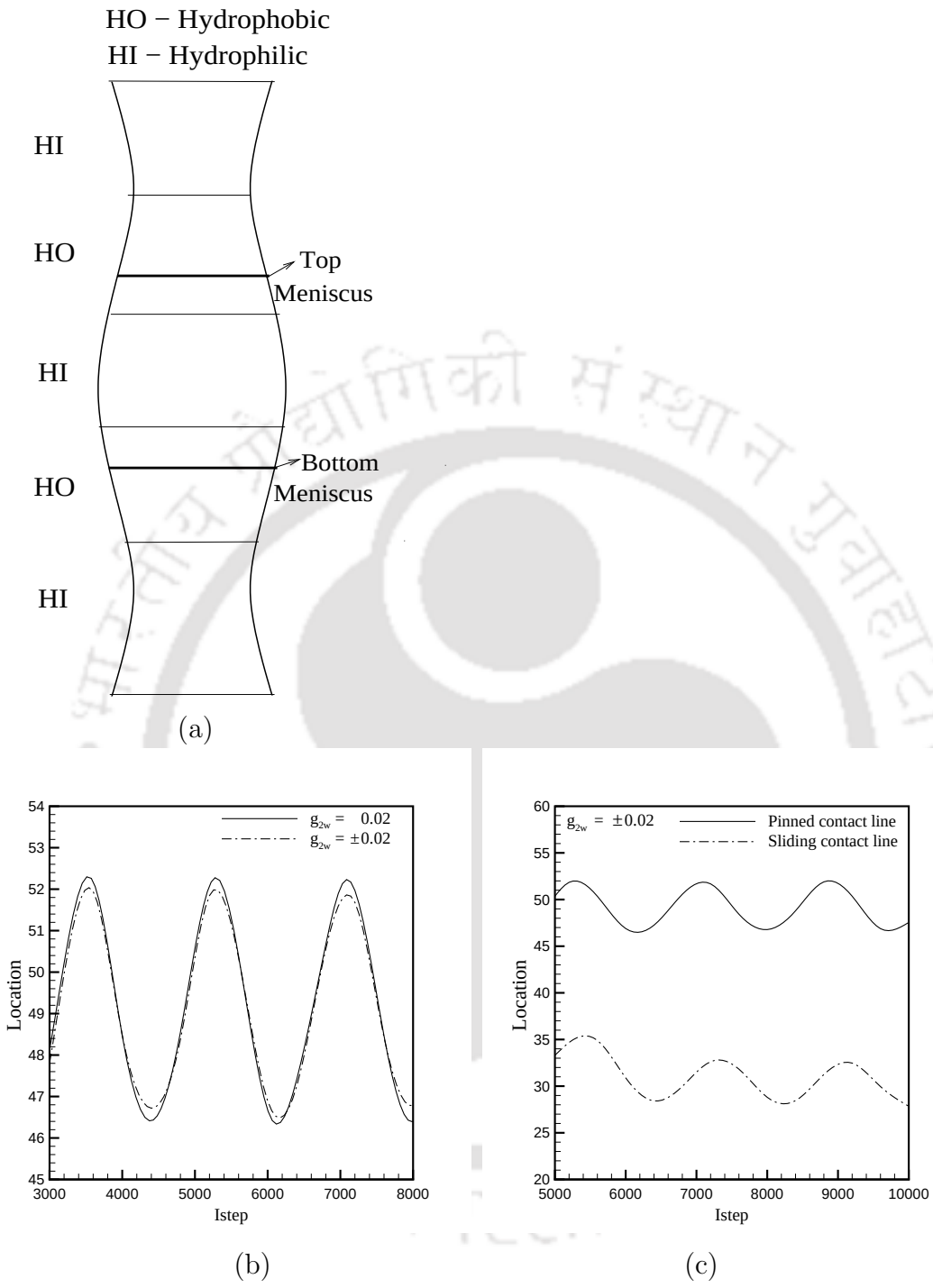

Figure 7.9: Effect of mixed wettability on the response of the blob: (a) schematic of the domain for mixed wettability surface, (b) effect of uniform and mixed wettability for pinned configuration, (c) effect of pinned and sliding contact configuration for mixed wettability surface

moving contact line in case of sliding configuration thus offsetting the displacement from initial position.

7.3.7 Effect of capillary number on the response of the blob

The shape of menisci of the liquid in contact with solid surface depends on the balance of capillary forces and acoustic excitation in the face of the wetting properties of the liquid/solid/gas system. Thus, wettability-capillarity interaction controls the displacement behavior of two-phase flows. It is very crucial to understand the resonance behavior of the trapped blob on the surface with different wettability for various capillary number which is novelty of this work. It may be noted that various capillary numbers are obtained by varying the δW, the magnitude of acoustic excitation. For a given δW, we determine Ca $= \frac{\rho_2 V \delta W}{\sigma h}$
where
ρ_2-density of non wetting phase
V-volume of the trapped blob
h-radius of the tube
However, the capillary number can also be varied by changing the blob size or the surface tension, but changing the magnitude of acoustic excitation force is the most convenient. Figure 7.10 (a) shows the displacement of the blob for different capillary number for the frequency near to the resonance frequency i.e., $\omega = 0.0035$. It can be observed that there is increase in the displacement of the blob from mean position with capillary number.

Figure 7.10 (b) also shows similar trend over the range of frequencies. At higher capillary number for instance Ca = 1.65 the system exhibits underdamped behavior whereas for Ca = 0.165, 0.825 the system exhibits the underdamped character showing peak displacement at around $\omega = 0.0035$. Contour plots (see Figs. 7.10 (c)-(e)) show the effect of capillary number keeping all other parameters constant. It can be observed that at higher capillary number, the deformation/bending of meniscus is more as compared to lower capillary number.

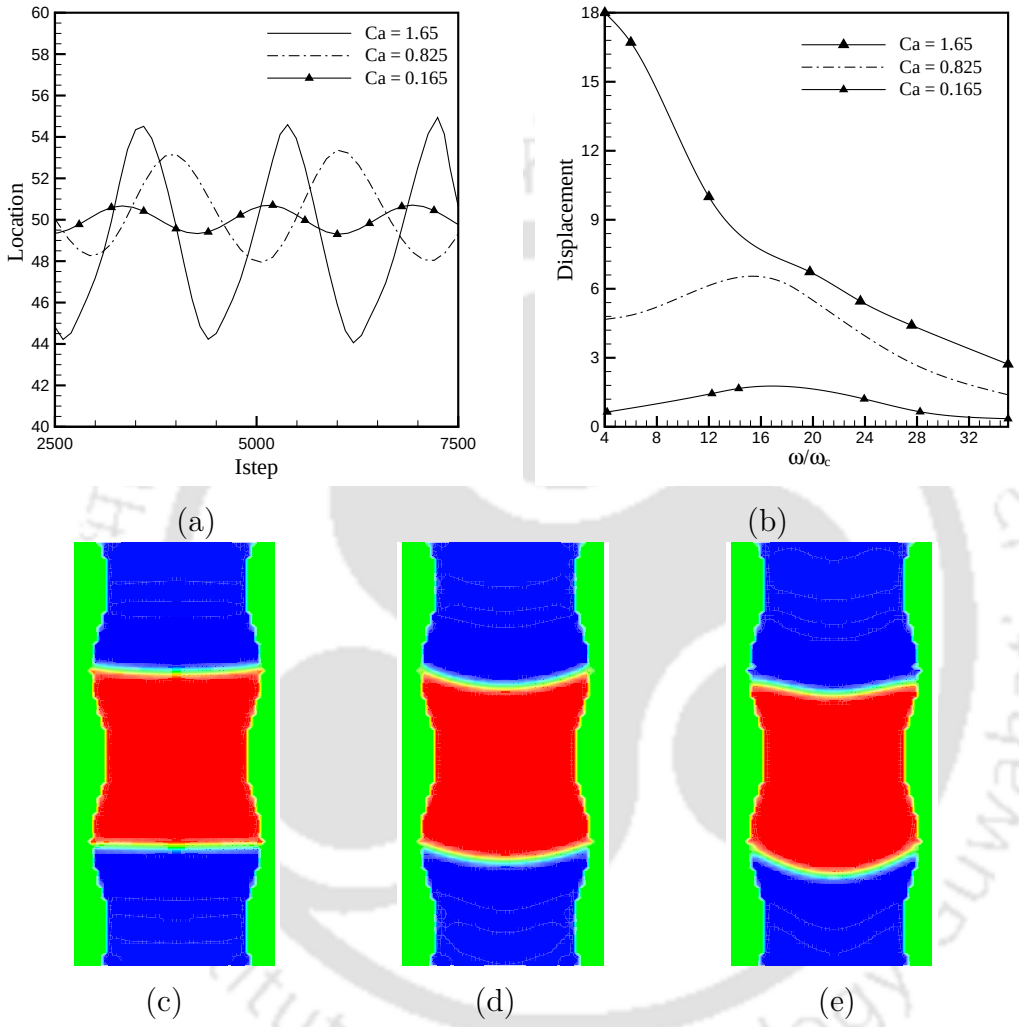

Figure 7.10: Effect of capillary number at $g_{2w} = 0.01$ (a) variation of displacement for $\omega = 0.0035$, (b) frequency response of the blob,(c)-(e) snapshots of the blob taken at time step = 4000 for Ca = 0.165, 0.825 and 1.65 respectively

7.3.8 Resonance behavior for different wettability configuration

The wettability of two immiscible fluids on a given surface is important factor which governs the shape of menisci and also the displacement. Hence, simulations are done to understand the resonance behavior on the surface with differently wettability for Ca = 0.165, 0.825, 1.65. The contour plots in Fig. 7.11 are plotted at resonance frequency $\omega = 0.0035$ for a range surface wettability. It has been seen that deformation/bending of the meniscus is more on hydrophilic surfaces i.e., $g_{2w} = -0.01, -0.02$ as compared to hydrophobic surfaces (non wetting phase blob) i.e., $g_{2w} = 0.01, 0.02$. However, for surfaces with mixed wettabilities i.e., $g_{2w} = \pm 0.01, 0.02$ the deformation is more as compared to the surface with uniform wettability. The blob is placed in such away that meniscus lies in hydrophilic region where it tends to wet to a more extent (see Fig. 7.9 (a)) and middle portion of the blob is kept in hydrophobic region. The deformation of meniscus is greater in case of the surface with $g_{2w} = \pm 0.02$ as compared to $g_{2w} = \pm 0.01$. This is quiet obvious since the variation in wettability is more in case of $g_{2w} = \pm 0.02$. When blob enters the hydrophilic strip/region with $g_{2w} = -0.02$ (see Figs. 7.11 (k), (l)), the highly wetting tendency stretches the meniscus resulting into more bending of the meniscus. The effect of capillary number can also be seen in terms of amount/magnitude of deformation of the meniscus. For higher capillary number, the deformation of meniscus and the mean displacement are found to be greater.

7.3.8.1 Capillarity wettability interaction

A generic capillarity-wettability interaction can be best summarized with the use of surface plots as shown in Fig. 7.12. The dependence of the blob displacement on wettability is explored for different capillary numbers for a range of frequencies. It can be seen that maximum displacement occurs at the resonance frequency i.e., $\omega = 0.0035$ (see Fig. 7.12 (a)). However, at higher capillary number for example, Ca = 1.65, the system exhibits overdamped behavior with more displacement throughout the range of frequency (see Fig. 7.12 (b)). The driving force predominates the effect of wettability of the surface. Hence, it can be safely concluded that wettability tends to be more influential particularly at lower capillary numbers. The optimal use of resonance frequency can be very instrumental for achieving maximum displacement.

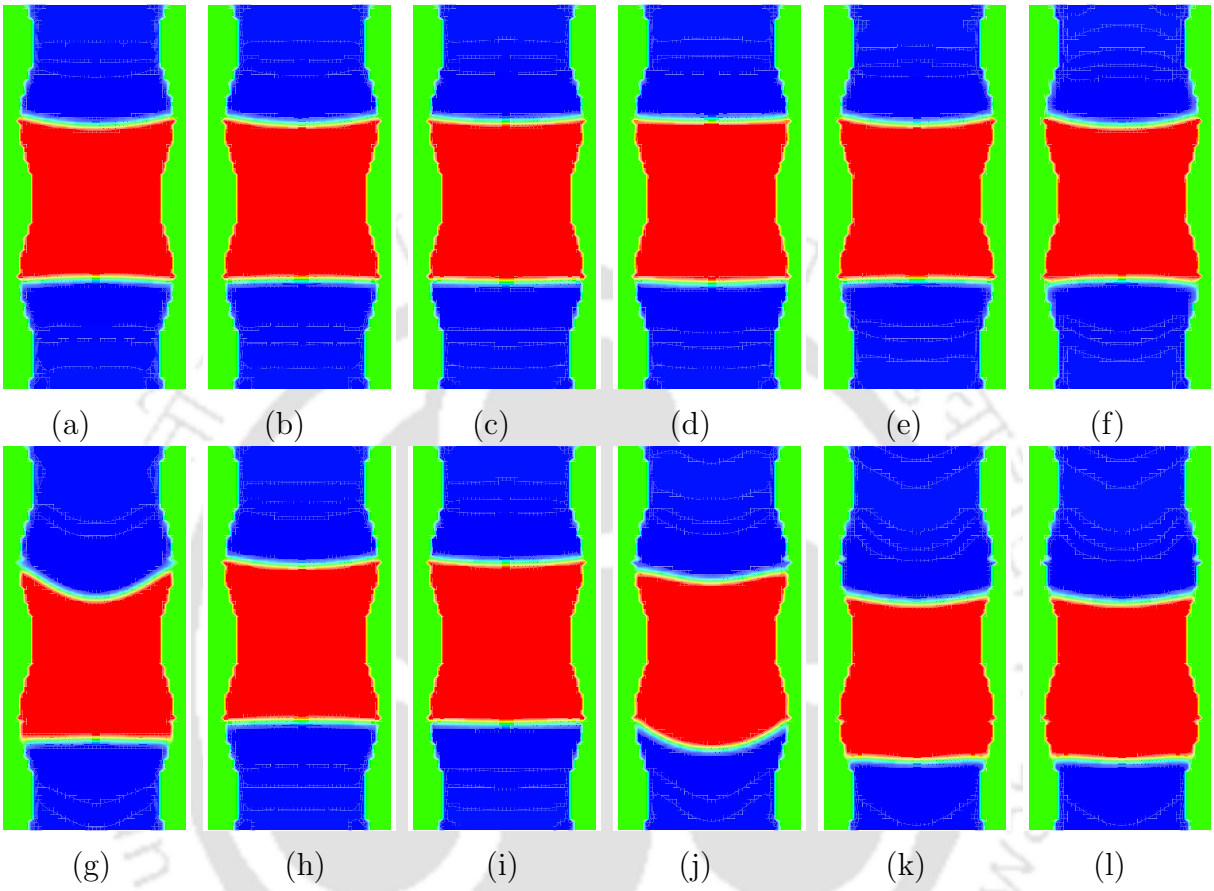

Figure 7.11: Effect of capillary number for different wettability configuration: (a)-(f) snapshots of the blob during excitation at Ca = 0.165, (a) g_{2w} = - 0.02 (b) g_{2w} = - 0.01 (c) g_{2w} = 0.01 (d) g_{2w} = 0.02 (e) g_{2w} = ± 0.02 (f) g_{2w} = ± 0.05, (g)-(l) snapshots of the blob during excitation at Ca = 1.65, (g) g_{2w} = - 0.02 (h) g_{2w} = - 0.01 (i) g_{2w} = 0.01 (j) g_{2w} = 0.02 (k) g_{2w} = ± 0.02 (l) g_{2w} = ± 0.05

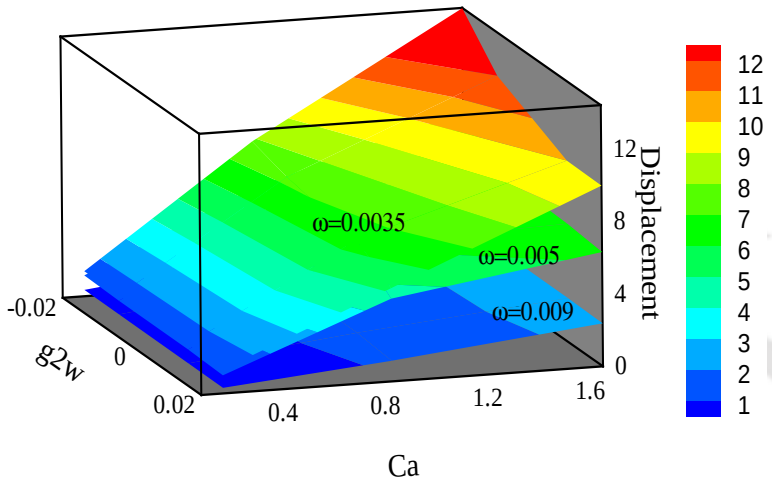

(a)

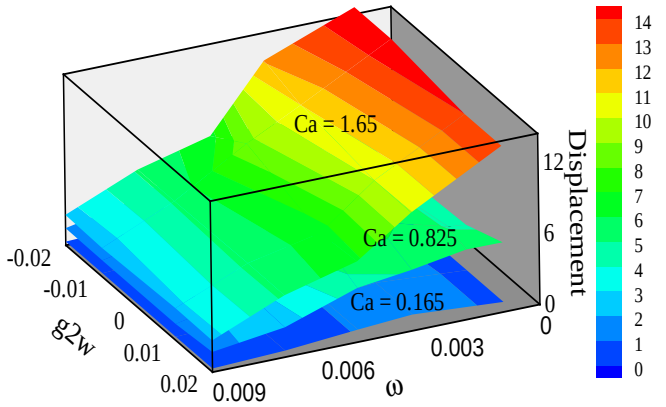

(b)

Figure 7.12: Capillarity wettability interaction for (a) ω = 0.003, 0.005 and 0.009, (b) Ca = 0.23, 1.15 and 2.30 respectively

This could be of great practical relevance while dealing with mobilization of the trapped blobs.

7.3.9 Mobilization of trapped blobs

It is already known that irregular geometry like tube with varying radius offers greater opportunities for the blob to be trapped than the simple shaped channels. This affects the displacement of the blob especially in network of pores. Hence, it becomes important to understand the physics behind the mobilization of trapped blob. In this section, we have investigated capillarity induced resonance of trapped blob in the tube with varying radius. The blob as shown in Fig. 8.2 (a) is subjected to acoustic excitation $\delta W = \sin(\omega t)$ for a range of frequencies. The frequency for peak displacement is found through these simulations and in this case it is ω_{max} = 0.0035. Then the mobilization of the blob is studied for an applied body force $f(t) = f_0 + \delta W \sin(\omega t)$ at selected frequencies ranging from 0 to 1.5 ω_{max}. The magnitude of applied force is chosen such as to result mobilization for a small number of excitation frequencies ω close to ω_{max}. In this case, the mobilization of the blob is observed at $f(0) = 0.000014$ and $\delta W = 0.000035$. It can be seen that, at frequency $\omega = 0.001$ mobilization of the blob is insignificant (see Figs. 8.2(a)-(c). However, for the frequency close to resonant frequency $\omega = 0.0035$, the appreciable amount of mobilization has taken place (see Figs. 8.2 (d)-(f)).

At frequency $\omega = 0.001$, the head (top) meniscus undergoes drainage, passes the throat. However, the blob gets trapped since the tailing (bottom) meniscus (undergoing imbibition) is stuck in a wide portion of the pore space (i.e., pore body). As a result, the blob oscillates around the equilibrium state (see Fig. 8.3 (a)). When the blob is excited at $\omega = 0.0035$ close to ω_{max}, the blob has been displaced significantly (see Fig. 8.3 (b)). The blobs tailing meniscus passed the pore body, the bottle-neck for imbibition. It can be inferred that mobilization of the blob is more when excited at $\omega = 0.0035$, which is near to ω_0 as compared to at $\omega = 0.001$, which is quiet below the resonant frequency ω_{max}.

To quantify the mobilization of the blob, the mean blob position is estimated by the time average value of $z(t)$ during the last excitation cycle, z for all values of ω as shown in Fig. 8.3 (c). The filled symbols show the mobilization of the blob. The frequency response χ of the blob is very high as expected for the value of ω near to ω_{max}. It is observed that the mobilization has occurred for only a few excitation

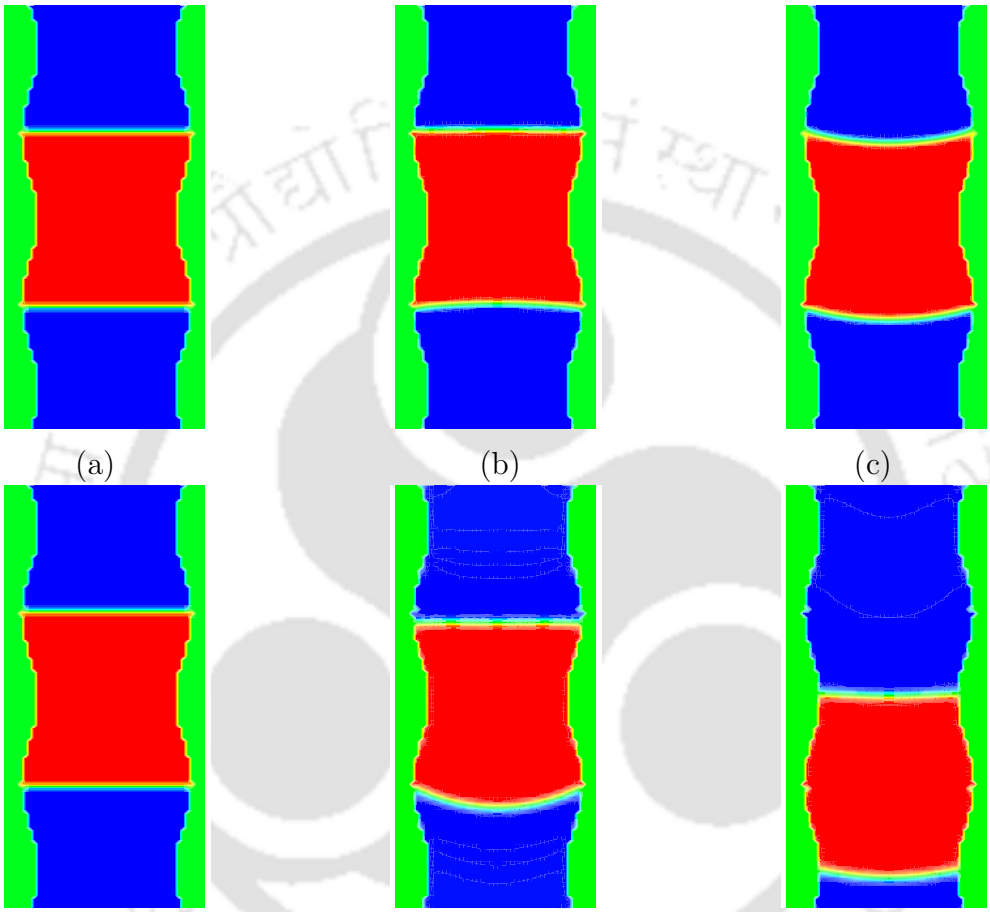

Figure 7.13: Snapshots of mobilized blob (a)-(c) at $\omega = 0.001$ and (d)-(f) at $\omega = 0.003$ for time step = 0, 4000 and 8200 respectively

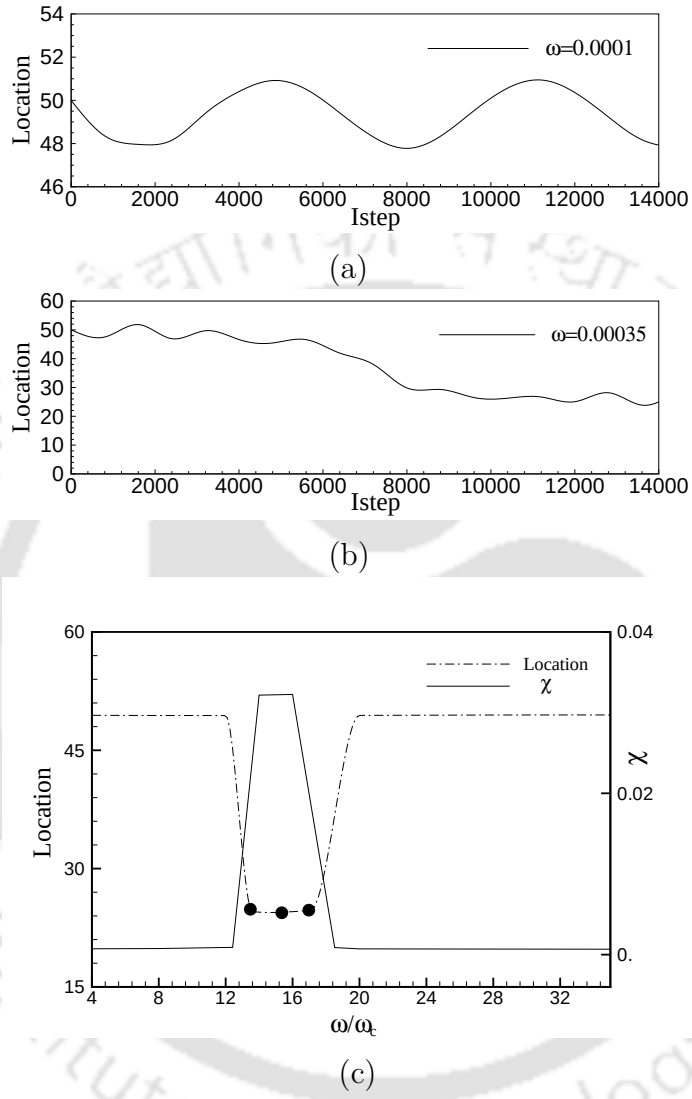

Figure 7.14: Mobilization of a blob in a sinusoidal pore channel (a) excitation at ω = 0.001, (b) excitation of the blob at $\omega = 0.0035$, (c) Mean blob position during the last excitation cycle at various values of ω

frequencies ($\omega = 0.0032$ and $\omega = 0.0035$), both of which are close to ω_{max}. The blob is displaced by around 25 lattice units. It can be seen that mobilization of the blob occurred for a few frequencies which are very close to ω_{max}. This could be very well used in designing the strategies dealing with the mobilization of the blob.

7.4 Closure

The blob response in the tube with varying constriction subjected to an oscillatory force is investigated for pinned and sliding contact surfaces. The effect of the parameters like wettability of the surface, frequency, capillary number and amplitude of the force applied on the displacement of the blob is analyzed and discussed. The displacement of the blob is found to be more for the wider tube as compared to that of the narrower ones'. Resonance study for a range of capillary numbers shows that meniscus bending also is governed by wettability of the surface. Wettability-capillarity interaction is studied in depth to reveal the resonance behavior of the trapped blob on differently wetted surface for a range of capillary number. Wettability proves to be more influential particularly at lower capillary numbers. Hence, application of resonance frequency for such configurations could be very instrumental in obtaining maximum displacement of the blob.

Chapter 8

Effect of Geometry on Blob Dynamics

8.1 Introduction

The complexity in understanding the physics of liquid displacement is attributed to the fact that it is a function of several physicochemical properties which includes wettability of the surface, capillary number and capillarity induced resonance [1]. Besides this, the nature of the geometry [155, 156] determines intra-pore fluid flow behavior. Thus, pore geometry is one of the most important governing factors in the flow of fluids through porous rocks. In most of investigations, a particularly useful conceptualization assumes the pore space as a collection of channels through which fluid can flow. The effective width of these channels may or may not vary along its length. The relatively wide portions of the channel is usually described as pore bodies. The narrow and the constrictive part of pore openings is called throat usually separate the pore bodies. The boundaries of these pores commonly consist of three distinct regions: (1) fluid interface with solid, (2) constriction or throat of pore space, or (3) interface with adjacent pore. Pore dimensions are commonly specified by an effective radius of the pore body or throat. Although the pore shape is not known, it could be assumed depending on the models like e.g. cylindrical pores cylindrical pores, circular in cross section and so on. It is important to note that the displacement of the blob depends on the exact geometry. For instance, the displacement is large for the polygonal and sinusoidal pore channels as compared

to the disc packing. The resonance frequency being one of the vital parameter in the mobilization is found out at the frequency a blob shows maximum response. In the present work, blob dynamics in the domains with constant (rectangular duct, tube) and varying cross sections (sinusoidal, convergent-divergent duct and tube with varying constriction) is investigated. The analysis of blob dynamics is focussed mainly on :

1. Extent of mobilization
2. Nature of entrapment opportunities
3. Resonant frequency
4. Magnitude of excitation required to mobilize the blob

8.2 Problem Specification

Present work studies the mobilization of the blob trapped in a channels with uniform and varying cross section. First the blob dynamics in a tube with uniform cross section has been studied followed by mobilization study for different geometrical configurations. Length and radius of tube used for the study (see Fig. 9.1) are taken as 100 and 20 (in lattice units) respectively. Bounce back boundary conditions at walls and periodic boundary conditions along the tube axis at $z = 0$ and $z = l$ are applied. The tube radius is denoted by R whereas the non wetting and wetting phase length are shown by L_n and L_w respectively. Later numerical experiments are conducted on channels of different shape with uniform and varying cross section namely, tube, convergent divergent, rectangular and tube with varying cross section to investigate the effect of geometrical configurations on the mobilization of blob for various wettability scenarios. Present work considers the system with two immiscible fluids in which blob (fluid 2) is placed in the domain filled with displacing fluid (fluid 1). The blob is initially positioned in the center of the domain at $z = 50$. It is subjected to the sinusoidal acoustic force along the negative z-direction as the driving force which causes its motion. The dynamics of the blob is studied for different physicochemical properties which include geometry, frequency applied and nature of the wettability. The interface between the two fluids being diffused is taken at the location where both the fluids have equal number density [11]. Displacement of meniscus of the blob is quantified by locating the interface at the mid-section along

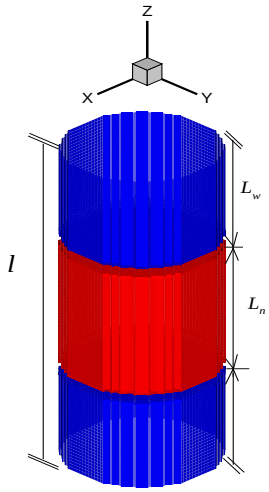

Figure 8.1: Computational domain showing tubular geometry

x axis. First, linear response of a blob inside a circular tube subjected to acoustic excitation is studied to understand capillarity induced resonance mechanism. This is followed by a investigation on effect of geometry on mobilization of trapped blob. It may be noted that the contact line between the fluid and the solid surface is considered to be pinned to surface. The surface roughness is created by addition of solid phase pixels on both sides of the tube for two selected locations where three-phase contact points could be pinned. The small roughness height is chosen so that it will not have considerable effect on the flow in the tube but will be able to 'trap' the three-phase contact line. The blob is subjected to a transient body force in the z- direction. LB simulations were performed to explore whether the numerical model can simulate the resonance of trapped non wetting phase blobs. The transient force on the blob can be given as given below.

$$W(t) = W(0) + \delta W \sin(\omega t) \tag{8.1}$$

where $W(0)$ and $\delta W \sin(\omega t)$ are constant body force and perturbation respectively. It may be noted that the constant body force $W(0)$ can be considered equivalent to an imposed pressure gradient in the wetting phase [1] whereas the perturbation $\delta W \sin(\omega t)$ can be taken as a vibration of the pore walls and/or an oscillatory pressure gradient with frequency (ω). Thus, capillarity induced resonance can mobilize trapped non wetting phase by acoustic and elastic waves. First, the non wetting

Table 8.1: Parameter values used to study the effect of geometry on mobilization of trapped blob

Parameter		Value
length (l)		100
Radius (w)		20
Density of fluid1		0.035
Density of fluid2		0.965
Relaxation time of the wetting phase τ_1		0.80
Relaxation time of the non wetting phase τ_2		0.80
Fluid-fluid interaction parameter	$g_{11} = g_{22}$	0
	$g_{12} = g_{21}$	0.1

phase blob was initialized for a pore tube and equilibrium was reached via numerical simulation. Tube used for numerical simulation is shown in Fig. 9.1. The fluid properties taken for the simulations are listed in Table 8.1.

8.3 Results and Discussion

The numerical experiments on mobilization of blobs due to capillary induced resonance were carried out to understand its mechanism. In this regard, first series of numerical simulations was carried out to unveil the physics behind blob motion for pinned contact surfaces.

8.3.1 Mobilization of trapped blobs

Mobilization of trapped blob can be done effectively if blob is excited at the resonance frequency which could lead to an enhanced mass transfer [157]. Hence, it becomes crucial to understand the physics behind the mobilization of trapped blob. In this section, we have investigated capillarity induced resonance of trapped blob

in the tube. First, the numerical experiments are conducted to ascertain the frequency at which the blob shows maximum response. The blob as shown in Fig. 8.2 (a) is excited with acoustic excitation $\delta W \sin(\omega t)$ for a range of frequencies. The maximum displacement of the blob is found at around $\omega_{max} = 0.003$. Then, the

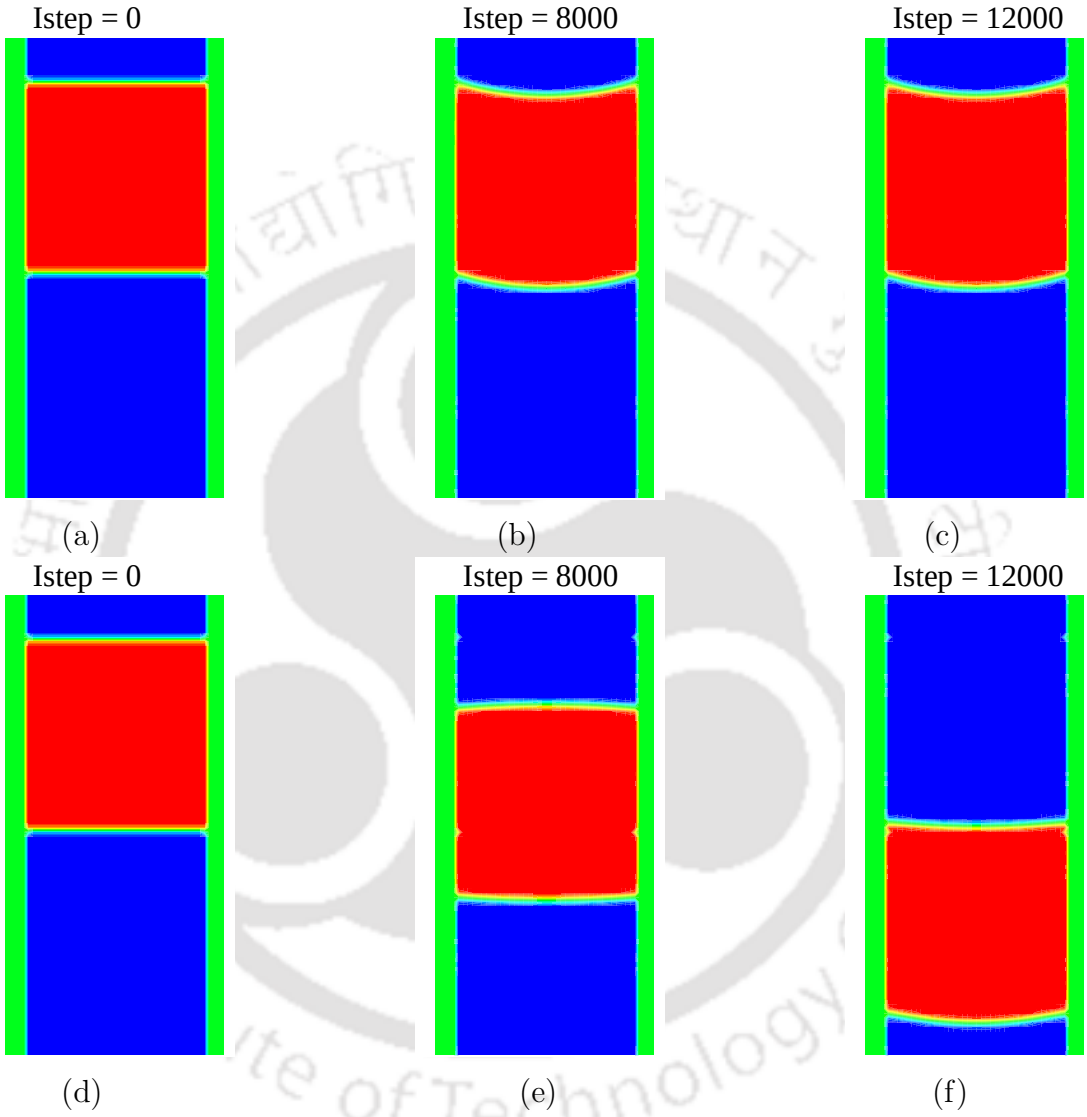

Figure 8.2: Snapshots of mobilized blob: (a)-(c) at $\omega = 0.001$, (d)-(f) at $\omega = 0.0032$

blob is subjected to the excitation at selected frequencies ω_n ranging from 0 to 1.5 ω_{max} with a force $W(t) = W(0) + \delta W \sin(\omega t)$. The amplitude of force δW is varied so that mobilization occurred for a small number of excitation frequencies ω presumably close to ω_{max}. It is observed that the mobilization occurred for $W_0 =$

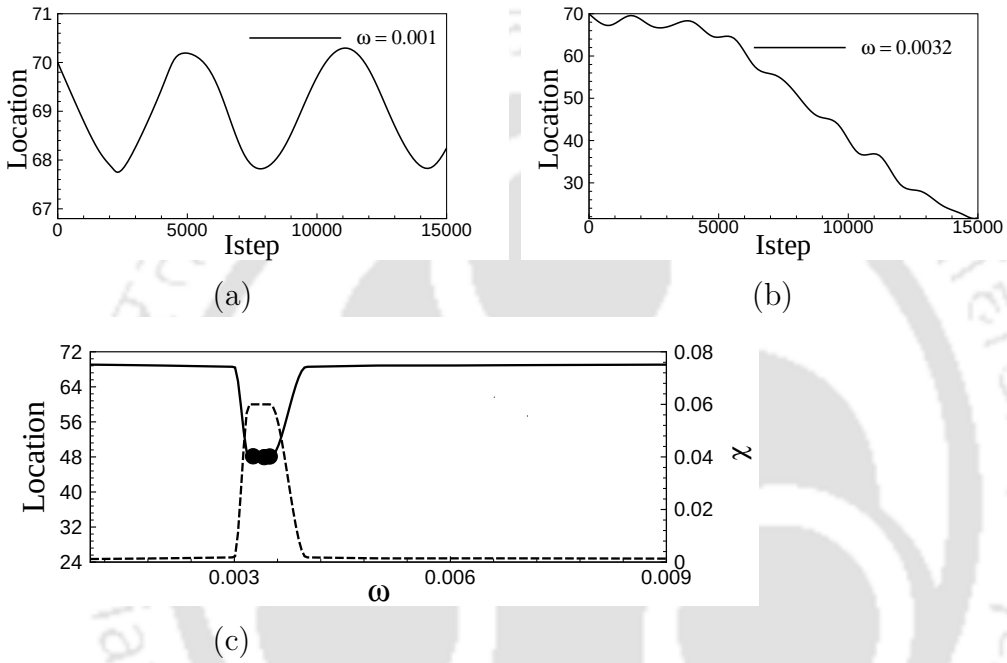

Figure 8.3: Mobilization of a blob in a tube (a) excitation at $\omega = 0.001$, (b) excitation of the blob at $\omega = 0.0032$, (c) mean blob position during the last excitation cycle at various values of ω

0.000014 and $\delta W = 0.000035$. Figures 8.2 (a)-(c) show the snapshots of the simulations for the blob for the frequency at which no mobilization has occurred whereas Figs. 8.2 (d) -(e) depict the snapshots at the highest excitation frequency at which mobilization has occurred. When the blob is excited at $\omega = 0.0032$ close to ω_{max}, the blob has been displaced significantly (see Fig. 8.3 (b)). Excitation of the blob at $\omega = 0.0032$ which is near to ω_0, causes blob mobilization whereas excitation at $\omega = 0.001$, which is below the resonant frequency ω_{max}, causes the blob to oscillate around the equilibrium state (see Fig. 8.3 (a)).

To know whether mobilization has occurred or not, the mean blob position is quantified by taking the time average value of $z(t)$ during the last excitation cycle, z for all values of ω as shown in Fig. 8.3 (c). The filled symbol indicates mobilization of the blob. The frequency response χ of the blob is more as expected for the value of ω close to ω_{max}. We can see that the blob has been displaced to a significant distance at a frequency near to ω_{max}. It is observed that the mobilization happened for only a few excitation frequencies ($\omega = 0.0032$ and $\omega = 0.0032$), both of which are near to ω_{max}. The blob is displaced by around 48 lattice units. Also, it can be observed that a net displacement i.e., mobilization of the blob has occurred for a few frequencies, which are very close to ω_{max}. These results confirm the hypothesis that blob can be optimally mobilized by excitation at its resonant frequency.

8.3.2 Effect of geometry on mobilization

A basic understanding of influence of pore geometry and surface properties like wettability on mobilization of the blob as far as the transport of multiphase flow is concerned is essential. After establishing the fact that capillarity induced resonance aids in mobilization of the trapped blob, it remains to be examined how the mechanism of mobilization get influenced by the surface properties like wettability for various geometrical configurations. In this context, the present section discusses the effect of geometry i.e., nature of curvature in conjunction with wettability on the mobilization of the blob. The study is undertaken on geometries (rectangular, tubular, convergent divergent and tube with varying cross sections) with same mean radius but different curvature i.e. uniform and varying cross section as shown in Fig. 8.4. The transient force ($\delta W \sin(\omega t)$) is applied keeping all other parameters constant. The mean displacement of the blob is found to be more in the case of the geometry with uniform cross section as compared to the varying cross section (see

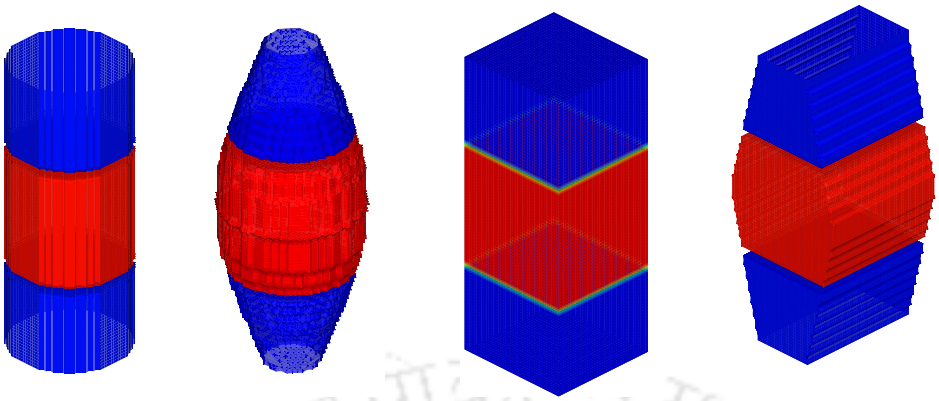

(a) (b) (c) (d)

Figure 8.4: Different geometries used for comparison: (a) tube with uniform cross section, (b) tube with varying cross section, (c) rectangular, (d) convergent divergent

Fig. 8.5). The mobilization study on trapped blob as explained earlier is further extended by considering channels of different shapes with uniform and varying cross section to investigate the effect of nature of curvature. The blob is excited with transient force $W(t) = W(0) + \delta W \sin(\omega t)$ to ascertain the response of the blob for different geometrical configurations. The contour plots shown in Figs. 8.6 and 8.7 clearly demonstrate the effect of curvature of the geometry on dynamics of the blob.

The mobilization of the trapped blob is also studied for different driving forces. It may be noted that each driving force term, responsible for initiating the blob motion, can be perceived as representative of a particular capillary number (Ca) [11]. The effect of different driving strengths i.e., capillary number for geometries with uniform and varying cross section is analyzed. It was found that at Ca = 0.75, the nature of geometry curvature dictates the mechanism of mobilization. For the tube with uniform cross section, the extent of mobilization is more in general and the effect of wettability can be seen with more mobilization in case of hydrophobic surface (see Fig. 8.8 (a)). Most interesting observation is that, for tube with varying cross section, the extent of mobilization of the blob is found to be less. Moreover, the effect of wettability is not so considerable (see Fig. 8.8 (b)). At higher Ca = 1.5, it is seen that the effect of wettability is negligible both for tube with uniform and varying cross section as shown in Figs.8.8 (c)-(d). The effect of capillary number on

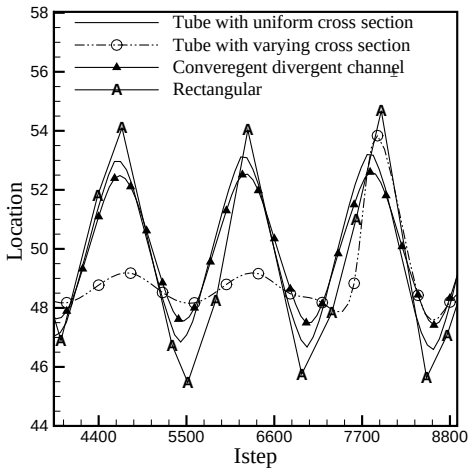

Figure 8.5: Effect of geometry on dynamic response of the blob at $\omega = 0.003$ on hydrophobic surface at Ca = 0.75

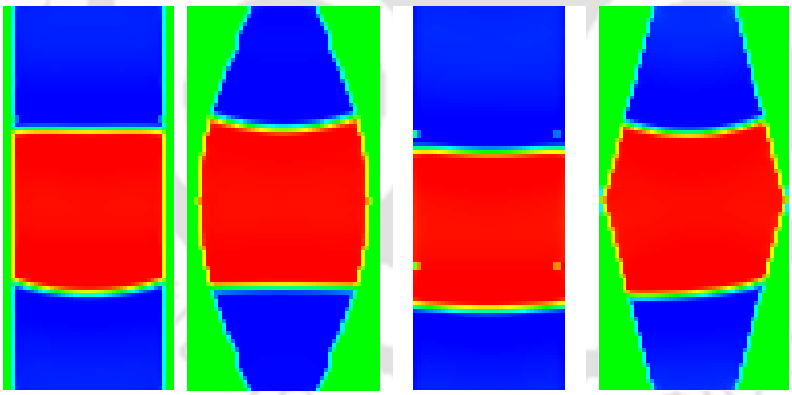

Figure 8.6: Contour plot at istep = 1600 for different geometries at Ca = 0.75: (a) tube with uniform cross section, (b) tube with varying cross section, (c) rectangular, (d) convergent divergent

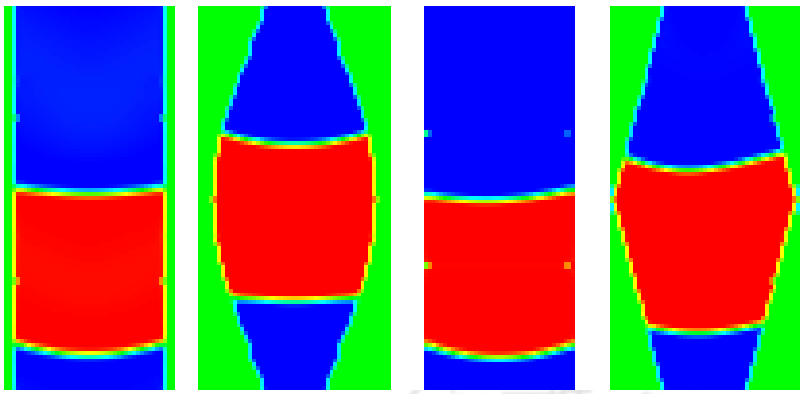

(a) (b) (c) (d)

Figure 8.7: Contour plot at istep = 1600 for different geometries at Ca = 1.5: (a) tube with uniform cross section, (b) tube with varying cross section, (c) rectangular, (d) convergent divergent

mobilization of blob can be observed as shown in Fig. 8.8 (c)-(d). This reiterates the fact that the mobilization of the blob is influenced to a great extent by wettability at low Ca only as explained earlier.

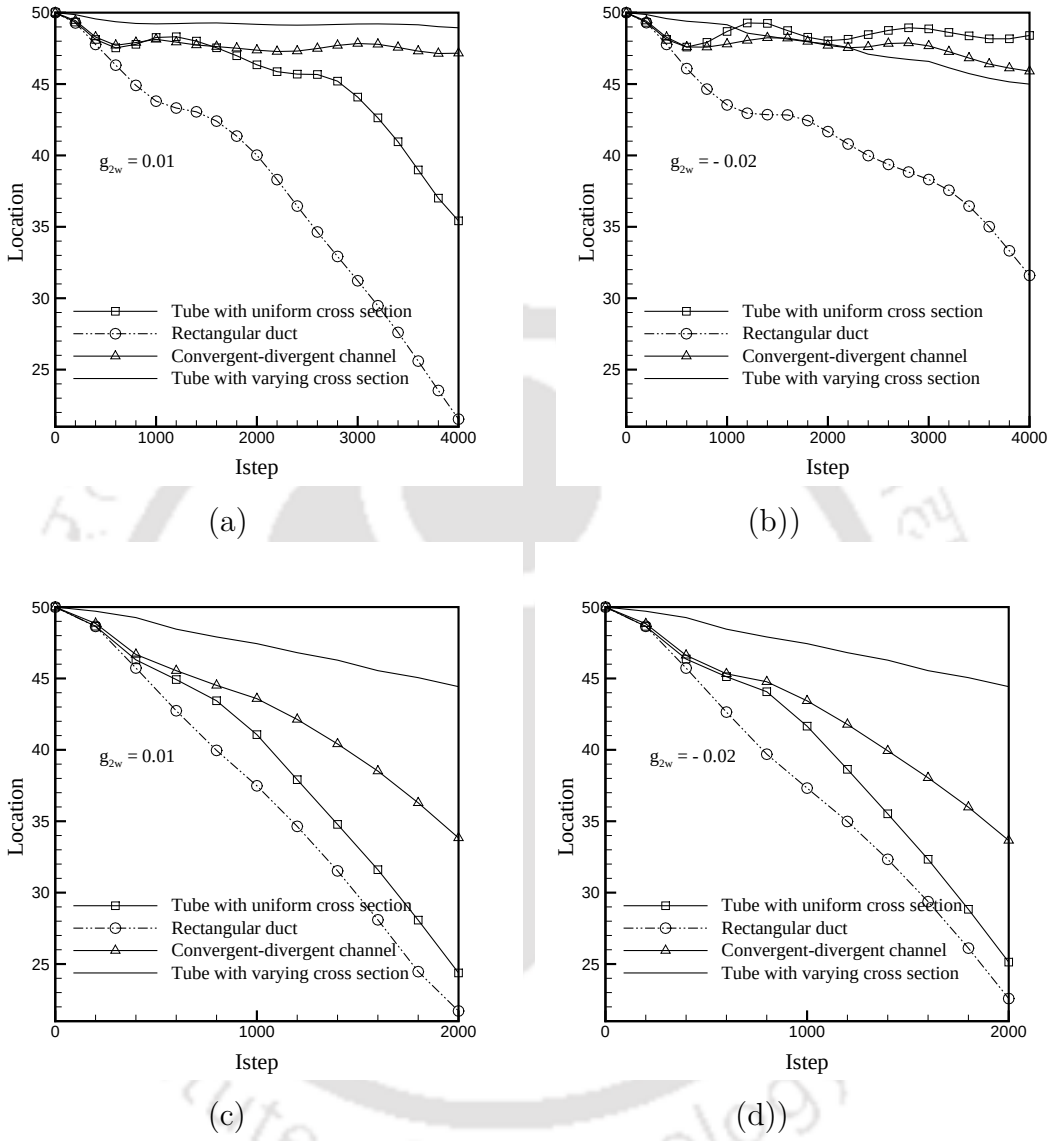

Figure 8.8: Effect of geometry on mobilization: (a) for hydrophobic surface at Ca = 0.75, (b) for hydrophilic surface at Ca = 0.75, (c) for hydrophobic surface at Ca = 1.5, (d) for hydrophilic surface at Ca =1.5

8.4 Closure

It has been observed that the mobilization of the blob is governed by the nature of geometry i.e. curvature of surface. The blob trapped in domain with varying cross section shows less mobilization as compared to the one with uniform cross section for the same input conditions. The study on combined effect of wettability and geometry reveals that mobilization is more for hydrophobic surface on the geometries with uniform cross section. However, effect of geometry and wettability would not be so significant at high capillary number.

Chapter 9

Mesoscopic Modeling of Fluid Flow in a 3-Dimensional Porous Medium

9.1 Introduction

Simulating multiphase fluid flow in porous media has been the field of interest owing to its several applications in physical sciences, life sciences, and engineering. The important applications include study of oil recovery, fuel cells, microfluidics and contaminant remediation in aquifers [23, 101, 129, 155, 158]. It is well known that immiscible flows exhibit different characteristics depending on the physicochemical properties like wettability, viscosity ratio and porosity of the microstructure affecting the advance of the fluid in the porous microstructure [159, 160]. In fact, the competition among the viscous, capillary and gravity forces determines fluid displacement behavior [160]. Recently Huang et al. [161] have studied the immiscible displacement in porous media using multiphase lattice Boltzmann method. They have analysed the stable displacement, viscous fingering and capillary fingering for a range of capillary number and viscosity ratio. However, the immiscible displacement of fluid front in conjunction with capillarity induced resonance in porous media remain largely overlooked. The objective of this study is to acquire an in-depth understanding of fluid flow in porous media. In this context, the present work addresses

the effect of porosity of microstructure, wettability and capillary number coupled with capillarity induced resonance on the advance of the fluid.

9.2 Problem Specification

Present work simulates the fluid flow in the porous media to bolster our understanding about the effect of physicochemical parameters like wettability, porosity and capillarity induced resonance on physical mechanism of mobilization. The dimensions of the computational domain (see Fig. 9.1) are as given in Table 9.1. Porous media generated can be uniquely defined by means of the physical topology which defines the locations of the solid obstructions with respect to the allowed fluid streams. In our simulations, the porous medium is generated by placing square pillars with same size (see Fig. 9.1). Any two square pillars are not allowed to overlap. This simplified idealized porous media is undertaken for the study of fluid flow to focus on wettability and porosity dependence of fluid flow behavior under the capillarity induced resonance. The S-C LB model considers the system with two immiscible fluids in which non wetting phase (fluid 2) is placed in domain filled with displaced fluid (fluid 1). The non wetting phase (NWP) is initially placed at the inlet of the domain. The motion of the fluid is induced by a constant pressure gradient along with sinusoidal acoustic force in the x-direction. The dynamics of the fluid flow were explored based on displacement of the fluid for different set of conditions namely, wettability, porosity and forcing strength i.e., the acoustic excitation applied. The inlet and outlet of the domain are kept at constant pressure. Periodic boundary conditions are applied in y- and z-directions. In the displacement simulations, the domain is initially occupied by the wetting fluid. The wetting fluid is displaced along x-direction by the non wetting fluid i.e., drainage. Study of the fluid flow is also presented for the porous structure with porosity $\phi = 0.54$, 0.65 and 0.80 in hydrophilic, hydrophobic and mixed-wet scenario. The porosity of the domain is 0.65 for all the simulations unless and otherwise explicitly mentioned. The different flow behavior stemming from the forcing strength and pressure gradient applied is analysed.

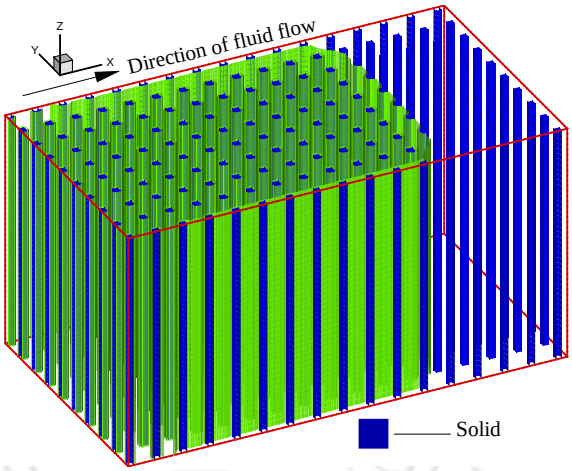

Figure 9.1: 3-D view of porous structure

9.3 Results and Discussion

The primary goal of this investigation is to evaluate mobilization of fluid through porous media due to capillary induced resonance via appropriate numerical experiments. The effect of various parameters like wettability (g_{2w}), porosity and frequency on displacement of fluid thorough porous media is discussed.

9.3.1 Simulation Setup

Based on the two-phase S-C LB model [22], a static capillary pressure experiment is designed assuming negligible influence of capillary number and viscosity ratio on the two-phase transport within the microporous media. Figure 9.2 schematically shows the numerical experiment, based on the work by Pan et al. [162], where immiscible displacement for two-phase flow through a porous structure has been conducted. A non wetting phase reservoir is added to the porous structure at the front end ($x = 0$) and a WP reservoir is added at the back end ($x = L$). It should be noted that for the primary drainage (PD) simulation in the hydrophobic structure, fluid 2 is the NWP and fluid 1 is the WP. Fixed pressure boundary conditions which are equivalent to fixed densities within the LB framework, were applied at the first layer of the NWP reservoir and the last layer of the WP reservoir. Fixed pressure boundary conditions were imposed by assigning the equilibrium distribution functions calculated with zero velocity and specified density at the reservoirs, to the distribution functions,

based on the early work by Grunau [163]. The primary drainage process has been started with zero capillary pressure, by assigning the NWP and WP densities in the first layer of the NWP reservoir to be 150 and 0 respectively, and 0 and 150 in the last layer of the WP reservoir. Thereafter, the capillary pressure is increased incrementally by decreasing the WP reservoir density while maintaining the NWP reservoir density at the fixed initial value. It may be noted that the pressure gradient drives the NWP into the initially WP saturated porous medium by displacing it. A lattice site is considered to be occupied by the NWP if the NWP density at that node is larger than half of the fixed NWP density; otherwise the node is assumed to be WP occupied. Since the interface is diffused, it is taken at the location where density of the fluid is more than or equal to the half of invading phase. The location of fluid front is tracked from the other extreme end in x-direction and averaged over the section to quantify the location of invading fluid. The two-

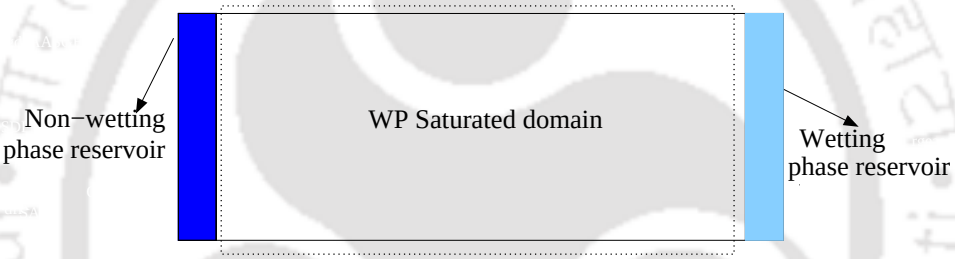

Figure 9.2: Schematic diagram of the capillary pressure experiment

phase LB modeling framework devised here could be further extended to simulate the scenario of fluid flow owing to additional transient force to the existing pressure gradient. This can be useful to understand the effect of capillarity induced resonance on fluid front movement under different configurations of porosity and wettability. This numerical experiment evaluates the response of driving force as function of percentage saturation and displacement as a direct manifestation of the underlying pore structure and wettability conditions. The term percentage saturation, here indicates the ratio of pore space occupied by the invading fluid to the total pore space. It may be noted that the pore space is considered to be occupied by the invading fluid when the density of the pore is more/equal to half of invading phase. The model input parameters for this numerical experiment are given below in Table 9.1.

Figure 9.3 shows the movement of fluid front with time for applied pressure

Table 9.1: Parameter values used to study the fluid flow through porous media

Parameter		Value
Length of the domain (l)		83
Width of the domain (W)		46
height of the domain (h)		45
Density of fluid1 at inlet		10^-5
Density of fluid2 at inlet		150
Density of fluid1 at outlet		150
Density of fluid2 at outlet		10^-5
Relaxation time of the wetting phase (τ_1)		1
Relaxation time of the non wetting phase (τ_2)		1.42
Fluid-fluid interaction parameter	$g_{11} = g_{22}$	0
	$g_{12} = g_{21}$	0.001

gradient. It can be seen that fluid has advanced into porous media occupying the pore space already filled with wetting phase.

9.3.2 Capillarity induced resonance in porous media

In this study, we address the dependence of fluid flow on physicochemical properties like on wettability and porosity in conjunction with capillarity induced resonance in a 3-dimensional porous medium. The behavior of fluid flow both under drainage and imbibition is studied for different porous structures. The driving force causing the fluid flow consist of pressure gradient at the inlet and outlet of porous structure in addition to the acoustic excitation at an appropriate frequency. The numerical experiments were conducted to ascertain the frequency and magnitude of acoustic excitation so as to get the maximum mobilization of fluid front under the specified conditions. This procedure is adopted as explained in the reported literature by various investigators [1].

The basic idea about adding the acoustic excitation is to achieve the considerable

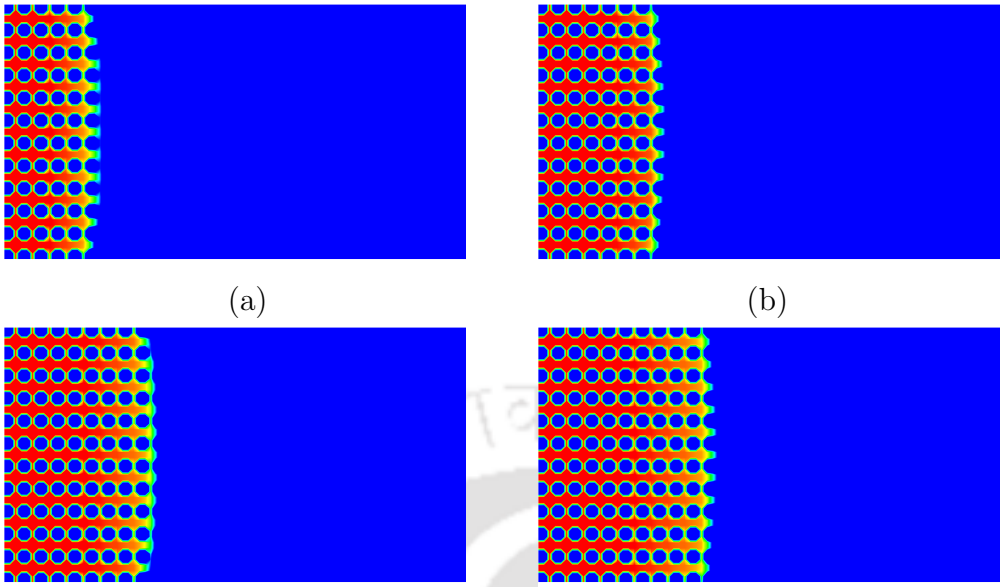

Figure 9.3: Advancement of fluid front without acoustic excitation: (a) time istep = 2000, (b) time istep = 4000, (c) time istep = 6000, (d) time istep = 8000

fluid front movement as suggested by Iassonov and Beresnev [86] who reported the effect of low frequency sonic vibrations on the flow of non aqueous phase liquids (NAPL) through a porous medium. They further stated that vibrations can considerably reduce minimum pressure gradient needed to mobilize entrapped fluid and increase the average flow rate. This could be of utmost importance to understand the mobilization of reservoir fluids with acoustic stimulation technologies. Thus vibrations becomes the most effective in the zones of relatively low pressure gradients. There is excellent review by Beresnev and Johnson [80] on the techniques of elastic wave stimulation of oil production to increase the efficiency of oil recovery methods. In this work, the fluid flow is excited by a transient body force in the x-direction. LB simulations were run to simulate the fluid flow under capillarity induced resonance. The transient force applied can be expressed as given below.

$$W(t) = W(0) + \delta W \sin(\omega t) \tag{9.1}$$

where
$W(0)$ and $\delta W \sin(\omega t)$ are a constant pressure gradient and the perturbation as acoustic excitation (with frequency ω and amplitude of excitation δW) respectively. The

constant body force $W(0)$ can be taken equivalent to an imposed pressure gradient in the wetting phase [1] whereas the perturbation ($\delta W \sin(\omega t)$) can be viewed as a vibration of the pore walls and/or an oscillatory pressure gradient. Hence, capillarity induced resonance can be exploited to mobilize fluid in porous media by acoustic waves. The fluid properties used in the simulations are listed in Table 8.1. It may be noted that all units are in lattice units unless otherwise stated specifically. In order

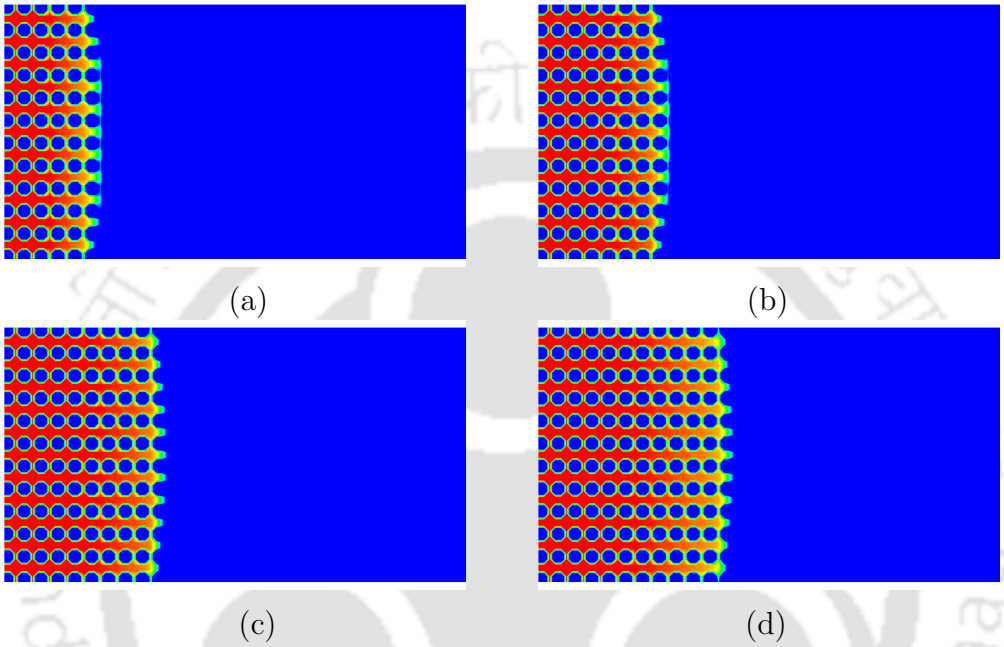

Figure 9.4: Advancement of fluid front with excitation: (a) time istep = 2000, (b) time istep = 4000, (c) time istep = 6000, (d) time istep = 8000

to get insight on the dynamic behavior of fluid flow, the mean displacement of the invading fluid for a range of excitation frequencies has been analyzed. It is evident from the contour plot shown in Fig. 9.4 that fluid front is displaced more when subjected to acoustic excitation in addition to the existing pressure gradient. Figure 9.5 also reiterates that the additional transient force like acoustic excitation can be of great help to mobilize the fluid flow through porous media. Numerical experiments were carried out for a range of frequency (ω) to find out the resonating frequency at which the mobilization of the fluid is maximum for a given magnitude of excitation (see Fig. 9.6) on the similar lines as that of Hilpert [1]. It can be observed that the displacement of the fluid front and percentage saturation are maximum for ω = 0.0001. For the frequencies more than $\omega = 0.0001$, the mean displacement of the

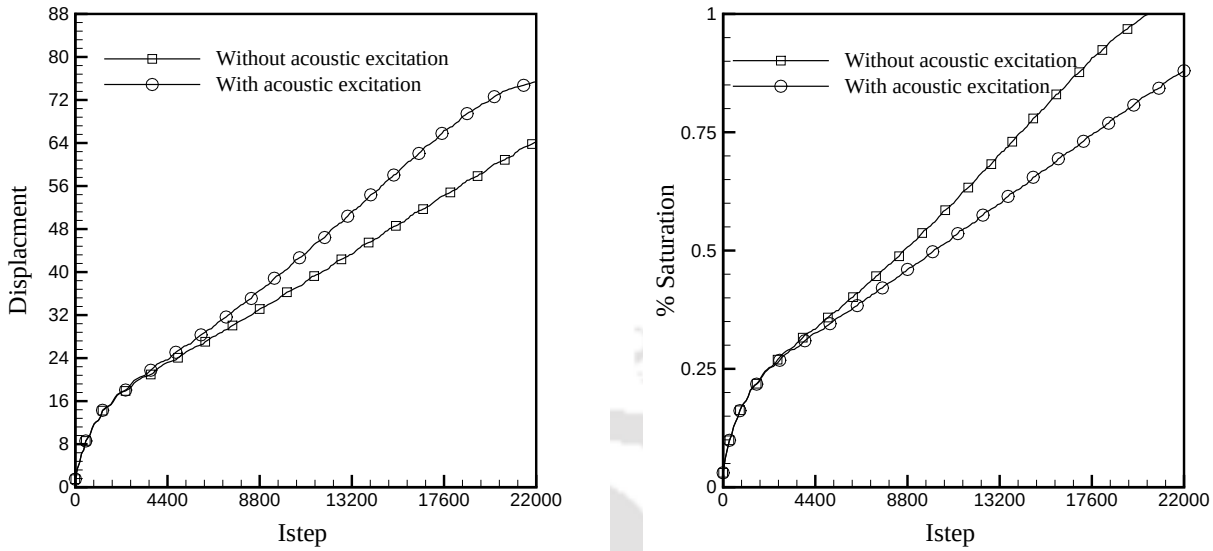

Figure 9.5: Effect of acoustic excitation on fluid flow: (a) mobilization of non wetting phase, (b) percentage saturation with time

fluid front gradually reduces and stable fluid front is formed. Also, the percentage saturation increases with time indicating that more and more pores are filled with invading fluid thereby displacing the existing phase.

9.3.3 Effect of force on the response of the blob

In order to study the influence of force on the response of the fluid flow, the simulations were performed for three different amplitudes of the force $\delta W = 0.0001$, 0.0005 and 0.001 for the same configuration. The displacement of the invading phase is found to be greater for $\delta W = 0.001$ as compared to $\delta W = 0.0001$ and 0.0005 as shown in Fig. 9.7. In the numerical simulations of fluid flow through porous media, a pressure gradient is applied to drive the system. In this context, numerical simulations have been carried out to ascertain the behavior of the fluid flow in response to the applied pressure gradient. It may be noted that the pressure gradient is established by keeping a density gradient in the system and this is the only approach to implement the boundary condition of a pressure gradient [164]. Figure 9.8 shows behavior of fluid flow for applied pressure gradient based on density. The contour plot in Fig. 9.9 also shows that mobilization of fluid flow with stable fluid front is

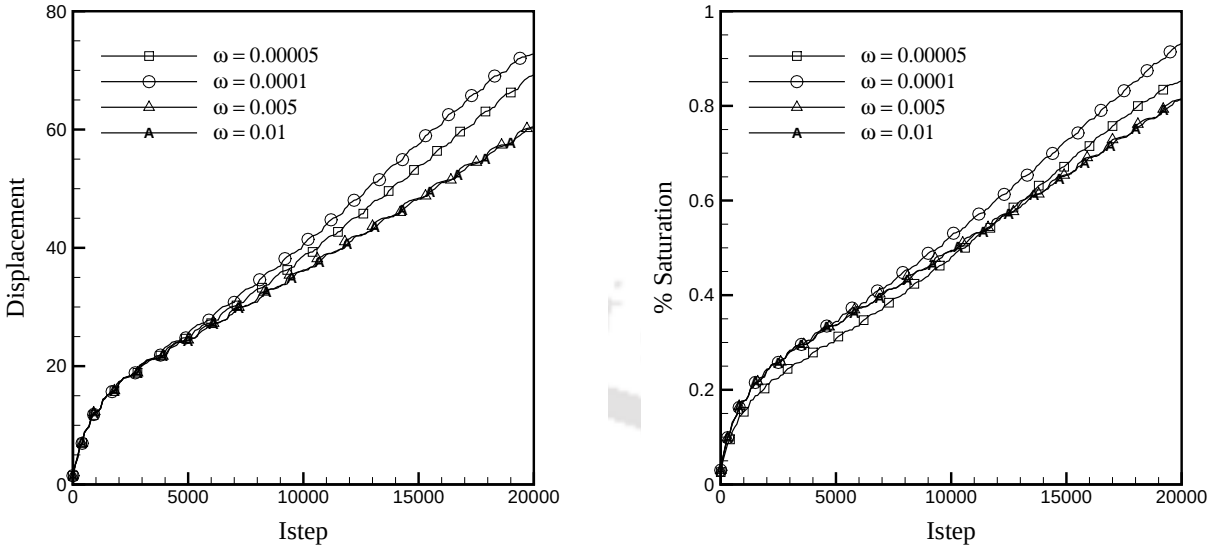

Figure 9.6: Effect of frequency on the advance of fluid flow: (a) mobilization of non-wetting phase, (b) percentage saturation with time

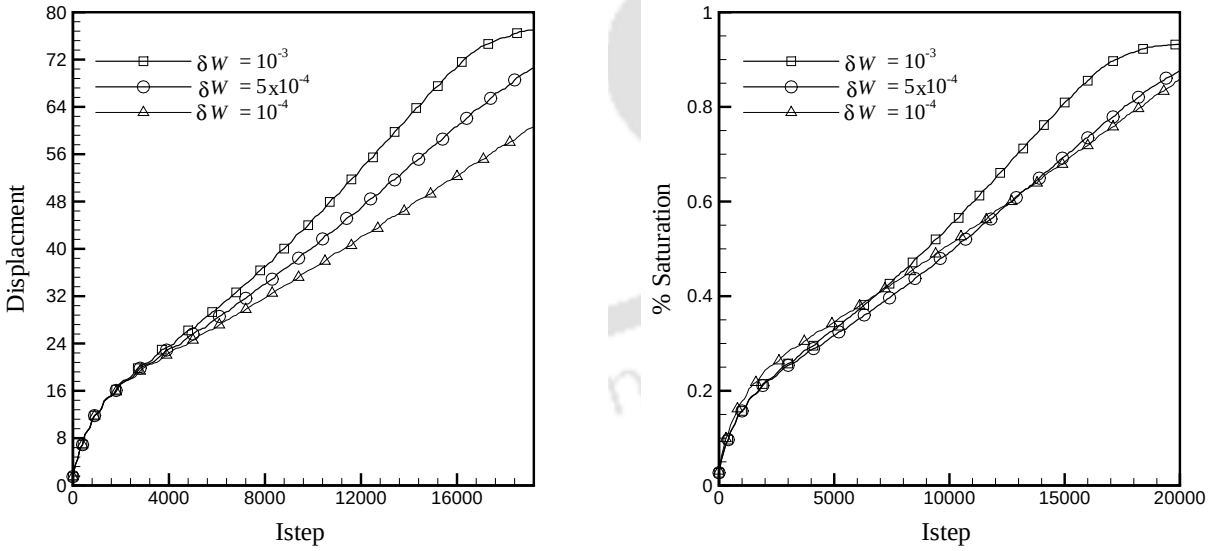

Figure 9.7: Effect of magnitude of acoustic excitation δW on the advance of fluid flow: (a) Mobilization of non wetting phase, (b) Percentage saturation with time

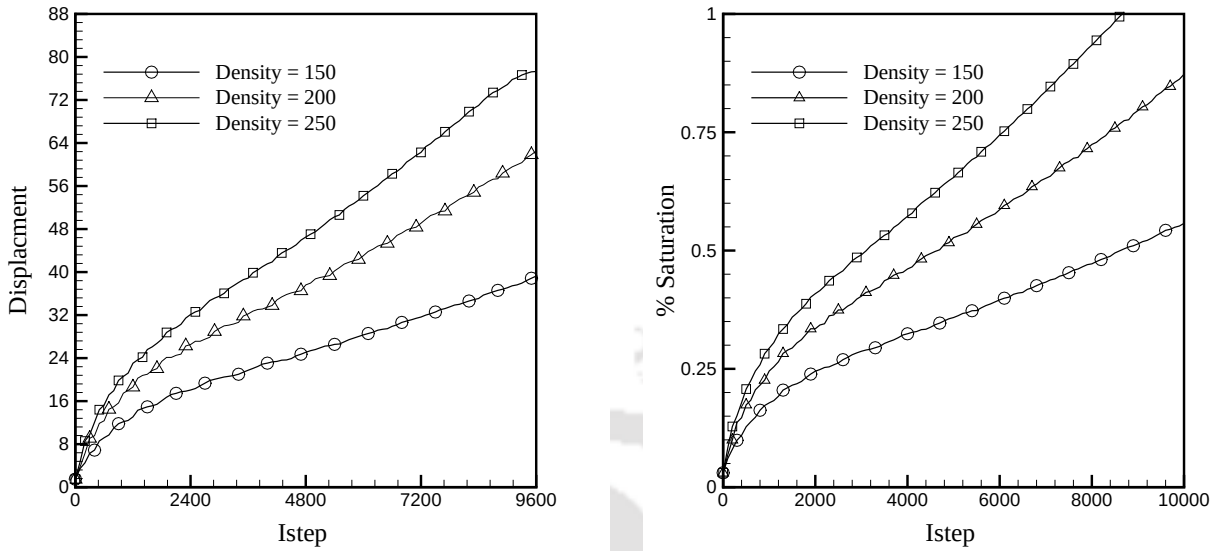

Figure 9.8: Effect of pressure on the advancement of fluid front: (a) mobilization of non-wetting phase, (b) percentage saturation with time

more for higher pressure gradient which is in line with our earlier observations in case of effect of force at the same time.

9.3.4 Effect of wettability on the response of the blob

In this section, an attempt is made to gain fundamental understanding about the effect of wall wetting characteristics on dynamics of the fluid flow through porous media. Wettability being the ability of one fluid to spread on a solid and form a wetting film [139] influences the fluid front movement. Also, there is a variation in the wettability of the rock surface depending on the composition of its constituents [154]. Hence the fluid flow is studied for the porous medium with uniform as well as mixed-wet surface. The mixed wettability describes the varying wetting characteristics of the solid wall comprised of hydrophilic (HI) and hydrophobic (HO) regions (see Fig. 9.10). Figure 9.11 shows the effect of wettability on fluid flow. If the invading fluid is wetting and fluid to be displaced to non wetting which is a typical case of imbibition; the advancement of fluid front is found to be more. This is mainly because the fluid already occupying the pore space is non wetting and its easier to move which reduces the resistance to the fluid flow through porous media.

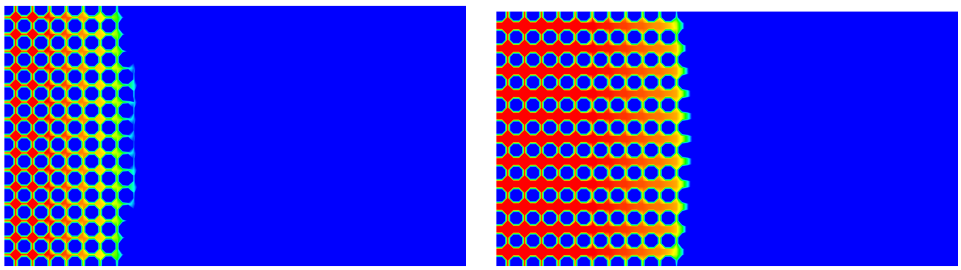

(a) (b)

Figure 9.9: Effect of pressure on fluid front movement at time istep = 8000 for ϕ = 0.65, (a) ρ = 150, (b) ρ = 250

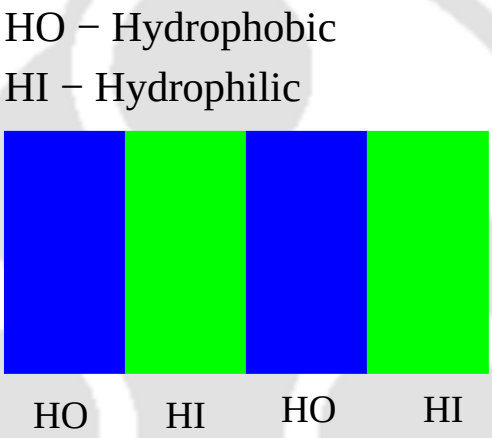

Figure 9.10: Schematic of the domain for mixed-wet configuration

Figure 9.12 shows the effect of strength of wettability on displacement of fluid. It can be seen that if the invading fluid is strongly wetting and fluid to be displaced is strongly non wetting, then displacement would be more. On the contrary, it is not same if the invading fluid is non-wetting in nature leading to less mean displacement. The percentage saturation also shows the same trend.

Figure 9.13 shows contour plot at time istep = 8000 for the invading fluid with different wettability. It can be seen that the invading fluid with g_{2w} = - 0.04 has undergone more displacement than that of the fluid with g_{2w} = - 0.02 and also the non wetting fluid with g_{2w} = 0.05 and 0.10. Displacement of fluid front is highly affected by the driving force although the capillary force remains significant. Figures

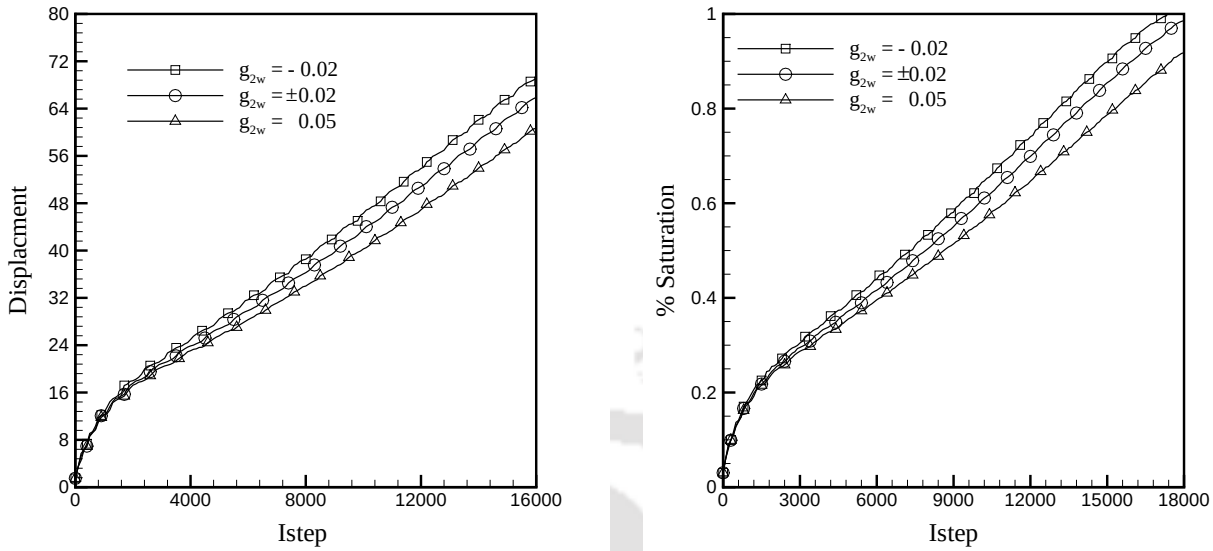

Figure 9.11: Effect of wettability on the advancement of fluid front: (a) mobilization of invading phase, (b) percentage saturation with time

9.14 and 9.15 show the location of fluid front at time istep = 8000 for magnitude of acoustic excitation keeping all other parameters constant. It can be observed that relative position of fluid front appears to be same when the magnitude of acoustic excitation is more i.e. $\delta W = 0.0005$ and the effect of wettability is not apparent. This is attributed basically to relative magnitude of forces causing the motion. Since driving force is more, the effect of wettability is not noticeable. On the contrary, it is very clear from Fig. 9.14 that the fluid front has travelled to a more extent when the invading fluid is hydrophilic. Here the driving force is relatively less and effect of wettability is clearly illustrated. Thus, it can be safely concluded that the flow of fluid is highly affected by the nature of wettability wherever driving force is not dominant.

9.3.5 Effect of porosity on the response of the blob

Porosity being the percentage of void space in a media is an indicative of the portion of the total volume that is not occupied by or isolated by solid material. The basic character of the pore space affects the nature of movement of water, air, and other fluids, the transport and the reaction of chemicals. The porosity of a rock depends

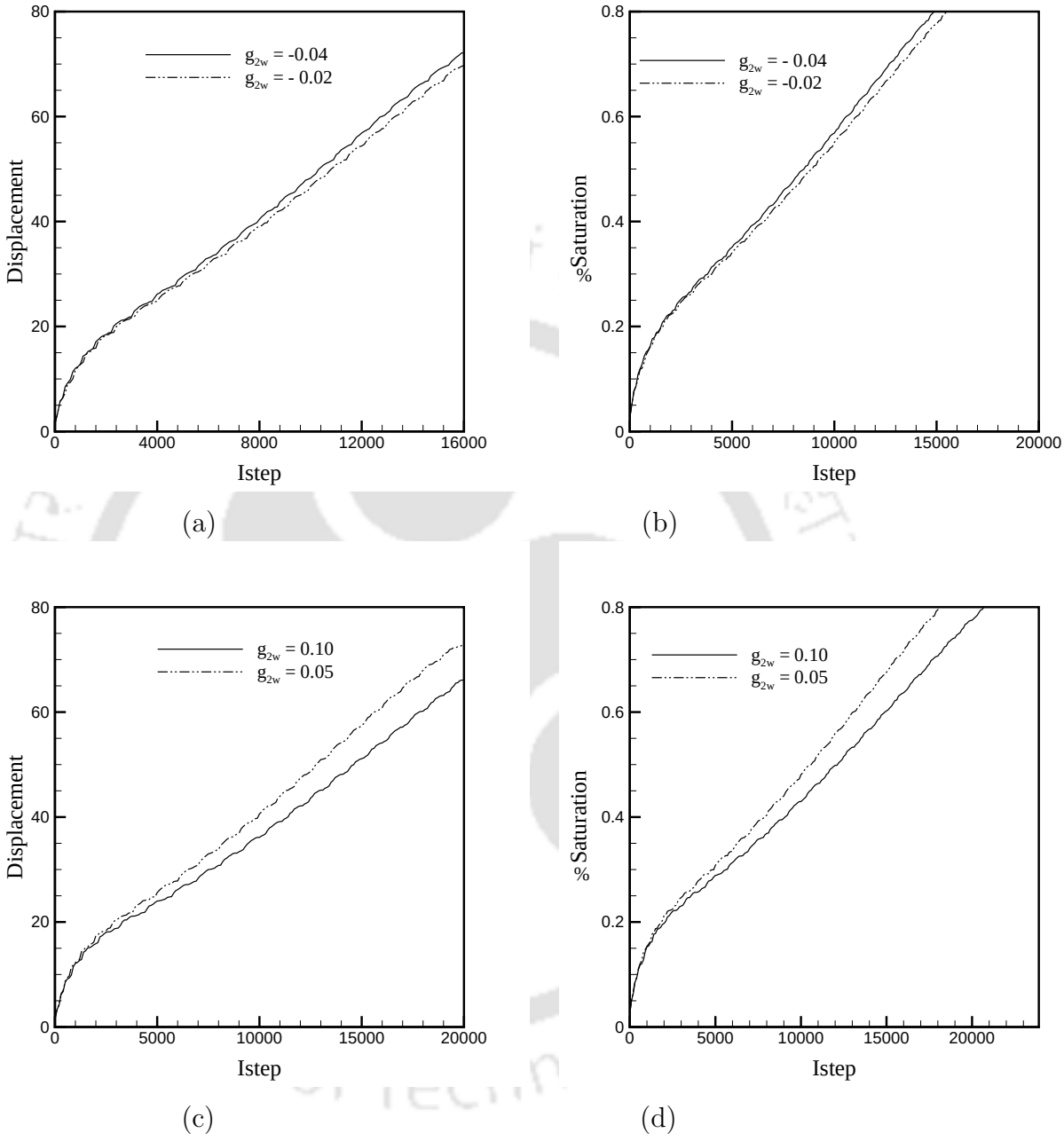

Figure 9.12: Effect of hydrophilicity: (a) mobilization of invading phase, (b) percentage saturation with time; Effect of hydrophobicity: (c) mobilization of invading phase, (d) percentage saturation with time

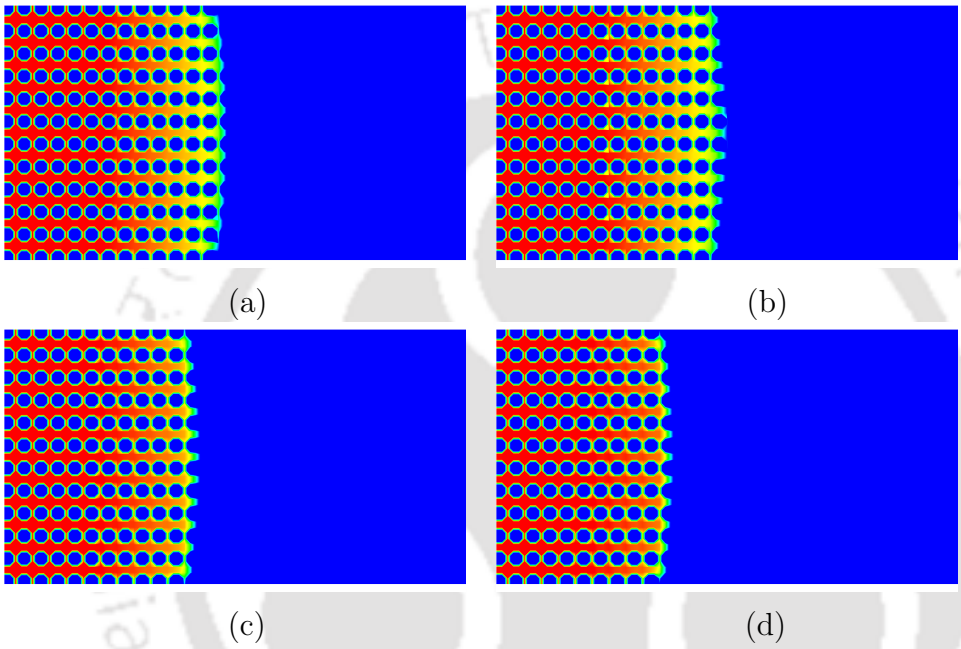

Figure 9.13: Effect of strength of wettability showing mobilization of wetting invading phase: Contour plot to show the effect of hydrophilicity, (a) g_{2w} = - 0.02, (b) g_{2w} = - 0.04; Contour plot to show the effect of hydrophobicity, (c) g_{2w} = 0.05, (d) g_{2w} = 0.10

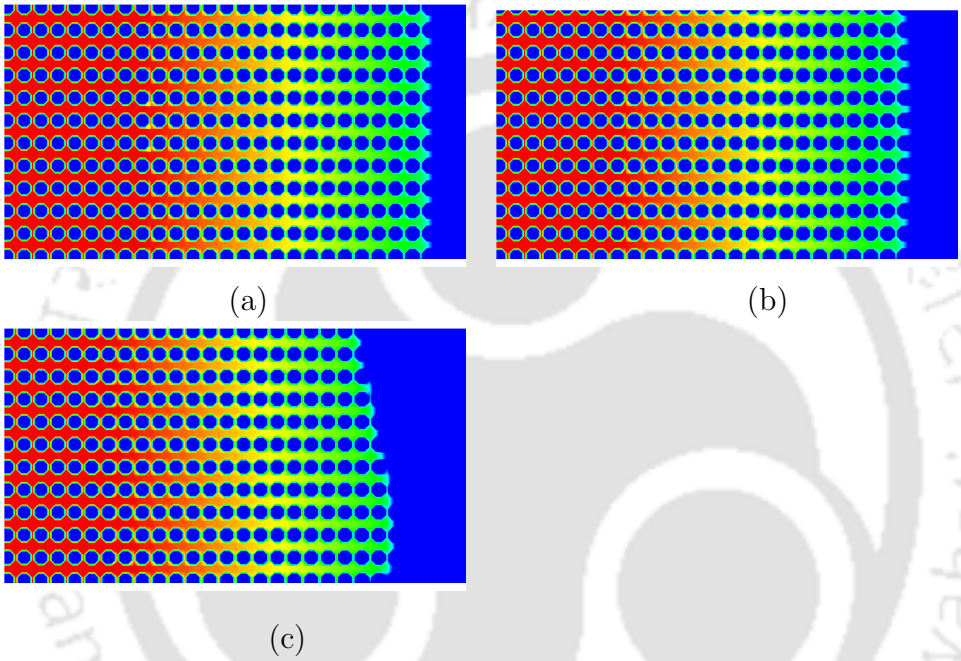

Figure 9.14: Effect of wettability on fluid front movement: contour plot at time istep = 22000 at $\phi = 0.65$ for $\delta W = 0.0001$: (a) g_{2w} = -0.02, (b) $g_{2w} = \pm$ 0.02, (c) $g_{2w} = 0.05$

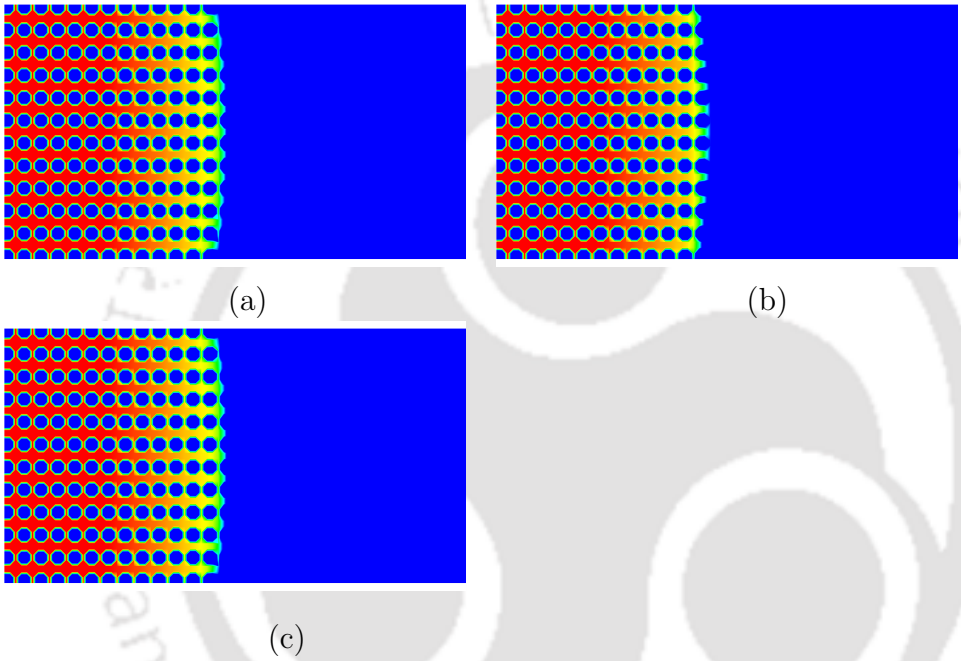

Figure 9.15: Effect of wettability on fluid front movement: contour plot at time istep = 22000 at $\phi = 0.65$ for $\delta W = 0.0005$: (a) g_{2w} = -0.02, (b) $g_{2w} = \pm$ 0.02, (c) $g_{2w} = 0.05$

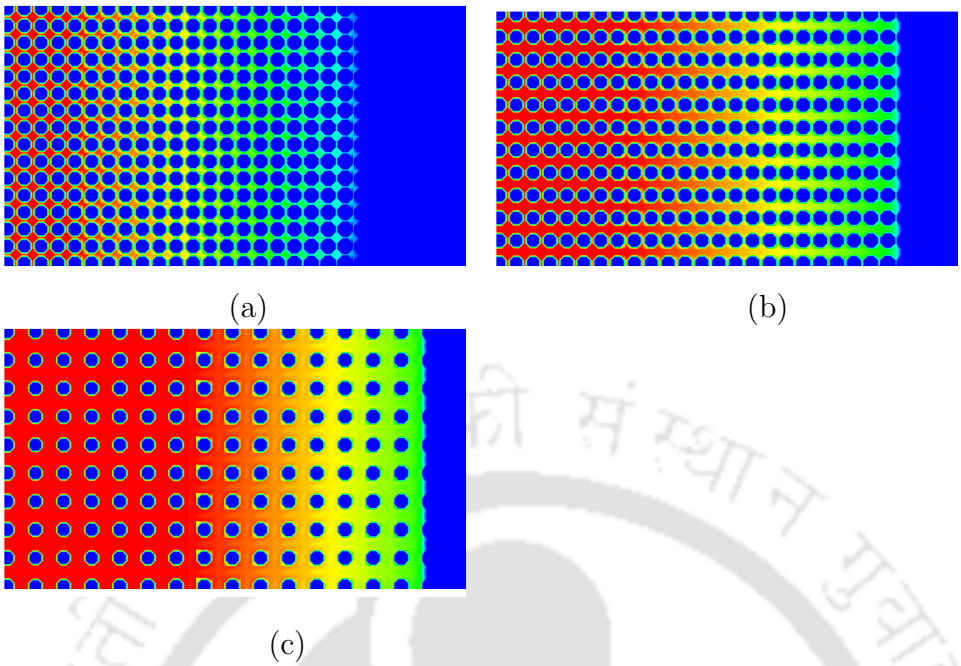

Figure 9.16: Effect of microporous structures with porosity: (a) $\phi = 0.54$, (b) $\phi = 0.65$, (c) $\phi = 0.80$

on many factors, including the type of rock and its composition along with the arrangement of grains of a rock. For example, crystalline rock such as granite has a very low porosity whereas the gas diffusion layer in the fuel cell shows [21] typically, have much higher porosities (0.6-0.65%). Porosity is very important in a porous medium, where the interface between the two fluids consists of many menisci and governs the nature of fluid flow. In this section, we have investigated the effect of porosity on the fluid flow. Figure 9.16 shows the different porous microstructures generated for the present study with porosity $\phi = 0.54$, 0.65 and 0.8.

It may be noted that the fluid advancement through porous media mainly depends on the relative magnitude of capillary forces, pressure gradient and acoustic force [160]. It can be seen from the Fig. 9.17 that the fluid front movement and also the percentage saturation are more in the porous media with higher porosity. This can be justified as the resistance to the flow is less at higher porosity due to less magnitude of capillary forces which tries to resist and restore the contact with surface. It can be seen from Fig. 9.18 at time istep = 8000 that the fluid has advanced more in case of higher porosity.

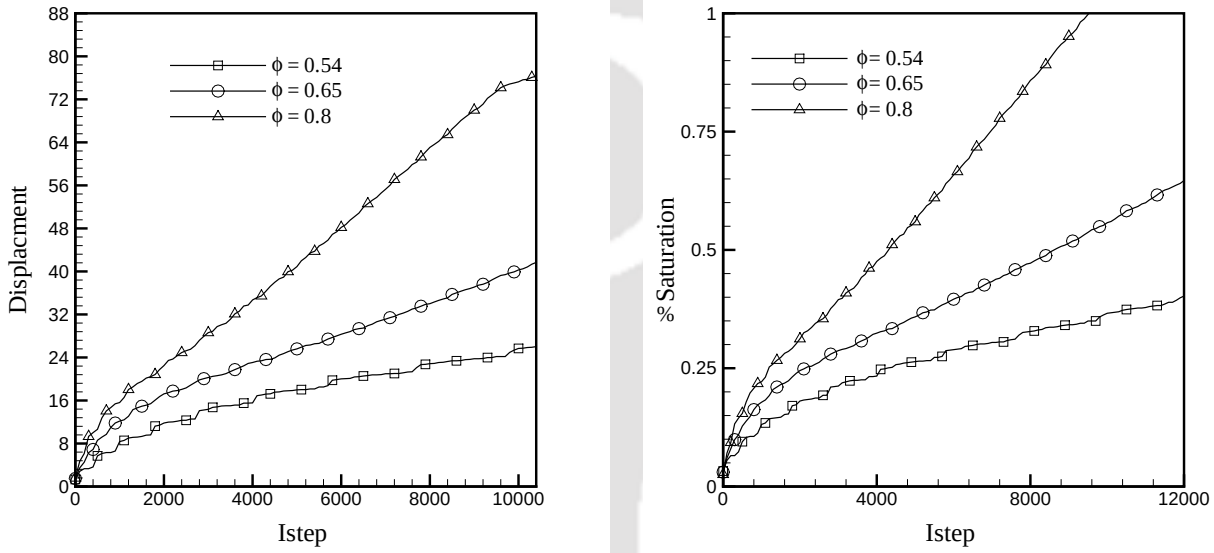

(a) (b)

Figure 9.17: Effect of porosity on the advancement of fluid front: (a) mobilization of non wetting phase, (b) percentage saturation with time

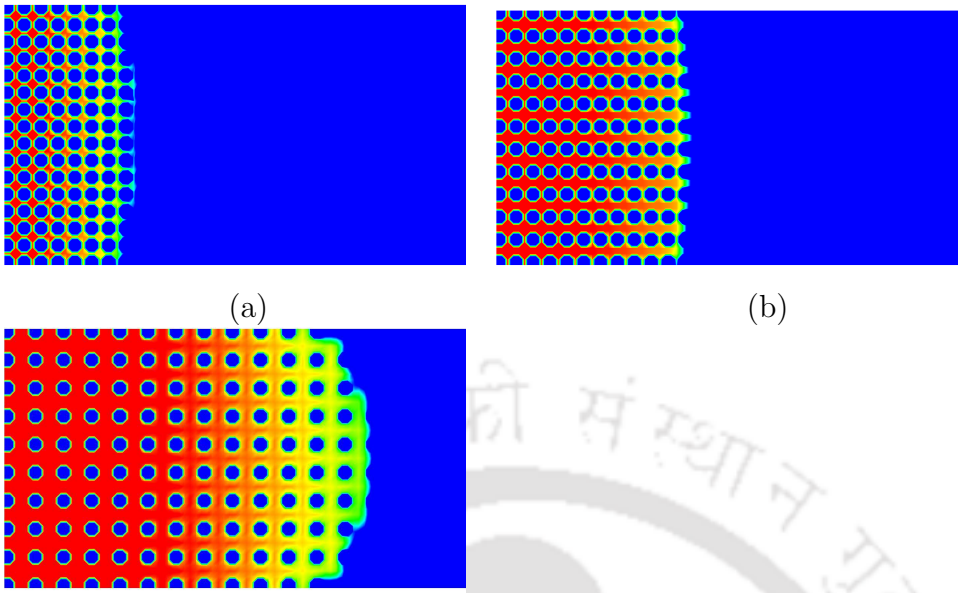

(a) (b)

(c)

Figure 9.18: Effect of porosity on fluid front movement for non wetting invading phase g_{2w}: contour plot at time istep = 8000 for (a) $\phi = 0.54$, (b) $\phi = 0.65$, (c) $\phi = 0.80$

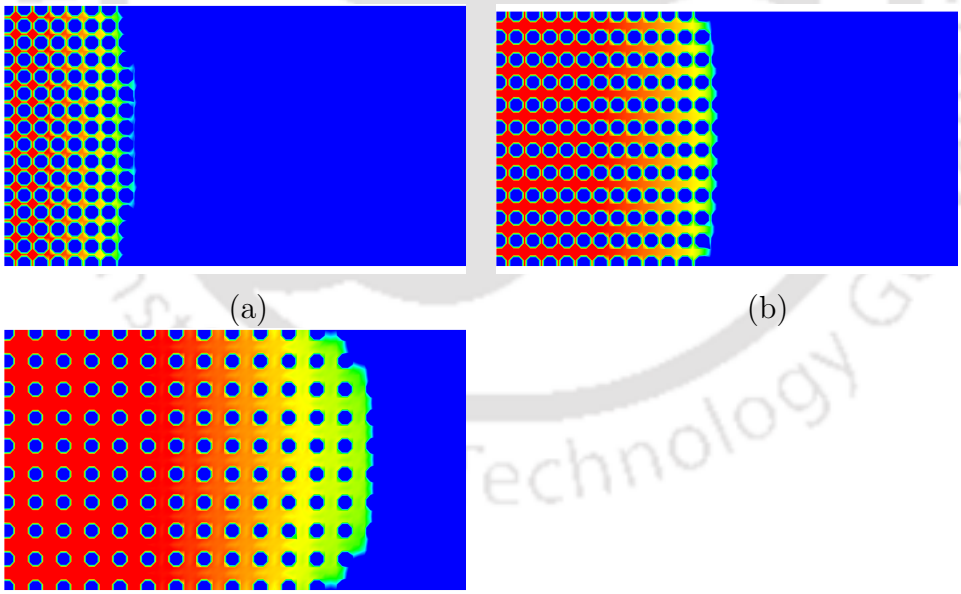

(a) (b)

(c)

Figure 9.19: Effect of porosity on fluid front movement for wetting invading phase g_{2w} : contour plot at time istep = 8000 for (a) $\phi = 0.54$, (b) $\phi = 0.65$, (c) $\phi = 0.80$

9.4 Closure

Fluid flow through porous media is studied to understand the effect of porosity and wettability on fluid flow under capillarity induced resonance. The present study reveals that the displacement of the fluid through porous media depends on parameters like wettability of the surface, frequency along with the porosity. Flow through the porous media with porosity $\phi = 0.54$, 0.65 and 0.8 has been discussed. It is found that the fluid advancement increases with porosity of medium. The study further emphasizes the importance of an optimal excitation of the fluid flow based on the frequency of excitation, amplitude of force applied and surface wettability for the mobilization of fluid flow which may be useful in porous networks.

Chapter 10

Conclusions and Future Work

10.1 Conclusions

The primary focus of this thesis work is to gain a detailed understanding of the underlying multiphase dynamics of liquid displacement due to gravitation and acoustic excitation. The capillarity wettability interaction in particular was explored to understand the effect of physicochemical parameters like wettability, geometry, angle of inclination, capillary number, confinement ratio and viscosity ratio on droplet dynamics. In addition to this, the transport of blob due to capillarity induced resonance was investigated in conjunction with the different wettability configuration. The fluid flow through the porous media is also studied to understand the effect of capillarity induced resonance, porosity and wettability on the advance of fluid front. In a nutshell, the overall influence of capillarity-wettability interaction on droplet and blob dynamics is discussed. The LBM Shan and Chen model is employed to study the above issues and the series of studies conducted to address these questions are summarised below.

Summary

In the chapter 1, the detailed background of the problems addressed in this research work is discussed. It is followed by the extensive literature survey including both experimental and numerical investigation on droplet and blob dynamics along with flow through porous media.

The LBM formulation with S-C model is discussed in chapter 2 in detail along with an analytical model implemented for studying the capillarity induced resonance. Also, the validation of the code and methodology is described in this chapter. The static droplet test and bubble test is carried out to calibrate the model. The validation results shows good agreement with that of the reported literature.

Chapter 3 discusses the importance of fundamental understanding of droplet dynamics and the concomitant implications of wall wettability. The mesoscopic illustration, based on the two-phase lattice Boltzmann model, of droplet dynamics in a microchannel is presented in order to unveil the role of superhydrophobicity and mixed wettability. The impact of critical physico-chemical determinants, including capillary number and droplet size is explored in the context of droplet-wettability interactions. Temporal evolution of wetted length and wetted area for a combination of wettability scenarios is furnished in detail in order to elucidate the droplet displacement dynamics. Although, the droplet motion on superhydrophobic surface is faster as compared to hydrophobic surface; the time evolution of wetted length and area exhibiting the similar character as that of hydrophobic region. For the mixed-wet surface, the wetted length and area keeps changing with time between maximum and minimum values. The alternately hydrophobic and hydrophilic nature of the surface results in elongation of droplet especially when it is in between these surfaces. It was observed that for higher capillary number effect of mixed wettabilty on droplet motion will not be significant anymore. However, for moderate capillary number effect of mixed wettability is important. The variation of wetted length and area for various wettabilty pattern is studied. It can be concluded that for the surface with the strong hydrophilicity followed by strong hydrophobicity i.e., $g_{2w} = \pm\ 0.16$ droplet motion is slower compared to other surfaces. It was observed that the effect of mixed wettability is not so significant for higher capillary number.

In chapter 4, the influence of wall wettability and viscosity on droplet dynamics are discussed to understand the viscosity-wettability interaction. Temporal evolution of wetted length and wetted area for a combination of viscosity ratios and wettability scenarios is furnished in detail in order to elucidate the droplet displacement dynamics. It is observed that capillary number and viscosity ratio play an important role with disparate droplet behavioral patterns stemming from uniform and mixed-wet

wall scenarios. It was observed that displacement of droplet is faster on hydrophobic and high viscosity ratio regimes. Time evolutions of wetted length and area show that with the increase in capillary number, droplet deforms to a more extent.

In Chapter 5, the effect of confinement on droplet dynamics is studied. The simulation has shown that the confinement ratio affects the dynamic behavior of droplet. The variation of wetted length and wetted area shows that change in droplet morphology is greater at low confinement ratios. However, the change in the droplet shape is a function of wettability also. It has been observed that the droplet shape is greatly affected by wettability and degree of confinement, especially at low capillary number. Excessive change in the morphology of the droplet is seen on hydrophobic surface as compared to hydrophilic surface for low confinement ratios.

Chapter 6 is devoted to the analysis of mobilization of trapped non wetting phase blob owing to capillarity induced resonance in a sinusoidal channel. The study deals with the dynamic behavior of a three dimensional blob subject to acoustic excitation using the lattice Boltzmann method. Both pinned and unpinned (sliding) configurations are studied. The effect of amplitude of the force, width of the channel, viscosity, wettability and frequency on mobilization of blob are discussed. The response of the blob at a resonant frequency on the surface with different wettabilities is explored. It has been observed that at resonating frequency blob exhibits peak displacement. The effect of wettability is not so significant at higher capillary numbers. However, at low capillary number, the wettability becomes the prominent factor to influence the mobilization of trapped blob.

Chapter 7 discusses effect of capillarity induced resonance on the mobilization of trapped non wetting phase blob in a tube with varying radius. In this context, the blob response in the tube with varying constriction subjected to an oscillatory force is investigated for pinned and sliding contact surfaces. The displacement of the blob is found to be more for the wider tube as compared to that of the narrower ones. The displacement of the blob is seen to be less for sliding contact line case as compared to the blob with pinned contact line. It can be concluded that the displacement of the blob decreases for the surfaces with mixed wettability as evident with less displacement as compared to the surface with uniform wettability. It can be observed that the excitation of a trapped blob near to its resonant fre-

quency results into a peak displacement of the blob. Resonance study for a range of capillary numbers shows that meniscus bending also is governed by wettability of the surface. Wettability-capillarity interaction is studied in depth to reveal the resonance behavior of the trapped blob on differently wetted surface for a range of capillary number.

Chapter 8 investigates the influence of geometrical configuration on transport of two-phase flows on the mobilization of the blob is concerned. The blob response has been found to be influenced with the structural resistance owing to the different geometries of the domain. The variable cross section of the domain affects the dynamics of the blob in a way that it offers more opportunities for the blob to get entrapped as compared to the domain with uniform cross-section. Thus, dynamics of the blob gets affected especially in terms of extent of displacement and the force required to mobilize the blob. Nevertheless, the resonance frequency will remain unaffected by the change in the curvature of geometry as long as the mean radius of the channel remains same. This is so because the resonating frequency is function of mean radius. The mobilization study for the trapped blob in a domain with variable cross-section is undertaken. The geometries considered for this study includes tube with varying constriction, sinusoidal and convergent-divergent channel. Although, present work does not intend to compare the mobilization of the blob with different geometries, it gives the insight into the effect of geometries on mobilization of the blob. It was observed that for the geometries with varying cross-section the overall extent of displacement is less for the same excitation as compared to the geometries with constant cross sections.

Chapter 9 presents the study on displacement of the fluid through porous media. The work reveals that the fluid flow depends on parameters like wettability of the surface, frequency along with the porosity. It is seen that vibration in form of acoustic excitation can prove to be significant in the mobilization of fluid through the porous media. The mean displacement of the fluid is more in the case of invading fluid with wetting phase.The effect is found to be more pronounced where the driving force is not dominant. It was seen that the fluid advancement increases with porosity of medium. The study further emphasizes the fact that optimal excitation of the fluid flow based on the frequency of excitation, amplitude of force applied and surface wettability for the mobilization of fluid flow which may be useful in porous networks.

Lastly, it can be argued that the optimal excitation strategy with regards to the mobilization of the blob needs the insight into the effect of the parameters such as wettability, capillarity induced resonance and capillary number. This study is one such attempt in this direction to understand the multiphase dynamics.

10.2 Future Scope of Work

The combined pore-scale modeling and mesoscopic analysis presented in the this thesis suggest the following recommendations for future study with the aim to enhance the overall understanding of capillarity-wettability interaction and also to address some of the important transport phenomena in multiphase flow.

The study of droplet motion described earlier indicates the importance of wall wettability on liquid water transport. Present lattice Boltzmann model does not consider the effect of temperature. However, temperature affects the fluid flow in geophysical applications such as oil recovery. Hence, there is a need to include the effect of temperature while studying the effect of wall wettability on liquid transport. In this regard, the present LB model can be extended to include non-isothermal effects. Furthermore, coalescence of droplets on a solid surface with different wettability configurations can be investigated. The present code can be used to study the wettability behavior of coalescence of two or more droplet on hydrophobic, superhydrophobic, hydrophilic or mixed-wettable surfaces. Also, investigation on droplet dynamics could be extended considering the effect of dynamic contact angle. This study will provide further insight into the structure-wettability relation and the underlying two-phase dynamics in general.

The study of blob dynamics is explored in conjunction with different wettability scenarios. It would be more insightful to investigate whether the continuous transport of a trapped blob is best achieved by constantly varying the excitation frequency ω. Also, the response of the blob with a spectrum of frequencies can be investigated in order to adjust to the constantly changing resonant frequency of a mobilized blob. Since the size and distribution of blob vary and so also, the resonant frequency, the details study can be undertaken to address this issue. Consideration of the effect of temperature variation on blob dynamics will make the predictions and the results

more accurate. The transport of non wetting phase through disc packings would be an interesting study to devise a more realistic and optimal excitation strategy which might result in a significant mobilization of residual non wetting phase.

The present work is an attempt to evaluate the fluid flow through porous media subject to acoustic excitation. The porous media used for the study is simple in configuration with uniform arrangement of pores. The study of fluid flow on random porous structure under capillarity induced resonance would bolster the understanding of transport through porous media.

References

[1] Hilpert M. (2007) 'Capillarity-induced resonance of blobs in porous media: analytical solutions, lattice-boltzmann modeling, and blob mobilization', *J. Collide Interface Sci.*, vol. 309, pp. 493–504.

[2] Gunstensen A.K., Rothman D.H., Zaleski S., and Zanetti G. (1991) 'Lattice boltzmann model of immiscible fluids', *Phys. Rev. A*, vol. 43, pp. 4320–4327.

[3] Shan X., Chen H., Prasad P.L.N., and Basu S. (1993) 'Lattice boltzmann model for simulating flows with multiple phases and components', *Phys. Rev. E*, vol. 47, pp. 1815–1817.

[4] Shan X. and Doolen G. (1995) 'Multicomponent lattice-boltzmann model with interparticle interaction', *J. Stat. Phys.*, vol. 81(4), pp. 379–393.

[5] Swift M., Osborn W., and Yeomans J. (1995) 'Lattice boltzmann simulation of nonideal fluids', *Phys. Rev. Lett.*, vol. 75, pp. 830–833.

[6] He B., Patankar N.A., and Lee J. (2003) 'Multiple equilibrium droplet shapes and design criterion for rough hydrophobic surfaces', *Langmuir*, vol. 19, pp. 4999–5003.

[7] Kulkarni M.M. (2003) 'Immsicible and miscible gas-oil displacements in poorus media', *Ph. D. thesis, Department of Petroleum Engineering, Louisiana State University, USA*.

[8] Bico J., Marzolin C., and Quere D. (1999) 'Pearl drops', *Europhys. Lett*, vol. 47, pp. 220–226.

[9] Protiere S., Bazant M.Z., Weitz D.A., and Stone H.A. (2010) 'Droplet break-up in flow past an obstacle: A capillary instability due to permeability variations', *Euro Phy. Letter*, vol. 92, pp. 54002(1–6).

[10] Kang Q., Zhang D., and Chen S. (2002) 'Displacement of a two dimensional immiscible droplet in a channel', *Phys. of Fluids*, vol. 40, pp. 3203–3214.

[11] Kang Q., Zhang D., and Chen S. (2005) 'Displacement of a two dimensional immiscible droplet in a channel', *J. Fluid Mech.*, vol. 545, pp. 41–66.

[12] Feuillebois F., Bazant M.Z., and Vinogradova O.I. (2010) 'Transverse flow in thin super hydrophobic channels', *Phy. Rev.E*, vol. 82, pp. 055301,(1–4).

[13] Quere D. (2005) 'Non-sticking drops', *Rep. Prog. Phys.*, vol. 68, pp. 2495–2532.

[14] Francois F., Bazant M.Z., and Vinogradova O.I. (2009) 'Effective slip over superhydrophobic surfaces in thin channels', *Phy. Rev. Letter*, vol. 102, p. 026001.

[15] Wang R. and Hashimot K. (1997) 'Light-induced amphiphilic surfaces', *Nature*, vol. 388, pp. 431–432.

[16] Choi K.S. and Yang. X. (1997) 'Turbulent drag reduction using compliant surfaces', *Phys. Eng. Sci*, vol. 453, pp. 2229–2240.

[17] Ou J., Perot B., and Rothstein J.P. (2004) 'Laminar drag reduction in microchannels using ultrahydrophobic surfaces', *Phys. of Fluids*, vol. 16, pp. 4635–4644.

[18] Tsai P., Pacheco S., Pirat C., Lefferts L., and Lohse D. (2009) 'Drop impact upon micro- and nanostructured superhydrophobic surfaces', *Langmuir*, vol. 25, pp. 12293–12298.

[19] Reyssat M., Richard D., Clanetab C., and Queer D. (2010) 'Dynamical superhydrophobicity', *Faraday Discuss. The J. Royal Society of Chemistry*, vol. 146, pp. 19–33.

[20] Kwak N.G., Lee M., Senthil K., and Yong K. (2010) 'Wettability control and water droplet dynamics on sic-sio2 core-shell', *Langmuir*, vol. 26, pp. 12273–12277.

[21] Mukherjee P.P. (2007) 'Pore-scale modeling and analysis of the polymer electrolyte fuel cell catalyst layer', *Ph. D. Thesis Department of Mechanical Engineering Pennsylvania State University,USA*.

[22] Mukherjee P.P., Wang C., and Kang Q. (2009) 'Mesoscopic modeling of two-phase behavior and flooding phenomena in polymer electrolyte fuel cells', *Electrochim. Acta*, vol. 54, pp. 6861–6875.

[23] Mukherjee P.P., Kang Q., and Wang C. (2011) 'Pore-scale modeling of two-phase transport in polymer electrolyte fuel cells-progress and perspective', *Energy Environ. Sci.*, vol. 4, pp. 346–369.

[24] Wang Y., Chen K., Mishler J., Cho S.C., and Adroher X.C. (2011) 'A review of polymer electrolyte membrane fuel cells: Technology, applications, and needs on fundamental research', *Applied Energy*, vol. 88, pp. 981–1007.

[25] Adroher X.C. and Wang Y. (2011) 'Ex-situ and modeling study of two-phase flow in a single channel of polymer electrolyte membrane fuel cells', *J. Power Sources*, vol. 196, pp. 9544–9551.

[26] Cho S.C., Wang Y., and Chen K.S. (2012) 'Droplet dynamics in a polymer electrolyte fuel cell gas flow channel: Forces, deformation, and detachment. i: Theoretical and numerical analyses', *J. Power Sources*, vol. 206, pp. 119–128.

[27] Cho S.C., Wang Y., and Chen K.S. (2012) 'Droplet dynamics in a polymer electrolyte fuel cell gas flow channel: Forces, deformation and detachment. ii: Comparisons of analytical solution with numerical and experimental results', *J. Power Sources*, vol. 210, pp. 191–197.

[28] Hao L. and Cheng P. (2010) 'Lattice boltzmann simulations of water transport in gas diffusion layer of a polymer electrolyte membrane fuel cell', *J. Power Sources*, vol. 195, pp. 3870–3881.

[29] Salah Y., Tabe Y., and Chikahisa T. (2012) 'Two phase flow simulation in a channel of a polymer electrolyte membrane fuel cell using the lattice boltzmann method', *J. Power Sources*, vol. 199, pp. 85–93.

[30] Chang Q. and Alexander J.I.D. (2006) 'Analysis of single droplet dynamics on striped surface domains using a lattice boltzmann method', *Microfluid Nanofluidics*, vol. 2(4), pp. 309–326.

[31] Zu Y.Q. and Yan Y.Y. (2011) 'Lattice boltzmann method for modelling droplets on chemically heterogeneous and microstructured surfaces with large liquidgas density ratio', *J. Applied Math.*, vol. 76(5), pp. 743–760.

[32] Huang J.J., Shu C., and Chew Y.T. (2008) 'Numerical investigation of transporting droplets by spatiotemporally controlling substrate wettability', *J. Colloid Interface Science*, vol. 328, pp. 124–133.

[33] Sinha P.K. and Wang C.Y. (2008) 'Liquid water transport in a mixed-wet gas diffusion layer of a polymer electrolyte fuel cell', *Chem. Eng. Sci.*, vol. 63, pp. 1081–1091.

[34] Lauga E. and Stone H.A. (2003) 'Effective slip in pressure-driven stokes flow', *J. Fluid Mech.*, vol. 489, pp. 55–77.

[35] Davies J., Maynes D., Woolford B., and Webb B.W. (2006) 'Laminar flow in a microchannel with superhydrophobic walls exhibiting transverse ribs', *Phys. of Fluids*, vol. 18, pp. 087110 (1–11).

[36] Zhang J. and Kwok D. (2006) 'Contact line and contact angle dynamics in superhydrophobic channels', *Langmuir,*, vol. 22, pp. 4998–5004.

[37] Osborn W.R., Orlandini E., Swift M.R., Yeomans J.M., and Banavar J.R. (1995) 'Lattice boltzmann study of hydrodynamic spinodal decomposition', *Phys. Rev. Letter*, vol. 75, pp. 4031–4034.

[38] He X.Y., Chen S.Y., and Zhang R.Y. (1999) 'A lattice boltzmann scheme for incompressible multiphase flow and its application in simulation of rayleigh-taylor instability', *J. Comp. Phys.*, vol. 152, pp. 642–663.

[39] Taylor G.I. (1932) 'The viscosity of a fluid containing small drops of another fluid', *Proc. R. Soc. London, Ser. A*, vol. 138, pp. 41–48.

[40] Taylor G.I. (1934) 'The formation of emulsions in definable fields of flow', *Proc. R. Soc. London, Ser. A*, vol. 146, pp. 501–523.

[41] Guido S. and Greco F. (2004) 'Dynamics of a liquid drop in a flowing immiscible liquid', *Rheology Reviews 2004, The British Society of Rheology 2004*, pp. 99–142.

[42] Borhan A. and Mao C.F. (1992) 'Effect of surfactants on the motion of drops through circular tubes', *Phys. of Fluids A*, vol. 4, pp. 2628–2640.

[43] Mangaa M. (1996) 'Dynamics of drops in cavity flows: Aggregation of high viscosity ratio drops', *Phys. of Fluids*, vol. 8(7), pp. 1732–1737.

[44] Dimitrakopoulos P. and Higdon J.J.L. (1997) 'Displacement of fluid droplets from solid surfaces in low reynolds number shear flows', *J. Fluid Mech.*, vol. 336, pp. 351–378.

[45] Schleizer A.D. and Bonnecaze R.T. (1998) 'Displacement of a two-dimensional immiscible droplet adhering to a wall in shear and pressure-driven flows', *J. Fluid Mech.*, vol. 383, pp. 29–54.

[46] Boonen E., Puyvelde P.V., and Moldenaers P. (2011) 'Droplet dynamics in mixed flow conditions: Effect of shear elongation balance and viscosity ratio', *J. Rheol.,*, vol. 54, pp. 1285–1306.

[47] Fakhari A. and Rahimian M.H. (2009) 'Simulation of falling droplet by the lattice boltzmann method', *Commun Nonlinear Sci. Numerical Simulation*, vol. 14, pp. 3046–3055.

[48] Zhang J. and Kwok D.Y. (2004) 'Lattice boltzmann study on the contact angle and contact line dynamics of liquid-vapor interfaces', *Langmuir*, vol. 20, pp. 8137–8141.

[49] Hazlett R.D. and Vaidya R.N. (2002) 'Lattice boltzmann simulations and contact angle hysteresis in convergent-divergent media', *J. Pet. Sci. Eng.*, vol. 33, pp. 161–171.

[50] Aminfar H. and Mohammad M. (2009) 'Lattice boltzmann method for electrowetting modelling and simulation', *Comput. Methods Appl. Mech. Engg*, vol. 198, pp. 3852–3868.

[51] Cui J., Li W., and Lam W. (2011) 'Numerical investigation on drag reduction with superhydrophobic surfaces by lattice-boltzmann method', *Comput. Math. Appl.*, vol. 61(12), pp. 3678–3689.

[52] Mukherjee. S. and Abraham J. (2007) 'Investigations of drop impact on dry walls with a lattice-boltzmann model', *J. Colloid Interface Sci*, vol. 312, pp. 341–354.

[53] Kawasaki A., Onishi J., Chen Y., and Ohashi H. (2008) 'A lattice boltzmann model for contact-line motions', *Comput. Math. Appl.*, vol. 55, pp. 1492–1502.

[54] Kumari N., Bahadur V., and Garimella S.V. (2008) 'Electrical actuation of dielectric droplets', *J. Micromech. Microeng.*, vol. 18, pp. 085018– 085026.

[55] Kumar A., Williams S.J., Chuang H., Greend N.G., and Wereleye S.T. (2011) 'Hybrid opto-electric manipulation in microfluidicsopportunities and challenges', *Lab Chip*, vol. 11, pp. 2135–2148.

[56] Dupuis A. and Yeomans J.M. (2005) 'Modeling droplets on superhydrophobic surfaces: Equilibrium states and transitions', *Langmuir*, vol. 21, pp. 2624–2629.

[57] McHale G., Shirtcliffe N.J., and Newton M.I. (2004) 'Contact-angle hysteresis on super-hydrophobic surfaces', *Langmuir*, vol. 20, pp. 10146–10149.

[58] Baumann N., Joseph D.D., Mohr P., and Renardy Y. (1992) 'Vortex rings of one fluid in another in free fall', *Phys. of Fluids A*, vol. 4, pp. 567–582.

[59] Wawersik W.R. (2000) 'Terrestrial sequestration of co 2: An assessment of research needs', *Adv. Geophys.*, vol. 43, pp. 97–177.

[60] Duhon R.D. (1964) 'An investigation of the effect of ultrasonic energy on the flow of fluids in porous media', *Ph. D. thesis, University of Oklahoma, USA*.

[61] Gadiev S.M. (1977) 'Use of vibrations in oil production', *(in Russian) Nedra Press, Moscow*.

[62] Steinbrugge K.V. and Moron D.F. (1954) 'An engineering study of the southern california earthquake of july 21, 1952, and its after shocks:', *Bull. Seis. Soc. Am.*, vol. 44, pp. 277–283.

[63] Gardescu I.I. (1930) 'Behavior of gas bubbles in capillary spaces', *Petroleum Transactions, AIME*, vol. 86, pp. 351–370.

[64] Taber J.J. (1969) 'Dynamic and static forces required to remove a discontinuous oil phase from porous media containing both oil and water', *SOC PETROL ENG J.*, vol. 9, pp. 3–12.

[65] Beresnev I.A. and Johnson P.A. (1994) 'Elastic-wave stimulation of oil production: A review of methods and results', *Geophys.*, vol. 59(6), pp. 1000–1017.

[66] Roberts P.M., Sharma A., Uddameri V., Monagle M., Dale D.E., and Steck L.K. (2001) 'Enhanced dnapl transport in a sand core during dynamic stress stimulation:', *Environ. Eng. Sci.*, vol. 18, pp. 67–79.

[67] Li W., Vigil R.D., Beresnev I.A., Iassonov P., and Ewing R. (2005) 'Vibration-induced mobilization of trapped oil ganglia in porous media: Experimental validation of a capillary-physics mechanism', *J. Colloid Interface Sci.*, vol. 289, pp. 193–199.

[68] Occidental (2005) 'Value of in-situ seismic wavesregain lost reserves, increase oil cut', *J. Petroleum Tech.*, pp. 24–25.

[69] Hilpert M., Stopper D., and Jirka G.H. (1999) 'Resonance of a liquid column in a capillary tube', *Z. Angew. Math. Phys.*, vol. 48, pp. 424–438.

[70] Hilpert M., Jirka G.H., and Plate E. (2000) 'Capillarity-induced resonance of oil blobs in capillary tubes and porous media', *Geophys.*, vol. 65, pp. 874–883.

[71] Margolus N., Toffoli T., and Vichniac G. (1986) 'Cellular-automata super computers for fluid-dynamics processing', *Phys. Rev. Letter*, vol. 56, pp. 1694–1696.

[72] Chen H., Chen S., Doolen G., and Lee Y.C. (1988) 'Simple lattice gas models for waves', *Complex Systems*, vol. 2, pp. 259–267.

[73] Mavko G. and Nur A. (1979) 'Wave attenuation in partially saturated rocks', *Geophys.*, vol. 44, pp. 161–178.

[74] Palmer I.D. and Traviolia M.L. (1980) 'Attenuation by squirt flow in under-saturated gas sands', *Geophys.*, vol. 45, pp. 1780–1792.

[75] Santos J.E., Corbero J.M., and Douglas J. (1990) 'Static and dynamic behavior of a porous solid saturated by a two-phase fluid', *J. Acoust. Soc. Am.*, vol. 87, pp. 1428–1438.

[76] Tuncay. K. and Corapcioglu M.Y. (1996) 'Body waves in poroelastic media saturated by two immiscible fluids', *J. Geophys. Res.*, vol. 101(3), pp. 25149–25159.

[77] Murphy W.F. (1982) 'Effects of partial water saturation on attenuation in massilon sandstone and vycor porous glass', *J. Acoust. Soc. Am.*, vol. 71(6), pp. 1458–1468.

[78] Kostrov S., Wooden W., and Roberts P. (2001) 'In situ seismic shockwaves stimulate oil. production', *Oil Gas J.*, vol. 99(36), pp. 47–52.

[79] Roberts P., Esipov L., and Majer E. (2003) 'Elastic wave stimulation of oil reservoirs: Promising eor technology?', *The Leading Edge*, vol. 22(5), pp. 448–453.

[80] Beresnev I. and Johnson A. (1994) 'Elastic-wave stimulation of oil production:a review of methods and results', *Geophys.*, vol. 59(6), pp. 1000–1017.

[81] Amili P. and Yortsos Y. (2006) 'Darcian dynamics: A new approach to the mobilization of a trapped phase in porous media', *Trans. Porous Media*, vol. 64, pp. 25–49.

[82] Dias M. and Payatakes A. (1986) 'Network models for two-phase flow in porous media. ii: Motion of oil ganglia', *J. Fluid Mech*, vol. 164, pp. 337–358.

[83] Hunt J.R., Sitar N., and Udell K.S. (1988) 'Nonaqueous phase liquid transport and cleanup: 1. analysis of mechanisms', *Water Resour. Res.*, vol. 24(8), pp. 1247–1258.

[84] Dimon P., Kushnick A., and Stokes J.P. (1988) 'Resonance of a liquid-liquid interface', *J. Phys.*, vol. 49(5), pp. 777–785.

[85] Charlaix E. and Gayvallet H. (1992) 'Dynamics of a harmonically driven fluid interface in a capillary', *J. Phys.*, vol. 75, pp. 2025–2038.

[86] Iassonov P.P. and Beresnev I.A. (2003) 'A model for enhanced fluid percolation in porous media by application of low-frequency elastic waves', *J. Geophys. Res.*, vol. 108, pp. 2138–2146.

[87] Palan P., Shepard W.S., and Williams K.A. (2006) 'Removal of excess product water in a pem fuel cell stack by vibrational and acoustical methods', *J. Power Sources*, vol. 161, pp. 1116–1125.

[88] Buick D.M., Cosgrove J.A., Campbell D.M., and Greated C.A. (2004) 'Numerical simulation of particle motion in an ultrasound field using the lattice boltzmann model', *J. Ultrasonics*, vol. 43, pp. 21–25.

[89] Lahbabi A. and Chang H.C. (1986) 'Flow in periodically constricted tubes:transition to inertial and nonsteady flows', *Chem. Eng. Sci.*, vol. 41, pp. 2487–2505.

[90] Payatakes A.C., Tien C., and Turian R.M. (1973) 'A new model for granular porous media: Parts 1 and 2', *AIChE J.*, vol. 19, pp. 58–67.

[91] Bernabe Y. and Olson J.F. (2000) 'The hydraulic conductance of a capillary with a sinusoidally varying cross-section', *Geophys. Res. Lett.*, vol. 27, pp. 245–258.

[92] Koplik J. (1982) 'Creeping flow in two-dimensional networks', *J. Fluid Mech.*, vol. 119, pp. 219–247.

[93] Pilitsis S. and Beris A.N. (1989) 'Calculations of steady-state viscoelastic flow in an undulating tube', *J. Non-Newt. Fluid Mech.*, vol. 31, pp. 231–287.

[94] Powers S.E., Abriola L.M., and Jr. W.J.W. (1992) 'An experimental investigation nonaqueous of phase liquid dissolution saturated subsurface systems: Steady state mass transfer rates', *Water Resour. Res.*, vol. 28(10), pp. 2691–2705.

[95] Miller C.T., Poirier-McNeill M.M., and Mayer A.S. (1990) 'Dissolution of trapped non aqueous phase liquids: Mass transfer characteristics', *Water Resour. Res.*, vol. 26(11), pp. 2783–2796.

[96] Reeves P.C. and Celia M.A. (1996) 'A functional relationship between capillary pressure, saturation and interfacial area as revealed by a pore-scale network model', *Water Resour. Res.*, vol. 32(8), pp. 2345–2358.

[97] Y.Zhao (2009) 'A novel lattice boltzmann method for direct numerical simulation of multiphase flows', *Ph. D. thesis, Ohio State University.*

[98] Hilpert M. and Ben-David A. (2009) 'Infiltration of liquid droplets into porous media: Effects of dynamic contact angle and contact angle hysteresis', *Int. J. Multiphase Flow*, vol. 35, pp. 205–218.

[99] Saffman P.G. and Taylor G. (1958) 'The penetration of a fluid into a porous medium or hele-shaw cell containing a more viscous liquid', *Proceedings of the Royal Society of London, Series A*, vol. 245, pp. 312–329.

[100] Larson R.G., Davis H.T., , and Scriven L.E. (1980) 'Displacement of residual nonwetting fluid from porous media', *Chem. Eng. Sci.*, vol. 36, pp. 75–85.

[101] Dullien F.A.L., *Porous Media: Fluid Transport and Pore Structure* (Academic Press, San Diego, CA, 1992).

[102] Jamaloei B.Y., Asghari K., and Kharrat R. (2011) 'Pore-scale flow characterization of low-interfacial tension flow through mixed-wet porous media with different pore geometries', *Experimental Thermal and Fluid Sci.*, vol. 35, pp. 253–264.

[103] de Gennes P.G. (1985) 'Wetting: Statics and dynamics', *Rev. Mod. Phys.*, vol. 57(3), pp. 827 – 863.

[104] Karapetsas G., Sahu K.C., and Matar O.K. (2013) 'Effect of contact line dynamics on the thermocapillary motion of a droplet on an inclined plate', *Langmuir*, vol. 29, pp. 8892–8906.

[105] Dawson G., Lee S., and Juel A. (2013) 'The trapping and release of bubbles from a linear pore', *J. Fluid Mech.*, vol. 722, pp. 437–460.

[106] Mondal B., Jiao K., and Li X. (2011) 'Three-dimensional simulation of water droplet movement in pem fuel cell flow channels with hydrophilic surfaces', *Int. J. Energy Research*, vol. 35(13), pp. 1200–1212.

[107] Kang Q., Lichtner P.C., and Janecky D.R. (2011) 'Lattice boltzmann method for reacting flows in porous media', *Adv. Appl. Math. Mech.*, vol. 2(2), pp. 545–563.

[108] Kang Q., Wang M., Mukherjee P.P., Lichtner P.C., and Janecky D.R. (2010) 'Mesoscopic modeling of multiphysicochemical transport phenomena in porous media', *Advances in Mechanical Engineering*, vol. 2(2), pp. 545–563.

[109] Cercignani C. (2005) 'The boltzmann equation and its applications', *J. Appl. Dynamical Systems*, vol. 4, pp. 711–732.

[110] Succi S., *The Lattice Boltzmann Equation: For Fluid Dynamics and Beyond* (Oxford University Press, 2001).

[111] Bhatnagar P.L., Gross E.P., and Krook M. (1954) 'A model for collision processes in gases. i. small amplitude processes in charged and neutral one-component systems', *Phys. Rev.*, vol. 94, pp. 511–525.

[112] Hardy J., Pomeau Y., and Pazzis O. (1973) 'Time evolution of a two-dimensional model system. i. invariant states and time correlation functions', *J. Math. Phys.*, vol. 14(12), p. 1746.

[113] Frisch U., Hasslacher B., and Pomeau Y. (1986) 'Lattice-gas automata for the navier-stokes equation', *Phys. Rev. Lett.*, vol. 56, pp. 1505–1508.

[114] Frisch U., Humieres D., Hasslacher B., Lallemand P., Pomeau Y., and Rivet J.P. (1987) 'Lattice gas hydrodynamics in two and three dimensions', *Complex Systems*, vol. 1, pp. 649–707.

[115] McNamara G.R. and Zanetti G. (1988) 'Use of the boltzmann equation to simulate lattice-gas automata', *Phys. Rev. Lett.*, vol. 61, pp. 2332–2335.

[116] Higuera F., Succi S., and Benzi R. (1989) 'Lattice gas dynamics with enhanced collisions', *Europhys. Lett.*, vol. 9(4), pp. 345–349.

[117] Chen H., Chen S., Martinez D., and Matthaeus W. (1991) 'Lattice boltzmann model for simulation of magnetohydrodynamic phenomena', *Phys. Rev. Lett.*, vol. 67, p. 3776.

[118] Yu D., Mei R., Luo L.S., and Shyy W. (2003) 'Viscous flow computations with the method of lattice boltzmann equation', *Prog. Aerosp. Sci.*, vol. 39, pp. 329–367.

[119] Welander P. (1954) 'On the temperature jump in a rarefied gas', *Ark. Fys*, vol. 7, pp. 507–553.

[120] Saint-Raymond L., *Hydrodynamic limits of the Boltzmann equation, Lecture Notes in Mathematics* (Springer, 1971).

[121] Wolf-Gladrow D.A., *Lattice Gas Cellular Automata and Lattice Boltzmann Model: An Introduction* (Springer, 2000).

[122] Young T. (1805) 'An essay oncohesion of fluids', *Tran.Royal Soc.London*, vol. 95, pp. 65–87.

[123] Extrand C.W. (2003) 'Contact angles and hysteresis on surfaces with chemically heterogeneous islands', *Langmuir*, vol. 19(9), pp. 3793–3796.

[124] Kijlstra J. (2002) 'Roughness and topology of ultra-hydrophobic surfaces', *Colloids and Surfaces A: Physicochem. Eng. Aspects*, vol. 206(1-3), pp. 521–529.

[125] Wolfram S. (1986) 'Cellular automaton fluids 1: Basic theory', *J. Stat. Phys*, vol. 45, pp. 471– 526.

[126] Lavallee P., Boon J.P., and Noullez A. (1991) 'Boundaries in a lattice gas flows', *Physica*, vol. 47, pp. 233–240.

[127] Nie X., Doolen G.D., and Chen S. (2002) 'Lattice boltzmann simulation of fluid flows in mems', *J. Stat. Phys.*, vol. 107, pp. 279–289.

[128] Blossey R. (2003) 'Self-cleaning surfaces virtual realities', *Nature Materials*, vol. 2, pp. 301–306.

[129] Homsy G.M. (1987) 'Viscous fingering in porous media', *Ann. Rev. Fluid Mech.*, vol. 19, pp. 271–311.

[130] Lu Z., Kandlikar S.G., Rath C., Grimm M., Domigan W., White A.D., Hardbarger M., Owejan J.P., and Trabold T.A. (2009) 'Water management studies in pem fuel cells,part ii: ex situ investigation of flow maldistribution, presure drop and two phase flow pattern in gas channels', *Int. J. Hydrogen Energy*, vol. 34, pp. 3445–3456.

[131] Owejan J.P., Gagliardo J.J., Sergi J.M., Kandlikar S.G., and Trabold T.A. (2009) 'Water management studies in pem fuel cells, part i: Fuel cell design and in situ water distribution', *Int. J. Hydrogen Energy*, vol. 34, pp. 3436–3444.

[132] Bazylak A. (2009) 'Liquid water visualization in pem fuel cells: a review', *Int. J. Hydrogen Energy*, vol. 34(9), pp. 3845–3857.

[133] Kang Q., Zhang D., and Chen S. (2004) 'Immiscible displacement in a channel: Simulations of fingering in two dimensions', *Adv. in Water Resour.*, vol. 27, pp. 13–22.

[134] Dimitrakopoulos P. and Higdon J.J.L. (2001) 'On the displacement of three-dimensional fluid droplets adhering to a plane wall in viscous pressure-driven flows', *J. Fluid Mech.*, vol. 435, pp. 327–350.

[135] Yan Y.Y. (2009) 'Physical and numerical modelling of biomimetic approaches of natural hydrophobic surfaces', *Chinese Science Bulletin*, vol. 54, pp. 541–548.

[136] Gao N. and Yan Y.Y. (2009) 'Modeling superhydrophobic contact angles and wetting transition', *J. Bionic Eng.*, vol. 6, pp. 335–340.

[137] Zu Y.Q. and Yan Y.Y. (2010) 'Wetting behaviours of a single droplet on biomimetic micro structured surfaces', *J. Bionic Eng.*, vol. 7, pp. 191–198.

[138] Huang H., Wang L., and Lu X. (2011) 'Evaluation of three lattice boltzmann models for multiphase flows in porous media', *Comput. Math. Appl.*, vol. 61, pp. 3606–3617.

[139] Laroche C., Vizika O., and Kalaydjian F. (1999) 'Network modeling as a tool to predict three-phase gas injection in heterogeneous wettability porous media', *J. Pet. Sci.Eng.*, vol. 24, pp. 155–168.

[140] Piri M. (2003) 'Pore-scale modelling of three-phase flow', *Ph. D. thesis, Department of Earth Science and Engineering, Imperial College London, UK.*

[141] Vananroye A., Puyvelde P.V., and Moldenaers P. (2006) 'Effect of confinement on droplet breakup in sheared emulsions', *Langmuir*, vol. 22, pp. 3972–3974.

[142] Vananroye A., Cardinael R., Puyvelde P.V., and Moldenaers P. (2008) 'Effect of confinement and viscosity ratio on the dynamics of single droplets during transient shear flow', *J. Rheol.*, vol. 52, pp. 1459–1475.

[143] Migler K.B. (2001) 'String formation in sheared polymer blends: Coalescence, breakup, and finite size effects', *Phys. ReV. Lett.*, vol. 86, pp. 1023–1026.

[144] Pathak J.A. and Migler K.B. (2003) 'Droplet-string deformation and stability during microconfined shear flow', *Langmuir*, vol. 19, pp. 8667–8674.

[145] Taylor G.I. (1932) 'The viscosity of a fluid containing small drops of another fluid', *Proc. R. Soc. Lond.*, vol. 138, pp. 41–48.

[146] Taylor G.I. (1934) 'The formation of emulsions in definable fields of flow', *Proc. R. Soc. Lond. Series a-Mathematical and Physical Sciences*, vol. 146, pp. 0501–0523.

[147] Graham D.R. and Higdon J.J.L. (2000) 'Oscillatory flow of droplets in capillary tubes. part 1. straight tubes', *J. Fluid Mech.*, vol. 425, pp. 31–53.

[148] Blunt M.J., Jackson M.D., Piri M., and Valvatne P.H. (2002) 'Detailed physics, predictive capabilities and macroscopic consequences for pore-network models of multiphase flow', *Water Resour. Res*, vol. 25, pp. 1069–1089.

[149] Leger L. and Joanny J.F. (1992) 'Liquid spreading', *Rep. Prog. Phys.*, vol. 55, pp. 431–486.

[150] Chen S. and Doolen G. (1998) 'Lattice boltzmann method for fluid flows', *Annu. Rev. Fluid Mech.*, vol. 30, pp. 329–364.

[151] Sheffield R. and Metzner A.B. (1976) 'Flows of nonlinear fluids through porous media', *AIChE Journal*, vol. 22(4), pp. 736–744.

[152] Lenormand R., Zarcone C., and Touboul E. (1988) 'Numerical models and experiments on immiscible displacement in porous media', *J. Fluid Mech.*, vol. 189, pp. 165–187.

[153] Chandler R., Koplik J., Lerman K., and Willemsen J.F. (1982) 'Capillary displacement and percolation in porous media', *J. Fluid Mech.*, vol. 119, pp. 249–267.

[154] Kovscek A.R., Wong H., and Radke C.J. (1993) 'A pore-level scenario for the development of mixed wettability in oil reservoirs', *AIChE Journal*, vol. 39(6), pp. 1072–1085.

[155] Bear J., *Dynamics of Fluids in Porous Media* (Elsevier, New York., 1972).

[156] Chaudhary K., Cardenas M.B., Deng W., and Bennett P.C. (2013) 'Pore geometry effects on intrapore viscous to inertial flows and on effective hydraulic parameters', *Water Resour. Res.*, vol. 49, pp. 1149–1162.

[157] Hilpert M. and Miller C.T. (1999) 'Experimental investigation on the resonance of a liquid column in a capillary tube', *J. Colloid Interface Sci.*, vol. 219, pp. 62–68.

[158] Valiei A., Kumar A., Mukherjee P.P., L. Y., and Thundat T. (2012) 'A web of streamers: biofilm formation in a porous microfluidic device', *Lab Chip*, vol. 12, pp. 5133–5137.

[159] Lenormand R. and Zarcone C. (1985) 'Invasion percolation in an etched network: measurement of a fractal dimension', *Phys. Rev. Letters*, vol. 54(20), pp. 2226–2229.

[160] Lvoll G., Meheust Y., Maly K.J., Aker E., and Schmittbuhl J. (2005) 'Competition of gravity, capillary and viscous forces during drainage in a two-dimensional porous medium, a pore scale study', *Energy*, vol. 30, pp. 861–872.

[161] Huang H., Huang J.J., and Lu X.Y. (2014) 'Study of immiscible displacements in porous mediausing a color-gradient-based multiphase lattice boltzmann method', *Computers and Fluids*, vol. 93, pp. 164–172.

[162] Pan C., Hilpert M., and Miller C.T. (2004) 'Lattice boltzmann simulation of two-phase flow in porous media', *Water Resour. Res.*, vol. 40, pp. W01501–W015014.

[163] Grunau D., Chen S., and Eggert K. (1993) 'A lattice boltzmann model for multiphase flow', *Phys. Fluids A*, vol. 5, pp. 2557–256.

[164] He X. and Luo L. (1997) 'Lattice boltzmann model for the incompressible navier-stokes equation', *J. Stat. Phys.*, vol. 88(3), pp. 927–944.